Measurements of observables sensitive to colour reconnection in $t\bar{t}$ events with the ATLAS detector at $\sqrt{s} = 13\,\text{TeV}$

Dissertation
zur
Erlangung des Doktorgrades (Dr. rer. nat.)
der
Mathematisch-Naturwissenschaftlichen Fakultät
der
Bergische Universität Wuppertal

vorgelegt von
Shayma Wahdan
aus
Tammun

Wuppertal, October 2022

Abstract

This thesis presents the measurement of observables sensitive to the effects of colour reconnection in top-quark pair-production events. The measurement is performed using $139\,\text{fb}^{-1}$ of 13 TeV proton–proton collision data collected by the ATLAS detector at the Large Hadron Collider. Events are selected by requiring exactly one isolated electron and one isolated muon with opposite charge and two or three jets, where exactly two jets are required to be b-tagged. For the selected events, measurements are presented for the charged-particle multiplicity, the scalar sum of the transverse momenta of the charged particles, and the same scalar sum in bins of charged-particle multiplicity. These observables are unfolded to the stable-particle level, thereby correcting for migration effects due to finite detector resolution, acceptance and efficiency effects. The particle-level measurements are compared with different colour reconnection models in Monte Carlo generators. These measurements disfavour some of the colour reconnection models and provide inputs to future optimisation of the parameters in Monte Carlo generators.

Contents

Introduction

Throughout history, attempts have been carried out to understand the composition of matter and the origin of the universe. This evolved from a naive four-element description of nature through theories and discoveries of atoms, arriving at the sub-atomic level with one of the most precise theories known as the Standard Model (SM) of particle physics [1–7]. However, the SM is not a complete theory since it can not explain some phenomena. For example, it provides no candidate for dark matter. Many theories have been proposed to extend the SM to address these shortcomings, referred to as Beyond the Standard Model (BSM) theories. Therefore, current particle physics research focuses, on the one hand, on precision measurements of SM parameters and, on the other hand, on searches to find evidence for BSM theories. For this purpose, several experiments are built to collide high-energy particle beams and analyse the resulting products.

The Large Hadron Collider (LHC) [8] is the largest particle accelerator in the world, where protons are brought to collisions at very high energies. It provides the opportunity to probe constituents of matter down to very small scales. At the LHC, detectors are positioned at the four collision points to collect the produced particles. One of them is the ATLAS (A Toroidal LHC ApparatuS) detector [9]. The ATLAS detector is a multi-purpose detector designed for studying various processes to provide stringent tests of SM predictions and to search for clues of BSM physics.

The SM describes the elementary particles and three of the four known fundamental interactions: electromagnetic, weak, and strong. The strong interaction is described by the theory of Quantum Chromodynamics (QCD) and is responsible for binding the constituents of the atomic nuclei. These constituent particles are called quarks and gluons. Theoretical predictions describing the strong interaction are to a large extent calculated perturbatively, which provides an approximate solution to QCD at high energies. At low energy transfer (soft QCD) between the interacting partons (quarks or gluons), the perturbation approximation is not valid, and therefore the interaction is described based on phenomenological models. However, these models are not derived from QCD's first principles and come with several free parameters that need to be adjusted to fit the experimental data. Comparisons to experimental data help to exclude specific models or to constrain their parameter space. This thesis focuses on phenomenological models that describe the so-called Colour Reconnection (CR) mechanism.

According to QCD, the strong interaction between quarks and gluons is related to their colour charges. The colour charge is a quantum number similar to the familiar electric charge. However, while electric charges can be observed individually, colour charges are not observed individually in

nature. Instead, colour-neutral bound states are observed. The colour charges are responsible for the colour connections that bind colour-neutral objects. In order to track the colour information, quarks and antiquarks are represented by colour lines with arrows pointing in the direction of the colour flow, and gluons are represented by a pair of colour lines with opposite arrows. The rules for colour connections are illustrated in Fig. 1.1. In the Leading Colour (LC) approximation, each successively emitted parton is colour connected to its parent emitter in the limit of an infinite number of colours. CR is a reconfiguration of the colour connections between partons, which allows colour lines to be formed between partons from different interactions and thus allows different colour topologies compared with the simple LC approach. The simulation of the CR mechanism is poorly understood and several models are implemented in the three parton-shower Monte Carlo (MC) programs, PYTHIA 8 [10], HERWIG 7 [11], and SHERPA 2 [12].

Figure 1.1: Rules for colour connection for elementary quark-gluon vertices [13]. Quark-gluon vertices are shown in black with Feynman diagrams, and colour connection lines are shown with coloured lines.

The inclusion of the CR mechanism in theory predictions allowed to explain the observed increase of the average transverse momentum as a function of charged-particle multiplicity [14, 15]. In addition, the importance of CR relies on the fact that it can shed light on the quest for precise SM measurements, such as the top-quark mass (m_{top}) measurement. The typical hadronisation scale is about 1 fm, while top quarks' average transverse decay length is 0.2 fm [16] at the LHC. Thus, top quarks may interact with the colour fields stretching between partons in the final state [17]. These interactions decrease the precision that can be achieved and result in an uncertainty as large as 400 MeV [18] on m_{top} measurements. Direct measurements of m_{top} reach a precision well below 1 GeV [18, 19]. Therefore, this uncertainty is becoming increasingly important as it becomes a limiting factor to the precision that could be achieved.

Several measurements (partially) sensitive to the modelling of the CR in different scattering processes, e.g. minimum-bias [20], Z boson production [21–23] and top-quark–antiquark ($t\bar{t}$) production [24] events, have been performed at the LHC. However, dedicated measurements of CR in top-quark events have not been performed yet.

This thesis presents a measurement of differential cross-sections of $t\bar{t}$ production as a function of observables sensitive to CR effects. The measurement is performed using 139 fb^{-1} of 13 TeV proton–proton collision data collected by the ATLAS detector at the LHC. The measured observables are the charged-particle multiplicity (n_{ch}), the scalar sum of the transverse momenta of these charged particles ($\sum_{n_{\text{ch}}} p_{\text{T}}$), and the double-differential measurement of the two quantities ($\sum_{n_{\text{ch}}} p_{\text{T}}$ in bins of n_{ch}). The observables are corrected for tracks from additional inelastic proton–proton (pp) collisions in the same or neighbouring bunch crossings (pile-up), for tracks from secondary vertices, and for the effect of tracking inefficiencies. The distributions of the corrected observables are unfolded to stable-particle level in a fiducial phase space chosen to maximise the sensitivity to CR effects. The particle-level measurements are compared with different CR models in MC event generators. Additionally, the total fiducial cross-section is obtained by integrating the differential cross-section. The results presented in this thesis are published in Ref. [25].

The chapters of this thesis are organised as follows: Chapter 2 gives a general overview of the SM

and the top-quark. Chapter 3 summarises the event simulation using theoretical calculations and phenomenological models, focusing on the different CR models. Chapter 4 describes the ATLAS experiment at the LHC. The object definitions and the event selection are introduced in Chapter 5, while the background estimation and the corrections applied to the observables are described in Chapter 6. Chapter 7 is devoted to the extraction of the differential cross-sections, and Chapter 8 details the systematic uncertainties. The results are presented in Chapter 9, and the conclusions are given in Chapter 10.

The Standard Model and the top quark

In this chapter, the theoretical basis of elementary particle physics is discussed. Section 2.1 introduces the SM of elementary particle physics, which describes the current knowledge of elementary particles and their interactions. In Section 2.2, a particular focus is dedicated to the top quark. The top quarks' characteristics, pair production and decay, are explained.

2.1 The Standard Model of particle physics

The SM is a relativistic quantum field theory that describes the elementary particles and their interactions. Measurements continuously confirm its predictions to astonishing levels of accuracy. Nevertheless, it is not a complete theory since it cannot explain some phenomena, such as gravity, dark matter and the asymmetry between matter and antimatter. These phenomena hint at the existence of physics beyond the SM.

The SM is built from two types of elementary particles, namely *fermions* and *bosons*. These names originate from the spin-statistics that these particles obey. Fermions are spin-$\frac{1}{2}$ particles and therefore are described by Fermi-Dirac statistics [26, 27]. Bosons have an integer spin and are, in turn, described by Bose-Einstein statistics [28]. While fermions are the building blocks of matter, spin-1 bosons are the mediators of the electromagnetic, weak and strong interactions. In addition, the SM includes a scalar boson (spin 0), called the *Higgs boson*, which is responsible for generating the mass of the elementary particles through the Higgs mechanism.

2.1.1 Matter particles: fermions

Table 2.1 summarises all fermions with some of their properties. There are 12 fermions (each with an antiparticle counterpart) arranged in three generations. The lightest particles are found in the first generation and the heaviest in the third generation. Particles of the first generation form the stable matter in the universe, while particles of the higher generations are unstable except for neutrinos. These 12 particles are further subdivided according to their quantum numbers into two classes, *quarks* and *leptons*.

The quarks come in six flavours and are further divided into up-type quarks with an electric charge of +2/3 and down-type quarks with an electric charge of −1/3. The up-type quarks are up *u*, charm *c*, and top *t*, while the down-type quarks are down *d*, strange *s*, and bottom *b*. In addition, quarks carry a

colour charge. Each flavour of quarks comes in three possible colours: red (r), green (g) and blue (b), which triples the number of quarks shown Table 2.1. Antiquarks, carry the anticolour charge ($\bar{r}, \bar{g}, \bar{b}$).

The leptons also come in six flavours, similar to the quarks, and are classified as electrically charged or neutral leptons. The charged leptons are the electron e, the muon μ and the tau τ. Each charged lepton is partnered with an electrically neutral lepton, called a neutrino. These neutrinos are named electron neutrinos ν_e, muon neutrinos ν_μ and τ neutrinos ν_τ. Leptons do not carry a colour charge. While charged leptons are reasonably well-understood in the SM, the nature of neutrinos remains a source of unanswered questions. The SM predicts massless neutrinos, but the observation of neutrino oscillation requires neutrinos to have mass [29–31].

Table 2.1: The elementary fermions of the SM and some of their properties. Their electric charge Q, whether the particle carries a colour charge, and mass are given [32].

Generation	Particle	Q	Colour?	Mass
	Quarks			
I	up, u	+2/3	Yes	2.2 MeV
	down, d	-1/3	Yes	4.7 MeV
II	charm, c	+2/3	Yes	1.3 MeV
	strange, s	-1/3	Yes	93 MeV
III	top, t	+2/3	Yes	172.7 GeV
	bottom, b	-1/3	Yes	4.2 GeV
	Leptons			
I	electron, e	-1	No	0.511 MeV
	electron neutrino, ν_e	0	No	< 2 eV
II	muon, μ	-1	No	106 MeV
	muon neutrino, ν_μ	0	No	< 2 eV
III	tau, τ	-1	No	1.78 GeV
	tau neutrino, ν_τ	0	No	< 2 eV

2.1.2 The fundamental interactions

The SM covers three fundamental interactions: the strong, electromagnetic and weak forces. The fourth fundamental force, gravity, is not described by the SM, which is one of its shortcomings. However, gravity is by far the weakest force, and its effect is assumed to be negligible in the interactions of elementary particles. The electromagnetic and weak forces were unified in one theory at energies above ~ 100 GeV, called the electroweak theory, proposed by Glashow [1], Weinberg [2] and Salam [3].

The fundamental forces in the SM are mediated by gauge bosons. Table 2.2 summarises these bosons with some of their properties. The massless photon, γ, mediates the electromagnetic interaction. The three massive bosons W^+, W^-, and Z^0 are responsible for the weak interaction. The eight massless gluons, g, are the generators of the strong interaction. There are eight gluons, due to the different

colour charges. Each gluon carries one unit of colour charge and one unit of anticolour charge in one of a set of mixed-colour states known as the *colour octet*. The eight gluon colour states are: $r\bar{g}, r\bar{b}, g\bar{r}, g\bar{b}, b\bar{r}, b\bar{g}, \frac{1}{\sqrt{2}}(r\bar{r} - g\bar{g})$, and $\frac{1}{\sqrt{6}}(r\bar{r} + g\bar{g} - 2b\bar{b})$. Other gauge bosons do not carry a colour charge. Each gauge boson couples with particles that are charged under the corresponding force's quantum numbers.

Table 2.2: The force-mediator bosons and some of their properties. The force they mediate, their electric charge Q, whether the particle carries a colour charge, and mass are given [32].

Particle	Force	Q	Colour?	Mass [GeV]
Photon, γ	Electroweak	0	No	0
$W^{\pm}$	Weak	± 1	No	80.4
Z	Weak	0	No	91.2
gluon, g	Strong	0	Yes	0

The strong interaction

The strong interaction is described by QCD, a gauge theory based on the non-abelian $SU(3)_C$ symmetry group. The colour charge is the quantum number responsible for the strong interaction (hence the subscript C). Quarks carry a colour charge, and therefore, they interact via the strong force by exchanging gluons. As gluons themselves carry a colour charge, they can interact with themselves.

The strength of the strong interaction is represented by the strong coupling constant, α_s, which depends on the momentum transfer Q^2 of the interaction and is defined at a reference scale μ_r, referred to as the *renormalisation scale*, as [33]:

$$\alpha_s(Q^2, \mu_r^2) = \frac{\alpha_s(\mu_r^2)}{1 + \frac{\alpha_s(\mu_r^2)}{12\pi} \left(11 n_C - 2 n_f\right) \ln\left(Q^2/\mu_r^2\right)} , \tag{2.1}$$

where n_C is the number of colours and n_f is the number of quark flavours accessible at this energy scale (i.e. whose mass is lower than the energy scale). The results of several measurements sensitive to α_s at different values of Q^2 are presented in Fig. 2.1. Taking the increase of α_s towards lower values of Q^2 into consideration, Eq. (2.1) can be written as:

$$\alpha_s(Q^2, \mu_r^2) = \frac{12\pi}{\left(11 n_C - 2 n_f\right) \ln\left(Q^2/\Lambda^2\right)} , \tag{2.2}$$

where Λ is the infrared cutoff scale of QCD at which the perturbative approximation of the coupling constant diverges. Below this scale, the perturbative approach breaks down because α_s becomes too large. It is estimated to be $\Lambda \simeq 220$ MeV. The dependence of α_s on Q^2, defines the characteristic properties of QCD interactions, as long as $n_f < \frac{11}{2} n_C$ holds:

- Asymptotic freedom [5]: It refers to the fact that the strong coupling constant goes to zero with

Q^2 going to infinity.

$$\lim_{Q^2 \to \infty} \alpha_s = 0 \,. \qquad (2.3)$$

Therefore, the strength of the interaction between colour-charged particles decreases with Q^2.

- Quark confinement: It refers to the fact that at small Q^2 or large distances, the coupling between quarks becomes strong and prevents quarks from existing as isolated particles. The increasing potential energy due to the increasing distance between the quarks is large enough to create additional quark-antiquark pairs in a process known as *hadronisation*. This results in the quarks forming colour-neutral bound states, called hadrons. Hadrons can be either baryons (qqq) or mesons ($q\bar{q}$). In this case, the momentum transfer Q^2 is similar to the QCD scale, $Q^2 \approx \Lambda^2$, therefore, perturbation theory is not valid. In practice, this problem is resolved by using the *factorisation theorem* which factorises the non-perturbative hadronisation process from the perturbative hard process as they occur at different energy scales.
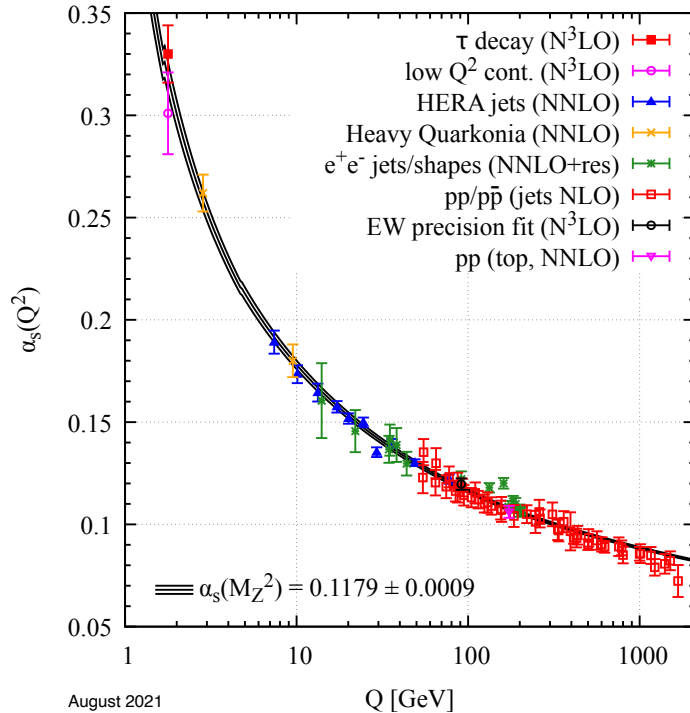
Figure 2.1: Summary of measurements of α_s as a function of the energy scale Q [32].

The electromagnetic interaction

The electromagnetic interaction is described by the theory of Quantum Electrodynamics (QED), which is based on the Abelian $U(1)_Q$ gauge symmetry group. The quantum number of the electromagnetic force is the electric charge. It is mediated by the photon γ, which is massless and electrically neutral. Therefore, photons couple to all quarks, charged leptons and charged gauge bosons. Neutrinos are

electrically neutral, and therefore they do not participate in the electromagnetic interaction. Similarly, since photons do not carry electric charge themselves, self-coupling is not possible. The strength of the electromagnetic interaction is represented by the coupling constant $\alpha_{em}(Q^2)$, which increases for larger energy scales of the interaction. At low energies, α_{em} is approximately $1/137$.

The weak interaction
The weak interaction is based on the non-abelian $SU(2)_L$ symmetry group of the weak isospin. The gauge bosons of the weak force are the massive $W^\pm$ and Z^0 bosons. The weak interaction is the only force acting on all elementary fermions. In addition, $W^\pm$ and Z^0 bosons can couple directly to one another and among themselves, resulting in triple- and quartic-gauge-couplings.

Interactions involving the exchange of the neutral Z^0 boson are called *neutral-current* interactions, while interactions arising from the charged $W^\pm$ boson exchanges are called *charged-current* interactions. The neutral-current interaction interferes with the electromagnetic interaction when coupling to charged leptons and quarks. A pure neutral-current interaction has to resort to neutrino scattering since the neutrinos do not interact via the electromagnetic interaction. The charged-current interactions are the only interactions that can change a fermion's flavour. In the SM, the flavour-changing neutral current is forbidden at the tree level.

The subscript L in the $SU(2)_L$ group indicates that the charged-current interaction only couples with left-handed[1] isospin fermions (and right-handed anti-fermions). The left-handed fermions and right-handed anti-fermions form doublets with weak isospin $I_3 = \pm 1/2$, while right-handed fermions and left-handed anti-fermions are singlets ($I_3 = 0$). The left-handed isospin doublets are written as:

$$\begin{pmatrix} \nu_e \\ e \end{pmatrix}, \begin{pmatrix} \nu_\mu \\ \mu^- \end{pmatrix}, \begin{pmatrix} \nu_\tau \\ \tau^- \end{pmatrix}, \begin{pmatrix} u \\ d' \end{pmatrix}, \begin{pmatrix} c \\ s' \end{pmatrix}, \begin{pmatrix} t \\ b' \end{pmatrix}. \tag{2.4}$$

where, $d', s',$ and b' are the weak eigenstates, which are not the same as the mass eigenstates of quarks, $d, s,$ and b. The mixing between these eigenstates is described by the Cabibbo-Kobayashi-Maskawa (CKM) matrix [34, 35]:

$$\begin{pmatrix} d' \\ s' \\ b' \end{pmatrix} = V_{CKM} \begin{pmatrix} d \\ s \\ b \end{pmatrix}, \tag{2.5}$$

where the elements of this unitary CKM-matrix have been determined experimentally [32]:

$$V_{CKM} = \begin{pmatrix} V_{ud} & V_{us} & V_{ub} \\ V_{cd} & V_{cs} & V_{cb} \\ V_{td} & V_{ts} & V_{tb} \end{pmatrix} = \begin{pmatrix} 0.974 & 0.224 & 0.004 \\ 0.221 & 0.975 & 0.041 \\ 0.008 & 0.042 & 1.014 \end{pmatrix}. \tag{2.6}$$

The diagonal elements of the matrix are close to one, while the off-diagonal elements are small. This has a consequence as it introduces the possibility of transitions between different quark generations. The transition amplitude for a quark i into quark j by the exchange of a W boson is proportional to the element V_{ij}. Therefore, the transitions of quarks in the same generation are the dominant ones.

---

[1] Left-handed describes a particle whose spin is oriented opposite its direction of motion.

Electroweak unification

In experiments with the decay of the Z^0, it was found that the coupling to quarks and leptons seems to be different. This was not expected as they both have the same weak isospin. Furthermore, it turned out that the coupling depends on the strength of the electric charge. This inconsistency could be solved by unifying the electroweak and the electromagnetic interactions at energies above $\sim 100\,\text{GeV}$.

The theory of electroweak interactions is based on the symmetry group $SU(2)_L \times U(1)_Y$. The conserved quantum numbers are the weak isospin for the $SU(2)_L$ gauge symmetry and the weak hypercharge Y for the $U(1)_Y$ gauge symmetry. The weak hypercharge is defined as $Y = 2(Q - I_3)$. The $SU(2)_L \times U(1)_Y$ group has four generators that lead to massless gauge bosons: W_1, W_2, W_3 generated by the weak isospin and the gauge boson B generated by the weak hypercharge.

In this theory, a linear combination of $SU(2)_L$ eigenstates gives rise to the weak charged-currents, corresponding to the physical $W^\pm$ bosons, while the physical neutral fields, Z^0 bosons and the photons, are obtained through the mixing of $SU(2)_L$ and $U(1)_Y$ eigenstates as follows:

$$W^\pm = \frac{1}{\sqrt{2}}(W_1 \pm iW_2)\,, \qquad (2.7)$$

and

$$\begin{pmatrix} \gamma \\ Z^0 \end{pmatrix} = \begin{pmatrix} \cos\theta_w & \sin\theta_w \\ -\sin\theta_w & \cos\theta_w \end{pmatrix} \begin{pmatrix} B \\ W_3 \end{pmatrix}\,, \qquad (2.8)$$

where θ_w is the electroweak mixing angle.

The experiments have confirmed the existence of the $W^\pm$ and Z^0 bosons, with masses of $m_W = 80.363 \pm 0.020\,\text{GeV}$ and $m_Z = 91.1876 \pm 0.0021\,\text{GeV}$ respectively [32]. However, including a mass term in the SM Lagrangian will violate the local $SU(2)_L \times U(1)_Y$ gauge invariance. This problem, in addition to the mass problem of fermions, was the motivation for developing the theory of spontaneous electroweak symmetry breaking, commonly known as the Higgs mechanism, which is briefly explained in the following section.

2.1.3 Higgs mechanism

The electroweak theory described above includes only massless gauge fields for the weak interaction. This contradicts various experimental evidence that the weak interaction has a very short range and is mediated by massive gauge bosons. However, adding mass terms spoils local gauge invariance under $SU(2)_L \times U(1)_Y$, which is a fundamental assumption of the theory. This implies that a piece of the puzzle is still missing for correctly describing the electroweak interaction. The solution has been found by the Brout-Englert-Higgs (BEH) mechanism [36–39] using the concept of spontaneous symmetry breaking. In this theory, a doublet of complex $SU(2)_L$ scalar fields, Φ, is introduced:

$$\Phi = \begin{pmatrix} \phi^+ \\ \phi^0 \end{pmatrix} = \frac{1}{\sqrt{2}} \begin{pmatrix} \phi_1 + i\phi_2 \\ \phi_3 + i\phi_4 \end{pmatrix}\,. \qquad (2.9)$$

where ϕ^0 and ϕ^+ are neutral and positively charged fields, respectively. This additional scalar field is defined to have weak hypercharge $Y = +1$. The potential for the doublet Φ is taken to be:

$$V(\Phi) = \mu^2 \Phi^\dagger \Phi + \lambda (\Phi^\dagger \Phi)^2\,, \qquad (2.10)$$

with $\mu^2 < 0$ and $\lambda > 0$. With this parameter choice, a non-vanishing vacuum expectation value v (corresponds to the minimum of the potential) exists $v = \left(\frac{-\mu^2}{\lambda}\right)^{1/2}$. The non-zero v results in the breaking of the electroweak symmetry to the electromagnetic component:

$$SU(2)_L \times U(1)_Y \to U(1)_Q. \tag{2.11}$$

A new particle, called the Higgs boson, occurs with a mass of $m_H = \sqrt{\frac{\lambda}{2}} v$. Furthermore, the W and Z bosons obtain mass, which depends on the coupling constants and the v of the Higgs field.

$$m_W = \frac{gv}{2} \quad , \quad m_Z = \frac{gv}{\cos\theta_w} \quad , \quad m_\gamma = 0. \tag{2.12}$$

The fermion masses are also generated by coupling the fermions to the Higgs field (Yukawa coupling). The Yukawa coupling is denoted by y_f and is related to the fermion masses by:

$$m_f = \frac{y_f}{\sqrt{2}} v. \tag{2.13}$$

This shows that more massive particles have stronger coupling to a Higgs boson, so the coupling to the top quark is the largest. More than forty years after its prediction, a particle consistent with the Higgs boson was discovered [40, 41], thus completing the SM framework.

2.2 The top quark

After the discovery of the b-quark in 1977 [42], an intensive search for its up-type partner, the top quark, began [43]. In 1995, almost twenty years later, the top quark was discovered by the CDF [44] and DØ [45] experiments at the Tevatron collider[2].

The top quark is the heaviest known elementary particle to date, with a mass almost 40 times heavier than the b-quark. The most recent combination by the ATLAS experiment puts the top-quark mass at [46]:

$$m_t = 172.69 \pm 0.48\,\text{GeV}. \tag{2.14}$$

Because of this large mass, the decay width of the top quark is very large, and consequently, it has a very short lifetime of about $\approx 0.5 \times 10^{-24}$ s [16]. This timescale is about one order of magnitude smaller than the timescale of the strong interaction to form hadrons [47]. Hence, the top quark decays before it forms hadrons, passing all its properties to its decay products. This is a unique feature of the top quark, as it allows one to study a 'bare' quark. The top quark's properties, such as the spin, are not affected by hadronisation and consequently can be directly studied using the decay products. Additionally, the large mass implies a large coupling to the Higgs boson (close to unity), which suggests that the top quark plays an important role in the electroweak symmetry-breaking.

At hadron colliders, top quarks are mainly produced in pairs via the strong interaction. Single top quarks are produced via the weak interaction in association with a b-quark, a light-quark or a W boson. This thesis presents a measurement in top-quark pair ($t\bar{t}$) production, single top-quark production is

---

[2] The Tevatron was a proton–antiproton collider operated at $\sqrt{s} = 1.8$ and $1.96\,\text{TeV}$ centre-of-mass energy at Fermilab, in operation from 1983 to 2011.

treated as a background process and is mentioned later. In the following, the $t\bar{t}$ pair production and the top-quark decay are explained.

2.2.1 Top-quark pair production

At the LHC, the dominant production process of the top quark is top-quark pair production via the strong interaction. At Leading Order (LO), the $t\bar{t}$ pair is produced either by gluon-gluon fusion (see Figs. 2.2(a) to 2.2(c)) or quark-antiquark annihilation (see Fig. 2.2(d)).

| (a) | (b) | (c) | (d) |
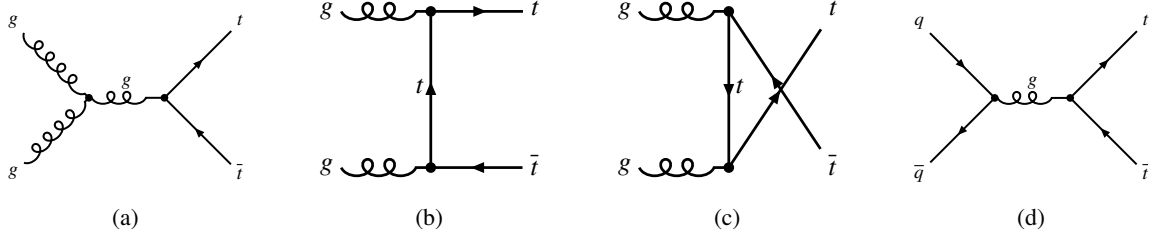
Figure 2.2: LO Feynman diagrams for top-quark pair production via the strong interaction at hadron colliders: the (a) t-channel, (b) s-channel and (c) u-channel diagrams for production via gluon-gluon fusion, (d) the production via quark-antiquark annihilation.

In the parton model, protons are composed of three valence quarks (u, u, and d), which are bound together by gluons, and virtual quark-antiquark pairs (sea quarks). Any of the constituents is referred to as parton. A hard scattering process in a pp collision occurs between partons of the two colliding protons. Each parton is primarily described by a Parton Distribution Function (PDF) $f(x, Q^2)$. The PDF $f_1(x_i, Q^2)$ represents the probability of finding the parton i inside the hadron 1 with a momentum fraction x of the total hadron momentum, where Q^2 is the energy scale of the interaction.

The production cross-section, σ, of a certain process can be calculated using the factorisation theorem [48], which states that the total cross-section can be factorised into a non-perturbative part, described by Parton Distribution Functions (PDFs), and a perturbative part:

$$\sigma_{pp\to t\bar{t}} = \sum_{i,j=q,\bar{q},g} \int dx_1 \, dx_2 f_i(x_1, \mu_f^2) f_j(x_2, \mu_f^2) \cdot \hat{\sigma}_{i,j\to t\bar{t}}(x_1, x_2, \hat{s}, \mu_r^2, \mu_f^2), \tag{2.15}$$

where $\hat{s}$ is the square of the pp centre-of-mass energy, $\hat{\sigma}_{i,j\to t\bar{t}}$ is the partonic cross-section, μ_f is the factorisation scale, which defines the boundary between the perturbative and the non-perturbative part. The sum runs over all pairs of partons (i, j) contributing to the process.

The partonic cross-section can be calculated using a perturbation series in orders of α_s. PDFs can be determined experimentally at a specific energy scale. Several collaborations extracted the PDFs from various measurements, such as CTEQ [49] and NNPDF [50]. The PDFs can be extrapolated to different μ_f^2 scales using the Dokshitzer-Gribov-Lipatov-Altarelli-Parisi (DGLAP) equations[51–53]. Fig. 2.3 shows an example of a PDF for two different energy scales.

The relative contribution from the annihilation and fusion processes depends on the PDFs of the hadron. In $p\bar{p}$ collision, both quarks and antiquarks can be valence quarks and thus the contribution from the quark-antiquark annihilation can dominate, as in the case of the Tevatron collider. However, in pp collisions, the only source of antiquarks is the quark sea of the proton. Thus, gluon fusion dominates the production. Additionally, the relative contribution depends on the centre-of-mass energy
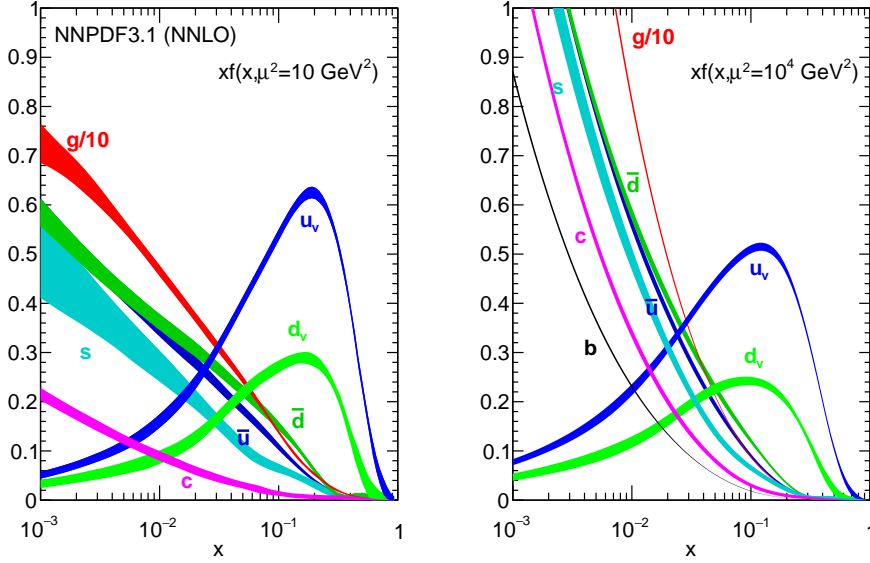
Figure 2.3: Examples of PDF obtained in NNLO NNPDF3.1 global analysis at different scales (left) $Q^2 = 10\,\text{GeV}^2$ and (right) $Q^2 = 10^4\,\text{GeV}^2$ [50].

of the colliding partons. At higher energy, the gluon PDFs increases, see Fig. 2.3, and thus dominates the production, irrespective of the collision type. Furthermore, the $t\bar{t}$ cross-section increases with the increased centre-of-mass energy, because a smaller fraction of the parton energy is needed to reach the $t\bar{t}$ production threshold ($x \sim \frac{2m_{\text{top}}}{\sqrt{s}} = 0.03$ for $\sqrt{s} = 13$ TeV).

The theoretical prediction of the $t\bar{t}$ production cross-section is calculated at Next-to-Next-to-Leading Order (NNLO) precision in QCD by the Top++ 2.0 program [54] including the resummation of Next-to-Next-to-Leading Logarithm (NNLL) soft-gluon terms which yields:

$$\sigma(t\bar{t}) = 832^{+47}_{-51}\,\text{pb}, \tag{2.16}$$

at a centre-of-mass energy of 13 TeV and assuming a top-quark mass m_t of 172.5 GeV. Fig. 2.4 shows a comparison of the theoretical prediction to the measurements of the $t\bar{t}$ production cross-section at different centre-of-mass energies.

2.2.2 Top-quark decay

The top quark decays via the electroweak interaction into a W boson and a down-type quark, $t \to Wq$. The branching ratio for each decay mode is proportional to the square of the corresponding CKM matrix element, where $V_{tb} \gg V_{ts}, V_{td}$. Therefore, the decay mode $t \to Wb$ is the dominant one with a branching ratio $\mathcal{B} \approx 99.9\,\%$. The decay modes $t \to Ws$ ($\mathcal{B} \approx 0.1\,\%$) and $t \to Wd$ ($\mathcal{B} \approx 0.01\,\%$) are suppressed due to the small values of the corresponding CKM matrix element.

The decay channels of the $t\bar{t}$ pair are determined according to the subsequent decays of the two W bosons, $t\bar{t} \to W^+bW^-\bar{b}$. The W boson decays leptonically into a charged lepton and its corresponding
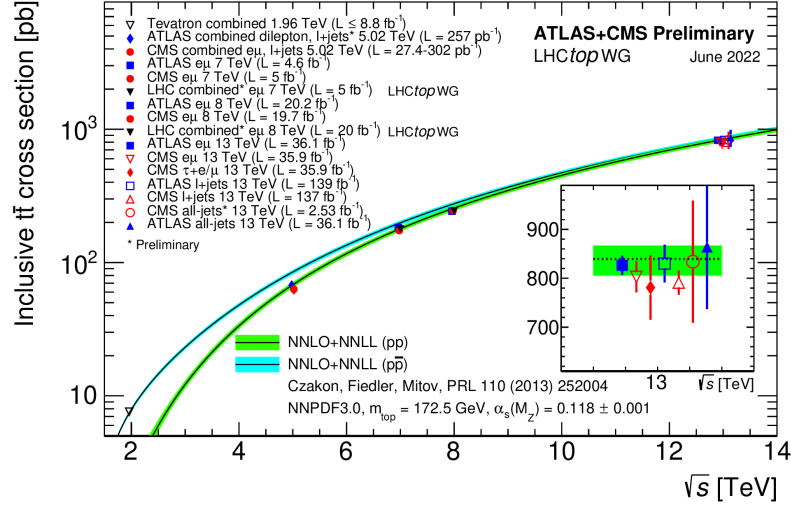
Figure 2.4: Summary of LHC and Tevatron measurements of the top-pair production cross-section as a function of the centre-of-mass energy compared to the NNLO QCD calculation complemented with NNLL resummation (Top++ 2.0). The theory band represents uncertainties due to renormalisation and factorisation scale, parton density functions and the strong coupling. The measurements and the theory calculation are quoted at $m_t = 172.5$ GeV. Measurements made at the same centre-of-mass energy are slightly offset for clarity [55].

neutrino with $\mathcal{B} \approx 32.6\,\%$ or hadronically into two quarks $q\,\bar{q}$ with $\mathcal{B} \approx 67.4\,\%$. Fig. 2.5 shows the decay chains of the top quark.
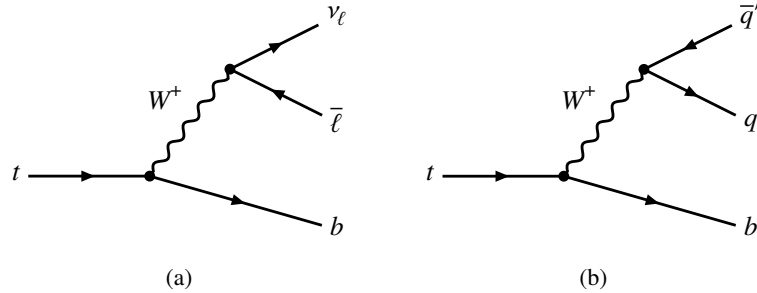
Figure 2.5: The decay of a top quark into a W^+ boson and a b-quark. The leptonic decay of the W^+ boson into a charged antilepton and its corresponding neutrino is shown in (a), while the hadronic decay of the W^+ boson into a quark-antiquark pair is shown in (b).

Therefore, the $t\bar{t}$ final state can be classified into three decay channels:

- Dilepton channel: In this channel, both W bosons decay leptonically, $t\bar{t} \rightarrow \ell^+ \nu b \ell^- \bar{\nu}\bar{b}$. This channel has the lowest branching ratio, which is 10.5 % but has the highest signal-to-background ratio compared to the other two channels. The presence of two charged leptons and high missing transverse momentum resulting from the two neutrinos leads to a clean signature in this channel. However, the presence of two neutrinos makes it difficult to reconstruct the event. The measurement presented in this thesis is performed in this channel, where one of the leptons is

an electron, while the other is an opposite sign muon.

- lepton+jets channel: One of the two W bosons decays hadronically, while the other decays leptonically, $t\bar{t} \rightarrow \ell \nu b q \bar{q}' \bar{b}$. The branching ratio for this channel is 43.8 %, which is much higher than the dilepton channel. However, the expected number of background events in this channel is also larger than in the dilepton channel.

- All-hadronic channel: Here, both W bosons decays hadronically, $t\bar{t} \rightarrow q\bar{q}' b q'' \bar{q}''' \bar{b}$. The branching ratio for this channel is the largest compared to the other two channels, which is 45.7 %. However, it suffers from a large number of background events from multijet production and large combinatorial background.

The $t\bar{t}$ decay rates are illustrated in Fig. 2.6. The charged lepton can be either an electron, a muon or a tau. The tau lepton has a short lifetime $\tau \approx \times 10^{-13}$s [32], and it decays either hadronically or leptonically. The hadronic decay is dominant with a branching ratio of 62.9 %. In the remaining decays, the tau decays into two neutrinos and either an electron or a muon. In the definition of the dilepton channel in this analysis, the leptonic decay of tau-leptons is included.
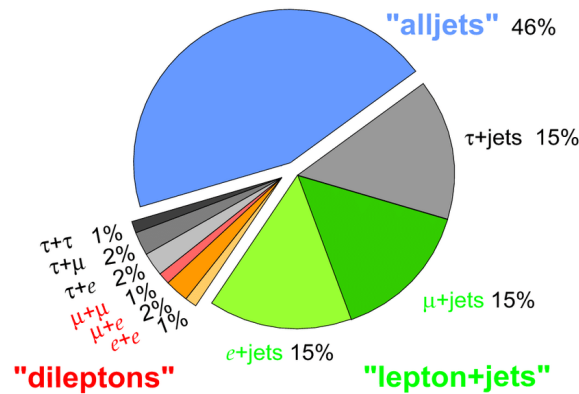
Figure 2.6: A pie chart representing individual $t\bar{t}$ pair decay rates [56]. The all jets (all hadronic) channel, the dilepton and the lepton+jets channel. The lepton+jets channel comprises the e +jets and μ +jets channel as well as τ +jets events with an electron or muon in the final state.

Event generation and simulation

Event simulation is a method of imitating real data events using theoretical calculations and phenomenological models. The tools employed to simulate physics events are called MC event generators. MC event generators are of utmost importance for experimental particle physics as a tool providing a source of simulated events for analysis design, signal and background modelling, and unfolding detector effects. Even though the overall performance of the event generators is good, the understanding of some phenomena is insufficiently understood or can be significantly improved. One of these is the modelling of CR.

In Section 3.1, the various steps of the event generation chain are briefly introduced, while a particular focus on the simulation of the CR mechanism is given in Section 3.2. The samples of simulated events used in this analysis are introduced in Section 3.3.

3.1 Event generation

The event generation is done in several steps as shown in Fig. 3.1. It starts at small distances, where the colliding protons can be viewed as collections of partons. The hard interaction occurs between two partons from the colliding protons leading to the hard scattering process. The generated partons from the hard process undergo a successive emission and evolution of particles, referred to as Parton Shower (PS). At larger distances, coloured partons combine to form colour-neutral hadrons during the hadronisation stage. Finally, the accompanying activity to the hard-scatter process, called Underlying Event (UE), is included in the simulation.

In this section, the various steps of the event generation are briefly described, followed by an overview of the MC event generators used in this analysis.

Hard scattering process

The hard scattering process, as indicated by the white blob in the centre of Fig. 3.1, describes the highest momentum interaction of two partons of the incoming protons and results in new massive particles. For example, a $t\bar{t}$ pair can be created in the collision of a pair of gluons from the incoming protons.

The simulation of the hard process follows the factorisation theorem, given in Eq. (2.15). The PDFs and the partonic cross-section need to be provided. The partonic cross-section, $\hat{\sigma}_{i,j\to X}$, of a final state
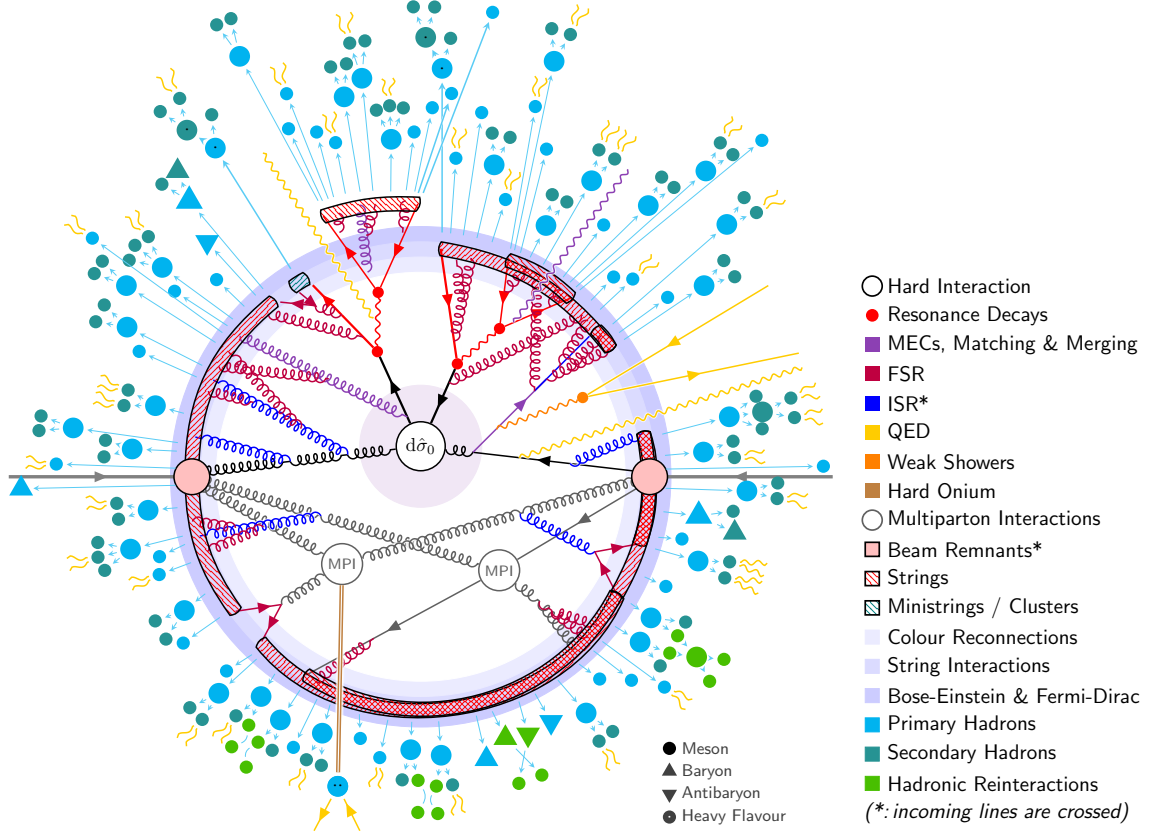
Figure 3.1: Illustration of a pp collision event, $t\bar{t}$, simulated by a MC event generator. The hard interaction is followed by the decay of both top quarks (small red blobs). Additional hard QCD radiation is produced and a secondary interaction takes place before the final-state partons hadronise and hadrons (blue blobs) decay. Photon radiation occurs at any stage (yellow) [57].

X can be obtained from the matrix element, $\mathcal{M}_{i,j\rightarrow X}$, for a specific initial state (i, j) as:

$$\hat{\sigma}_{i,j\rightarrow X} = \int \mathrm{d}\Omega |\mathcal{M}_{i,j\rightarrow X}|^2 (\Omega, \mu_\mathrm{f}^2)\,, \tag{3.1}$$

by integrating over the full solid angle Ω. The matrix element $\mathcal{M}_{i,j\rightarrow X}$ corresponds to the scattering amplitude of the process to occur and can be obtained from the Feynman diagrams to a certain order of the perturbative series in α_s. Higher-order corrections are important for the precision and stability of the calculation. For some processes Next-to-Leading Order (NLO) or even NNLO calculations are available. Fig. 3.2 shows an example of three Feynman diagrams for a $t\bar{t}$ final state at tree level and NLO with an additional emission or including a virtual correction. Once the ME is determined, it is integrated over the phase space. In higher-order Matrix Element (ME) calculations, divergent terms occur which are removed by a renormalisation procedure, using the renormalisation scale μ_r.

Parton shower

The PS describes the process of quark and gluon radiation from the incoming and outgoing partons
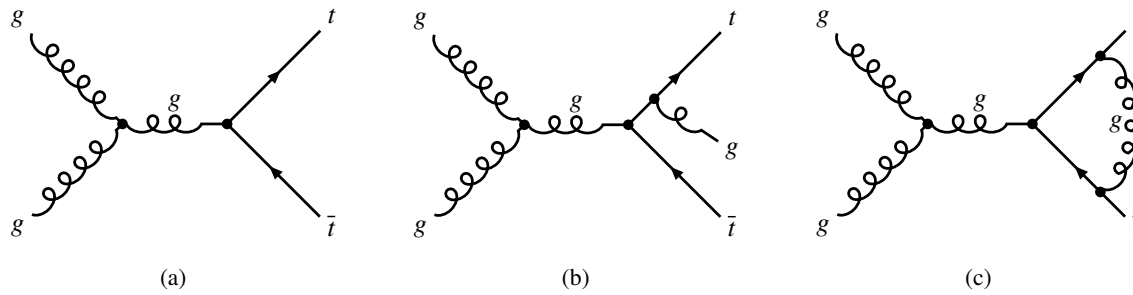
Figure 3.2: Example of Feynman diagrams of a $t\bar{t}$ production (a) at LO, (b) NLO with an additional emission, and (c) NLO with virtual correction.

of the hard-scatter interaction. The PS consists of the Initial State Radiation (ISR) of the incoming partons, represented by the blue lines connected to the hard interaction in Fig. 3.1, and the Final State Radiation (FSR) of the outgoing partons, indicated by the dark red lines in Fig. 3.1. The PS evolution starts from the hard scatter process energy scale and evolves to lower energy scales until a cutoff scale Λ where the perturbative approximation breaks down.

Hadronisation

After the PS is terminated, the resulting coloured partons combine to form colour-neutral hadrons. This process is called hadronisation, shown as blue blobs or triangles in Fig. 3.1. The hadronisation cannot be calculated using perturbation theory. Hence, the simulation relies on phenomenological models. The two main models are the string model [58] and the cluster model [59].

The string model is based on the fact that the potential energy between two partons with opposite colour charges increases linearly with the distance between them[1]. The model pairs quarks with opposite colour and connects them by one-dimensional strings representing the potential. As the quarks move apart, the potential rise breaks the string via the formation of quark-antiquark ($q\bar{q}$) pairs. If the energy of the $q\bar{q}$ pair is low enough a meson is created, otherwise the string breaks repeatedly and a new $q\bar{q}$ pair is created. In addition, the string can break and produce a pair of diquarks allowing the production of baryons.

The cluster model is based on the concept of colour preconfinement [60]. That is, the quarks and gluons produced in the showering are grouped to form colour-neutral combinations of partons, called clusters, after splitting each final state gluon into a $q\bar{q}$ pair. Clusters with high mass are repeatedly split into lower masses clusters. Low energy clusters form a single on-shell meson. As the last step, low-mass clusters are decayed into pairs of mesons or baryons.

After hadronisation, the unstable hadrons decay into stable particles (with a mean lifetime $> 30\,\mathrm{ps}$), shown as dark-green blobs in Fig. 3.1.

Underlying events

The UE comprises all additional interactions and activities in a pp collision that do not take part in the hard scattering process [61]. The UE is colour connected to the hard process and includes partons not participating in the hard-scattering process (beam remnants), radiation processes and an other

---

[1] This applies at distances greater than about a femtometer

contribution is from the Multiple Parton Interactions (MPI), represented by the two parallel white blobs in Fig. 3.1, where several parton pairs undergo secondary hard or semi-hard interactions.

Due to the low energy scale of these processes in which non-perturbative QCD takes place, their simulation relies on phenomenological models. These models come with several free parameters that need to be adjusted to fit the experimental data, in a process called tuning.

Monte Carlo event generators

MC generators are divided into multi-purpose generators that perform all the steps of the event generation and ME generators. ME generators simulate the hard scatter process and need to be interfaced to the multi-purpose generators to simulate the PS, the hadronisation, decay of unstable hadrons, the UE and the CR mechanism.

Event generators used in the scope of this analysis are:

- POWHEG [62, 63]: It is an ME event generator. It performs the ME calculations of a specific hard scatter process at (N)NLO accuracy in perturbative QCD. In addition, it provides the POWHEG method for the matching of the (N)NLO calculation with a parton-shower generator, which generates the hardest emission as part of the ME. This method generates events without negative weights.

- MADGRAPH5_aMC@NLO [64]: It is an ME event generator. As the name implies, it performs the ME calculations of a specific hard scatter process at NLO accuracy in perturbative QCD. The matching of the generated hard process to the PS is performed using the MC@NLO method. The overlap from the PS is subtracted in the ME calculation. This method generates a sizable fraction of events with negative weights.

- PYTHIA 8: It is a multi-purpose event generator. The hard scattering process is calculated at LO accuracy in QCD. The parton-shower simulation is ordered in transverse momentum and the Lund string model is used for the hadronisation. In addition, several models are provided to simulate the CR mechanism, which is detailed in Section 3.2.1.

- HERWIG 7 [65]: Similar to PYTHIA 8, HERWIG 7 is a multi-purpose event generator. The hard scattering process can be calculated up to NLO accuracy in QCD. It uses the angle-ordered shower model as default. The hadronisation is performed based on the cluster model. In addition, several models are provided to simulate the CR mechanism, which is detailed in Section 3.2.2.

- SHERPA [12]: It is a complete multi-purpose event generator, which provides an NLO ME calculation of the hard scattering process. It uses the dipole-shower model and the cluster model as default for the hadronisation. It uses a variant of the MC@NLO method for the matching and the MEPS@NLO method for the merging of the NLO ME and PS. SHERPA 2 has an MPI model based on the PYTHIA 8 one, but without any CR.

In addition, the EVTGEN [66] program is used to simulate the decay of heavy-flavour hadrons, which runs after PYTHIA 8 or HERWIG 7.

3.2 Colour reconnection models

CR introduces a mechanism of reassigning colour connections between partons during the hadronisation, other than the predefined connections according to the simple LC [67] approximation. Fig. 3.3 illustrates the LC approach, in which each successively emitted parton is colour connected to its parent in the limit of infinite number of colours. On the other hand, the CR mechanism allows colour lines to be formed between partons also from different interactions and thus allows different colour topologies compared with the simple LC approach. At the LHC, this is expected to occur at a significant rate due to the high density of coloured partons originating from the PS, the MPI and the beam remnants.

The simulation of the CR mechanism is one of the big unsolved issues and it is poorly understood. Therefore, several phenomenological models are implemented, which need to be confronted and tuned to data.

In the following, the various CR models implemented in the two multi-purpose MC generators, PYTHIA 8 and HERWIG 7, are described. In the SHERPA 2 event generator, the CR mechanism is not simulated, but it is being implemented in the upcoming SHERPA 3.
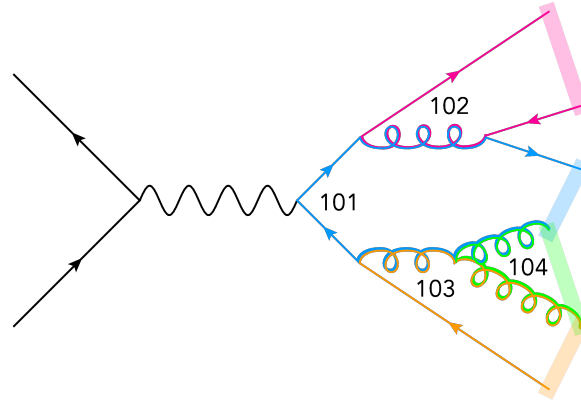
Figure 3.3: Illustration of LC colour flow in a simple $e^+e^- \to q\bar{q} \otimes$ shower event. The shaded regions represent the resulting unique LC string topology [57].

3.2.1 Colour reconnection models in PYTHIA 8

The modelling of CR in PYTHIA 8 is generally based on reconstructing a colour potential that depends on the minimisation of the total string length λ of the colour field, which is defined as [17]:

$$\lambda \approx \sum_{ij} \ln \left(1 + \frac{m_{ij}^2}{m_0^2} \right),$$

(3.2)

where the ij sum runs over all parton pairs connected by a string piece and m_0 is of the order of a typical hadronic mass scale (i.e. the ρ mass). The average hadronic multiplicity of a string piece grows roughly logarithmically with its mass. Therefore, a reduction of λ corresponds to a reduction of the average hadron multiplicity [68].

In the following, the MPI-based, the QCD-inspired and the Gluon-move CR models are described. These models come with a set of parameters that have been tuned based on experimental data. In

addition, a class of CR models has been introduced in Ref. [17] to probe the full effect of the CR mechanism on a $t\bar{t}$ final state, referred to as top-quark-specific CR models.

MPI-based model

The MPI-based CR model [17], referred to as CR0, is the simplest model implemented in PYTHIA 8. Here, the partons are classified by the MPI system they belong to. The reconnection probability for an MPI system with hardness scale p_T is defined as:

$$P_{\text{rec}}(p_T) = \frac{\left(R_{\text{rec}} p_{T0}\right)^2}{\left(R_{\text{rec}} p_{T0}\right)^2 + p_T^2} \, , \tag{3.3}$$

where $0 \leq R_{\text{rec}} \leq 10$ is a phenomenological tunable parameter, called colour-reconnection range. The energy-dependent dampening parameter p_{T0} is used for MPIs. This parameter regularises the partonic cross-section to avoid divergence at low p_T, and it depends on the centre-of-mass energy, E_{CM}, given by:

$$p_{T0} = p_{T0}^{\text{ref}} \left(\frac{E_{\text{CM}}}{E_{\text{CM}}^{\text{ref}}}\right)^{E_{\text{CM}}^{\text{pow}}} \, , \tag{3.4}$$

where p_{T0}^{ref} is the value of p_{T0} at a reference energy $E_{\text{CM}}^{\text{ref}}$, and $E_{\text{CM}}^{\text{pow}}$ is a tunable parameter.

The colour reconnection procedure can be divided into two main steps. First, starting from the lowest-p_T interaction in a set of MPIs, the reconnection probability with the next-highest system in p_T is determined. Then, a uniform random number is drawn from the interval [0, 1]. If the reconnection probability is larger than this number, the systems are reserved to be reconnected. Otherwise, the systems are not connected and the procedure is repeated consecutively with the next-higher systems. In the second step, the reconnection is carried out. Starting from the highest-p_T system, all colour dipoles are found. Next, the gluons from the softer system are inserted on the dipole that gives the smallest total string length. The insertion of a gluon is equivalent to the replacement of a dipole with two new ones. The $q\bar{q}$ pairs originating from the splitting of a gluon are treated similarly, while quarks attached to the beam remnants are ignored in the reconnection process.

QCD-inspired model

This model [69] evolved from the CR0 model. To decide between which partons strings should form, in addition to the minimisation of the string length, it includes the QCD colour rules. The main feature compared to the CR0 model is the introduction of reconnections that form junction structures, in addition to the common string-string reconnections, as shown in Fig. 3.4. This model constructs all pairs of dipoles that are allowed to reconnect by QCD colour rules. This is done iteratively until no further allowed reconnection lowers the total string length. In the following, this model is referred to as CR1.

(a)

(b)
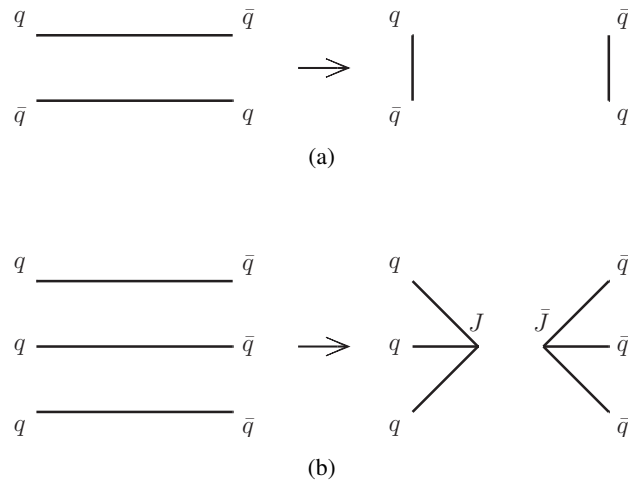
Figure 3.4: Examples of allowed reconnection types in the CR1 model. (a) The ordinary dipole-style reconnection. (b) The formation of baryon-style junction reconnection, where the junction and anti junction are not directly connected [69].

Gluon move model

In this model [68], the reconnection is performed in the same way as in the CR0 model. The main difference with the CR0 model is that only gluons are considered for reconnection. The reconnection is based on the minimisation of the total string length and is performed in two steps. The gluon-move and the gluon-flip.

In the gluon-move step, illustrated in Fig. 3.5(a), all final-state gluons are identified or alternatively a fraction of them, as well as all colour-connected parton pairs. For each final-state gluon, the change in the string length, resulting from moving the gluon from its current location to any other string piece is calculated. The gluon is moved to the string piece for which the move gives the shortest string length.

In the gluon-flip step, shown in Fig. 3.5(b), the quarks have the possibility to be mixed up. This mechanism flips the colour lines between two strings when this minimises the total string length.

(a)   (b)
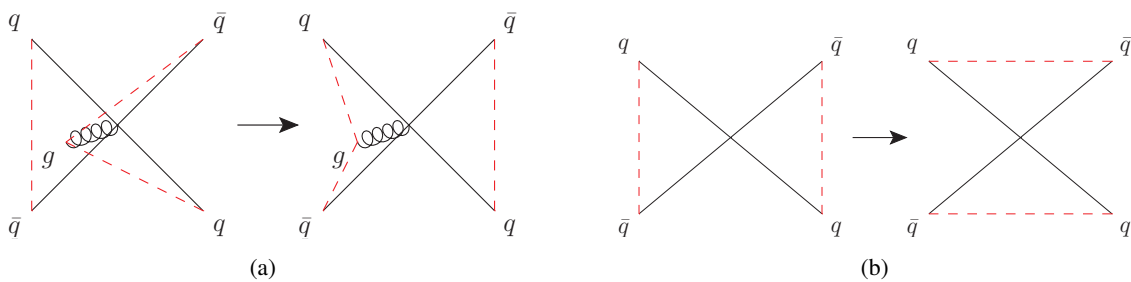
Figure 3.5: Example of (a) gluon-move and (b) gluon-flip reconnections in the gluon-move model. The dashed lines represent the colour configuration of the partons [68].

Top-quark-specific models

In the three default models presented above, the top-quark decay is carried out after the CR has taken

place. Therefore, only the top quark itself is involved in the CR mechanism. In Ref. [17] a class of five CR models involving the top-quark decay products has been introduced.

The CR is performed in two steps. First, the default CR is carried out, involving the undecayed top-quark. Then, the top quark is allowed to decay, and the resulting partons are allowed to reconnect with the rest of the event. To perform the reconnection involving the top-quark decay products, two collections of gluons are constructed, one containing the gluons radiated from the top-quark decay products, referred to as g_t, and the other containing the gluons from the rest of the event, referred to as g_r. Iterating randomly over g_t, gluons from g_t are forced to exchange colour with a gluon from g_r in various ways, leading to five models:

- Forced random (TCR1): g_t is forced to exchange colour with a random gluon from the g_r set.

- Forced nearest (TCR2): g_t is forced to exchange colours with the g_r that minimises $m(g_t, g_r)^2$.

- Forced farthest (TCR3): g_t is forced to exchange colours with the g_r that maximises $m(g_t, g_r)^2$.

- Forced smallest $\Delta\lambda$ (TCR4): a gluon from the set of g_t and a gluon from the set of g_r is forced to exchange colour for which the change in λ, the string length, is minimal.

- Smallest $\Delta\lambda$ (TCR5): same as the previous mode, but the gluons exchange colour only if the change in λ is negative.

Some of these models can give unrealistically large effects. Therefore, a phenomenological strength parameter s, $0 \leq s \leq 1$, can be used to reduce this effect, where each gluon from the set g_t is tested only for reconnection with a probability s.

3.2.2 Colour reconnection models in Herwig 7

The CR algorithm is implemented directly before the cluster fission takes place in the hadronisation. Three models are currently available. The plain and the statistical models are based on the minimisation of the invariant cluster mass, and the baryonic model allows the formation of baryonic clusters. In the following, these models are described.

Plain model

The plain model [70] is the default CR model in Herwig 7. It is based on finding alternative cluster configurations that reduce the sum of invariant cluster masses. The only parameter of this model is the reconnection probability (p_R) which steers the amount of CR.

The reconnection is illustrated in Fig. 3.6 and done in several steps. First, a list of all quarks in the events is created. Then, randomly a quark is picked and for this quark which is part of a cluster, labelled A, a reconnection with all other clusters is considered. The potential reconnection cluster partner is labelled B. The invariant mass of the original clusters configuration A and B is compared to the masses of the possible new clusters C and D. The cluster configuration that results in the smallest sum of invariant cluster masses is then accepted with a certain probability p_R.

This model typically leads to clusters with smaller invariant mass and thus the overall activity in the UE is reduced.

24

(a)	(b)
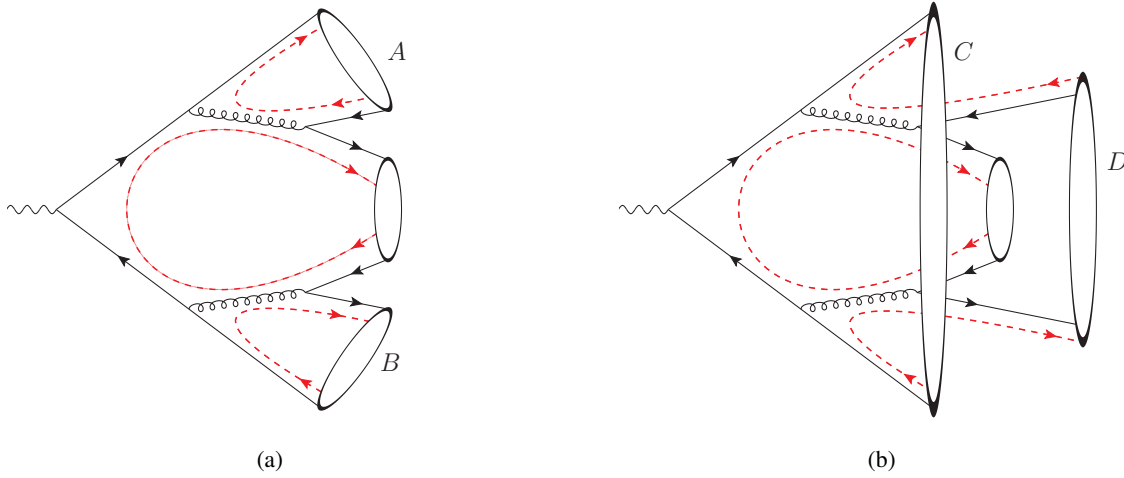
Figure 3.6: Example of clusters colour reconnection in the Plain CR model. (a) Colour-singlet clusters and (b) a possible colour-reconnected state, the partons of the clusters A and B are arranged in new clusters, C and D. Clusters are represented by the ovals and colour lines are dashed [70].

Statistical model

The statistical CR model [70] is a more sophisticated model compared to the plain model. It is based on the simulated annealing optimisation algorithm to find the configuration of clusters that results in the absolute lowest value of the colour length, which is defined as the sum of the squared invariant masses of all clusters in the event.

This model is computationally intensive and the tuning results have shown that the statistical model prefers to have a parameter that forces a quick cooling of the system, which does not result in a global minimum of the colour length. Hence, the results of this model are similar to the plain model.

Baryonic model

The baryonic CR model [71, 72] uses a more sophisticated algorithm that uses geometric measures instead of the colour length and introduces baryonic clusters. Two types of reconnection are possible. The mesonic (ordinary) reconnection occurs if the quarks and antiquarks are flying in the opposite direction, and baryonic reconnection occurs if the quarks and the antiquarks are flying in the same direction.

For each cluster (A) in the event, the rapidity of the cluster constituents is calculated with respect to the z-axis of cluster A for each other cluster (B) in the event. Depending on the cluster constituents' rapidity, the cluster is reserved for mesonic reconnection or baryonic reconnection. In the mesonic case, see Fig. 3.7(a), if the candidate cluster B with the largest rapidity span has a quark axis oriented in the opposite direction to cluster A, the mesonic reconnection is considered with probability p_m. Once the reconnection is accepted, two new mesonic clusters (C and D) are formed. In the baryonic case, see Fig. 3.7(b), given a cluster A, it searches for two other clusters that have the same orientation of the quark axis in rapidity space. Then, the pairs of clusters which have the largest rapidity span is considered for reconnection with probability p_B. Once the reconnection is accepted, two baryonic clusters are formed out of the three mesonic ones.
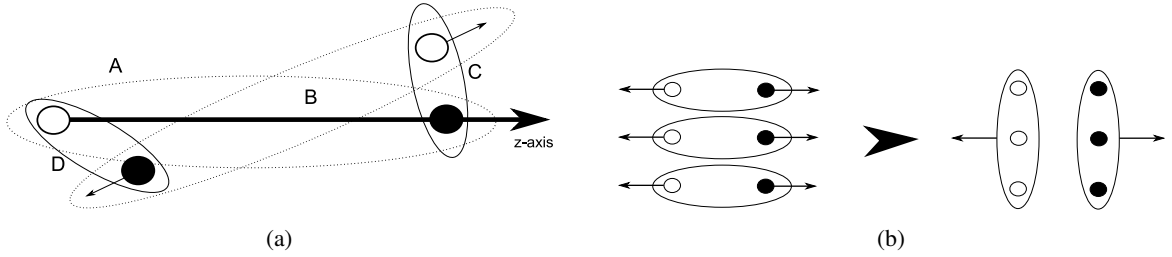
Figure 3.7: (a) Illustration of the mesonic reconnection, the original clusters (A) and (B) are reconnected into two new clusters (C) and (D). (b) Illustration of the baryonic reconnection, the three mesonic clusters on the left are reconnected and two new baryonic clusters are formed on the right. The small black arrows indicate the direction of the quarks. [70].

3.3 Samples of simulated events

In the following, samples of simulated $t\bar{t}$ signal and background events are briefly described. Complete lists of simulated samples used in this analysis can be found in Appendix A.

Signal samples

The nominal sample of simulated $t\bar{t}$ events was generated using the POWHEG ME generator, setting m_{top} to 172.5 GeV and using the NNPDF3.0NLO PDF set [73]. The h_{damp} parameter, which controls the ME to PS matching and effectively regulates the amount of radiation emitted from the $t\bar{t}$ system, was set to $1.5 \times m_{\text{top}}$ [74]. The renormalisation scale μ_{r} and factorisation scale μ_{f} are dynamically set on an event-by-event basis to $\sqrt{m_{\text{top}}^2 + p_{\text{T}}^2(t)}$, where $p_{\text{T}}(t)$ is the top-quark transverse momentum. PS, hadronisation and the UE were modelled with PYTHIA 8, using the A14 tune [75] and the NNPDF2.3LO PDF set [76]. The decays of bottom and charm hadrons are simulated using the EVTGEN program.

Samples with alternative generator settings were produced to estimate systematic uncertainties. A sample with the h_{damp} parameter set to $3 \times m_{\text{top}}$ is used to evaluate the impact of the scale choice used for matching the matrix-element calculation of the $t\bar{t}$ process to the PS. The uncertainty in modelling the PS was evaluated with POWHEG interfaced to HERWIG signal samples, for which the PS were generated with HERWIG 7.1 using the MMHT2014LO [77] PDF set and the HERWIG 7.1-default tune [11, 78]. In addition, three POWHEG+PYTHIA 8 simulated samples, with CR0, CR1, and CR2 colour reconnection models were produced to evaluate the uncertainties in the choice of the CR model. In the CR0 model, the CR setting was modified compared to the default A14 tune [79] to have a consistent tuning to the same data.

To study the sensitivity of the measured observables to the various CR models and UE parameters, additional samples with alternative generators settings were used:

- POWHEG+PYTHIA 8 sample without simulation of the colour reconnection.

- POWHEG+PYTHIA 8 sample with the CR range parameter R_{rec}, introduced in Eq. (3.3), set to its maximal value of ten.

- POWHEG+PYTHIA 8 sample with the MPI $p_{\text{T0}}^{\text{ref}}$ varied down to 2.0 and up to 2.2. The parameter value for the default A14 tune is 2.09 [80].

- POWHEG+HERWIG 7.2 sample with the variation of the CR model to the statistical or the baryonic model.

- POWHEG+HERWIG 7.2 sample without simulation of the colour reconnection.

The samples were normalised to the $t\bar{t}$ cross-section prediction at NNLO in QCD including the resummation of NNLL soft-gluon terms. A value of $\sigma(t\bar{t}) = 832^{+47}_{-51}$ pb was used, assuming $m_{\text{top}} = 172.5$ GeV.

tW and $t\bar{t}V$

The production of a single top-quark via the electroweak interaction in association with a W boson, known as tW channel, is the main background process. An example Feynman diagram of tW production is shown in Fig. 3.8(a). In case both of the W bosons decay leptonically, where one W boson decays to an electron and the other to a muon, the LO final state signatures are one prompt electron and one prompt muon, a neutrino and one b-jet. As the initial b-quark originates from gluon-splitting ($g \to b\bar{b}$), the presence of an additional $\bar{b}$-quark leads to a final-state signature identical to $t\bar{t}$ in the dilepton channel. The simulated tW samples were produced by the POWHEG generator interfaced to PYTHIA 8 using the A14 tune. Similarly to the $t\bar{t}$ samples, only leptonic decays of the two W bosons occurring in the tW process were considered, including $e^{\pm}$, $\mu^{\pm}$ or $\tau^{\pm}$ leptons. The Diagram Removal (DR) scheme was employed to handle the interference with $t\bar{t}$ production [81]. Samples with the Diagram Subtraction (DS) scheme were produced to evaluate the impact of the scheme choice used to handle the interference of the tW process with $t\bar{t}$ production [81]. The total cross-section for tW production was computed at NLO in QCD with the addition of third-order corrections of soft-gluon emissions by resuming NNLL terms [82] and the simulated event sample was scaled to $\sigma(tW + \bar{t}W) = 71.7 \pm 3.8$ pb.

The associated production of $t\bar{t}$ with a vector boson, Z/W boson, referred to as $t\bar{t}V$, is a small background contribution. Feynman diagrams of the ttW and ttZ production are shown in Figs. 3.8(b) and 3.8(c) respectively. The production of $t\bar{t}V$ is modelled using the MADGRAPH5_aMC@NLO generator with the NNPDF3.0NLO set of PDFs. The events were interfaced to PYTHIA 8 for modelling PS, hadronisation and UE, using the A14 tune. Cross-sections were calculated at NLO QCD and NLO EW accuracy using MADGRAPH5_aMC@NLO as reported in Ref. [83]. The predicted values are $0.88^{+0.09}_{-0.11}$ pb and $0.60^{+0.08}_{-0.07}$ pb for $t\bar{t}+Z$ and $t\bar{t}+W$, respectively, where the uncertainties were estimated from variations of α_{s} and the renormalisation and factorisation scales.

Decays of bottom and charm hadrons were simulated using the EVTGEN program for all samples involving top-quark production.

Z+jets and diboson

The production of a Z boson in association with jets, referred to as Z+jets, is a tiny background process. An example Feynman diagram is shown in Fig. 3.9(a). To be selected, the Z boson should decay into two τ leptons and be produced in association with a heavy quark pair, in which the τ leptons decay further into an electron and a muon, $Z \to \tau\tau \to e\mu$.

Another tiny background contribution arises from the production of vector boson pairs (WW, WZ, and ZZ). Two examples of diboson production (WZ and ZZ) are shown in Figs. 3.9(b) and 3.9(c). In the case of WW or WZ, one of the vector bosons decays leptonically and the other decays hadronically;
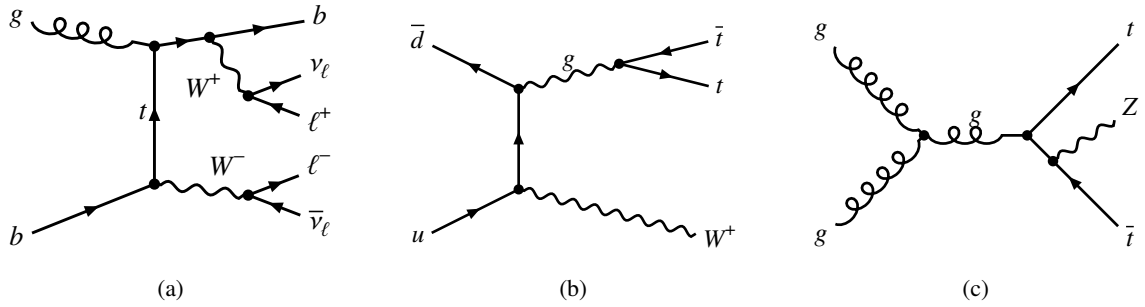
Figure 3.8: Examples of LO Feynman diagrams of background process: (a) single top-quark tW channel, (b) $t\bar{t}W$ process, and (c) $t\bar{t}Z$ process.

this can lead to similar final states as $t\bar{t}$ production in the dilepton channel. The event has a non-prompt lepton that appears isolated and two b-jets. In the case of the ZZ process, one of the two leptons from the leptonic decay of the Z boson is misidentified to mimic the dilepton signature of $t\bar{t}$.

The Z+jets (diboson) samples are simulated with SHERPA with NLO-accurate MEs for up to two (one) additional partons and LO-accurate MEs for up to four (three) additional parton emissions. The samples employ the dedicated tune developed by the SHERPA authors and the NNPDF3.0NLO PDF set.
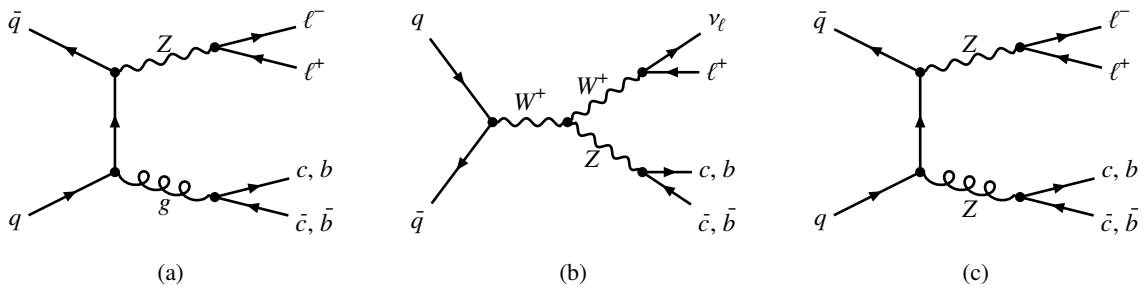
Figure 3.9: Examples of LO Feynman diagrams of background events: (a) Z+jets process, (b) WZ process, and (c) ZZ process.

The LHC and the ATLAS experiment

This chapter describes the experimental setup used to produce and record the pp collisions analysed in this thesis. The pp collisions were produced at the LHC and were collected with the ATLAS detector. An overview to the LHC is given in Section 4.1, followed by a detailed description of the ATLAS detector in Section 4.2. Finally, the dataset recorded in the years from 2015 to 2018 is described in Section 4.3. An overview of the ATLAS detector simulation is presented in Section 4.4

4.1 The LHC

The LHC, located at the European Organization for Nuclear Research (CERN) near Geneva, is currently the largest and most powerful particle accelerator in the world. It is a circular particle accelerator constructed in the former tunnel of the Large Electron Positron (LEP) collider [84], which was operational until 2000. The LHC tunnel has a circumference of 27 km and lies at an average of 100 m underground.

The LHC produces pp, lead–lead or proton–lead collisions. The particles are brought to collision at four interaction points, where the four main detectors are located. The detectors are: ATLAS, CMS (Compact Muon Solenoid) [85], LHCb (LHC beauty) [86], and ALICE (A Large Ion Collider Experiment) [87], see Fig. 4.1. The ATLAS and CMS detectors are multipurpose detectors to explore a wide range of physics, while the LHCb and ALICE experiments are specialised for b-hadron physics and heavy-ion collisions, respectively. The following chapter focuses on the pp collision mode, as this thesis presents a measurement performed in pp collisions.

Fig. 4.1 shows an overview of the CERN accelerator complex. Protons are obtained from hydrogen atoms and formed into bunches of about 10^{11} protons. These bunches are sent through a chain of pre-accelerators that gradually build up their energy. First, the bunches are accelerated to 50 MeV by the linear accelerator LINAC2, then to 1.4 GeV within the Proton Synchroton Booster and to 25 GeV within the Proton Synchroton. After that, they are injected into the Super Proton Synchroton, where their energy is increased to 450 GeV. Finally, the proton bunches are injected into the LHC ring, where they are accelerated to the final energy, which was 6.5 TeV per beam in the years from 2015 to 2018.

The proton bunches are accelerated within the LHC using sixteen radio-frequency cavities, which provide an accelerating field strength of $5\,\mathrm{MV\,m^{-1}}$. The LHC can be filled with up to 2556 bunches per beam, which are separated by 25 ns and bent by an 8 T magnetic field. The magnetic field is created by a series of superconducting dipole and quadrupole magnets cooled down to 1.9 K using
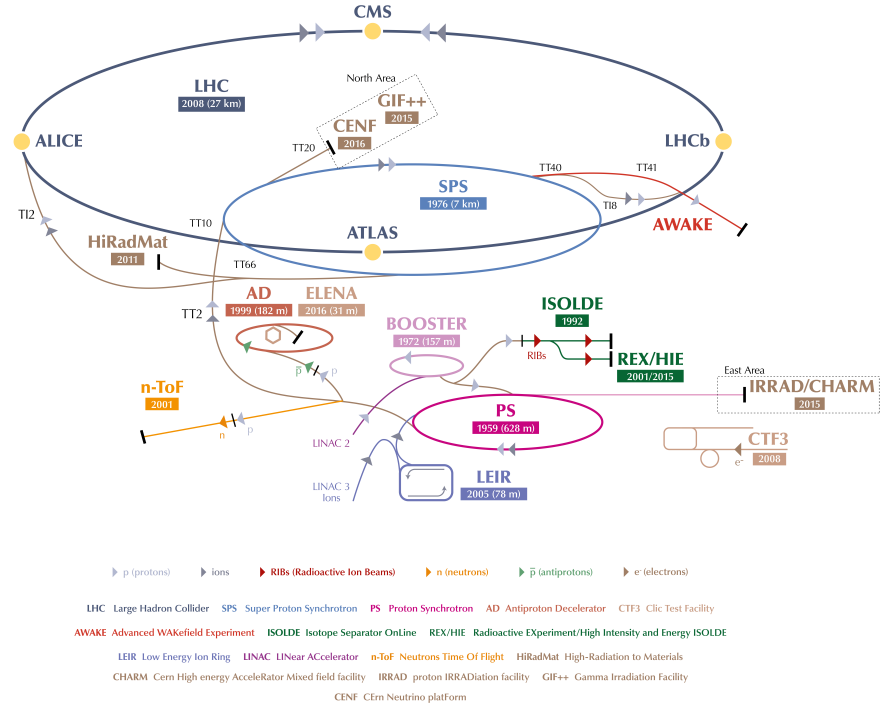
Figure 4.1: A schematic of the CERN accelerator complex. The LHC is the largest ring (dark blue line) with its four main experiments marked as yellow dots and the pre-accelerators chain [88].

liquid helium, to maintain superconductivity. To prevent collisions between the accelerated protons and the gas atoms in the beam pipe, an ultra-high vacuum is maintained to bring the pressures below 10^{-13} atm.

In addition to the high centre-of-mass energy, a high integrated luminosity ($\mathcal{L}_{\text{int}}$) is needed to achieve a high production rate of rare physics processes. The expected number of events for a process with cross-section σ is given by [8]:

$$N_{\text{events}} = \sigma \mathcal{L}_{\text{int}} = \sigma \int \mathcal{L} \, dt \,, \qquad (4.1)$$

where $\mathcal{L}$ is the instantaneous luminosity, which depends on various parameters of the LHC and can be written as [8]:

$$\mathcal{L} = \frac{N_b^2 n_b f_{\text{rev}} \gamma_r}{4\pi \epsilon_n \beta^*} F \,, \qquad (4.2)$$

where N_b is the number of protons per bunch, n_b is the number of bunches per beam, f_{rev} is the revolution frequency of the proton bunches, γ_r is the relativistic gamma factor, ϵ_n is the normalised transverse beam emittance, β^* is the beta function at the Interaction Point (IP) which quantifies how narrow the beam is, and F is the geometric luminosity reduction factor due to the crossing angle at the

IP. Table 4.1 presents the different LHC parameters for 2015-2018 data-taking periods compared to the design values.

Table 4.1: The LHC beam parameters in the 2015–2018 data-taking period, compared to the nominal design values [89].

Parameter	2015-2018	Design
Beam energy [TeV]	6.5	7
Bunch spacing [ns]	25	25
Protons per bunch N_b	1.15×10^{11}	1.15×10^{11}
Number of bunches n_b	2556	2808
Revolution frequency f_{rev} [kHz]	11.2	11.2
Normalised transverse emittance ϵ_n [µm]	2.2	3.75
Beam focus β^* [cm]	25	55
Geometric reduction factor F	0.858	0.836
Peak luminosity $[\text{cm}^{-2}\,\text{s}^{-1}]$	2×10^{34}	1×10^{34}

The high instantaneous luminosity increases the number of produced events, but it also comes with difficulties. The increased number of protons per bunch, increases the number of additional pp interactions per bunch crossing, referred to as pile-up interactions. The additional pp interactions per bunch crossing are called in-time pile-up, while additional pp interactions that originate from neighbouring bunch crossings are referred to as out-of-time pile-up. The average number of interactions per bunch crossing ($\langle \mu \rangle$) in the 2015-2018 dataset was 33.7 [90].

4.2 The ATLAS detector

ATLAS [9] is the largest LHC detector. It is 25 m high, 46 m long and weighs about 7 000 t. Fig. 4.2 shows an overview of the detector which has a typical onion-shell-like structure. It is composed of multiple layers of subsystems, that are arranged in concentric cylinders to cover almost the full 4π solid angle around the IP. Each subsystem is specialised in the identification and processing of various types of experimental signals. The Inner Detector (ID) is responsible for measuring the tracks of charged particles. Around the ID, a thin solenoid magnet is located, followed by the calorimeter system. The calorimeter system is used to measure the energy of produced particles like electrons, photons, and hadrons. The outermost part is the muon spectrometer, which is impeded in a magnetic field from toroid magnets, allowing to measure the position and energy of muons with high accuracy. The following sections briefly describe the individual subsystems and their roles.

The ATLAS coordinate system and definition of common variables
ATLAS uses a right-handed coordinate system (x, y, z) with its origin at the IP in the centre of the detector and the z-axis along the beam pipe. The xy- plane is transverse to the beam. The positive x-axis points from the IP to the centre of the LHC ring, and the positive y-axis points upwards. Due to the cylindrical shape of the detector, it is natural to transform to polar coordinates (r, θ, ϕ), in which θ
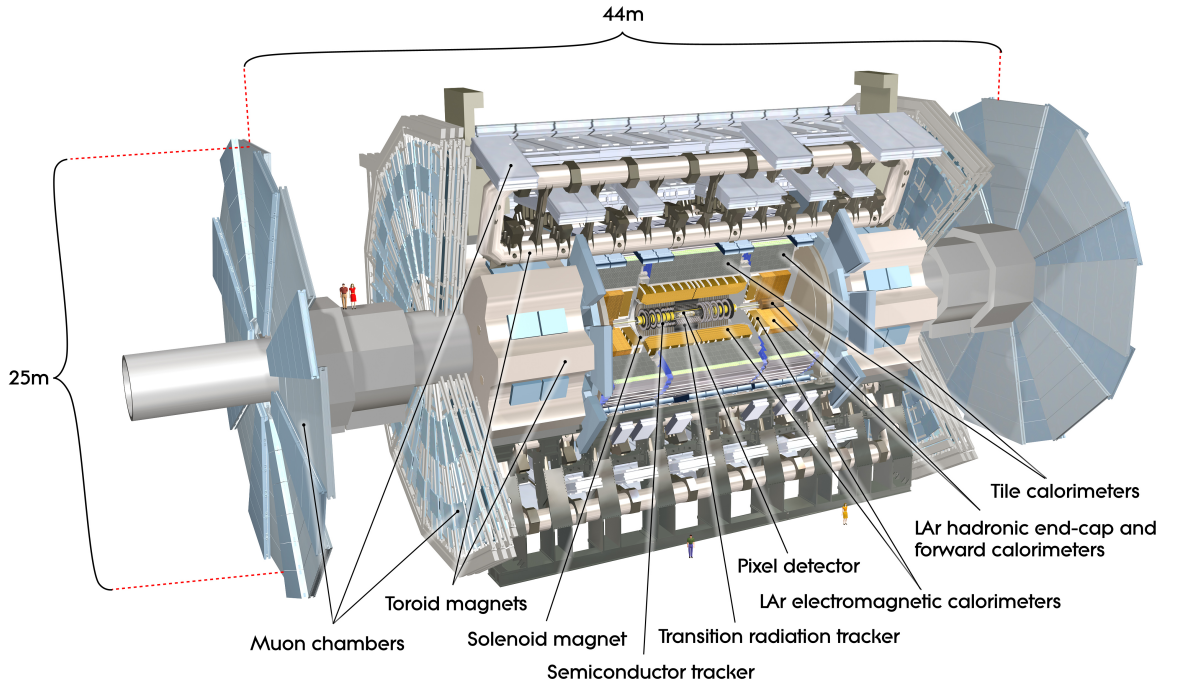
Figure 4.2: The ATLAS detector with its sub-detector and magnet systems [9].

is the polar angle defined with respect to the positive z-axis and ϕ being the azimuthal angle in the transverse plane with respect to the positive x-axis. The pseudorapidity is defined in terms of the polar angle θ as:

$$\eta = -\ln\left[\tan(\frac{\theta}{2})\right].$$

(4.3)

The angular distance between two particles in the $\eta - \phi$ plans is defined as:

$$\Delta R = \sqrt{(\Delta\eta)^2 + (\Delta\phi)^2}.$$

(4.4)

The transverse momentum of a particle is given by:

$$p_\mathrm{T} = \sqrt{p_x^2 + p_y^2}.$$

(4.5)

The sum of transverse momenta of all particles produced in a pp collision is expected to be zero. That is due to momentum conservation and the initial p_T of the colliding partons is known to be zero. However, measuring a non-zero-sum of p_T of all visible particles (n) hints at the existence of undetected particles. For-example neutrinos are not seen in the detector. This momentum imbalance

is referred to as missing transverse momentum and is defined as:

$$E_T^{miss} = - \left| \sum_i^n \vec{p}_T(i) \right| .$$

(4.6)

4.2.1 The inner detector

The ID [91] is the innermost layer of the ATLAS detector. Its main purpose is to reconstruct tracks of charged particles in a high track density environment. It is immersed in a 2 T magnetic field that bends the trajectory of charged particles, allowing the measurement of their electric charge and momentum. Additionally, the ID helps to identify the electrons and is crucial to determine the position of primary and secondary vertices. The ID, shown in Fig. 4.3, is around six meters long, two meters high and provides a coverage in the region of $|\eta| < 2.5$. It consists of three subsystems: the pixel detector, the Semi-Conductor Tracker (SCT), and the Transition Radiation Tracker (TRT). Each subsystem is split into cylindrical layers in the barrel region and disks perpendicular to the beamline in the endcaps region.
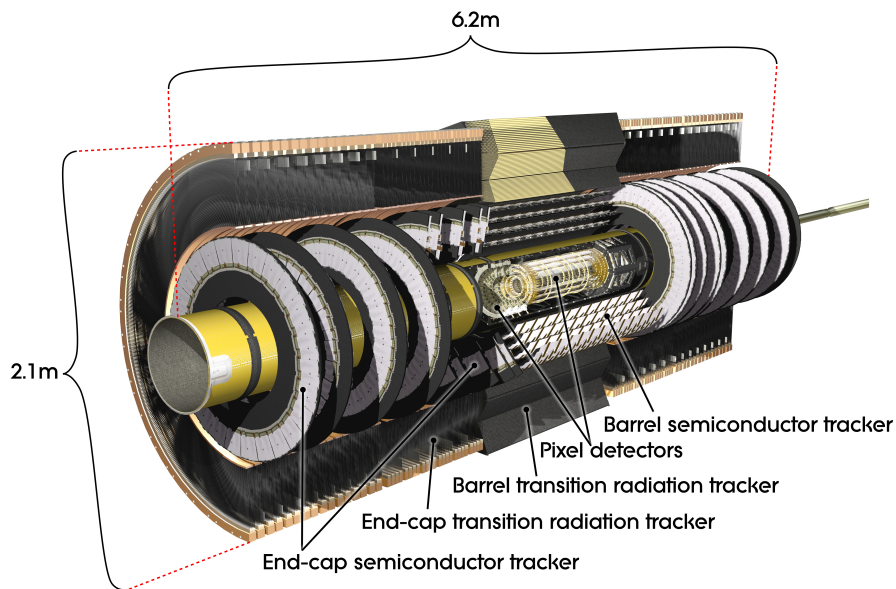
Figure 4.3: A cut-away view of the inner detector showing its various subsystems, except the Insertable B-Layer (IBL) which was added during the first long shut-down of the LHC in 2013-2014 [9].

The pixel detector

The pixel detector is the detector closest to the IP, see Fig. 4.3. It is a semiconductor (silicon) pixel detector and covers up to $|\eta| < 2.5$. It consists of 2024 modules that are arranged in four-barrel layers, which are located at radii of 3.35, 5.05, 8.85, and 12.25 cm from the IP, and three discs at each side in the endcap regions. The modules are the building blocks of the pixel detector and contain both the silicon sensors and the front-end electronics (FE). In the outer three layers and endcap regions, the

sensor is subdivided into 46080 pixels which are connected to 16 FE chips. In the innermost layer, the IBL [92], two different types of modules are used: planar modules and 3D modules. A planar module has two FE chips and a 3D module has a single FE chip. Each chip is connected to 26880-pixel cells. The size of the silicon sensor is $50 \times 400\,\mu m^2$ in the three outer barrel layers and endcap regions and $50 \times 250\,\mu m^2$ in the innermost barrel layer. The innermost IBL layer plays an important role in the tracking precision due to its close location to the IP.

When a charged particle passes through a pixel module, electron-hole pairs are created in the semiconductor material in an amount related to the energy of the particle. The electron and the holes then drift to the electrodes and induce an electrical current, which is then detected by readout chips. The recorded signals allow for determining the position of the particle. This finely granulated structure results in an intrinsic resolution of approximately $10\,\mu m$ in the direction orthogonal to the beamline. In the z-direction, the IBL resolution is approximately $66.5\,\mu m$, while the external layers have a resolution of approximately $115\,\mu m$.

The semiconductor tracker
The SCT surrounds the pixel detector. It is a microstrip detector with a similar purpose and technology as the pixel detector. It consists of 4088 modules arranged in four-barrel layers and located at radii between 30 and 50 cm from the IP, and nine discs on either end-caps as shown in Fig. 4.3. An SCT module uses silicon sensors segmented in strips rather than individual pixels. Each strip is 12 cm long and made of two sensors that are connected back-to-back to another pair of sensors (double layer). It covers a region of up to $|\eta| < 2.5$. The spatial resolution is $17\,\mu m$ in the direction orthogonal to the beam pipe and $580\,\mu m$ in the z-direction for the barrel and in the R-direction for the endcaps. An average particle will have three measurements provided by the pixel detector and eight by the SCT.

The transition radiation tracker
The TRT is the outermost layer of the ID, see Fig. 4.3. It is a straw-tube tracking detector and covers a region of up to $|\eta| < 2.0$. It consists of about 370000 straw tubes arranged in 73 barrel layers and 2×122 endcap layers. In the barrel region, the straw tubes are 144 cm long and situated parallel to the beam axis, while in the endcap regions, they are 37 cm long and arranged perpendicular to the beamline. The straw tubes are 4 mm in diameter and filled with a mixture of Xenon-based gas, which ionises as charged particles traverse through. The resulting electrons drift to an anode wire placed in the centre of the tube, where they are amplified and the current is measured.

In addition to the tracking information, the TRT provides electron identification capability through the detection of transition radiation. The spaces between the straws are filled with a material with different refraction indices. As charged particles traverse through this material, transition radiation is emitted that is proportional to the Lorentz factor of the particles. This factor is very large for the lightest particles as electrons, making it possible to distinguish electrons from other light particles like pions. The spatial resolution of the TRT of $130\,\mu m$ in a plane perpendicular to the wire is lower compared to the silicon detectors, but it is compensated for by a large number of hits per track; a typical track leaves 30 hits in the TRT.

4.2.2 The calorimeter

The ATLAS calorimeter system is used to measure the energy and direction of electrons, photons and jets as well as the $E_{\mathrm{T}}^{\mathrm{miss}}$. It covers a wide pseudorapidity range of up to $|\eta| < 4.9$ and uses the

so-called "sampling" technique. A sampling calorimeter is composed of alternating layers of active medium and passive absorber material. Particles traversing the absorber material interact with it and induce a shower of secondary particles, which are measured by the active material. Fig. 4.4 shows the structure of the calorimeter system. It is composed of the Liquid Argon (LAr) calorimeter and the tile hadronic calorimeter.
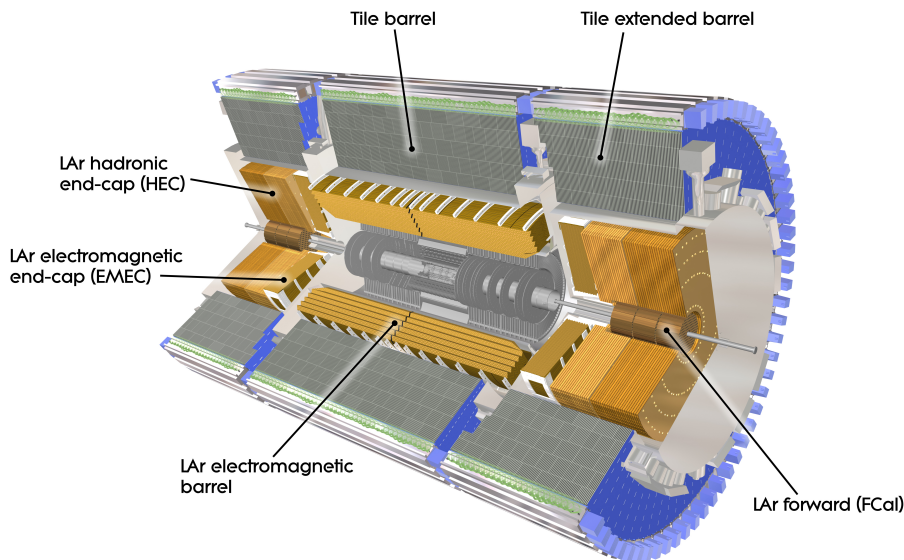
Figure 4.4: A cut-away view of the ATLAS calorimeter system [9].

The liquid argon electromagnetic and hadronic calorimeter

The LAr [93] calorimeter uses LAr as an active material and either lead, copper or tungsten as a passive absorber medium. It is divided into three parts, as shown in Fig. 4.4: the electromagnetic barrel region with $|\eta| < 1.475$, two endcaps regions with $1.357 < |\eta| < 3.2$ which consist of both electromagnetic and hadronic calorimeters and the forward calorimeter with $3.1 < |\eta| < 4.9$. When electrons and photons interact with the absorber medium, they lose their energy progressively (and fully) via the radiation of photons (bremsstrahlung) and e^+e^- pair production, resulting in a particle shower which ionises the LAr.

The tile hadronic calorimeter

The tile hadronic calorimeter surrounds the LAr calorimeter, as shown in Fig. 4.4. It is divided into two parts: the barrel with $|\eta| < 1.0$ and two extended barrels with $0.8 < |\eta| < 1.7$. It is designed to measure the energy of jets resulting from energetic quarks or gluons. It uses plastic scintillating tiles as an active material and steel as a passive absorber medium. It extends from an inner radius of 2.28 m to an outer radius of 4.25 m. When particles interact with the steel layers via inelastic hadronic interactions, they generate a hadronic particle shower. The scintillator tiles then produce photons, which are converted into an electrical signal.

4.2.3 The muon spectrometer

Muons are not stopped in the calorimeter system and penetrate the whole detector. Therefore, the Muon Spectrometer (MS) [94] is the outermost part of the ATLAS detector. It is designed to measure the momentum of the muons within $|\eta| < 2.7$ and to trigger high-energetic muon events within $|\eta| < 2.4$.

The MS, shown in Fig. 4.5, consists of three concentric barrel layers at radii between 5 and 10 m from the IP and four large wheels perpendicular to the IP at each side in the endcap regions. The MS is embedded in a magnetic field created by the toroid magnets with a magnetic field strength of 0.5 T in the barrel and 1.0 T in the endcaps. The toroid magnets generate a magnetic field perpendicular to the expected muon trajectories. Thus, the muon trajectory is bent by the magnetic field, allowing for high precision tracking.

The tracks of muons are measured with drift tubes, namely the Monitored Drift Tubes (MDT) and the Cathode Strip Chambers (CSC), see Fig. 4.5. The MDT are used within $|\eta| < 2.0$ and they consist of aluminium tubes filled with a gas mixture and a tungsten wire in the middle. When a muon passes through a drift tube, it ionises the gas the resulting drifting electrons create an electrical signal that is used to measure the position of the muons. In $1.05 < |\eta| < 2.4$, the CSC are used instead. They are multi-wire proportional chambers with cathodes divided into strips, that measure the ionisation charge from a passing particle. The trigger chambers are the Resistive Plate Chambers (RPC) in the barrel and the Thin Gap Chambers (TGC) which provide a fast $(15 - 25 \text{ ns})$ information about muon tracks to the trigger system.
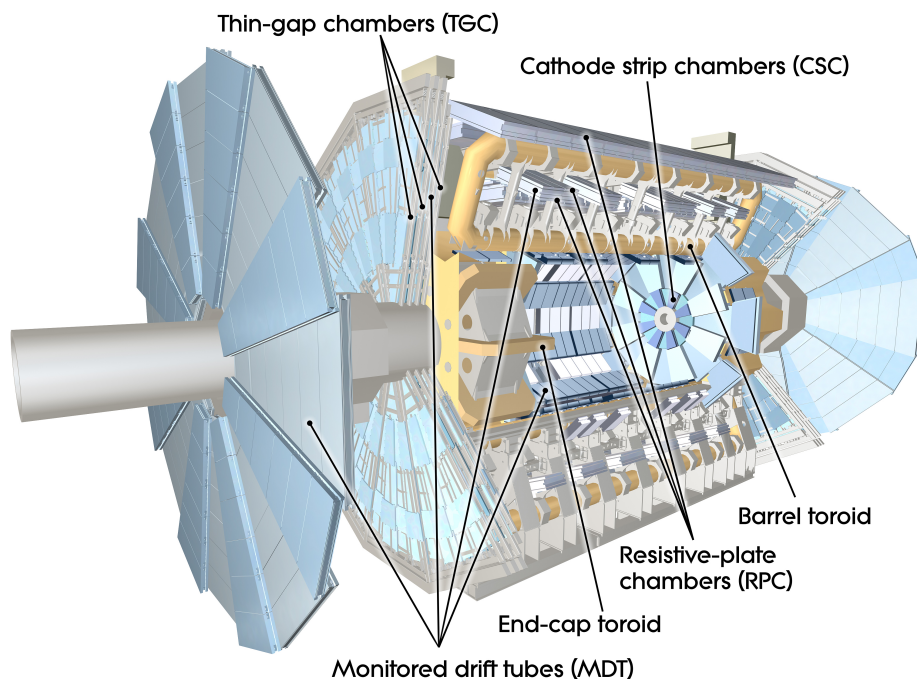
Figure 4.5: A cut-away view of the ATLAS muon spectrometer [9].

4.2.4 The trigger system

The ATLAS experiment is designed to observe approximately 40 million collisions per second. With each event representing about 1Mbyte of information, it is impossible to store all events delivered by the LHC. Therefore, the trigger system is used to perform an online selection of interesting events only to reduce the amount of stored data. The trigger system is split into two levels. The Level 1 (L1) [95] trigger is a hardware-based trigger that uses information from the calorimeter, the RPC and the TGC to identify events with high p_T leptons, photons and jets. It reduces the data rate from the 40 MHz bunch crossings to a rate below 100 kHz. The information is then passed to the High Level Trigger (HLT) [96], which is a software-based trigger that uses information from the entire detector and reduces the events rate to 1 000 Hz. Events passing both trigger levels are written to disk and used later in physics analyses.

4.3 The 2015-2018 dataset

The analysis uses pp collision data which were recorded with the ATLAS detector during Run 2 of the LHC in the years from 2015 to 2018 at a centre-of-mass energy of 13 TeV.

Fig. 4.6(a) shows the total integrated luminosity delivered by the LHC (green), the luminosity collected by ATLAS (yellow), and in blue the luminosity certified to be good quality data. The recorded luminosity differs from the delivered due to the inefficiency of the data acquisition, as well as inefficiency due to the time required for the tracking detectors to reach the optimal working point at the start of stable beams. The recorded data is subjected to certain quality criteria which require the data to be taken under stable beam conditions and all detector sub-components are in a fully operational status. More than 94% of the recorded data fulfil the good data quality criteria and are used in physics analyses. Thus, the data used correspond to an integrated luminosity of 139 fb^{-1} with a relative uncertainty of 1.7 % [97].

Changing the LHC beam conditions between and within each year of the data-taking periods affects the luminosity, the number of additional interactions per collision (pile-up), and the trigger menu. The integrated luminosities corresponding to a good quality data, split by year, are 3.22 fb^{-1} for 2015, 33.0 fb^{-1} for 2016, 44.3 fb^{-1} for 2017, and 85.5 fb^{-1} for 2018. The average number of interactions per bunch crossing increased from 13 to 36 from 2015 to 2018, as illustrated in Fig. 4.6(b), due to the increase in the instantaneous luminosity. Events are selected online during data taking by single-electron or single-muon triggers [98, 99].

4.4 ATLAS simulation

The previous chapter provided a description of event generation. The results of the MC event generators do not take into account any effects of the detectors. These effects need to be simulated in order to be able to compare the simulated events directly with the measured data. The particles' interaction with the detector material is simulated based on the GEANT4 framework [100].

The simulation performs a detailed description of the interactions between the particles and the various sub-detector parts and the collection of the energy deposits is recorded as hits with position and time. The hits are then transformed into detector responses (voltage and current) through the
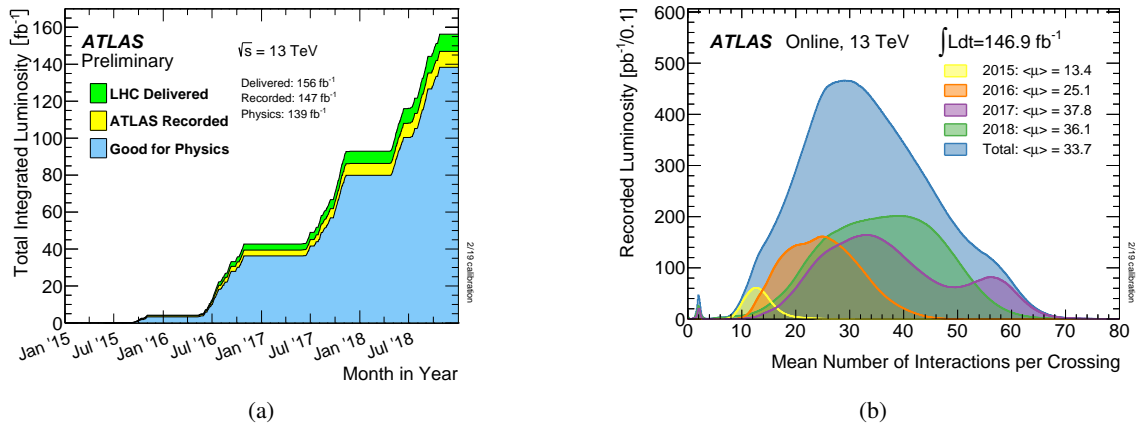
Figure 4.6: (a) Cumulative luminosity versus time delivered to ATLAS (green), recorded by ATLAS (yellow), and certified to be good quality data (blue) during stable beams and (b) the mean number of interactions per bunch-crossing for pp collisions at $\sqrt{s} = 13$ TeV in 2015–2018 [90].

digitisation step. The digitisation output is a data format identical to the real data. Thus, the same trigger and reconstruction algorithms can be applied for simulated and real data.

Because of the complicated detector geometry, the full detector simulation requires large computing resources. This is mainly due to simulating particles traversing the calorimeters. To reduce the usage of resources from several minutes to a few seconds per event, a fast simulation algorithm [101] is provided with parametrised showers in the calorimeters instead of simulating them fully. In this analysis, a fast simulation algorithm is used for systematics samples, where high precision is not required.

To take into account the effect of additional interactions in the same and neighbouring bunch crossing, pile-up events with low momentum exchange are overlayed over the hard-scatter events after the digitisation step. Pile-up events are simulated using minimum-bias events generated using PYTHIA 8 with the A3 [102] tune. The distribution of the number of pile-up interactions in the simulation is re-weighted to match the pile-up level observed in the data.

Physics objects and observables definition

Physics object reconstruction and identification in the ATLAS detector rely on their properties and interaction with the material of the various detector parts. Fig. 5.1 illustrates the interaction of different particles with the ATLAS detector. Different particles leave diverse signatures, which allows to distinguish them.

Physics objects can be identified in various stages. The full reconstruction of a given object through the ATLAS detector is referred to as detector level. However, it is also possible to define physics objects in a state where stable particles are defined after the parton shower and hadronisation, but before the decays and propagation through the detector. This stage is referred to as particle level. In measured data, only detector-level information is accessible, while both stages are accessible in simulation.

This chapter provides the definition of charged-particle tracks and objects needed in the reconstruction of $t\bar{t}$ events. The signature of a dileptonic $t\bar{t}$ pair comprises charged leptons and jets, including b-quark-initiated jets. An overview of detector-level objects reconstruction and definition is given in Section 5.1. The particle-level objects definition is discussed in Section 5.2. Then, the event selection applied to identify $t\bar{t}$ events is explained in Section 5.3. The observables which are measured in this thesis are introduced in Section 5.4. Finally, an overview of the analysis strategy is presented in Section 5.5

5.1 Detector-level objects definition

Tracks of charged particles

Tracks are reconstructed from position measurements in the ID caused by the passage of charged particles. Track reconstruction uses an inside-out track-finding algorithm, followed by an outside-in tracking. The track reconstruction algorithm begins by assembling hits from the deposited energy in the pixel and SCT detectors. From these hits, three-dimensional measurements referred to as space-points are created, which represent the point where the charged-particle traversed the active material of the ID. Then, track seeds are formed from a combination of three space-points followed by a combinatorial Kalman filter [104] to build track candidates from the chosen seeds and by incorporating additional space-points from the remaining layers of the pixel and SCT detectors which are compatible with the preliminary trajectory. Ambiguities between the track candidates with overlapping or incorrectly
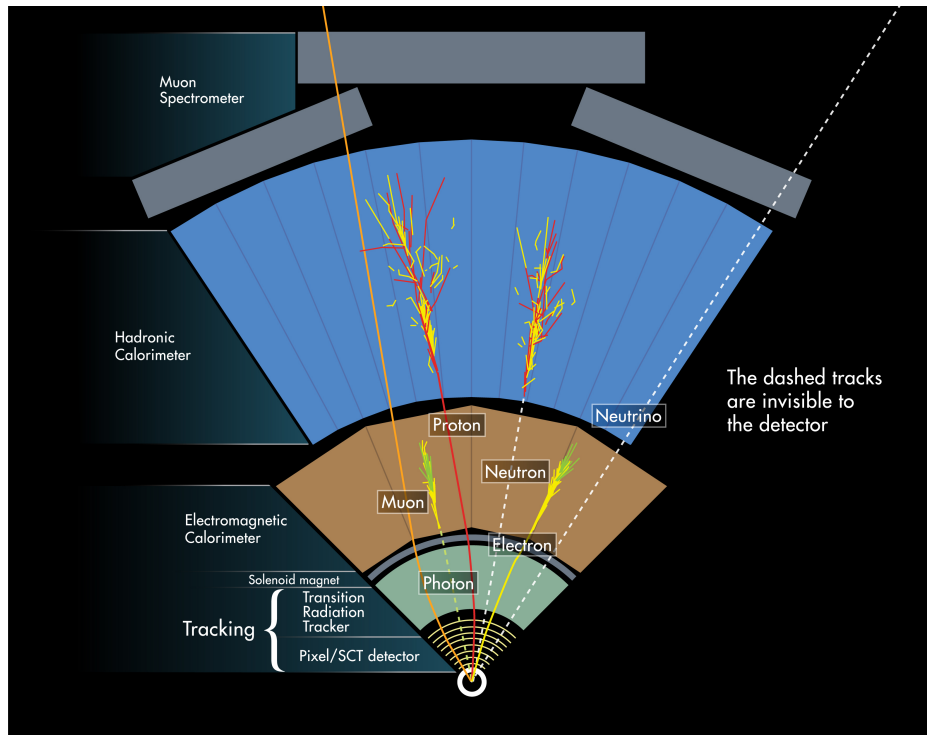
Figure 5.1: Transverse view of the ATLAS detector representing the various particle interactions with each layer of the detector. Dashed tracks are invisible to the detector layers. Muon tracks and neutrinos pass through the entire detector. Electrons, photons and hadrons are fully absorbed by the calorimeters. Charged particle trajectories are bent in the tracking system due to the presence of magnetic fields [103].

assigned space-points are then resolved by assigning a relative track score to each track with respect to another. Quality criteria are applied to suppress combinations of space-points unlikely to originate from a single charged particle. Finally, silicon seeded tracks that survived the ambiguity solving are extended into the outer TRT detector and a high-resolution fit is performed to provide the final estimate of the track parameters. The resulting track-collection marks the end of the inside-out chain of the ATLAS ID track reconstruction [105, 106].

The inside-out chain is followed by an outside-in tracking pass to reconstruct tracks that were missed by the previous algorithm or tracks from secondary-decay vertices or from photon conversions. A reverse sequence that starts by reconstructing TRT track segments, which are then extended back into the silicon detectors. Track segments are reconstructed from space-points that have not been already assigned to an existing track from the inside-out tracking pass.

The resulting tracks from both the inside-out and outside-in strategies represent the final collection of reconstructed tracks. Tracks are described by a set of five parameters, defined as $(d_0, z_0, \phi, \theta, q/p)$ and depicted in Fig. 5.2. The transverse impact parameter, d_0, is defined as the shortest distance between the track and the beam line in the transverse plane. The longitudinal impact parameter, z_0, is defined as the distance along the beam line between the point on the track used to evaluate d_0 and the primary vertex. The azimuthal angle ϕ and the polar angle θ of the track momentum and the ratio q/p of the charge of the reconstructed track divided by the magnitude of its momentum.

In this analysis, reconstructed tracks used to compute measured observables are selected by applying the tight primary quality criteria [107]. In particular, they must have $p_T > 5\,\text{GeV}$ and be within $|\eta| < 2.5$. At least one hit in the two innermost pixel layers is required if the extrapolated track crosses the sensitive region of an active sensor module. The number of silicon hits in the pixel and SCT detectors must be larger than nine for $|\eta| \leq 1.65$ or larger than 11 for $|\eta| > 1.65$, with no more than two missing SCT hits on a track if the respective SCT modules are operational and no missing pixel hits. Additionally, track-to-vertex-association criteria are applied to mitigate the effect of pile-up tracks and improve the rejection of tracks from secondary interactions: $|d_0| < 0.5\,\text{mm}$, and the longitudinal impact parameter calculated relative to the event primary vertex, $|z_0 \sin(\theta)| < 0.5\,\text{mm}$. Furthermore, in order to best describe the colour-reconnection effect, tracks within $\Delta R = 0.4$ of a jet or within $\Delta R = 0.01$ of the electron or muon from the top-quark decay are discarded. These selection criteria have a significantly high rejection of tracks originating from pile-up interactions and result in an efficiency of $65 - 80\,\%$ depending on the track p_T.
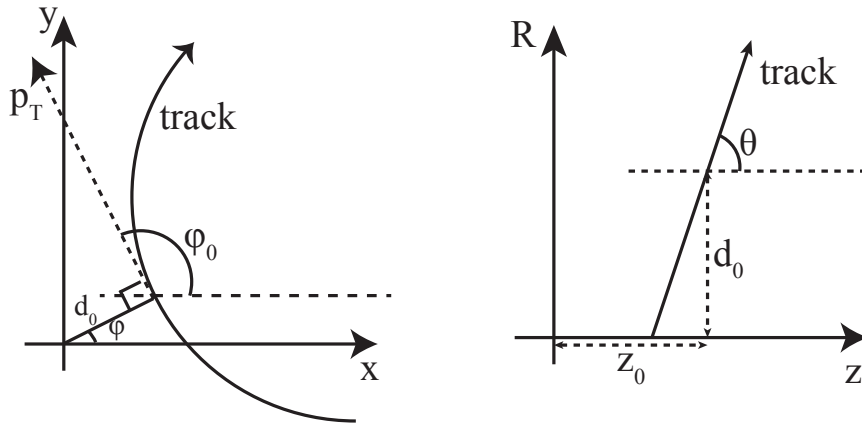
Figure 5.2: Illustration of the perigee parameters of a track in the transverse plane (left) and the longitudinal plane (right) [108].

Primary vertex

A typical collision of two proton bunches in the LHC results in multiple interactions per bunch crossing, on average 33.7 over the full Run 2 [90]. Given the multiple interactions per bunch crossing, the identification and precise reconstruction of the primary vertex which arises from the hard inelastic collision among many soft pp interactions is essential.

Primary vertex reconstruction uses a collection of reconstructed tracks, selected with the tight primary quality criteria. The reconstruction can be generally divided into two stages: the iterative primary vertex finding, where reconstructed tracks are associated to a particular vertex candidate, and an adaptive vertex fitting where the vertex position and their corresponding uncertainties are determined [109, 110].

The presence of pile-up events increases the number of reconstructed vertices, which are usually soft. Therefore, the vertex with the highest sum of squared transverse momenta of all associated tracks is considered to correspond to the hardest pp interaction and is defined as the primary vertex of the

event. Other primary vertices are assumed to be coming from pile-up interactions. Vertices which are incompatible with the estimated beam-spot[1] region are secondary (or tertiary) vertices [111].

Electrons

Electrons are charged particles interacting electromagnetically with the ATLAS detector, leaving hits in the ID and depositing their energy in the electromagnetic calorimeter. In this analysis, only electrons with $|\eta| < 2.5$ are considered.

Electron reconstruction is performed in several steps [112]. First, topo-clusters, defined as topologically connected electromagnetic and hadronic calorimeter cells, are reconstructed using energy deposits in the electromagnetic calorimeter, except in the transition region $1.37 < |\eta| < 1.52$ between the central and the end-cap electromagnetic calorimeter. In the next step, tracks are reconstructed as described in Section 5.1 with a bremsstrahlung-aware refit. Then, tracks are matched to the selected topo-cluster. After that, variable-size superclusters are formed, an example diagram of a supercluster is given in Fig. 5.3, and initial position corrections are applied and tracks are matched to the electron superclusters. Finally, an ambiguity resolution is performed to remove electron and photon overlap.

To distinguish electrons from non-electron objects, a likelihood-based algorithm is used to simultaneously evaluate several input variables of electron candidates including quantities measured in the ID, the calorimeter and the combined ID and calorimeter [112]. Three identification working points are provided: *loose*, *medium* and *tight* [112]. This analysis uses electrons with the *tight* identification working point for high rejection of background electrons.

To differentiate prompt electrons from the signal process from background processes such as semileptonic decays of heavy quarks, hadrons misidentified as leptons, and photons converting into electron–positron pairs additional isolation criteria are applied. To quantify the activity near the electron, two isolation variables are defined: the sum of transverse energies deposited in a cone of radius $\Delta R = 0.2$ around the electron candidate in the electromagnetic calorimeter, and the sum of the transverse momenta of tracks within a cone centred around the candidate electron track, excluding the candidate itself. This analysis uses electrons with the *tight* isolation working point to achieve the highest background rejection [112].

The energy of the electron candidates is calibrated to correct for energy losses before and inside the calorimeter [113]. The energy resolution is optimised using a multivariate approach. The absolute energy scale is adjusted using a sample of Z boson decays into electron-positron pairs. Finally, the calibration is validated using $J/\psi \rightarrow e^+ e^-$ events.

In this analysis, the transverse momentum of the reconstructed electron is required to be $p_T > 25\,\text{GeV}$. The tracks matched to the electrons have to be compatible with the primary vertex which is ensured by the requirements $|d_0/\sigma_{d_0}| < 5.0$, and $|z_0 \sin(\theta)| < 0.5\,\text{mm}$.

---

[1] The beam spot is referred to as the spatial region around the interaction point where the profiles of the two beams overlap.
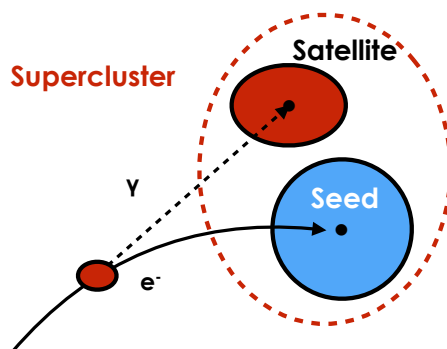
Figure 5.3: Diagram of an example supercluster showing a seed electron cluster and a satellite photon cluster [114].

Muons

Muons are minimum-ionising charged particles. They leave hits in the ID, deposit a small amount of energy in the electromagnetic and hadronic calorimeters and reach the MS. Hence, muons are reconstructed based primarily on information from the ID and the MS. In this analysis, only muons with $|\eta| < 2.5$ are considered.

The reconstruction is performed independently in the ID and MS and then the information is combined. ID tracks reconstruction is performed as described in Section 5.1. MS track reconstruction starts with forming local track segments in each MS layer. Then, segments from all layers are combined together to form MS track candidates. The ID and MS track candidates are then combined with a global refit procedure. The larger part of the muons is reconstructed using the outside-in chain where the muons are reconstructed starting from the MS track and then extrapolated inward and matched to an ID track [115].

Muon identification is performed to select prompt muons and suppress muons from backgrounds mainly coming from charged pion or kaon decays. Several variables offer good discrimination between prompt muons and background muons; those are: the absolute value of the difference between the ratio of the charge and momentum of the muons measured in the ID and MS divided by the sum in quadrature of the corresponding uncertainties (q/p), the absolute value of the difference between the transverse momentum measurements in the ID and MS divided by the p_T of the combined track (ρ') and the normalised χ^2 of the combined track fit. Four working points are defined depending on the selection criteria applied on these variables: *medium*, *loose*, *tight* and *High-p_T* [116]. This analysis uses muons with the *medium* identification working point, which minimises the systematic uncertainties associated with muon reconstruction and calibration [115]. The *medium* requirements are: at least three hits in at least two MDT layers except for tracks in the $|\eta| < 0.1$ region, where tracks with at least one MDT layer but no more than one MDT hole layer are allowed. q/p significance is required to be smaller than seven to suppress the contamination due to hadrons misidentified as muons.

Similarly to the electrons, muons are required to pass additional isolation criteria to suppress muons originating from semileptonic decays of heavy hadrons. To quantify the activity near the muon the same variables used for electron isolation are used: the sum of transverse energies of clusters deposited in a cone of radius $\Delta R = 0.2$ around the muon candidate in the calorimeters and the sum of the transverse momentum of tracks within a cone centred around the candidate muon track, excluding the

candidate itself. This analysis uses muons with the *tight* [116] isolation working point to achieve the highest background rejection.

The reconstruction and identification efficiencies are measured in data and simulation using the tag-and-probe method [115] in $Z \rightarrow \mu^- \mu^+$ and $J/\psi \rightarrow \mu^- \mu^+$ events. Discrepancies between data and simulation are accounted for by applying scale factors to the simulated events. Moreover, the muon momentum scale and resolution are measured. Correction factors are derived and applied to the muon momentum scale and resolution of simulated events to match those observed in data [115].

In this analysis, the transverse momentum of the reconstructed muon is required to be $p_T > 25$ GeV. Matched tracks to muons have to be compatible with the primary vertex, which is ensured by requirements imposed on the transverse impact parameter significance, $|d_0/\sigma_{d_0}| < 3.0$, and the longitudinal impact parameter, $|z_0 \sin(\theta)| < 0.5$ mm.

Jets

Quarks and gluons are colour charged particles. Therefore, they cannot be observed as free particles, they form stable colour-less hadrons. These hadrons form a stream of collimated particles that are considered as a single object, called a jet, that describes the kinematics of the original quark or gluon. Jets are observed as energy deposits in the calorimeters. In addition, ID tracks are observed for charged particles.

Jet reconstruction is performed using the particle-flow algorithm [117], in which tracking and calorimetric information are combined. The reconstruction can be divided into three steps: First, jet constituents are reconstructed, which are energy clusters in the calorimeters and measured tracks in the ID. In the next step, the reconstructed tracks are matched to the energy clusters. In case of a successful match, the energy deposit in the calorimeter by the charged particle is subtracted from the matched clusters and replaced by the corresponding track momentum. Finally, the anti-k_t jet-finding algorithm [118] is applied as implemented in the *FastJet* software package [119]. The inputs to this algorithm are the clusters that survived the energy subtraction and the tracks that match the hard-scattering primary vertex.

The anti-k_t algorithm combines nearby objects based on the distance between two entities i and j, defined as

$$d_{ij} = min(p_{Ti}^{-2}, p_{Tj}^{-2}) \frac{\Delta R_{ij}^2}{R^2}$$

and the distance to the beam, defined as $d_{iB} = p_{Ti}^{-2}$ for object i. Where $p_{Ti}(p_{Tj})$ is the transverse momentum of object $i(j)$, ΔR_{ij} is the angular distance between objects i and j, and R is the radius of the jet cone, which is set to 0.4 for this analysis. These distances are calculated for each object in the event and the smallest distance is identified. If d_{ij} is the smallest distance, the two objects are combined by summing their four-momenta. If d_{iB} is the smallest, the object i is identified as a jet and removed from the list of entities. The distances are then recalculated and the same procedure is repeated until no entities are left. The anti-k_t algorithm is collinear and infrared safe [120]. That means collinear splittings or soft emissions do not change the collection of reconstructed jets. Infrared and collinear unsafe concepts are illustrated in Fig. 5.4.

Reconstructed jets are then subject to a series of energy calibrations to correct their energy in the detector to correspond to the energy of the initial partons. First, corrections for pile-up interactions are applied. Then, an absolute jet energy scale and η calibration are applied to correct the reconstructed
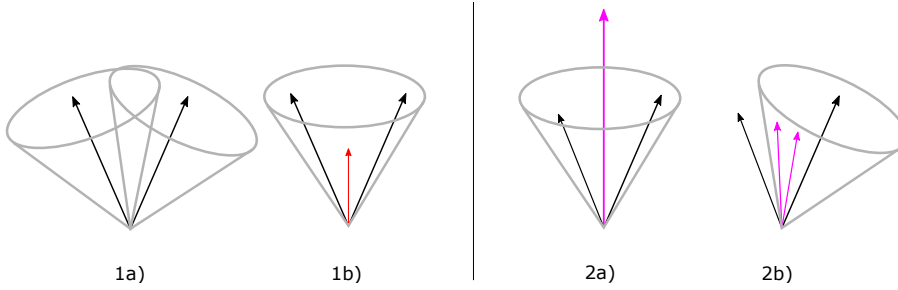
Figure 5.4: Illustration of (1) an infrared unsafe and (2) a collinear unsafe jet reconstruction. The arrows represent particles and the grey cones the reconstructed jets. (1) Soft radiation between two jets in 1a) causes merging of the jets in 1b). (2) Collinear splitting of hard jets in 2a) leads to different jet clustering in 2b) [121].

jet four-momentum to the particle-level energy scale, taking into account the η biases using MC simulated events. In the next step, the Global Sequential Calibration [122] is applied to account for the residual dependence of jet energy on the longitudinal and transverse features of the jets, mainly due to differences in the shower between jets initiated by gluons and jets initiated by quarks. Finally, in-situ calibration is applied to data to account for differences in jet response between data and MC simulation [122].

To suppress jets originating from pile-up interactions, jets with $p_T < 60$ GeV and $|\eta| < 2.4$ are required to pass a requirement on the jet-vertex-tagger (JVT) discriminant [123]. In this analysis, jets are required to pass $|JVT| > 0.5$, which corresponds to an efficiency of 92 % for non-pile-up jets. Furthermore, jets are required to have $p_T > 25$ GeV and $|\eta| < 2.5$.

Identification of b-quark jets

The identification of jets containing b-hadrons is referred to as b-tagging. There are two b-quarks in the final state of the $t\bar{t}$ process. Therefore, the identification of b-jets is of major importance to identify top-quark pair events and discriminate them from background events.

Algorithms designed to identify b-jets exploit the relatively long lifetime of b-hadrons (≈ 1.5 ps) to differentiate b-jets from other jets that contain c-hadrons or light-flavour hadrons (u, d or s). The long lifetime translates into a flight distance of a few millimetres resulting in a secondary vertex associated with their decay, see Fig. 5.5.

In this analysis, the DL1r[2] b-tagging algorithm [124] is employed. DL1r combines the outputs of low-level b-tagging algorithms by using a deep neural network into a single discriminant. Three different low-level algorithms are used. The first set of algorithms uses both the transverse and longitudinal impact parameter significance, and their correlations and combines them into a likelihood discriminant. The second is based on the reconstruction and identification of a displaced secondary vertex and its properties. The last algorithm exploits the topological structure of b-hadron and c-hadron decays inside the jet using the Kalman filter [104] technique as implemented in the JetFitter [125]

---

[2] DL1r is an extension of the DL1 b-tagging algorithm. DL1r adds a new low-level tagger, which exploits correlations between the track impact parameters.
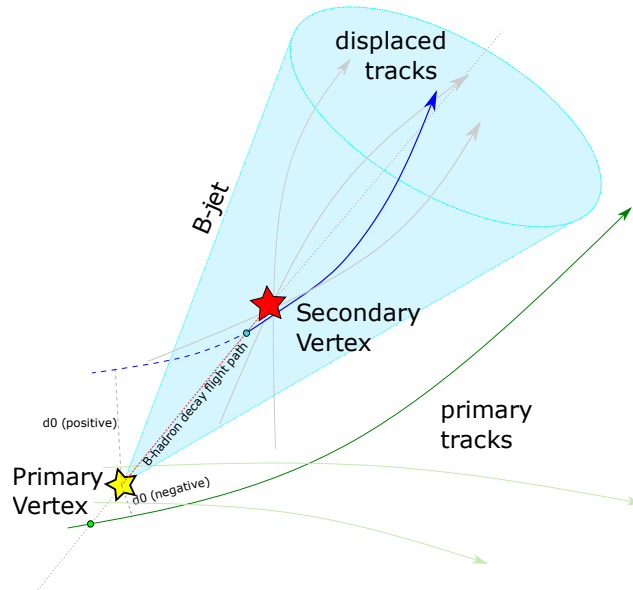
Figure 5.5: Schematic view of a b-hadron decay with a relatively long lifetime resulting in a secondary vertex [121].

algorithm. The output variables from the three algorithms, in addition to the jet p_T and $|\eta|$ are given as input to the DL1r deep neural network that combines the information in a discriminant used to separate the different jet flavours. Working points are defined by a single cut-value on the discriminant output distribution. They are defined by the efficiency to tag b-jets in $t\bar{t}$ events. This analysis uses a working point corresponding to a b-tagging efficiency of 70 %. Jets are considered as b-tagged if the DL1r discriminant is larger than 3.245.

To correct for the differences in b-tagging efficiencies as a function of the jet p_T between simulated events and observed data, scale factors are derived from the observed discrepancies to simulated events. The calibration for b-jets is done in dileptonic $t\bar{t}$ events [124]. These calibrations can vary between the different event generators and parton shower models. Therefore, MC-to-MC scale factors are derived and applied to MC events as described in Ref. [126].

Overlap removal

After object reconstruction, an overlap-removal procedure is applied to remove ambiguities in case the same detector signature is reconstructed as multiple objects. First, an electron sharing a track with a muon is removed. Then, jets within $\Delta R = 0.2$ of an electron are removed, thereby avoiding double-counting electron energy deposits as jets. After that, electrons within $\Delta R = 0.4$ of a jet are removed, to reduce the impact of non-prompt electrons from heavy-flavour decay and to avoid reconstructing electrons as jets. Next, jets within $\Delta R = 0.2$ of a muon are removed if they have less than three associated tracks. Finally, muons within $\Delta R = 0.4$ of a jet are removed, reducing the rate of non-prompt muons.

5.2 Particle-level objects definition

A selection based on particle-level objects is needed to perform the differential cross-section measurements, which are presented in Chapter 7. In order to reduce the extrapolation over objects from detector level to particle level, the selection of particle-level objects is chosen to match detector-level objects as closely as possible. Particle-level objects are defined using stable particles with a mean lifetime $\tau > 30$ ps.

Charged particles are required to have $p_T > 500$ MeV and $|\eta| < 2.5$. Charged particles that are produced from the decay of stable particles, called secondary particles, are excluded. Particles from pile-up and from interactions with the detectors are not included by definition. Additionally, charged particles within $\Delta R = 0.4$ of a jet or within $\Delta R = 0.01$ of the electron or muon from the top-quark decay are excluded.

Electrons and muons are required to not originate from hadron decays, either directly or through a τ decay. This ensures that they originate from the W-boson decay without requiring a direct match. The four-momenta of the bare leptons are modified (dressed) by adding the four-momenta of prompt photons within $\Delta R = 0.1$. The dressed leptons are then required to have $p_T > 25$ GeV and $|\eta| < 2.5$.

Jets are reconstructed with the anti-k_t algorithm using a radius parameter of 0.4. All stable particles are considered for jet clustering, except for the selected electron or muon and photons associated with them. Jets are required to have $p_T > 25$ GeV and $|\eta| < 2.5$ and are identified as b-jets via ghost-matching [118] to a b-hadron with $p_T > 5$ GeV.

To avoid double-counting, particle-level objects are subject to overlap removal criteria. Dressed muons and electrons with a separation $\Delta R < 0.4$ from a jet are excluded.

5.3 Event selection

After defining physics objects, a series of selection criteria is applied to measured and simulated events to reject background events as much as possible. The choice of the selection criteria is inspired by $t\bar{t}$ differential cross-section measurements in $e\mu$ dilepton events [127].

Events are required to pass a single-electron or single-muon trigger. Due to the different LHC beam conditions between each year of data-taking periods, the trigger had to be readjusted in the 2016-2018 data-taking period, compared to 2015. Therefore, several triggers are used. For the 2015 data-taking period, both electrons and muons are required to have $p_T > 25$ GeV, while for the 2016-2018 data-taking periods, electrons and muons are required to have $p_T > 27$ GeV. Simulated data events are also required to pass the same trigger requirements. In addition, events are required to have at least one primary vertex reconstructed from at least two tracks with $p_T > 5$ GeV.

In Fig. 5.6, an example Feynman diagram of $t\bar{t}$ production and decay in the $e\mu$ channel is shown. The final state consists of exactly one electron and one muon, an electron neutrino and a muon neutrino and two b-quarks. Hence, based on the object's definition, events are required to have exactly one electron and one muon, two or three jets, of which two are b-jets[3]. The third jet is mainly accepted in order to increase the statistics of the selected sample while keeping the modelling uncertainties manageable. Hadronic resonances are suppressed by requiring the dilepton invariant mass to satisfy $m_{\ell\ell} > 15$ GeV. In addition, events with track multiplicities above 100 are excluded because the

---

[3] Events involving $W \to \tau\nu$ decays with a subsequent decay of the τ lepton to either $e\nu_e\nu_\tau$ or $\mu\nu_\mu\nu_\tau$ are included.

dominating contribution is due to pile-up tracks[4].

Events with an Opposite Sign (OS) $e\mu$ pair define the nominal sample, whilst events with a Same Sign (SS) $e\mu$ pair are used to estimate the background from fake leptons.

The particle-level events are required to pass the same selection requirements as the data selection but applied to the particle-level objects. In the case of the lepton p_T, a lower requirement of 25 GeV is applied.
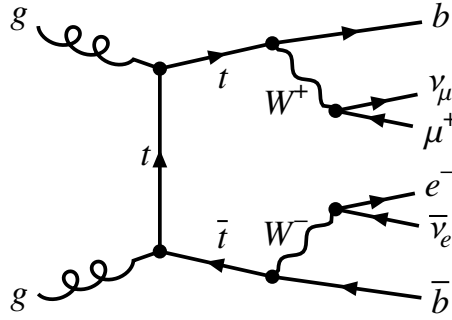
Figure 5.6: An exemplary Feynman diagram for the $t\bar{t}$ production via gluon fusion and the full decay chain in the $e\mu$ channel.

5.4 Observables definition

The colour reconnection mechanism aligns colours between partons, leading to a reduction of the available energy to produce new $q\bar{q}$ pairs. Hence, the particle multiplicity is reduced. The produced particles carry, on average, more momentum than particles produced in events without CR. Therefore, the sensitive observables to CR are related to the charged-particle multiplicity and their momentum.

To determine the observables sensitive to CR effects, a study is performed at the particle level, using the RIVET framework [128]. The candidate observables are inspired from previous measurements [24] and constructed using charged particles as defined in Section 5.2. Fig. 5.7 shows a comparison between the $t\bar{t}$ nominal prediction to the predictions of the CR0, CR1 and CR2 models that have been introduced in Section 3.2.1.

Figs. 5.7(a) and 5.7(b) show the charged-particle multiplicity n_{ch}, and the scalar sum of the transverse momenta of the charged particles $\sum_{n_{ch}} p_T$, respectively. In the lower panels, the ratio with respect to the nominal sample is shown. It can be seen, that the n_{ch} observable has a discrimination power, i.e maximum deviation, of up to 30 %, while in the $\sum_{n_{ch}} p_T$ variable the deviation reaches up to 20 %. The latter observable is highly correlated with n_{ch} but contains additional information about the kinematic configuration of the event. Therefore, both observables are considered to be measured.

Figs. 5.7(c) and 5.7(d) shows the $\sum_{n_{ch}} p_T$ and the average transverse momenta $\langle p_T \rangle$ as a function of n_{ch}, respectively. From the lower panels, it can be seen, that these two observables have a similar discrimination power between the various models. Therefore, only the $\sum_{n_{ch}} p_T$ as a function of n_{ch} is considered to be measured.

---

[4] The fraction of selected data events with track multiplicities above 100 is below 0.2 %.
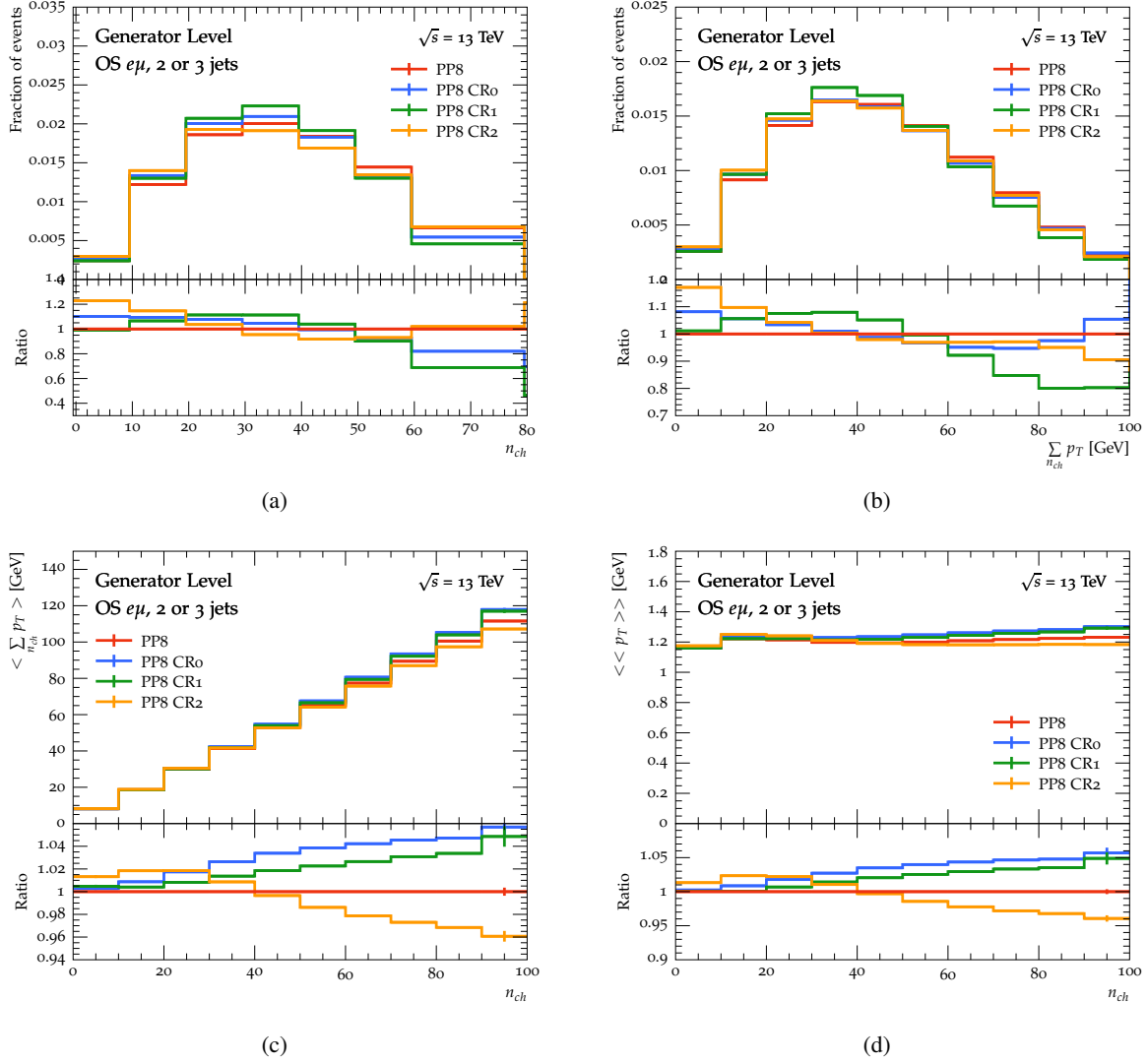
Figure 5.7: Comparison of the nominal POWHEG+PYTHIA 8 $t\bar{t}$ to CR0, CR1 and CR2 models implemented in PYTHIA 8 event generator. Distributions of (a) n_{ch}, (b) $\sum_{n_{ch}} p_T$, (c) $\sum_{n_{ch}} p_T$ as a function of n_{ch} and (d) the average tracks p_T as a function of n_{ch}. The distributions are normalised to unity. The lower panel shows the ratio calculated with respect to the nominal sample.

Detector-level observables

At the detector level, the observables are calculated using tracks defined in Section 5.1. The corresponding variables are then defined as:

- $n_{\mathrm{trk,out}}$: Number of tracks outside of jets with the binning given by $[0, 10, 20, 30, 40, 50, 60, 80, 100]$.

- $\sum_{n_{\mathrm{trk,out}}} p_{\mathrm{T}}$: Scalar sum of the transverse momenta of tracks outside of jets with the binning given by $[0, 10, 20, 30, 40, 50, 60, 70, 80, 90, 100, \infty)$ in units of GeV.

- $\sum_{n_{\mathrm{trk,out}}} p_{\mathrm{T}}$ in bins of $n_{\mathrm{trk,out}}$: This two-dimensional observable is built from the two variables above, as the $\sum_{n_{\mathrm{trk,out}}} p_{\mathrm{T}}$ in bins of $n_{\mathrm{trk,out}}$ with the binning given in Table 5.1.

The binning of the observables is chosen according to a predefined procedure described in Section 7.4. The same binning is used for each observable both at the detector level and particle level.

Table 5.1: Binning used for the $\sum_{n_{\mathrm{ch}}} p_{\mathrm{T}}$ in bins of the n_{ch} observable. For each n_{ch} bin, the $\sum_{n_{\mathrm{ch}}} p_{\mathrm{T}}$ binning is given in units of GeV.

n_{ch} bin	$\sum_{n_{\mathrm{ch}}} p_{\mathrm{T}}$ binning [GeV]
$[0, 20)$	$[0, 10, \infty)$
$[20, 40)$	$[0, 35, \infty)$
$[40, 60)$	$[0, 60, \infty)$
$[60, 80)$	$[0, 80, \infty)$
$[80, 100]$	$[0, \infty)$

5.5 Analysis strategy

This analysis aims to measure the $t\bar{t}$ production differential cross-section as a function of the observables presented in the previous section. The analysis strategy, illustrated in Fig. 5.8, operates according to the following recipe:

- Selection criteria are applied to the events and the different physics objects to obtain a dataset enriched in $t\bar{t}$ events in the dilepton ($e\mu$) final state. The detector-level and corresponding particle-level selections are detailed in Section 5.3.

- Observables that are sensitive to colour reconnection effects are constructed from tracks of charged particles as described in Section 5.4.

- Background events with a final state similar to $t\bar{t}$ signal events are estimated using a combination of simulation and partially data-driven estimates as described in Section 6.1.

- Backgrounds to primary hard-scatter tracks are estimated and subtracted as detailed in Section 6.2. This yields the *background-subtracted* distributions for each observable.

- The background-subtracted distributions are corrected for the effect of the limited track-reconstruction efficiency. This yields the *corrected-level* distributions for each observable as explained in Section 6.3.

- The corrected-level data of the differential distributions is corrected for detector resolution and migration effects among bins (unfolded). The details of the unfolding method are shown in Chapter 7.

- The impact of the various sources of uncertainties of the measurement are summarised in Chapter 8.

- The particle-level cross sections are obtained from the unfolded yields and compared with different theoretical predictions in Chapter 9.
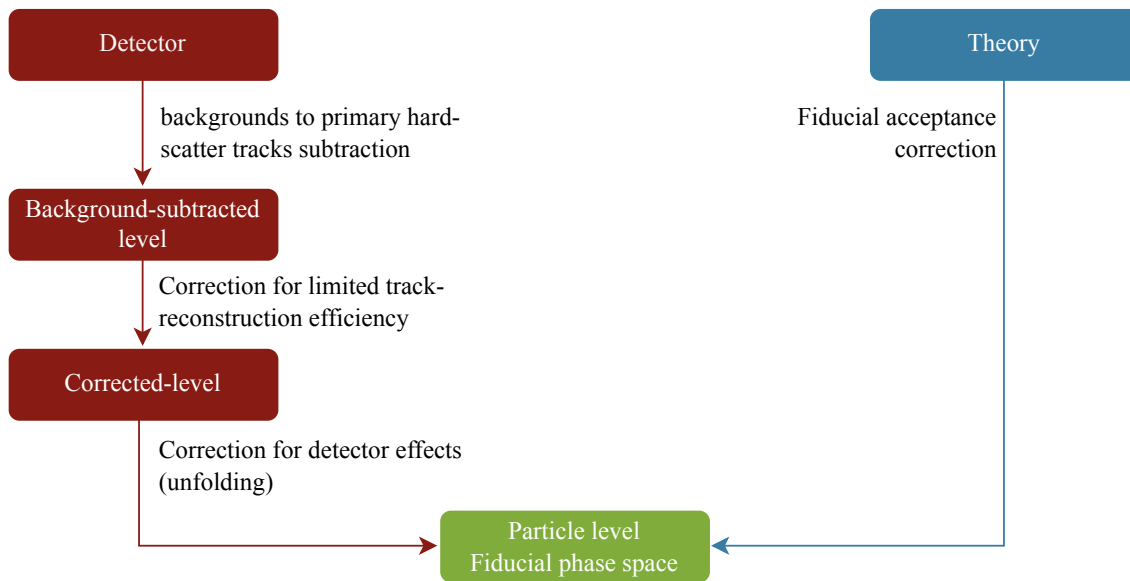
Figure 5.8: Schematic representation of the analysis strategy. In red, the various analysis levels performed on quantities measured by the detector, while blue represents the stage involving quantities predicted by theory. The measured quantities at the particle level are compared to theory and shown in green.

Backgrounds estimation and corrections to observables

The previous chapter introduced the selection criteria to obtain a dataset enriched in $t\bar{t}$ events in the dileptonic ($e\mu$) final state (Section 5.3), as well as the observables that are sensitive to colour reconnection effects (Section 5.4). In the following sections, the procedure to estimate and correct for the background contamination is explained.

Two different sources can lead to background contamination: event-based contributions from background processes with a final state similar to $t\bar{t}$ dileptonic events, discussed in Section 6.1, and track-based contributions originating from sources other than the hard-scattering process, discussed in Section 6.2. Finally, in Section 6.3, a correction to the observables is introduced, which accounts for the effect of track reconstruction inefficiencies.

6.1 Event-based backgrounds estimation

Background processes with a final state similar to signal $t\bar{t}$ events that pass the event selection are presented in Section 3.3. The expected number of events for these backgrounds and kinematic variables are obtained as follows:

- Single-top tW, $t\bar{t}V$, $Z(\to \tau\tau \to e\mu)$+jets and diboson production: The expected number of events is calculated using the theoretical cross-sections, as given in Section 3.3, and the acceptance from the simulated samples scaled to the integrated luminosity. The kinematic distributions are also determined from the simulated samples.

- Fake lepton events are those where at least one of the selected leptons is wrongly reconstructed as a prompt lepton. Fake leptons can arise either from the decay of a bottom or charm hadron, an electron from a photon conversion, a misidentified hadron, or a muon produced from the decay-in-flight of a pion or kaon. The number of expected fake-lepton background events is estimated using a partially data-driven method. This method is explained in the following section. The kinematic distributions of the fake-lepton background are determined from the simulated $t\bar{t}$ events with single-lepton and dilepton final states.

6.1.1 Fake-lepton background

The background from events with at least one fake lepton is estimated using a combination of data and simulation, using the method employed in Ref. [127]. This method relies on selecting events with a same-sign $e\mu$ pair, keeping all other selection criteria as defined in Section 5.3, as they are enriched with fake-lepton contributions. The samples of simulated events are those discussed in Section 3.3.

The number of expected fake-lepton background events, N^{fake}, is obtained using the number of observed same-sign events in data ($N^{\text{data,SS}}$), according to Eq. (6.1). The total predicted contribution of same-sign $e\mu$ pair events with prompt leptons, $N^{\text{sim,prompt,SS}}$, is subtracted and the result is scaled by the ratio of opposite-sign-to-same-sign events with fake leptons, R, obtained from simulation.

$$
N^{\text{fake}} = R \cdot \left(N^{\text{data,SS}} - N^{\text{sim,prompt,SS}} \right) ,
$$
$$
R = \frac{N^{\text{sim,fake,OS}}}{N^{\text{sim,fake,SS}}} .
$$
(6.1)

Simulated events with prompt leptons are those where both selected leptons are prompt, which includes events where the lepton charge sign has been misidentified, referred to as prompt wrong-sign, and events with two genuine same-sign prompt leptons, referred to as prompt right-sign. On the other hand, simulated events with fake leptons include several contributions which are classified according to the lepton type into four different event categories:

- Photon conversion electrons: The muon is prompt, while the electron is produced from a photon conversion which is itself produced via bremsstrahlung from a prompt electron ($e \to \gamma \to e$).

- Heavy-flavour electrons: The muon is prompt, while the electron is produced from the decay of a bottom or charm hadron.

- Heavy-flavour muons: The electron is prompt, while the muon is produced from the decay of a bottom or charm hadron.

- Other: Including all other cases. For example, a hadron is misidentified as an electron, a muon is coming from an in-flight decay of a pion or a kaon, or both leptons are non-prompt.

The ratio R factor is found to be 2.4 ± 0.1. Table 6.1 shows the estimates from simulation of prompt and fake lepton contributions to the opposite-sign and same-sign events compared with the observed event yields. The uncertainties are due to the finite number of simulated events, also called the MC statistical uncertainty. The prediction is broken down into prompt leptons and the various fake-lepton categories. The prompt contributions are about 35 % of the same-sign sample. They include wrong-sign (WS) contributions, dominated by $t\bar{t}$ dilepton events where the electron charge sign has been wrongly reconstructed, and right-sign (RS) contributions, with same-sign prompt leptons, from $t\bar{t}+V$ events, Z+jets and diboson production. The fake-lepton contributions are dominated by electrons from photon conversions, which represent 62 % of the same-sign sample. Sub-leading contributions come from leptons produced in semileptonic decays of heavy-flavour hadrons, and other sources. The prompt contributions are about 99 % of the opposite-sign samples, while the fake-lepton contributions are very small. Fig. 6.1 illustrates the different contributions in the OS and SS regions as a function of the electron p_{T}. A conservative 50 % uncertainty is assigned to the normalisation of the fake-lepton background estimation [127].

Table 6.1: The expected event yields from the combined signal and background events in the OS and SS $e\mu$ event samples compared with the observed event yields. The different event categories are described in the text. The quoted uncertainties are from MC statistical only.

Lepton category	OS	SS
Prompt right-sign	$197\,360 \pm 440$	75 ± 9
Prompt wrong-sign	0	243 ± 16
Photon conversion e	$1\,253 \pm 35$	561 ± 24
Heavy-flavour e	18 ± 4	8 ± 4
Heavy-flavour μ	45 ± 7	6 ± 3
Others	63 ± 8	6 ± 3
Total expected	$198\,740 \pm 450$	900 ± 30
Observed	$195\,507$	874
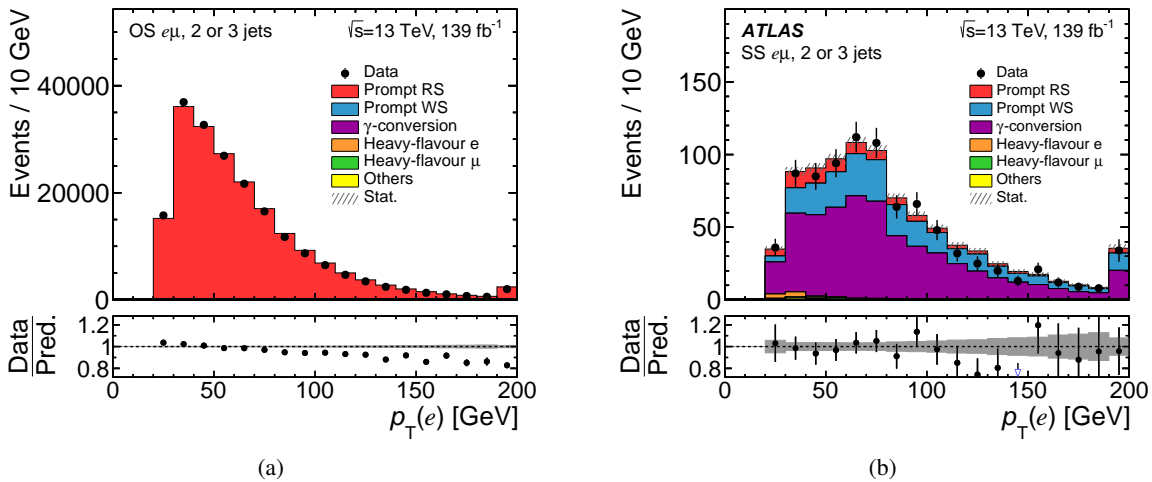
Figure 6.1: Distributions of the electron p_T in events with (a) an opposite-sign and (b) a same-sign $e\mu$ pair. The observed data is compared with the combined expectation from simulated $t\bar{t}$ and background events. The simulation's prediction is normalised to the number of expected events and broken down into contributions where both leptons are prompt right-sign (RS) or wrong-sing (WS), or one is a fake lepton from a photon conversion, from heavy-flavour decay or from other sources. The lower panel shows the ratio of data to the prediction in each bin. The hatched (grey) uncertainty band represents the MC statistical uncertainty. Events beyond the x-axis range are included in the last bin. The blue triangular marker in the lower panel point to data-to-prediction ratio values which lie beyond the shown y-axis range.

6.1.2 Event yields and kinematic distributions

Table 6.2 shows the expected event yields of the $t\bar{t}$ and background processes, which are compared with the number of observed events. The expected signal purity is approximately 96 % and the remaining background is dominated by the single top-quark production with a smaller contribution from fake-lepton background events estimated according to Eq. (6.1). Kinematic distributions that include signal and all background contributions are shown in Figs. 6.2 to 6.4, which illustrate the agreement between the prediction and the observed data. The different background processes are combined into a single histogram labelled "Background". The uncertainty band includes the MC statistical uncertainty and the total systematic uncertainty as described in Chapter 8.

Fig. 6.2 shows kinematic distributions of the leading jet, the electron and the muon. It can be seen that the observed data agrees well with the prediction within the uncertainties. In the leading jet p_T distribution, shown in Fig. 6.2(a), a slope can be seen in the ratio of data to prediction. This is in agreement with previous differential cross-section measurements by ATLAS [127, 129–131], and CMS [132–135], which have consistently observed a softer top-quark p_T spectrum (and related distributions) than what is predicted by NLO+PS MC generators. This discrepancy is at least partially due to missing NNLO corrections [136–140]. The difference between data and prediction is covered by systematic uncertainties. Fig. 6.3 shows distributions of the tracks p_T and η. It can be seen, that the tracks p_T distribution is underestimated by the prediction, particularly in the tail of the distribution. However, the deviations are covered by the systematic uncertainties, which are dominated by the parton shower modelling uncertainty. Fig. 6.4 shows distributions of the $n_{\text{trk,out}}$ and $\sum_{n_{\text{trk,out}}} p_T$ observables, in which considerable differences between the observed data and the nominal prediction can be seen, reflecting non-optimal tuning of the UE and MPI.

Table 6.2: Event yields obtained after the event selection. The expected event yields from the signal and the various background processes are compared with the observed event yields. The fractional contributions of the signal and the background processes to the expected event yield are given in %. The process labelled by 'Others' includes Z+jets and diboson background events. The quoted uncertainties are from MC statistics only.

Process	Selected events	Fraction [%]
$t\bar{t}$	$190\,640 \pm 440$	96
Single-top tW	$6\,310 \pm 80$	3.2
Fake leptons	$1\,318 \pm 36$	0.7
$t\bar{t}V$	213 ± 14	0.1
Others	91 ± 10	< 0.1
Total expected	$198\,610 \pm 450$	
Observed	195507	
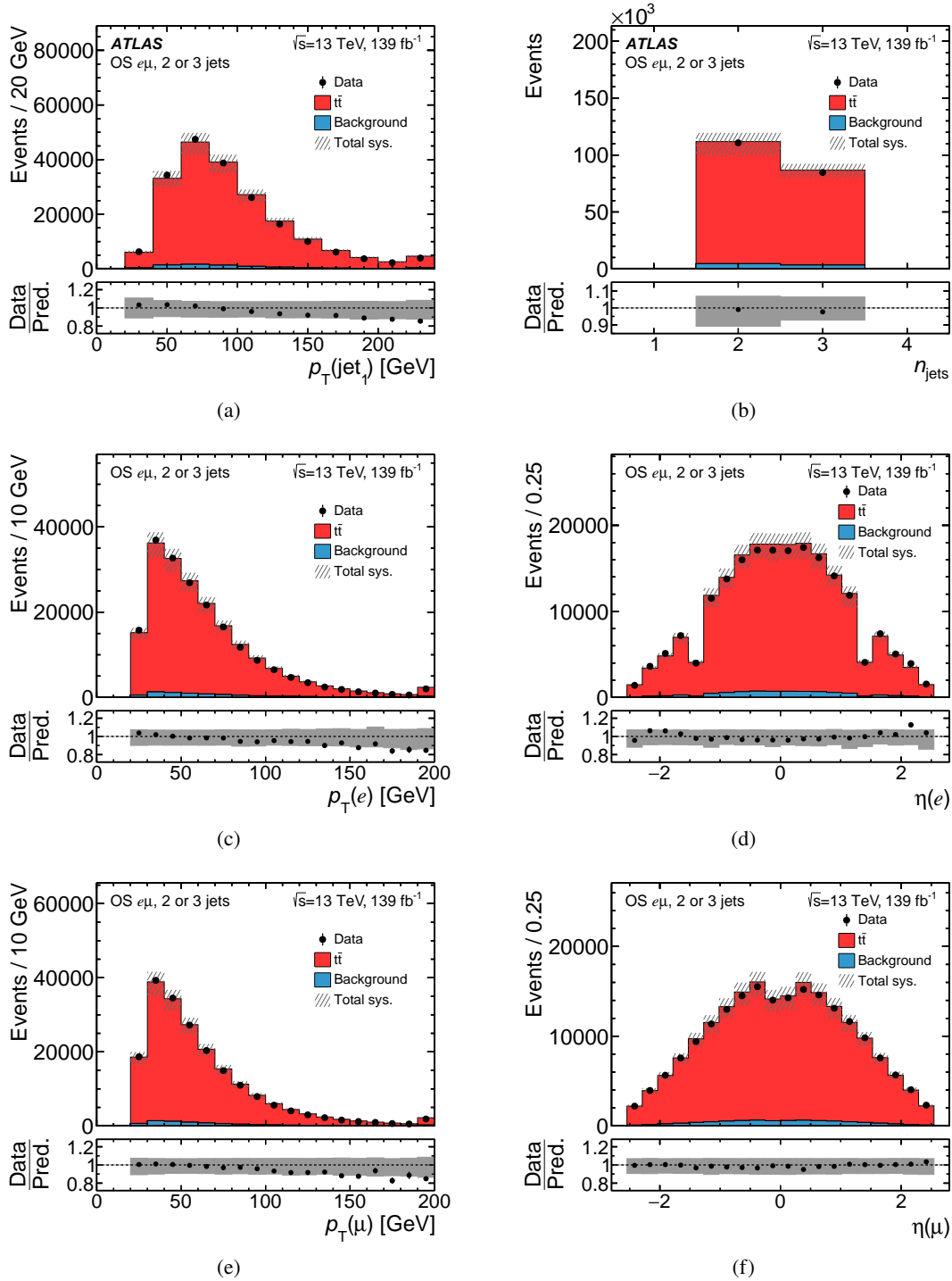
Figure 6.2: Distributions of (a) the leading jet p_T, (b) the jet multiplicity, (c) the electron p_T, (d) the electron η, (e) the muon p_T and (f) the muon η. The observed data is compared with the expectation from simulated $t\bar{t}$ and background events, where the background process includes contributions from tW, $t\bar{t}V$, Z+jets and diboson, and the estimated fake-lepton background. The lower panel shows the ratio of data to the prediction in each bin. The hatched (grey) uncertainty band includes the MC statistical uncertainty, background normalisation uncertainties, detector systematic uncertainties and $t\bar{t}$ modelling systematic uncertainties. Events beyond the x-axis range are included in the last bin.

(a)

(b)
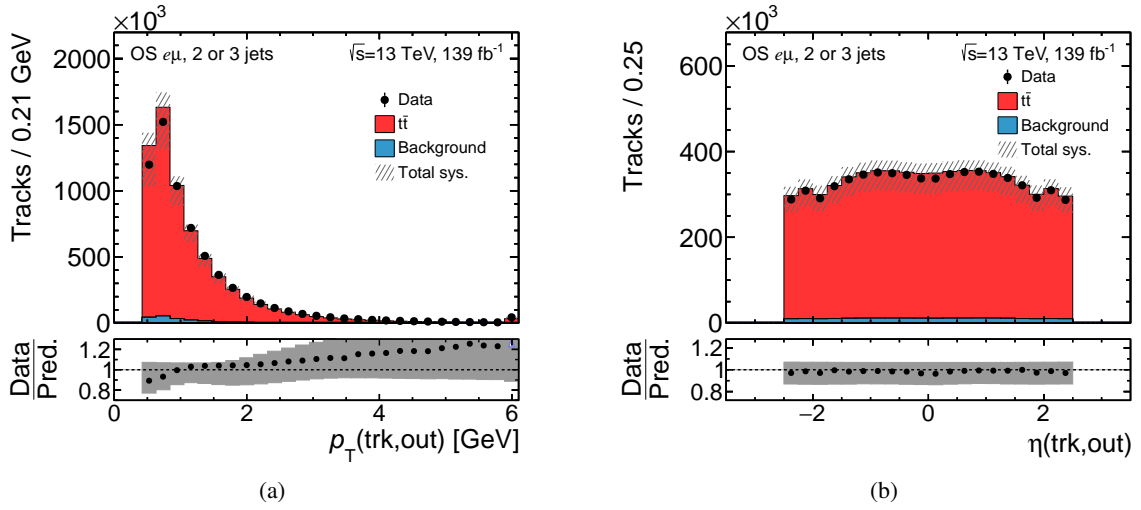
Figure 6.3: Distributions of (a) the tracks p_T and (b) the tracks η. The observed data is compared with the expectation from simulated $t\bar{t}$ and background events, where the background process includes contributions from tW, $t\bar{t}V$, Z+jets and diboson, and the estimated fake-lepton background. The lower panel shows the ratio of data to the prediction in each bin. The hatched (grey) uncertainty band includes the MC statistical uncertainty, background normalisation uncertainties, detector systematic uncertainties and $t\bar{t}$ modelling systematic uncertainties. Events beyond the x-axis range are included in the last bin.

(a)

(b)
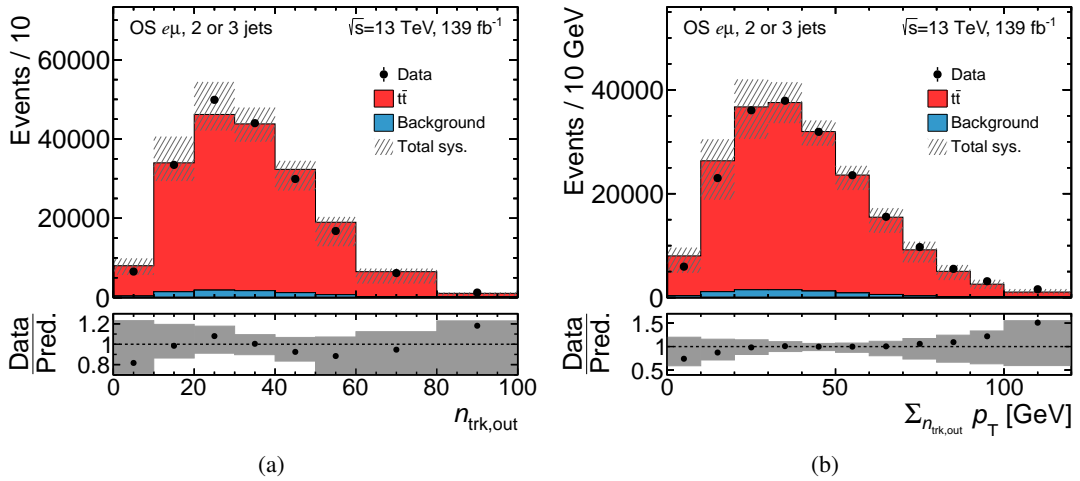
Figure 6.4: Distributions of (a) track multiplicity and (b) the scalar sum of the tracks transverse momenta. The observed data is compared with the expectation from simulated $t\bar{t}$ and background events, where the background process includes contributions from tW, $t\bar{t}V$, Z+jets and diboson, and the estimated fake-lepton background. The lower panel shows the ratio of data to the prediction in each bin. The hatched (grey) uncertainty band includes the MC statistical uncertainty, background normalisation uncertainties, detector systematic uncertainties and $t\bar{t}$ modelling systematic uncertainties. Events beyond the x-axis range are included in the last bin.

6.2 Track-based backgrounds estimation

Selected tracks other than the hard-scatter primary tracks can arise from additional sources. Pile-up tracks originating from additional nearby pp interactions and matched to the primary vertex. In addition, secondary tracks are mostly due to hadronic interactions with the detector material and the decay of long-lived particles. Finally, tracks formed by a random combination of hits or from a combination of hits from several truth particles, referred to as *fake tracks*. The pile-up tracks background is dominant, while secondary and fake-track backgrounds have a small contribution. Therefore, both secondary and fake-track backgrounds are combined and referred to hereafter by *secondary* tracks.

In order to estimate the pile-up and secondary track background contributions to each of the one-dimensional measured observables, simulated samples and data-driven techniques are used. These background contributions are estimated and subtracted individually for each of the sources on an event-by-event basis, yielding the 'background-subtracted' quantities $n_{\mathrm{trk,prim}}$ and $\sum_{n_{\mathrm{trk,prim}}} p_{\mathrm{T}}$, in the following way:

$$n_{\mathrm{trk,prim}} = n_{\mathrm{trk,out}} - c_{\mathrm{sec}} \cdot n_{\mathrm{sec}} - c_{\mathrm{PU}}(\mu, n_{\mathrm{trk,out}}) \cdot n_{\mathrm{PU}} \,, \tag{6.2}$$

$$\sum_{n_{\mathrm{trk,prim}}} p_{\mathrm{T}} = \sum_{n_{\mathrm{trk,out}}} p_{\mathrm{T}} - \sum_{i=1}^{c_{\mathrm{sec}} \cdot n_{\mathrm{sec}}} p_{\mathrm{T}}^{i} - \sum_{j=1}^{c_{\mathrm{PU}} \cdot n_{\mathrm{PU}}} p_{\mathrm{T}}^{\mathrm{corr},j} \,. \tag{6.3}$$

First, the number of pile-up and secondary tracks (n_{PU} and n_{sec}) is estimated in a stochastic way based on a method using MC simulated templates, described in Section 6.2.1. Then, the estimated numbers are scaled to account for differences in the rate of secondary and pile-up tracks between the expected and the observed events. For each background source, an individual scale factor is estimated. In the case of secondary tracks, the scale factor is referred to as c_{sec}, while for the pile-up tracks, the scale factor is referred to as $c_{\mathrm{PU}}(\mu, n_{\mathrm{trk,out}})$ and it depends on the number of interactions per bunch crossing μ and the track multiplicity. Therefore, $c_{\mathrm{PU}}(\mu, n_{\mathrm{trk,out}})$ is determined for different intervals of μ and $n_{\mathrm{trk,out}}$. Both scale factors estimation is described in Section 6.2.2, followed by the estimation of systematic uncertainties of $c_{\mathrm{PU}}(\mu, n_{\mathrm{trk,out}})$ in Section 6.2.3. Due to the small rate of secondary tracks, which is about 0.5 %, no uncertainties are assigned to the secondary tracks scale factor.

To obtain the $\sum_{n_{\mathrm{trk,prim}}} p_{\mathrm{T}}$ observable, a similar procedure to that for $n_{\mathrm{trk,prim}}$ observable is used. Templates are created from simulated $t\bar{t}$ events for pile-up and secondary-particle tracks p_{T}. In order to compensate for deficiencies in the modelling of pile-up in simulation, a reweighting method is used and a corrected p_{T} distribution ($p_{\mathrm{T}}^{\mathrm{corr}}$) is obtained. Since the contribution of tracks from secondary particles is small, no correction is applied in this case. Then, to estimate secondary tracks and pile-up tracks contribution $\left(\sum_{i=1}^{c_{\mathrm{sec}} \cdot n_{\mathrm{sec}}} p_{\mathrm{T}}^{i} \text{ and } \sum_{j=1}^{c_{\mathrm{PU}} \cdot n_{\mathrm{PU}}} p_{\mathrm{T}}^{\mathrm{corr},j} \right)$, a stochastic method is used, as explained in Section 6.2.4.

Track classification in MC simulation

In MC simulation, it is possible to distinguish the different track types using hits on tracks. Reconstructed tracks are classified into hard scattering, pile-up, secondary or fake tracks by matching the hits that contributed to the track fit to the energy deposited by the charged particle in the GEANT4 simulation [107].

A truth-matching probability, P_{match}, is defined using the ratio of the weighted number of hits which are common to a given track and the corresponding truth particle ($N^{\text{common}}_{\text{Pixel, SCT, TRT}}$), to the weighted number of all hits used in the track fit ($N^{\text{track}}_{\text{Pixel, SCT, TRT}}$):

$$P_{\text{match}} = \frac{10 \cdot N^{\text{common}}_{\text{Pixel}} + 5 \cdot N^{\text{common}}_{\text{SCT}} + 1 \cdot N^{\text{common}}_{\text{TRT}}}{10 \cdot N^{\text{track}}_{\text{Pixel}} + 5 \cdot N^{\text{track}}_{\text{SCT}} + 1 \cdot N^{\text{track}}_{\text{TRT}}} . \tag{6.4}$$

A real track is required to have a truth-match probability above 0.5, otherwise it is treated as a fake track. In the case of pile-up tracks, the associated generated particles are not stored, and that is used to identify them uniquely. In addition, secondary tracks can be identified through the event record.

The different track type multiplicities obtained using this procedure are labelled with *truth*, i.e the number of primary hard-scatter tracks is labelled $n^{\text{truth}}_{\text{HS}}$, the number of pile-up tracks is labelled as $n^{\text{truth}}_{\text{PU}}$, and the number of secondary-particle tracks including the contribution from fake tracks is referred to as $n^{\text{truth}}_{\text{sec}}$.

Table 6.3 shows the expected track yields from the $t\bar{t}$ process compared with the observed track yield. The rate of pile-up tracks is approximately 12 % out of the total selected tracks, while the rate of secondary tracks is only 0.5 %.

Table 6.3: The expected number of tracks from $t\bar{t}$ simulated events passing the event and tracks selection are compared with the number of observed tracks. The expectation from simulation is broken down into contributions from the hard scatter primaries, pile-up, and secondary tracks. The fractional contributions are given in %. The quoted uncertainties are from MC statistics only.

Track process	Selected tracks	Fraction [%]
Hard scatter primaries	$5\,622\,300 \pm 2400$	87
Pile-up	$799\,800 \pm 900$	12
Secondaries	$31\,900 \pm 180$	0.5
Total expected	$6\,454\,000 \pm 2500$	
Observed	$6\,559\,513$	

6.2.1 Estimation of the number of secondary and pile-up tracks

The number of secondary and pile-up tracks, n_{sec} and n_{PU} in Eqs. (6.2) and (6.3), are estimated per event in a stochastic way based on a method using MC templates. The procedure can be summarised in two steps. First, templates are created from simulated $t\bar{t}$ events for both $n^{\text{truth}}_{\text{sec}}$ and $n^{\text{truth}}_{\text{PU}}$ in bins of the track multiplicity. Exemplary distributions are shown in Figs. 6.5 and 6.6. It can be seen that the background contamination in $n_{\text{trk,out}}$ is higher for higher track multiplicities since more tracks are likely to be selected from additional pile-up vertices overlapping with the primary vertex. In the next step, for each event two random numbers are drawn n_{sec} (n_{PU}) from the templates of $n^{\text{truth}}_{\text{sec}}$ ($n^{\text{truth}}_{\text{PU}}$), corresponding to the $n_{\text{trk,out}}$ value of the event. In this way, the contamination is subtracted from the measured observables in a stochastic way.

In order to validate the procedure, a closure test is performed, comparing the estimated hard-scatter track multiplicity distribution with the true one. Fig. 6.7 shows the result of this test. In the lower histogram, the ratio of the estimated distribution to the true one is shown. The difference between both

distributions is up to 2 %, which is taken into account as an uncertainty in the background-estimation procedure.
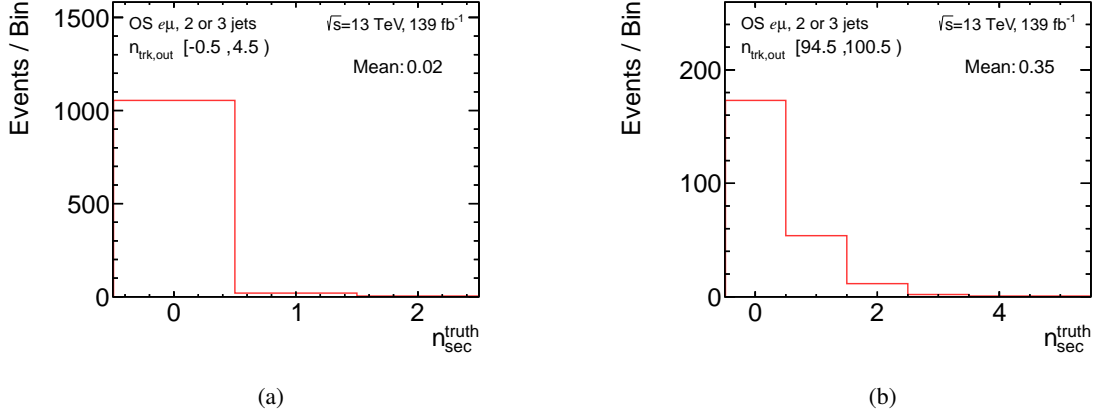
Figure 6.5: The truth number of secondary tracks, $n_{\mathrm{sec}}^{\mathrm{truth}}$, in bins of the track multiplicity, $n_{\mathrm{trk,out}}$, in simulated $t\bar{t}$ events. (a) $0 \leq n_{\mathrm{trk,out}} < 5$ and (b) $95 \leq n_{\mathrm{trk,out}} \leq 100$.
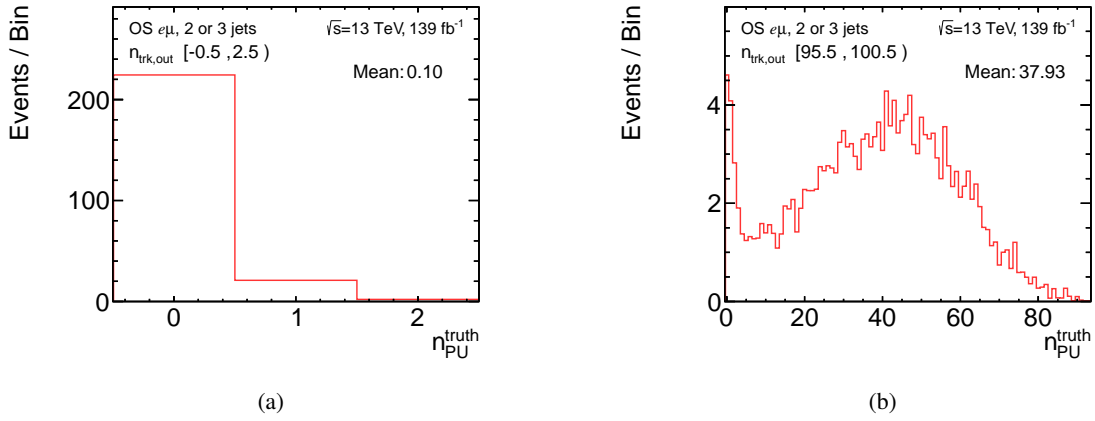
Figure 6.6: The truth number of pile-up tracks, $n_{\mathrm{PU}}^{\mathrm{truth}}$, in bins of the track multiplicity, $n_{\mathrm{trk,out}}$, in simulated $t\bar{t}$ events. (a) $n_{\mathrm{trk,out}} < 3$ and (b) $96 \leq n_{\mathrm{trk,out}} \leq 100$.
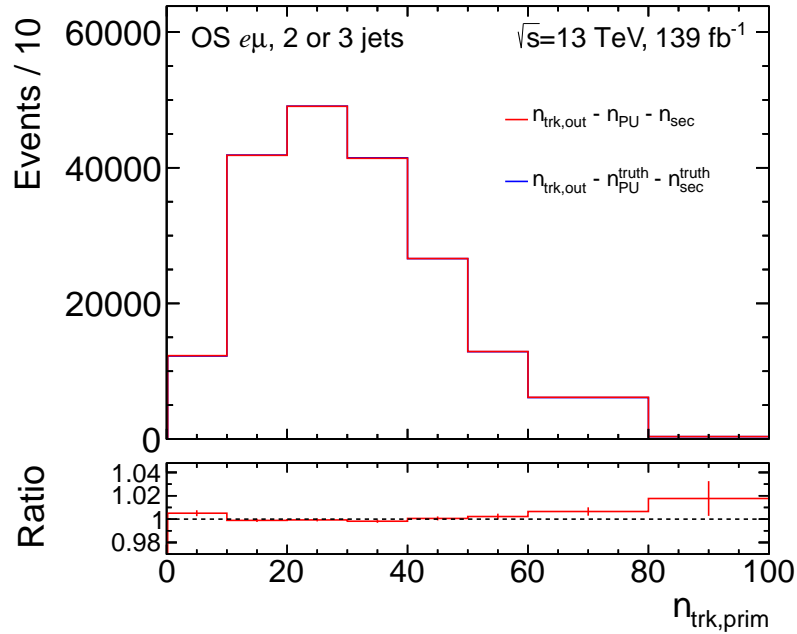
Figure 6.7: Distribution of the hard scatter primary track multiplicity in $t\bar{t}$ events. The estimated hard-scatter primary-tracks multiplicity distribution (red) is compared with the true one (blue). The lower panel shows the ratio of the estimated to the true multiplicity in each bin.

6.2.2 Estimation of the secondaries and pile-up scale factors

Differences between the expected and the observed rates of pile-up tracks and secondary-particle tracks are accounted for by estimating the scale factors c_{sec} and c_{PU}. The scale factor is estimated using a binned maximum-likelihood fit to data on a variable that shows discriminating shapes between the secondaries (pile-up) process and the hard-scatter and pile-up (secondaries) processes. The fit is carried out separately for secondaries and pile-up tracks. The discriminating variables are the d_0/σ_{d_0} distribution for secondary-particle tracks, see Fig. 6.8(a), and the z_0 distribution for pile-up tracks, see Fig. 6.8(b). The fits are performed after applying all track selection criteria, described in Chapter 5, except for the $|z_0 \sin(\theta)| < 0.5$ mm, which is extended to 1.5 mm to increase the variables range and therefore improve the stability of the fits. In the following, the determination of each of the scale factors is described.

Correction of the pile-up tracks distributions

Before the fits are performed, the d_0/σ_{d_0} and z_0 distributions for pile-up tracks are corrected for differences between collision data and simulation. These differences mainly originate from the difference in the beam spot width along the z-direction, σ_z. The width of the beam spot determines the density of pile-up interactions and it was varied throughout the data-collection periods as shown in Fig. 6.9. It has an average of 44 mm in 2015 and between 34 mm and 38 mm in 2016–2018 compared to 42 mm in MC simulation [141]. To account for the different densities of pile-up interactions in data and simulation, this correction is introduced.

(a)   (b)
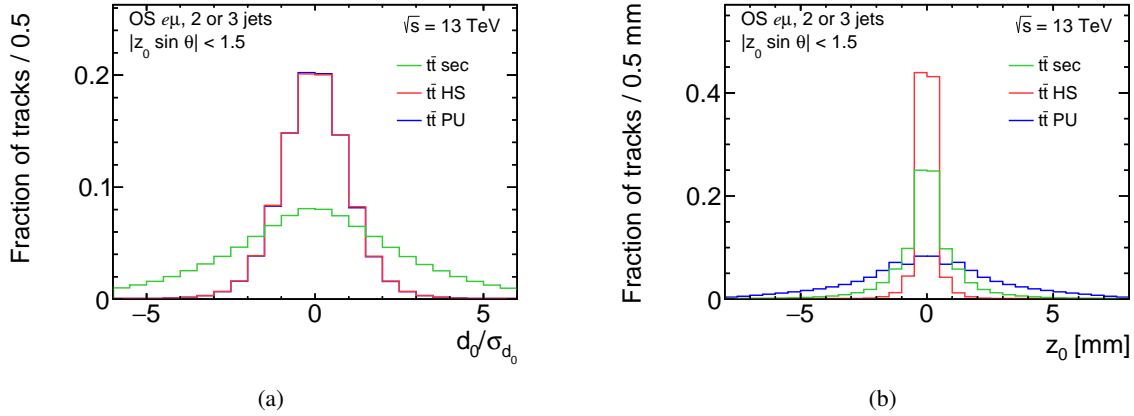
Figure 6.8: Distributions of (a) d_0/σ_{d_0} and (b) z_0, of secondary, hard scatter and pile-up tracks in simulated $t\bar{t}$ events. The distributions are normalised to unit area.

The correction is derived using high-purity pile-up tracks originating from pile-up vertices. For this purpose, events were selected with a pile-up vertex that is chosen randomly among all pile-up vertices in the event, which have at least ten reconstructed tracks associated with that vertex. The obtained data-to-MC ratio of the d_0/σ_{d_0} and z_0 distributions, shown in the lower panels in Fig. 6.10, is applied as a reweighting factor to the pile-up prediction of the respective distribution from tracks associated with the primary vertex. In this way, the d_0/σ_{d_0} and z_0 distributions for pile-up tracks match the data and they can be used to perform binned maximum-likelihood fits to data.
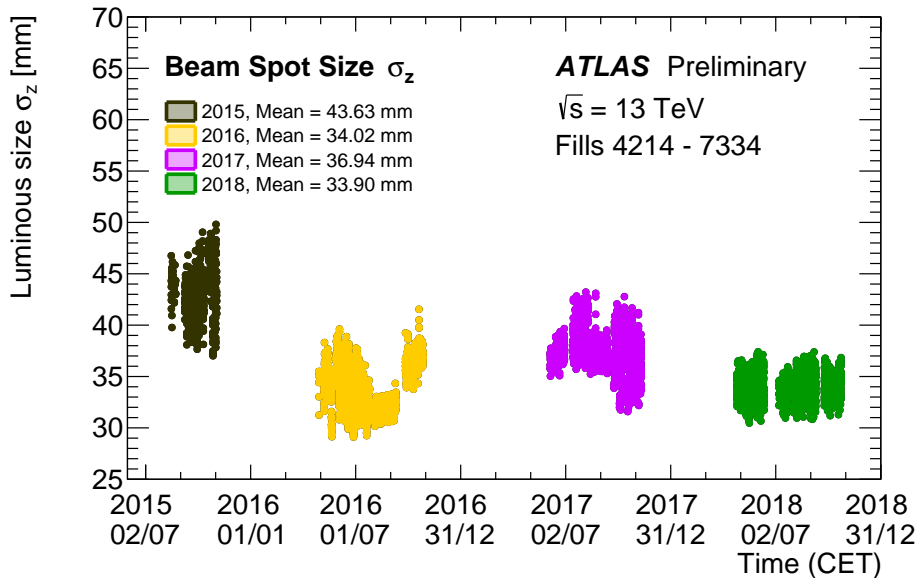
Figure 6.9: The width of the beam spot along the z-direction as a function of time for the years 2015–2018 [142].
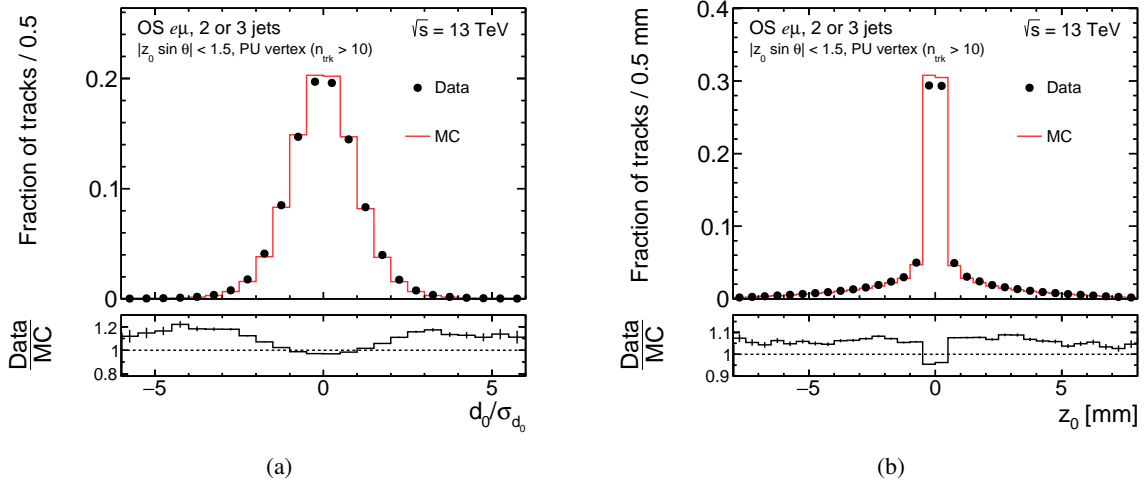
Figure 6.10: Distributions of (a) d_0/σ_{d_0} and (b) z_0 for pile-up tracks originating from pile-up vertices in data compared with $t\bar{t}$ events. In the lower panels, the ratio of the data-to-MC is shown. The distributions are normalised to unit area.

Estimation of the secondaries scale-factor

To determine c_{sec}, the hard-scatter prediction is combined with the (corrected) pile-up prediction of the d_0/σ_{d_0} distribution in one process, referred to as 'HS+PU'. Then, a binned maximum-likelihood fit is performed to the combined HS+PU prediction templates and the secondaries template to data. The distributions before performing the fit are referred to as *pre-fit*, and after performing the fit are referred to as *post-fit*. Fig. 6.11 shows the pre-fit d_0/σ_{d_0} distribution compared to the post-fit distribution, which is normalised to the fit result. The estimated scale-factor c_{sec} is 2.3 ± 0.02 where only the statistical uncertainty is taken into account. This large value is not a problem, as the rate of secondary tracks is only 0.5 % out of the total selected tracks. No systematic uncertainties are assigned to c_{sec} due to the small contribution from the secondary-track background.

Estimation of the pile-up scale-factor

The estimation of the pile-up scale factor, $c_{\text{PU}}(\mu, n_{\text{trk,out}})$, is more complex compared to the c_{sec}, as it depends on the number of interactions per bunch crossing μ and the track multiplicity $n_{\text{trk,out}}$. Here, the hard-scatter tracks prediction is combined with the secondary-tracks prediction of the z_0 distribution in one process, referred to as 'HS+sec'. Then, a binned maximum-likelihood fit is performed of the (corrected) pile-up template and the combined HS+sec template to data in bins of μ and $n_{\text{trk,out}}$. A separate fit is performed in each μ and $n_{\text{trk,out}}$ bin. Table 6.4 shows the resulting pile-up scale factor values, which range from 0.9 to 1.4, where higher values are obtained for higher μ and $n_{\text{trk,out}}$ values. Fig. 6.12 exemplarily shows the pre-fit z_0 distribution in three regions compared to their respective post-fit distributions which are normalised to the fit result. A clear improvement in data to MC agreement is observed after the fit. The next section presents systematic uncertainties in the pile-up scale factor.

(a)   (b)
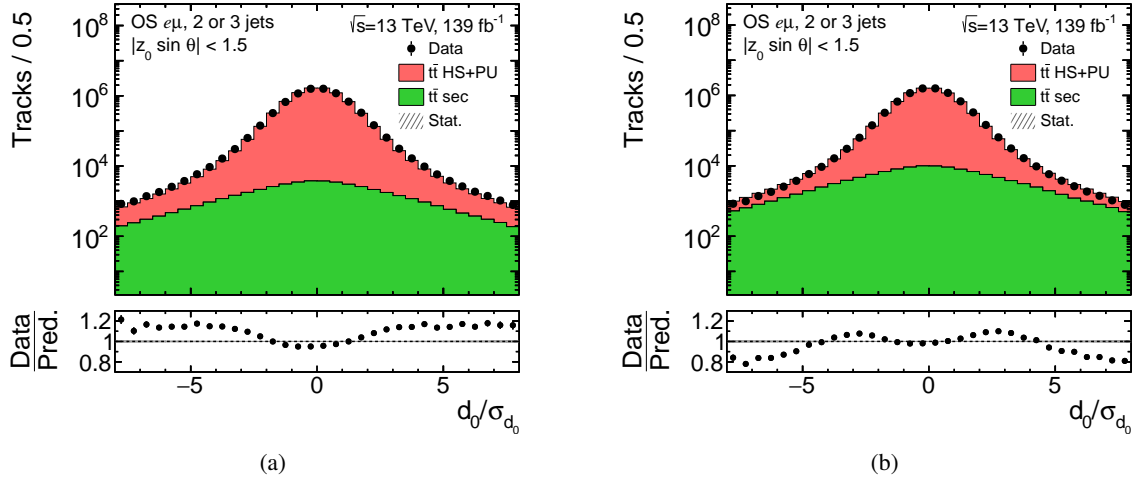
Figure 6.11: Distribution of the d_0/σ_{d_0}. (a) Without and (b) with the fraction of tracks from secondary particles scaled to the result of the binned maximum-likelihood fit. The observed data is compared with $t\bar{t}$ prediction from POWHEG+PYTHIA 8, broken down into the combined hard scatter and re-weighted pile-up-track contribution in red and the secondary-track contribution in green.

Table 6.4: Summary of the estimated pile-up scale factors c_{PU}, parameterised in μ and $n_{\mathrm{trk,out}}$. The quoted values have a statistical precision of 0.01.

Region	$n_{\mathrm{trk,out}} < 20$	$20 \leq n_{\mathrm{trk,out}} < 40$	$40 \leq n_{\mathrm{trk,out}} < 60$	$60 \leq n_{\mathrm{trk,out}} < 80$	$80 \leq n_{\mathrm{trk,out}} \leq 100$
$\mu < 20$	0.91	1.04	0.97	1.05	1.08
$20 \leq \mu < 40$	0.91	1.08	1.08	1.07	1.11
$\mu \geq 40$	0.95	1.15	1.23	1.27	1.36
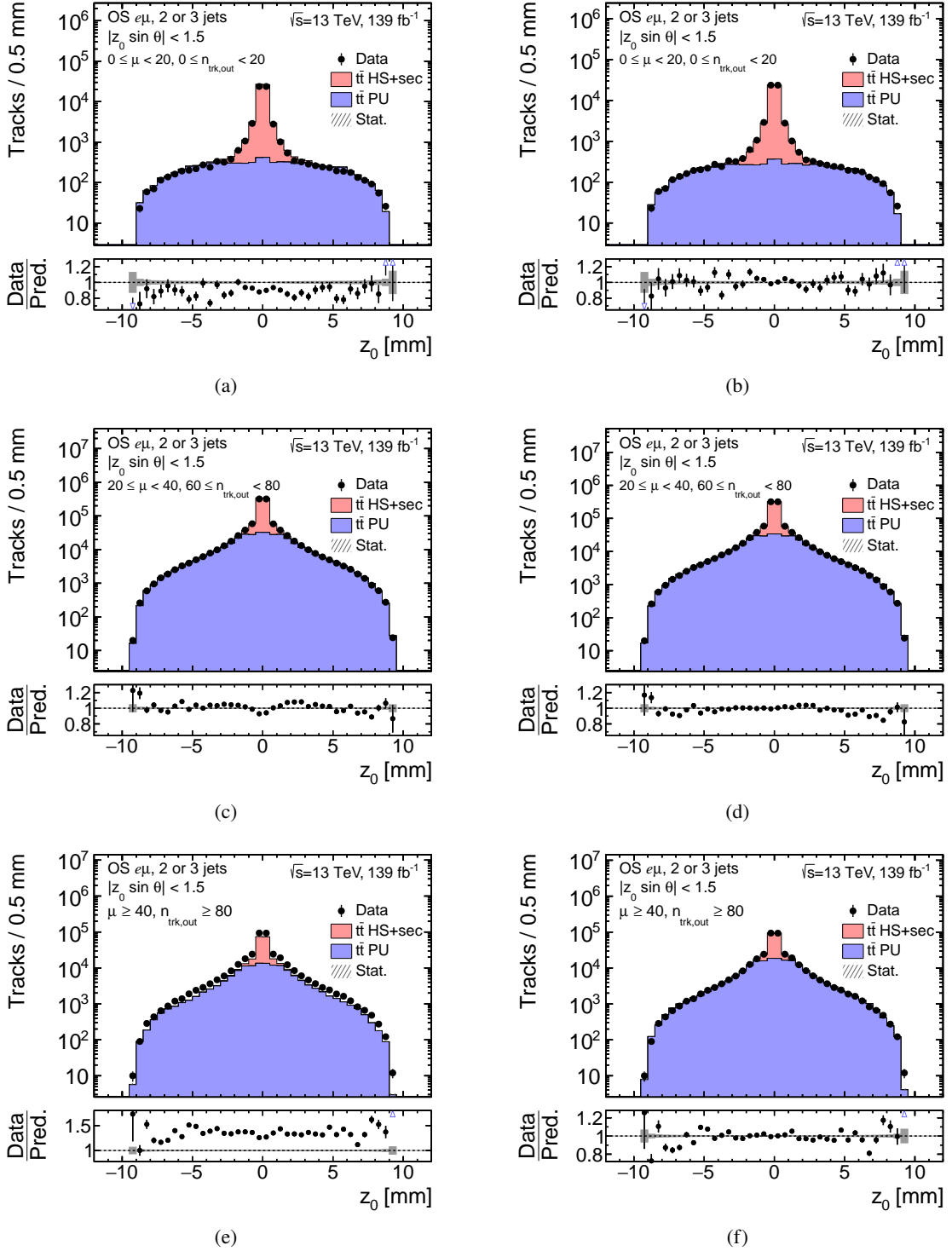
Figure 6.12: Distributions of the longitudinal impact parameter z_0. The observed data is compared with $t\bar{t}$ prediction from POWHEG+PYTHIA 8, broken down into the combined hard-scatter and secondary-tracks contribution in red and the (corrected) pile-up tracks contribution in blue. The distribution is shown without (left) and with (right) the fraction of pile-up tracks scaled to the result of the binned maximum-likelihood fit, (a-b) in the $\mu < 20$ and $n_{trk,out} < 20$ bin, (c-d) in the $20 \leq \mu < 40$ and $60 \leq n_{trk,out} < 80$ bin and (e-f) in the $\mu \geq 40$ and $80 \leq n_{trk,out} \leq 100$ bin.

6.2.3 Systematic uncertainties in the pile-up scale factor estimation

Several sources of systematic uncertainties affect the estimated pile-up scale factor. These uncertainties include the uncertainty due to the effect of different beam conditions, uncertainties due to the influence of hard-scatter primary tracks, uncertainties in the signal modelling, the uncertainty associated with the tracks reconstruction, and the uncertainty in the correction procedure to the pile-up tracks distributions. In the following, the estimation of each uncertainty is presented, followed by a summary of the total uncertainty.

Effect of different beam conditions

Due to changing LHC beam conditions and alignment settings between and within each period of the data-taking periods, the number of pile-up interactions is affected and consequently, the estimated $c_{\mathrm{PU}}(\mu, n_{\mathrm{trk,out}})$ [141]. A closure test is performed to demonstrate that the estimated $c_{\mathrm{PU}}(\mu, n_{\mathrm{trk,out}})$ accounts for these differences.

To perform the closure test, the estimated $c_{\mathrm{PU}}(\mu, n_{\mathrm{trk,out}})$ scale factor is used to scale the predicted number of pile-up tracks and another binned maximum-likelihood fit of the pile-up tracks background-rate to data is performed. The fit is carried out separately in the three data-taking periods, namely 2015–2016, 2017 and 2018. The scale factor obtained from the fit, c'_{PU}, is summarised in Table 6.5, which is as expected close to unity. The non-closure is within $10\,\%$ for the 2015–2016, $-6\,\%$ for 2017 and $-1\,\%$ for the 2018 data-taking periods, respectively. This leads to a weighted average of the non-closures of $0.4\,\%$, which is assigned as an uncertainty.

Table 6.5: Scale factors obtained from the $c_{\mathrm{PU}}(\mu, n_{\mathrm{trk,out}})$ closure test, c'_{PU} obtained for different data-taking periods. The uncertainty represents the statistical uncertainty of the fit.

Data taking period	c'_{PU}
2015-2016	1.102 ± 0.002
2017	0.935 ± 0.001
2018	0.994 ± 0.001

Influence of hard-scatter primary tracks

Uncertainties due to the influence of hard-scatter primary tracks are estimated by performing the fit in a sideband of the z_0 distribution, namely $|z_0| > 1$ mm. In this sideband region, a large contribution from hard-scatter primary tracks is excluded, allowing to study their influence on the estimated pile-up scale factor. Fig. 6.13 exemplarily shows the post-fit z_0 distributions which are normalised to the fit result. Table 6.6 summarises the relative difference between the sideband and the nominal $c_{\mathrm{PU}}(\mu, n_{\mathrm{trk,out}})$ scale factor. The resulting uncertainties range from less than $1\,\%$ for most regions up to $14\,\%$ in the high $n_{\mathrm{trk,out}}$ and low μ region.

Table 6.6: The sideband relative uncertainty in the pile-up scale-factor parameterised in μ and $n_{\text{trk,out}}$ and expressed in percent.

Region	$n_{\text{trk,out}} < 20$	$20 \leq n_{\text{trk,out}} < 40$	$40 \leq n_{\text{trk,out}} < 60$	$60 \leq n_{\text{trk,out}} < 80$	$80 \leq n_{\text{trk,out}} \leq 100$
$\mu < 20$	-0.5	2.5	0.6	0.5	-14.1
$20 \leq \mu < 40$	-0.1	0.4	0.3	-1.1	-6.7
$\mu \geq 40$	-1.6	0.6	1.2	-2.7	-1.8
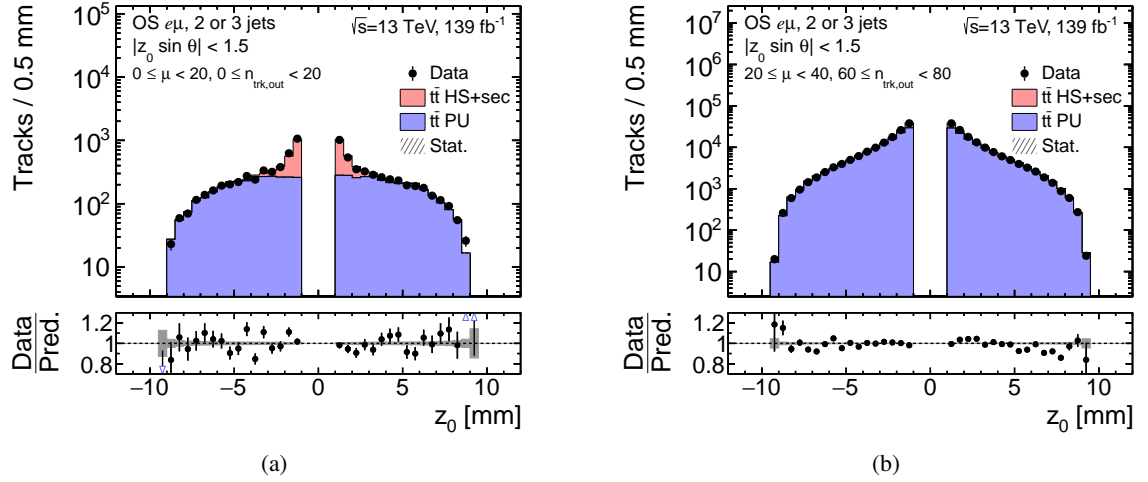
Figure 6.13: Distribution of the longitudinal impact parameter for $|z_0| > 1$ mm. The observed data is compared with the $t\bar{t}$ prediction from Powheg+Pythia 8, broken down into the combined hard-scatter and secondary-track contribution in red and the (corrected) pile-up-track contribution in blue. The fraction of tracks from pile-up tracks is scaled to the result of the binned maximum-likelihood fit in the (a) $\mu < 20$ and $n_{\text{trk,out}} < 20$ and the (b) $\mu \geq 40$ and $80 \leq n_{\text{trk,out}} \leq 100$ bins.

Signal modelling uncertainty

Uncertainties in the modelling of parton showers, hadronisation and underlying event, are assigned by varying the nominal $t\bar{t}$ sample to an alternative sample for which Powheg is interfaced to Herwig 7 instead of Pythia 8. Since the pile-up interactions modelling is identical in both samples, as described in Section 4.4, the main difference is caused by the different underlying-event models and thus by a modified z_0 distribution of the hard-scatter primary tracks used in the fit. Fig. 6.14 exemplarily shows the post-fit z_0 distributions which are normalised to the fit result. Table 6.7 summarises the relative difference between the $c_{\text{PU}}(\mu, n_{\text{trk,out}})$ scale factor obtained from this setup and the nominal scale factor. The resulting uncertainties range from less than 1 % for most regions up to 17 % for low $n_{\text{trk,out}}$ values.

Track reconstruction uncertainties

Several uncertainties are associated with the track reconstruction, which are described in Section 8.1. The impact parameter resolution uncertainty is the only uncertainty that has a non-negligible effect on the z_0 variable, which is used in the fit. Fig. 6.15(a) shows the variation of the z_0 distribution for the $t\bar{t}$ sample due to the z_0 resolution uncertainty. Table 6.8 summarises the relative difference between

Table 6.7: The signal-modelling relative uncertainty in the pile-up scale-factor parameterised in μ and $n_{\text{trk,out}}$ and expressed in percent.

Region	$n_{\text{trk,out}} < 20$	$20 \leq n_{\text{trk,out}} < 40$	$40 \leq n_{\text{trk,out}} < 60$	$60 \leq n_{\text{trk,out}} < 80$	$80 \leq n_{\text{trk,out}} \leq 100$
$\mu < 20$	15.7	-0.4	2.3	4.9	5.6
$20 \leq \mu < 40$	16.1	-0.3	-0.4	2.8	5.8
$\mu \geq 40$	17.6	1.3	-0.6	3.2	4.9

(a)   (b)
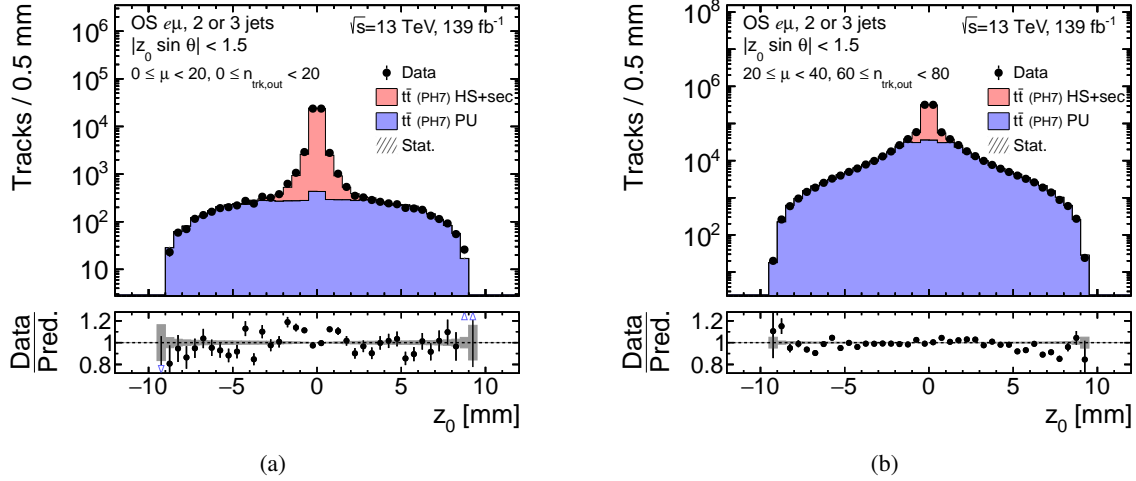
Figure 6.14: Distribution of the longitudinal impact parameter z_0. The observed data is compared with $t\bar{t}$ prediction from POWHEG+HERWIG 7, broken down into the combined hard-scatter and secondary-track contribution in red and the (corrected) pile-up-track contribution in blue. The fraction of tracks from pile-up tracks are scaled to the result of the binned maximum-likelihood fit in the (a) $\mu < 20$ and $n_{\text{trk,out}} < 20$ and the (b) $\mu \geq 40$ and $80 \leq n_{\text{trk,out}} \leq 100$ bins.

the $c_{\text{PU}}(\mu, n_{\text{trk,out}})$ scale factor obtained from this setup and the nominal scale factor. The resulting relative difference is found to be smaller than 2 % in all μ and $n_{\text{trk,out}}$ bins.

Table 6.8: The relative difference between the pile-up scale estimated to account for the z_0 impact parameter resolution and the nominal one. The values are given in percent.

Region	$n_{\text{trk,out}} < 20$	$20 \leq n_{\text{trk,out}} < 40$	$40 \leq n_{\text{trk,out}} < 60$	$60 \leq n_{\text{trk,out}} < 80$	$80 \leq n_{\text{trk,out}} \leq 100$
$\mu < 20$	-1.1	-1.2	-1.2	-0.9	-1.1
$20 \leq \mu < 40$	-0.8	-0.9	-0.9	-0.7	-0.6
$\mu \geq 40$	-0.7	-0.7	-0.6	-0.6	-0.5

Uncertainty in the correction procedure to the pile-up-track-distribution

The uncertainty in the correction procedure to the pile-up-track modelling, described in Section 6.2.2, is evaluated by varying the selection of the pile-up vertex. The pile-up-vertex selection is varied from the nominal choice of a vertex with at least ten reconstructed tracks to two other options: a downward variation to a vertex with at least five reconstructed tracks and an upward variation to a vertex with at
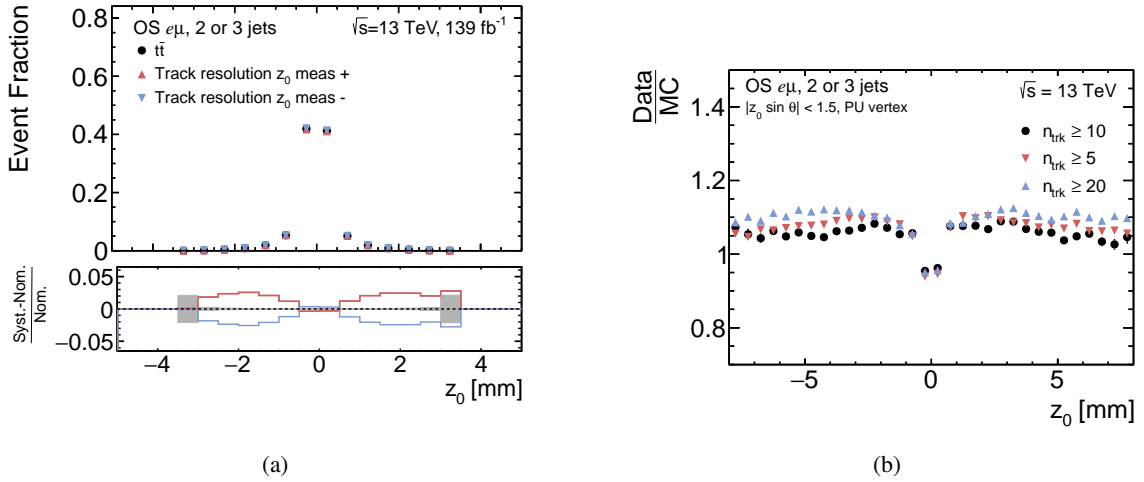
Figure 6.15: Systematic uncertainty templates for the longitudinal impact parameter resolution and the pile-up track correction procedure for the $t\bar{t}$ process. (a) The distribution variation due to the uncertainty in the z_0 resolution for the $t\bar{t}$ process is illustrated. (b) The ratio of data to MC of the longitudinal impact parameter z_0 for tracks originating from a pile-up-vertex.

least twenty reconstructed tracks. Fig. 6.15(b) shows the z_0 distribution associated with these two variations. The usage of the upward variation in the c_{PU} estimation results in a scale factor of 1.12, while the downward variation results in a c_{PU} of 1.11. Comparing the obtained scale factors to the inclusive nominal scale factor of 1.10 leads to an uncertainty of the pile-up scale factor of 1.4 %.

Summary

The systematic uncertainties in the pile-up scale factor estimation can be summarised as follows:

- The uncertainty due to different beam conditions and alignment settings is evaluated by re-fitting the rate of background pile-up-tracks for different collision-data periods and leads to an uncertainty of 0.4 % in the pile-up scale factor.

- Uncertainties due to the influence of hard-scatter primary tracks are estimated by fitting a sideband region with $|z_0| > 1$ mm. The resulting uncertainty ranges from less than 1 % for most regions to as much as 14 % in the high $n_{\mathrm{trk,out}}$ and low μ region.

- Uncertainties in the modelling of parton showers, hadronisation and the underlying event, are evaluated by comparing the nominal sample to an alternative sample for which POWHEG is interfaced to HERWIG 7.1 instead of PYTHIA 8. The main difference is caused by the different underlying-event models and thus by a modified z_0 distribution of the hard-scatter primary tracks used in the fit. The largest and dominant uncertainty is found for low $n_{\mathrm{trk,out}}$ values, being at a level of 17 %, while otherwise the uncertainty is a few percent.

- The uncertainty associated with the z_0 impact parameter resolution is evaluated using systematically varied $t\bar{t}$ samples, and it is found to be smaller than 2 %.

- The uncertainty in the reweighting procedure used to correct the modelling of pile-up tracks in simulation is evaluated by varying the selection of pile-up vertices and leads to an uncertainty of 1.4 % in the pile-up scale factor.

All pile-up scale-factor uncertainties are added in quadrature and the resulting relative uncertainties are presented in Table 6.9. The largest uncertainty is observed for events with $n_{\text{trk,out}} < 20$, mainly due to differences in the modelling of the UE between PYTHIA 8 and HERWIG 7.1.

Table 6.9: The total pile-up scale-factor relative uncertainty parameterised in μ and $n_{\text{trk,out}}$ and expressed in percent.

Region	$n_{\text{trk,out}} < 20$	$20 \leq n_{\text{trk,out}} < 40$	$40 \leq n_{\text{trk,out}} < 60$	$60 \leq n_{\text{trk,out}} < 80$	$80 \leq n_{\text{trk,out}} \leq 100$
$\mu < 20$	16	3	3	5	15
$20 \leq \mu < 40$	16	1	1	3	9
$\mu \geq 40$	18	2	2	4	5

6.2.4 Estimation of track-backgrounds contamination to the $\sum_{n_{\text{trk,out}}} p_{\text{T}}$ observable

The estimation of the track-backgrounds contamination to the $\sum_{n_{\text{trk,out}}} p_{\text{T}}$ observable, $\sum_{i=1}^{c_{\text{sec}} \cdot n_{\text{sec}}} p_{\text{T}}^i$ and $\sum_{j=1}^{c_{\text{PU}} \cdot n_{\text{PU}}} p_{\text{T}}^{\text{corr},j}$ in Eq. (6.3), is performed in a similar procedure to that for the $n_{\text{trk,out}}$ observable.

Templates are created from simulated $t\bar{t}$ events for both secondary-particle and pile-up tracks p_{T}, as shown in Fig. 6.16. In the next step, the p_{T}^{PU} distribution is corrected for differences between collision data and simulation using high-purity pile-up tracks. The obtained data-to-MC ratio of the track p_{T} distribution is applied as a reweighting function to p_{T}^{PU} and the corrected distribution is referred to as $p_{\text{T}}^{\text{corr}}$. These templates, together with the previously estimated n_{PU} (n_{sec}), are then used to estimate the pile-up (secondary-particle) track contamination in the measured $\sum_{n_{\text{trk,out}}} p_{\text{T}}$ observable, by drawing random numbers n_{PU} (n_{sec}) times from the corresponding track p_{T} template for each event.

In order to validate the procedure, a closure test is performed, comparing the estimated scalar sum of transverse momenta of hard-scatter tracks with the true one, and similarly comparing the same scalar sum in bins of $n_{\text{trk,prim}}$. Fig. 6.17 shows the result of this test. In the lower histogram, the ratio of the estimated distribution to the true one is shown. The difference between both distributions is up to 10 % for $\sum_{n_{\text{trk,prim}}} p_{\text{T}}$ and up to 20 % for the two-dimensional observable, which are taken into account as uncertainty in the background-estimation procedure.
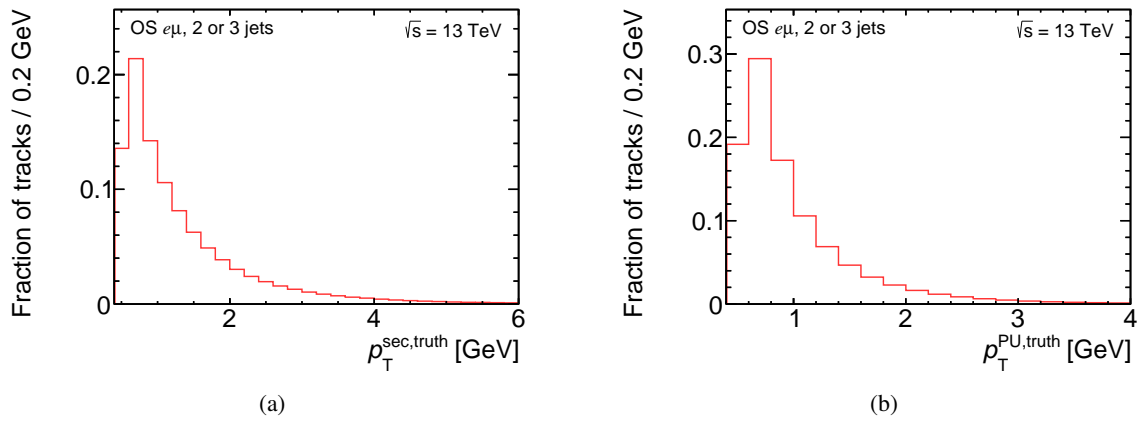
Figure 6.16: Distributions of the (a) pile-up track and (b) secondary-track transverse momentum in $t\bar{t}$ events.
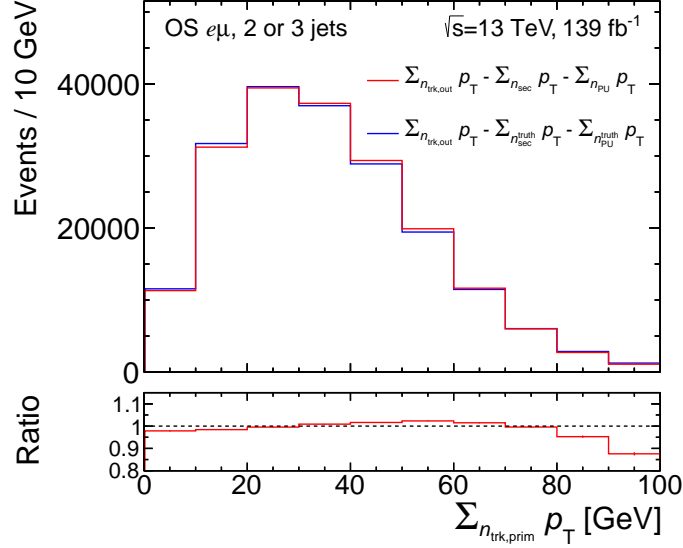
(a)
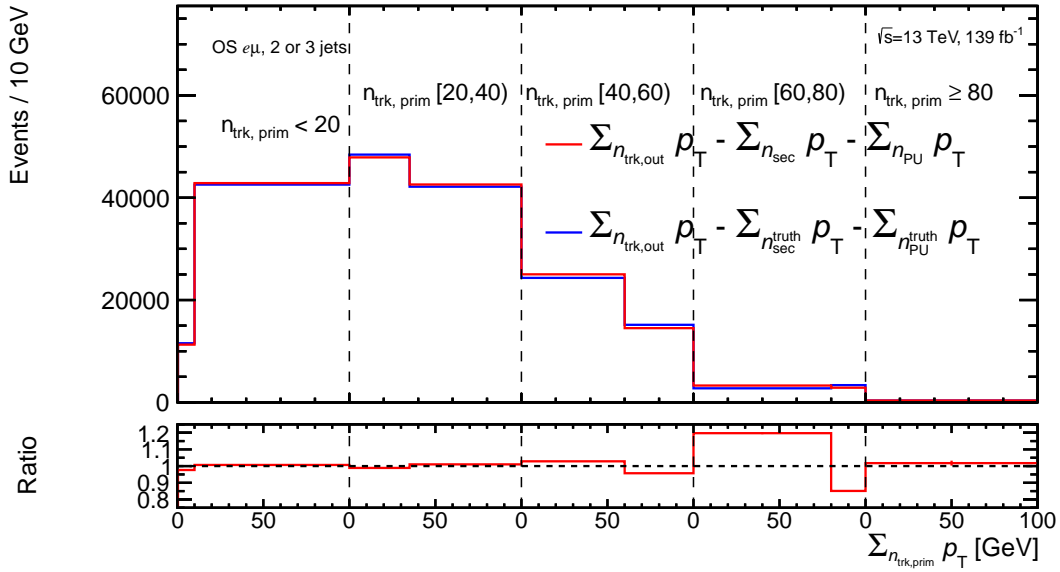
(b)

Figure 6.17: Distributions of (a) the scalar sum of hard scatter track p_T and (b) the scalar sum of hard scatter tracks p_T in bins of hard-scatter tracks multiplicity in $t\bar{t}$ events. The estimated quantity/observable (red) is compared with the true one (blue). The lower panel shows the ratio of the estimated to the true multiplicity in each bin.

6.3 Corrections to observables

To place the leading elements of the migration matrix[1] on the main diagonal, the background-subtracted quantities, $n_{\text{trk,prim}}$ and $\sum_{n_{\text{trk,prim}}} p_{\text{T}}$, are scaled with correction factors C_{ntrk} and $C_{\text{sum-pt}}$, respectively, accounting for the limited track-reconstruction efficiency.

$$n_{\text{trk}} = \frac{n_{\text{trk,prim}}}{C_{\text{ntrk}}(n_{\text{trk,prim}})} \qquad \sum_{n_{\text{trk}}} p_{\text{T}} = \frac{\sum_{n_{\text{trk,prim}}} p_{\text{T}}}{C_{\text{sum-pt}}(\sum_{n_{\text{trk,prim}}} p_{\text{T}})} \qquad (6.5)$$

The correction factors are calculated in bins of the background-subtracted quantity by averaging the ratio of the quantity at the background-subtracted level to its value at the particle level across all selected events of the nominal simulated $t\bar{t}$ sample. The function $C_{\text{ntrk}}(n_{\text{trk,prim}})$ has values between 0.68 and 0.89 in its range from 0 to 100, while the function $C_{\text{sum-pt}}(\sum_{n_{\text{trk,prim}}} p_{\text{T}})$ rises stepwise from 0.66 to 0.89 across the bins of its full range.

The corrections are applied to the observables in measured data events, in simulated events from all scattering processes (i.e. the $t\bar{t}$ process and all background processes), and in simulated events of the samples with systematically varied parameters. The corrected quantities (n_{trk}, $\sum_{n_{\text{trk}}} p_{\text{T}}$ and $\sum_{n_{\text{trk}}} p_{\text{T}}$ in bins of n_{trk}) are the final corrected-level observables forming the distributions to be unfolded (see Chapter 7), and are shown in Fig. 6.18. The uncertainty band includes detector systematic uncertainties and the pile-up background-track-rate uncertainty. Within these experimental uncertainties, there are considerable differences between the observed data and the nominal prediction, reflecting non-optimal tuning of the UE and MPI. Table 6.10 summarises the naming convention for the observables at different levels of the analysis.

Table 6.10: Naming convention for the observables at different levels of the analysis. At the background-subtracted level, the contributions of tracks from pile-up collisions and tracks from secondary vertices are subtracted. At the corrected level the Tracking Efficiency Correction factor is applied. The observables at the particle level are the analysis results.

Analysis level	Number of charged particles outside of jets	Scalar sum of track p_{T}
Detector level	$n_{\text{trk,out}}$	$\sum_{n_{\text{trk,out}}} p_{\text{T}}$
Background-subtracted level	$n_{\text{trk,prim}}$	$\sum_{n_{\text{trk,prim}}} p_{\text{T}}$
Corrected level	n_{trk}	$\sum_{n_{\text{trk}}} p_{\text{T}}$
Particle level	n_{ch}	$\sum_{n_{\text{ch}}} p_{\text{T}}$

---

[1] The migration matrix is one of the inputs to the unfolding method that is explained in Chapter 7. It is defined as the probability of an event generated in bin i in the fiducial volume at the particle level to be observed in bin j at the background-subtracted level.

(a)

(b)

(c)
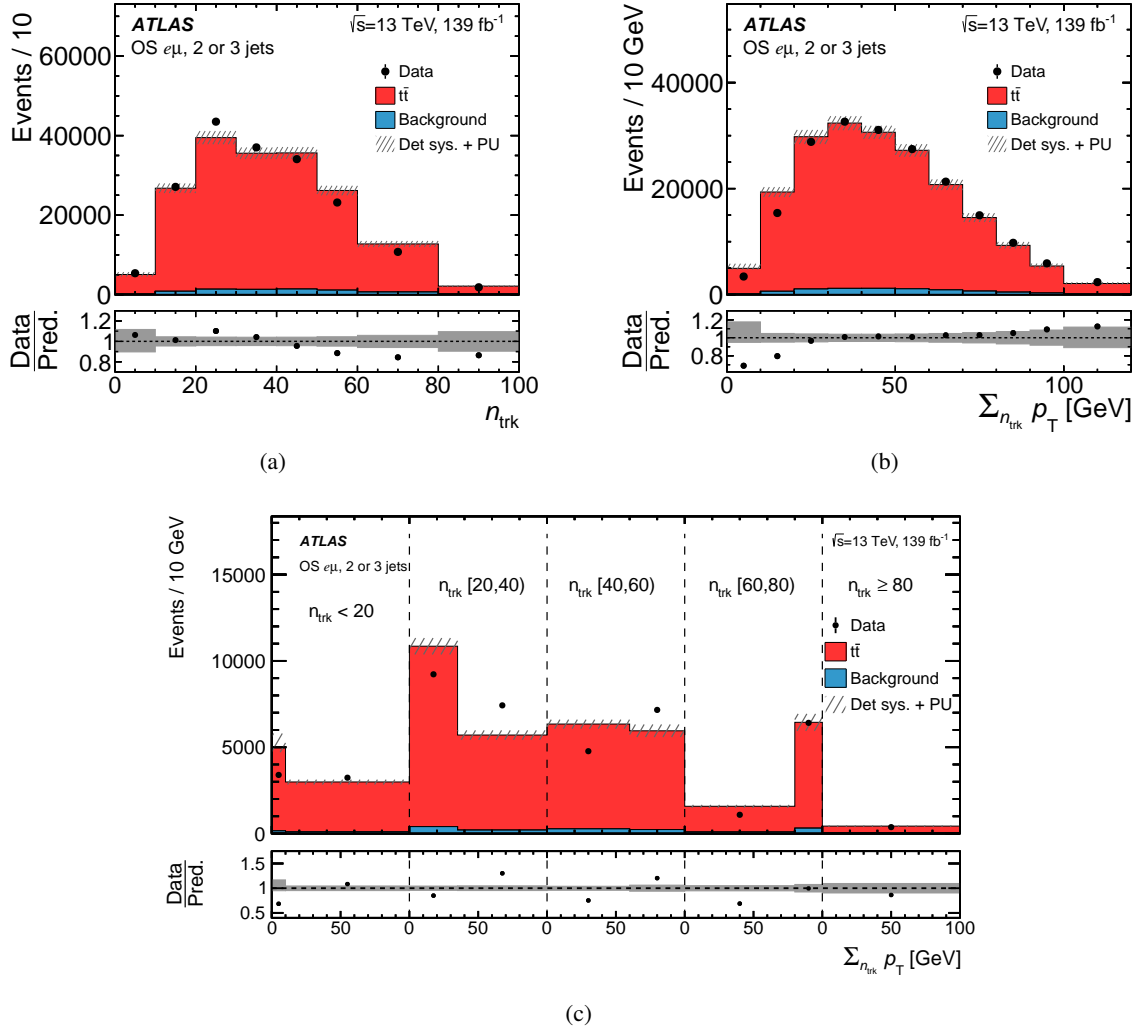
Figure 6.18: Distributions of (a) n_{trk}, (b) $\sum_{n_{\mathrm{trk}}} p_{\mathrm{T}}$ and (c) $\sum_{n_{\mathrm{trk}}} p_{\mathrm{T}}$ in bins of n_{trk}. The corrected-level observed distributions are compared with the expectation from simulated $t\bar{t}$ and background events, where the background includes contributions from tW, $t\bar{t}V$, Z+jets and diboson processes and the estimated fake-lepton background. The estimated contributions from pile-up tracks and secondary particles are subtracted from measured data events and simulated $t\bar{t}$ events. The tracking-efficiency correction factor is applied to all processes. The lower panel shows the ratio of data to the prediction in each bin. The hatched (grey) uncertainty band includes detector systematic uncertainties and the pile-up background-track-rate uncertainty. Events beyond the x-axis range are included in the last bin.

Differential cross-section measurement

This analysis aims to measure the differential $t\bar{t}$ production cross-section as a function of the charged-particle multiplicity, the scalar sum of the transverse momenta of the charged particles, and the same scalar sum in bins of charged-particle multiplicity. The previous chapter presented the estimation of the various background sources as well as the application of the tracking-reconstruction efficiency correction factor, yielding the *corrected-level* data distributions. Because the detector has a finite resolution and limited efficiency and acceptance, the corrected-level data distributions are distorted by detector effects and differ from their true value. The procedure of correcting for these effects in order to measure the differential and the total fiducial cross-sections is called unfolding [143]. A sketch illustrating the unfolding problem is shown in Fig. 7.1.

In Section 7.1, the unfolding problem is formulated, followed by a brief description of the used Iterative Bayesian Unfolding (IBU) method [144] in Section 7.2. Then, the procedure to extract the differential and total fiducial cross-sections using the IBU method is presented in Section 7.3. The optimised binning for the differential variables is motivated in Section 7.4. Finally, Section 7.5 presents the various tests that are performed to validate the unfolding procedure.
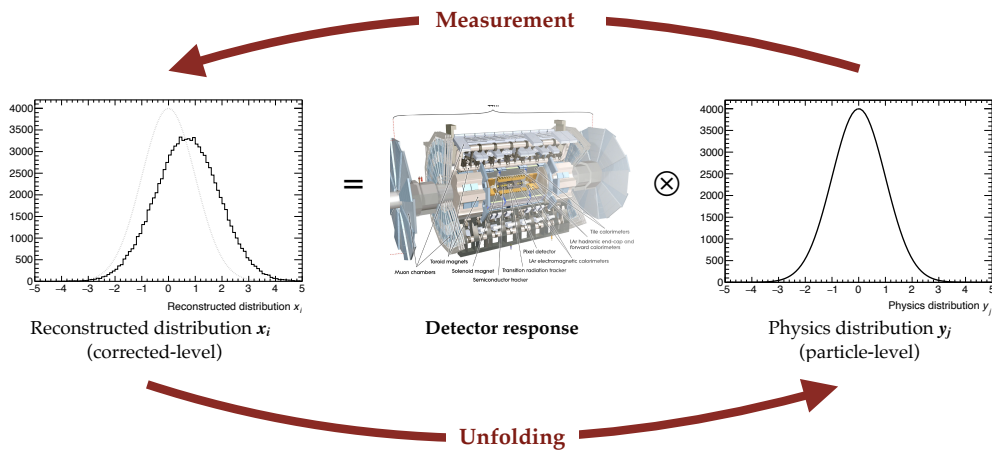
Figure 7.1: Illustration of the unfolding problem [145].

7.1 Formulation of the unfolding problem

The relation between a measured quantity x to its unknown true underlying value y can be expressed as follows:

$$f_{\text{meas}}(x) = \int R(x|y) f_{\text{true}}(y) \mathrm{d}y , \tag{7.1}$$

where $f_{\text{meas}}(x)$ is the probability distribution function (p.d.f) of the measured quantity x, $f_{\text{true}}(y)$ is the p.d.f of the true underlying physics effects, and the response function $R(x|y)$ encodes the smearing effects of the experimental apparatus used. In practice, measured data of a variable is captured as histograms with a specific binning. Therefore Eq. (7.1) can be rewritten as:

$$x_i = \sum_{i=1}^{N} R_{ij} y_j , \tag{7.2}$$

where N is the number of bins of the histogram of the true quantity y, i and j represent the various bins of the distributions at corrected-level and truth-level, respectively. The detector response matrix is further interpreted as a conditional probability:

$$R_{ij} = \mathcal{P}(\text{observed in bin } i | \text{true value in bin } j) . \tag{7.3}$$

There is a non-negligible fraction of events produced by the experimental setup but lost due to the limited detector resolution. The probability that an event leads to a measured value is called *efficiency* and is defined as:

$$\epsilon_j = \sum_{i=1}^{M} R_{ij} = \mathcal{P}(\text{observed anywhere} | \text{true value in bin } j) . \tag{7.4}$$

where M is the number of bins of the histogram of the corrected-level quantity x. In this analysis, the binning of the true distribution y_j and the corrected-level distribution x_i is the same, i.e. $M = N$. Including the expected background contribution, Eq. (7.2) is then modified to be:

$$x_i = \sum_{i=1}^{N} R_{ij} y_j + \beta_i , \tag{7.5}$$

where β_i is the number of expected background events in bin i. The task of the unfolding is to invert Eq. (7.5) to obtain the vector of true values $\vec{y}$ from the corrected-level vector $\vec{x}$, i.e. $\vec{y} = (\vec{x} - \vec{\beta})\mathbf{R}^{-1}$. The straightforward approach is the inversion of the response matrix, which is possible but has a major disadvantage. The resulting unfolded distributions have unacceptably large variances and strong negative correlations from bin to bin. The cause can be large off-diagonal elements of the response matrix or too small bin size compared to the resolution of the detector (see Ref. [143] for more details). However, the matrix inversion provides an unbiased solution from a statistical point of view. Therefore, alternative approaches exist, where one accepts small bias (added as a systematic uncertainty) in exchange for a large reduction in the variance. The IBU method is used in this analysis, which is explained in the following section.

7.2 The Iterative Bayesian unfolding method

The IBU method was developed by D'Agostini [144, 146] to circumvent the problem of inverting the response matrix. It is based on Bayes' theorem to estimate the inverse of the response matrix $P(\text{true}_i|\text{observed}_j) \equiv P(\text{true value in bin } i|\text{observed in bin } j)$:

$$P(\text{true}_i|\text{observed}_j) = \frac{P(\text{observed}_j|\text{true}_i) \cdot P_0(\text{true}_i)}{\sum_{\text{true}_k} P(\text{observed}_j|\text{true}_k) \cdot P_0(\text{true}_k)} , \qquad (7.6)$$

where $P_0(\text{true}_i)$ is the prior. Then, the truth event yield is obtained as:

$$y_i = \frac{1}{\epsilon_i} \sum_{\text{observed}_j} x_i P(\text{true}_i|\text{observed}_j) . \qquad (7.7)$$

The drawback of this method is that the result will depend on the prior $P_0(\text{true}_i)$. To overcome this limitation, an iterative approach is used to minimise the model dependence. After each iteration, the obtained unfolded distribution is fed back in as the subsequent prior. The initial prior is set to the particle-level distribution of the nominal signal sample. The iterations end at the step for which modifications to the unfolded results introduced by additional steps are smaller than a given tolerance value. With higher iterations, the statistical fluctuations increase as well as negative correlations. The following section describes the optimisation of the number of iterations.

Iterations optimisation

The number of iterations is determined by minimising the average global correlation factor, ρ_{avg} [147]. After several iterations, it is expected to observe a minimum of ρ_{avg}, as the correlations between neighbouring bins are expected to go from positive to negative with higher iterations. The iteration that minimises ρ_{avg} is taken as the optimal value. The global correlation factor in bin i is defined by:

$$\rho_i = \sqrt{1 - \left(\text{Cov}_{ii} \cdot \text{Cov}_{ii}^{-1} \right)^{-1}} , \qquad (7.8)$$

while the average global correlation factor is calculated as:

$$\rho_{\text{avg}} = \frac{1}{N_b} \sum_{i=1}^{N_b} \rho_i \qquad (7.9)$$

where N_{b} is the number of bins, Cov represents the statistical covariance matrix. The covariance matrix is calculated using 1000 pseudo-experiments, obtained by smearing the MC corrected-level distribution 1000 times using a Poisson distribution with a mean equal to the bin content. Each pseudo-experiment is passed through the unfolding machinery. The covariance matrix is derived from the unfolded pseudo-experiments and recalculated for each iteration. Fig. 7.2 shows the resulting ρ_{avg} as a function of N_{iter} for the three measured observables. The test suggests three iterations for both n_{ch} and $\sum_{n_{\text{ch}}} p_{\text{T}}$ in bins of n_{ch} observables, while five iterations are suggested for the $\sum_{n_{\text{ch}}} p_{\text{T}}$, which is adjusted to three iterations to ensure good closure of the unfolding test, described in Section 7.5. Thus, three iterations are used for all measured observables.

(a)

(b)

(c)
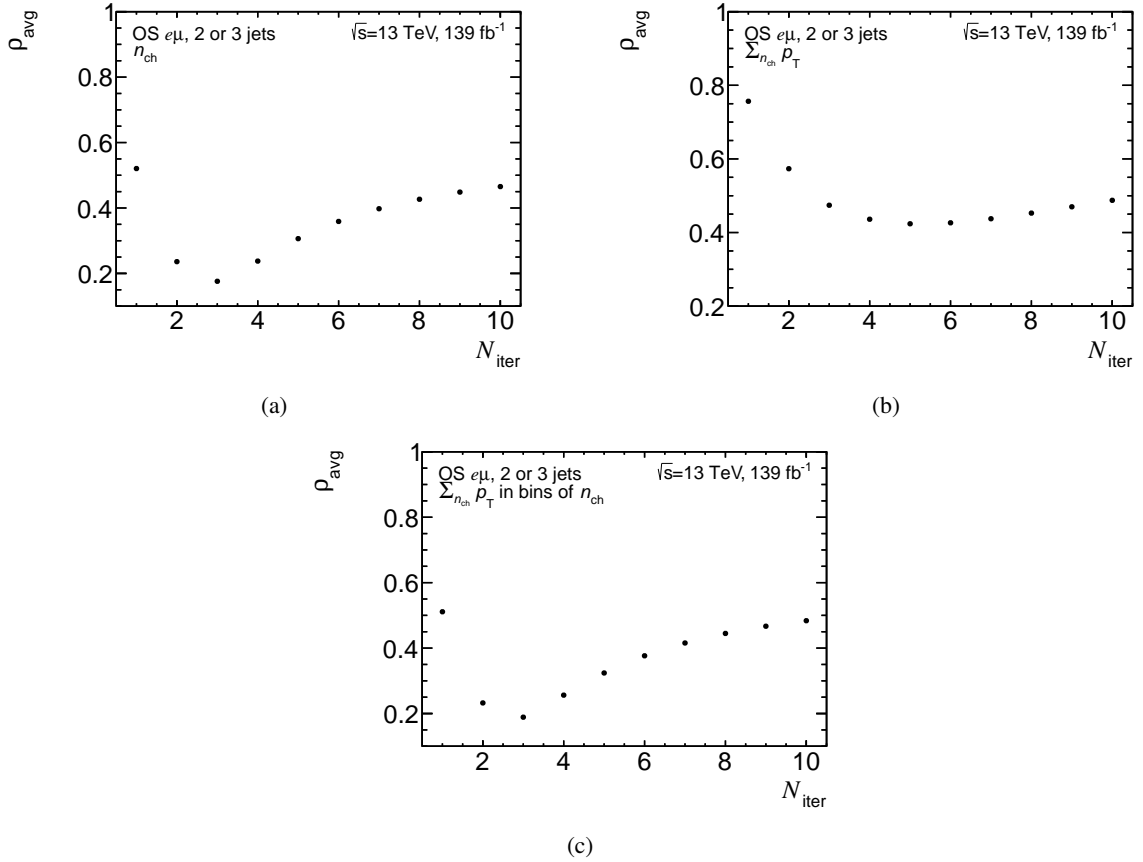
Figure 7.2: Average global correlation coefficient ρ_{avg} as a function of the number of iterations N_{iter} for the (a) n_{ch}, the (b) $\sum_{n_{\text{ch}}} p_{\text{T}}$ observables, and (c) the $\sum_{n_{\text{ch}}} p_{\text{T}}$ in bins of n_{ch}.

Migration matrices

The response matrix visualises the effect of the detector by relating the reconstructed (corrected-level) events and the true (particle-level) events using a 2D histogram. It is determined from the nominal simulated $t\bar{t}$ events. The off-diagonal elements of this matrix represent events that migrated to neighbouring bins after the measurement by the detector. The so-called migration matrix is simply a row-normalised version of the response matrix. The migration matrix is presented here as it makes the visual inspection easier by simply reporting the percentage of migration from the particle-level bin to the corrected-level one, as shown in Fig. 7.3. The migration matrices for the observables n_{ch}, $\sum_{n_{\text{ch}}} p_{\text{T}}$, and $\sum_{n_{\text{ch}}} p_{\text{T}}$ in bins of n_{ch} are shown. The corrected-level observable is shown on the x-axis, while the particle-level observable is shown on the y-axis. The values are normalised so that each row sums to unity. It can be seen from the principal diagonal of the migration matrix of the $\sum_{n_{\text{ch}}} p_{\text{T}}$ observable that the probability for particle-level events to be reconstructed in the same bin is above 50% in seven bins out of eleven. In the last bin, only 41% of particle-level events are reconstructed in the same bin, while 60% of the events migrate to the lower $\sum_{n_{\text{trk}}} p_{\text{T}}$ bin.
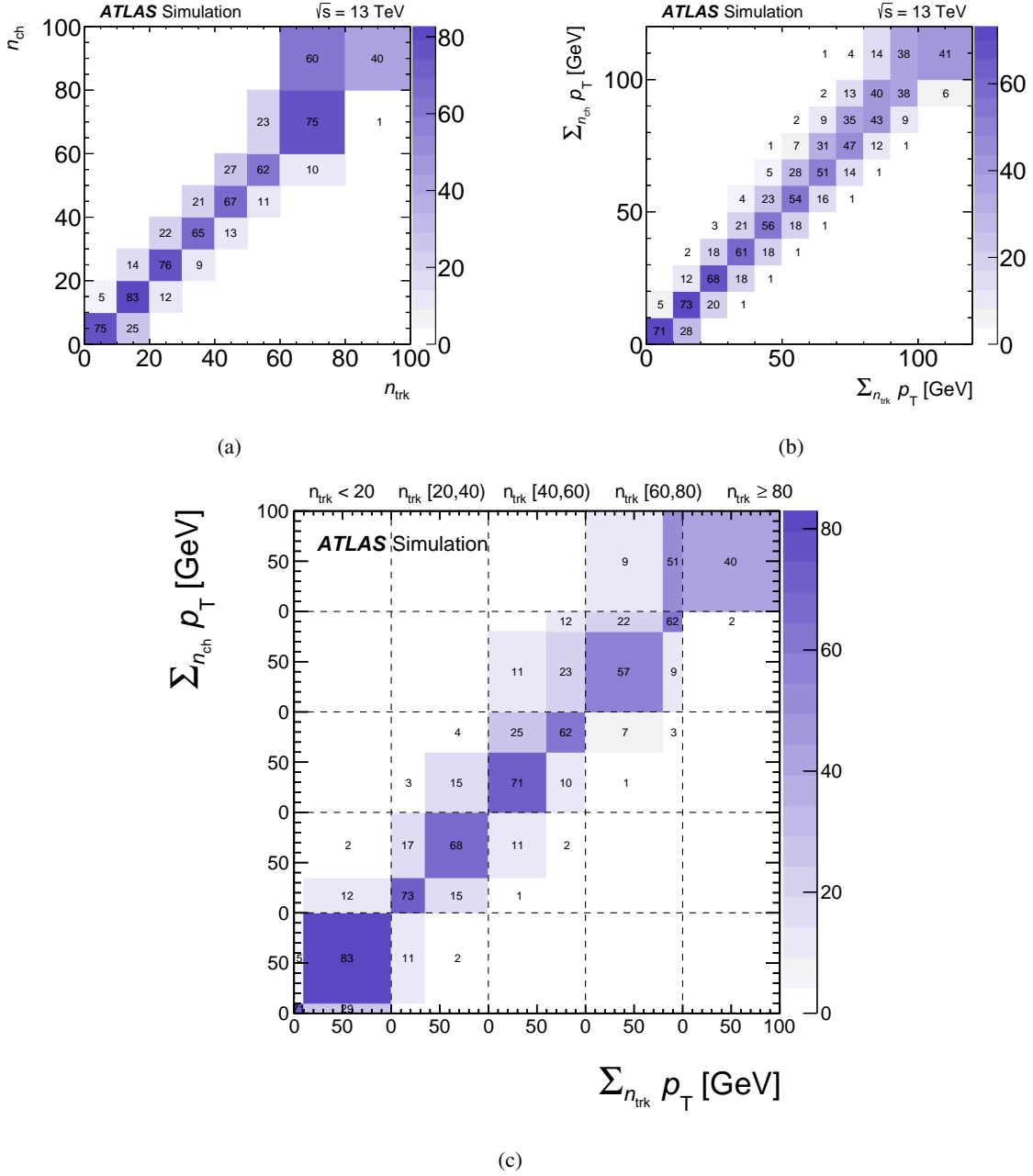
Figure 7.3: Migration matrix of the observables (a) n_{trk}, (b) $\sum_{n_{\mathrm{trk}}} p_{\mathrm{T}}$, and (c) $\sum_{n_{\mathrm{trk}}} p_{\mathrm{T}}$ in bins of n_{trk}. The values are normalised per row and shown as percentages. The numerical value of the bin is displayed if it is > 1%. Events beyond the x-axis or y-axis range are included in the last bin.

7.3 Extraction of differential cross-sections

The fiducial integrated and differential cross-section distributions in the fiducial phase space defined in Section 5.3 are obtained from the corrected-level events using the IBU unfolding technique that corrects for acceptance and detector effects.

The strategy used to measure the absolute differential cross-section of a variable X can be summarised in the following equation:

$$\frac{\mathrm{d}\sigma^{\mathrm{fid}}}{\mathrm{d}X_i} = \frac{N_i^{\mathrm{unf}}}{\mathcal{L}\Delta X_i} \, ,$$

$$N_i^{\mathrm{unf}} = \frac{1}{\epsilon_i} \sum_j R_{ij}^{-1} f_j^{\mathrm{acc}} \left(N_j^{\mathrm{corr}} - N_j^{\mathrm{bkg}} \right) \, .$$

(7.10)

In the first step, the number of unfolded events N_i^{unf} in particle-level bin i is determined. The event-based background contributions N_j^{bkg} in corrected-level bin j, summarised in Table 6.2, are subtracted from the track-based background-subtracted and tracking-efficiency-corrected distribution N_j^{corr}. The yields are then corrected with the factor f^{acc} to account for $t\bar{t}$ events that fall outside the fiducial acceptance at the particle level. Then, the distributions are unfolded using the IBU as implemented in RooUnfold [148], denoted by R_{ij}^{-1}. Afterwards, the efficiency correction factor, ϵ_i, is applied to account for events selected in the particle-level fiducial phase space but not reconstructed at the corrected level. In the next step, the events are corrected for the integrated luminosity $\mathcal{L}$ and the bin width ΔX_i. The same strategy is used to extract the double differential cross-section, according to the following equation:

$$\frac{\mathrm{d}^2\sigma^{\mathrm{fid}}}{\mathrm{d}X_i\mathrm{d}Y_j} = \frac{N_{ij}^{\mathrm{unf}}}{\mathcal{L} \cdot \Delta X_i \Delta Y_j} \, .$$

(7.11)

The total fiducial cross-section, σ^{fid}, is obtained by integrating the absolute differential cross-section over all bins and its value is used to determine the normalised differential cross-section $1/\sigma^{\mathrm{fid}} \cdot \mathrm{d}\sigma^{\mathrm{fid}}/\mathrm{d}X_i$.

The efficiency and acceptance correction factors are also taken from the nominal simulated $t\bar{t}$ sample, similar to the response matrix, and defined as:

$$f_j^{\mathrm{acc}} = \frac{N^{\mathrm{corr}\wedge\mathrm{part}}}{N^{\mathrm{corr}}} \qquad\qquad \epsilon_i = \frac{N^{\mathrm{corr}\wedge\mathrm{part}}}{N^{\mathrm{part}}} \, ,$$

(7.12)

where $N^{\mathrm{corr}\wedge\mathrm{part}}$ is the number of corrected-level events that pass the particle-level selection, N^{part} is the number of particle-level events. Fig. 7.4 exemplarily shows the unfolding corrections of the n_{ch} observable. The f_j^{acc} correction is around 90%, while the ϵ_i starts with 28% and drops to 22% in the tails.
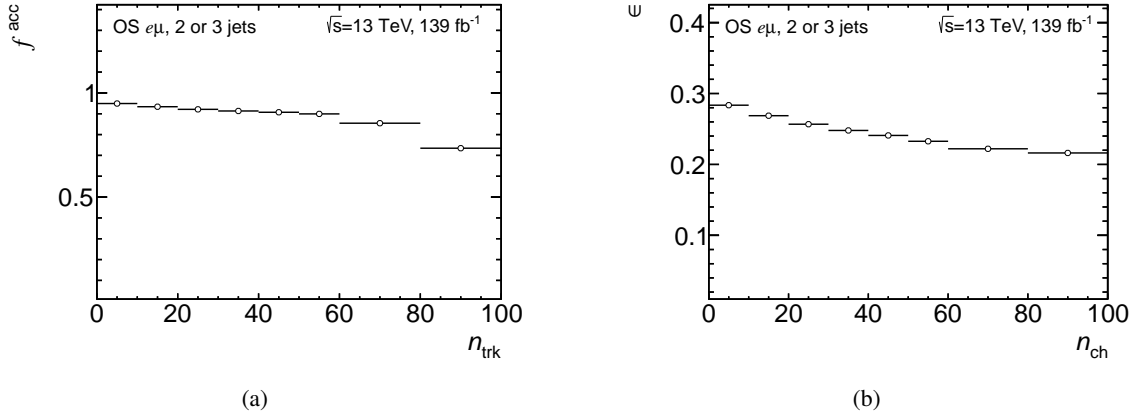
Figure 7.4: Unfolding corrections for the n_{ch} observable for the nominal simulated $t\bar{t}$ events. The fiducial acceptance f^{acc} correction factor (a) is shown as well as the selection efficiency correction factor ϵ (b).

7.4 Binning optimisation

The choice of the binning for the differential variables, which is introduced earlier in Section 5.4, is performed before the unfolding. The optimal binning is chosen based on the following criteria:

- decrease migrations to neighbouring bins in order to reduce the uncertainties from the unfolding procedure and ensure stable unfolding results. Migration effects are sensitive to the resolution of the reconstructed variable. The resolution is calculated as the Root Mean Square (RMS) of the corrected-level distribution for each particle-level bin. The resolution gives an insight into how good a variable is reconstructed as a function of its particle-level value. Therefore, the bin width is chosen to be larger than the resolution, and the migrations to neighbouring bins are preferred to be close to or lower than 40 %. Fig. 7.5 shows the resolution for the three measured observables. The resolution of the $n_{trk,prim}$ observable gets worse for higher charged-particle multiplicities. The fact that the resolution gets worse is expected since for higher track densities, the reconstruction of all tracks is more challenging. Similar behaviour is found for the $\sum_{n_{trk,prim}} p_T$ observable. Therefore, a minimum bin width of the n_{ch} is six, which is adjusted to 10 to decrease the migrations, while for the $\sum_{n_{ch}} p_T$ a bin width of ten is chosen. For the 2D observable, an asymmetric binning is chosen based on the resolution and bin migrations.

- increase the number of events in each bin, to avoid having bins with low statistics as they can cause large statistical uncertainties in less populated bins. Therefore, the data statistical uncertainty is required to be less than 10 % in each bin. It has been checked that this condition is achieved in all bins of the three measured observables.

Afterwards, the tracking-efficiency correction factor, explained earlier in Section 6.3, is applied to shift the leading elements of the migration matrix to the main diagonal. Fig. 7.6 exemplarily shows the migration matrix of n_{ch} observable before applying this factor, in which large migrations to neighbouring bins can be seen.

(a)

(b)

(c)
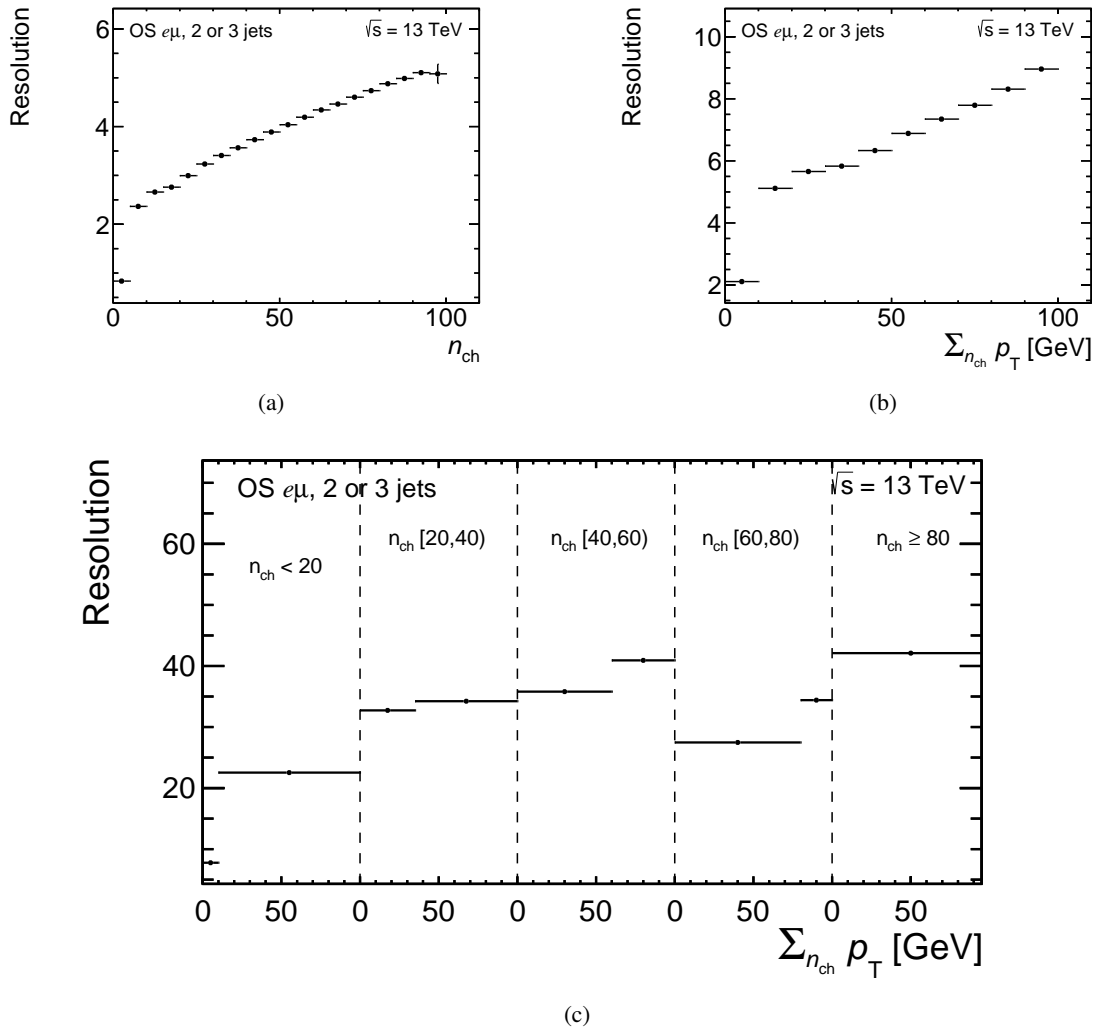
Figure 7.5: Resolution of (a) $n_{\text{trk,prim}}$, (b) $\sum_{n_{\text{trk,prim}}} p_{\text{T}}$, and (c) $\sum_{n_{\text{trk,prim}}} p_{\text{T}}$ in bins of $n_{\text{trk,prim}}$ as a function of the corresponding variable defined at the particle level in simulated $t\bar{t}$ events. The horizontal axis in (c) is split into five bins of n_{ch} by the dashed vertical lines and within each bin, the $\sum_{n_{\text{ch}}} p_{\text{T}}$ is presented. The horizontal error bar shows the width of the bin.
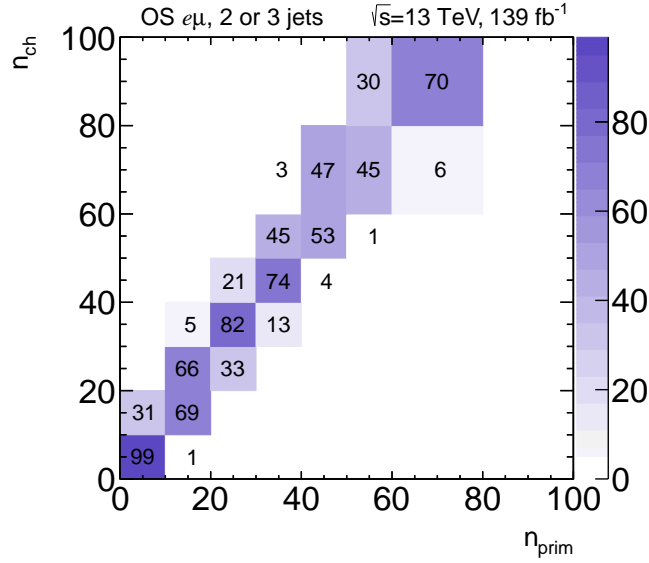
Figure 7.6: Migration matrix for the n_{ch} observable mapping the particle level value shown on the *y*-axis and the background-subtracted-level value shown on the *x*-axis. This matrix is not used for unfolding due to the large off-diagonal elements. Instead the matrix shown in Fig. 7.3 is used.

7.5 Unfolding validation tests

The IBU method employs information from the nominal simulated $t\bar{t}$ sample, and it is used with three iterations. Several tests are performed to validate the unfolding of each distribution and to verify that the chosen parameters in the simulation or the chosen number of iterations do not bias the results. In the following, three tests are explained: the technical closure test, the stress test and the pull test.

7.5.1 Technical closure test

The first check is a simple closure test. It is performed by unfolding the corrected-level distribution taken from the same MC events used to build the unfolding machinery (migration matrix and unfolding corrections). The unfolding procedure should perfectly correct the effect of the migration matrix, and the unfolded distribution is expected to agree exactly with the particle-level distribution from the nominal signal sample. In this way, this check ensures that the implementation of the unfolding method is working as expected and no technical issues are introduced. However, this test is not very meaningful, since it does not provide information on the actual precision or bias of the unfolding method and it will trivially result in the expected particle-level distribution from the signal sample, even without iterations.

The result of the technical closure test is shown in Fig. 7.7 for each of the measured observables. The corrected-level distribution from the nominal signal sample (in blue) is unfolded, yielding the unfolded distribution (black dots). The expected particle-level distribution, labelled as 'truth', is shown in red. In the lower histogram, the ratio of the unfolded distribution to the expected particle-level distribution is plotted. A perfect closure is observed, i.e. the ratio is perfectly at unity over the full observable range. Thus, the technical closure test is successfully passed for the three observables.

(a)

(b)

(c)
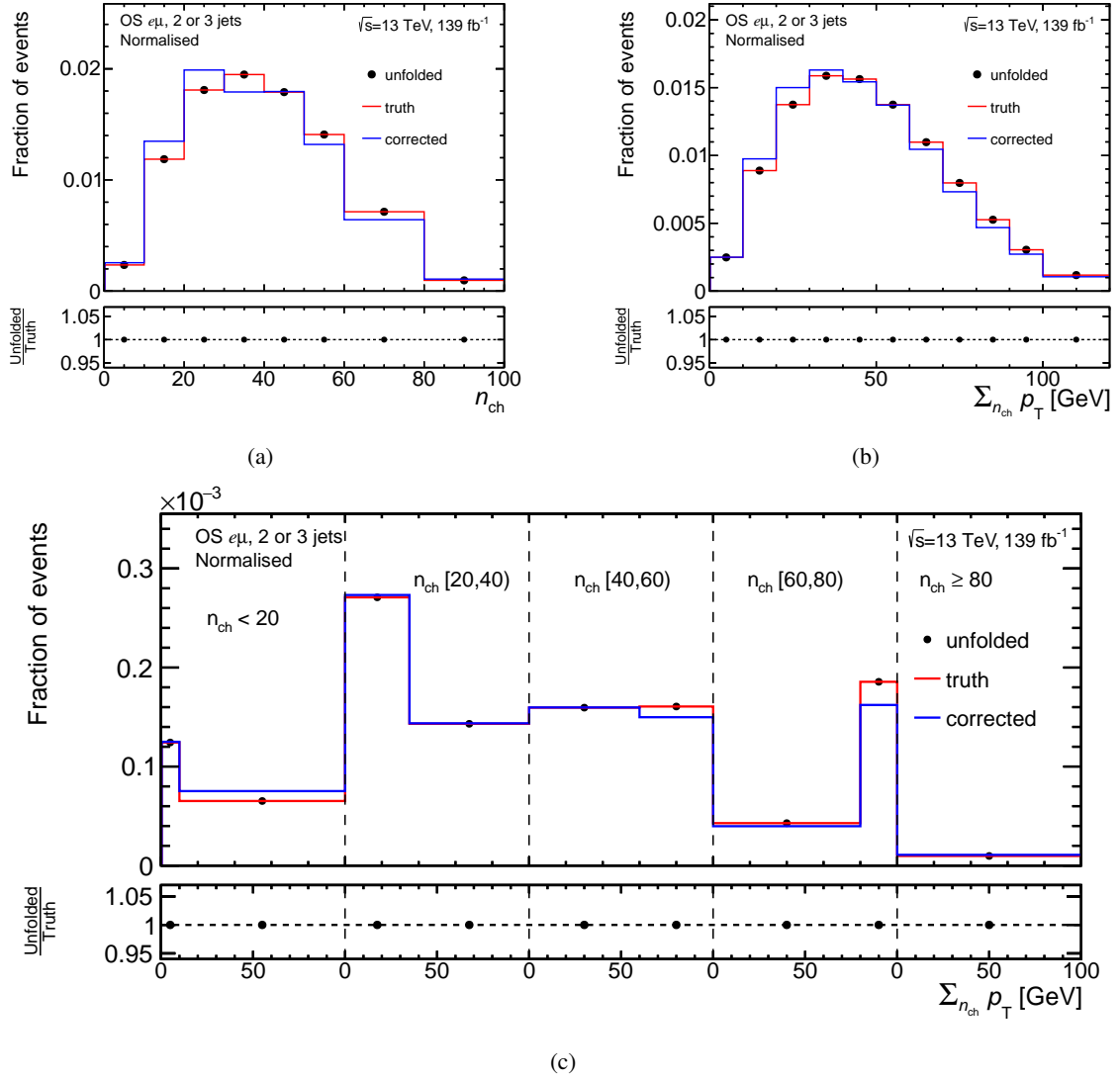
Figure 7.7: Technical closure test of the unfolding procedure for (a) n_{ch}, (b) $\sum_{n_{\mathrm{ch}}} p_{\mathrm{T}}$, and (c) $\sum_{n_{\mathrm{ch}}} p_{\mathrm{T}}$ in bins of n_{ch} observables. The x-axis in (c) is split into five bins of n_{ch} by the dashed vertical lines and $\sum_{n_{\mathrm{ch}}} p_{\mathrm{T}}$ is presented in each bin. The corrected-level distribution, labelled as 'corrected', is unfolded. The unfolded distributions are compared with the expected particle-level distributions, labelled as 'truth'. In the lower panel, the ratio of the unfolded to the truth is shown. The distributions are normalised to unit area.

7.5.2 Stress test

This test is more interesting than the technical closure test. Here, the underlying particle-level distribution from the nominal signal sample is reweighted to change the shape of the distribution at both the particle level and the corrected level. The reweighted corrected-level distribution is then unfolded using the unchanged migration matrix. The deviation between the unfolded and the reweighted particle-level distributions, referred to as 'non-closure', provides a quantitative assessment of the capacity of the unfolding method with its regularisation techniques to recover shapes different from those in MC and therefore its ability to maintain unexpected features present in the data. Additionally, this test demonstrates the sensitivity of the unfolding method to discrepancies between data and MC simulations in variables other than the unfolded observables. Therefore, non-closure indicates a bias introduced by the unfolding procedure and is considered as a systematic uncertainty (see Section 8.4).

This test is done using the nominal $t\bar{t}$ events that pass the selection criteria at both particle and detector levels. The particle-level and corrected-level distributions are reweighted with a smooth function, which is chosen such that the data-MC agreement at the corrected level is significantly improved after reweighting. Two different kinds of stress tests are performed, based on the reweighting strategy:

- Data-driven stress test: In this test, the reweighting function is defined for each observable as the ratio of the background-subtracted data to the nominal $t\bar{t}$ MC at the corrected level. Here, the ratio is fitted with a spline function in order to obtain a smooth function. After reweighting, the data-MC agreement improved significantly at the corrected level.

  Fig. 7.8 shows the result of this test for the three measured observables. The reweighted distributions are shown in red, compared with the nominal (unweighted) in black. The middle panel shows the ratio of the reweighted to the nominal particle-level distributions. It can be seen that variations of up to 30 % are applied. In the lower panel, deviations between the unfolded distribution and the reweighted particle-level distribution are shown in red. For n_{ch} and $\sum_{n_{\mathrm{ch}}} p_{\mathrm{T}}$ observables, the non-closure ranges between 0.1 % and 1.9 % and is contained in the data-statistical uncertainty, while for the $\sum_{n_{\mathrm{ch}}} p_{\mathrm{T}}$ in bins of n_{ch} observable the non-closure ranges between 0.3 % and 3.6 %, being above the data-statistical uncertainty in five out of nine bins.

- Data-driven cross-reweighting stress test: The obtained reweighting function from a specific observable is not applied to the observable itself, instead it is applied to the other two measured observables. Therefore, it is referred to as "cross-reweighting". In this way, this test explores the impact of hidden data-MC discrepancies on the measured observables. For example, differences in the tracks p_{T} observable, as can be seen in Fig. 6.3(a).

  The reweighting function is defined as the ratio of the measured n_{ch} distribution (unfolded data) to the distribution obtained from simulated $t\bar{t}$ events at the particle level. This ratio is applied to the events forming the $\sum_{n_{\mathrm{ch}}} p_{\mathrm{T}}$ and $\sum_{n_{\mathrm{ch}}} p_{\mathrm{T}}$ in bins of n_{ch} distributions. Similarly, the reweighting function obtained from the ratio of the measured $\sum_{n_{\mathrm{ch}}} p_{\mathrm{T}}$ distribution (unfolded data) to the distribution obtained from simulated $t\bar{t}$ events at the particle level, and is used to form reweighted distributions of the n_{ch} and $\sum_{n_{\mathrm{ch}}} p_{\mathrm{T}}$ in bins of n_{ch} observables.

For n_{ch} and $\sum_{n_{ch}} p_T$ observables, the non-closure is of a similar size as seen in the data-driven stress test and ranges between 0.1 % and 2.2 % and is thus contained in the data-statistical uncertainty, while for the $\sum_{n_{ch}} p_T$ in bins of n_{ch} observable the non-closure ranges between 0.3 % and 3.6 %, being above the data-statistical uncertainty in five out of nine bins.

Table 7.1 summarises the result of the two stress tests for the three measured observables. Comparing the non-closure of the cross-reweighting to the nominal stress test. It can be seen that they are of a similar size for the n_{ch} and $\sum_{n_{ch}} p_T$ observables and they range between 0.1 % and 2.2 %, while for the $\sum_{n_{ch}} p_T$ in bins of n_{ch} observable the non-closure for the cross-reweighting stress test ranges from 0.1 % to 1.7 % and is thus smaller for the cross-reweighting stress test than for the regular data-driven stress test.

Table 7.1: Stress test non-closure results for each bin of n_{ch}, $\sum_{n_{ch}} p_T$, and $\sum_{n_{ch}} p_T$ in bins of n_{ch} observables. For each observable, the non-closure of "data-driven" (top) and the "data-driven cross-reweighting" (bottom) stress tests is given. The values are given in percent. For the $\sum_{n_{ch}} p_T$ in bins of n_{ch} observable, in addition to the non-closure of the regular data-driven stress test, the non-closure of the two variations of the "data-driven cross-reweighting" stress test are given.

	bin 1	bin 2	bin 3	bin 4	bin 5	bin 6	bin 7	bin 8	bin 9	bin 10	bin 11
n_{ch}	0.5	0.1	0.2	0.2	0.0	0.2	0.5	0.5	–	–	–
	2.2	0.8	0.1	0.4	0.1	0.2	0.4	0.4			
$\sum_{n_{ch}} p_T$	1.9	0.2	0.2	0.1	0.2	0.2	0.1	0.3	0.1	0.4	0.2
	0.7	0.2	0.5	0.1	0.0	0.1	0.3	0.4	0.5	0.5	0.6
$\sum_{n_{ch}} p_T$ in-	−1.4	3.6	−2.9	3.5	−1.9	0.3	−0.5	−1.3	1.0	–	–
-bins of n_{ch}	0.6	0.2	0.3	0.4	0.2	0.3	0.6	1.0	0.3	–	–
	1.7	1.2	0.2	0.3	0.2	0.1	0.2	0.1	0.5	–	–

(a)

(b)

(c)

Figure 7.8: Data-driven stress test of the unfolding procedure for (a) the n_{ch}, (b) the $\sum_{n_{ch}} p_T$, and (c) the $\sum_{n_{ch}} p_T$ in bins of n_{ch} observables. The x-axis in (c) is split into five bins of n_{ch} by the dashed vertical lines and $\sum_{n_{ch}} p_T$ is presented in each bin. The reweighted unfolded and truth distributions are shown in the red dots and red line respectively, while the nominal (unweighted) unfolded and truth distributions are shown in the black dots and black line, respectively. In the middle panel, the ratio of the reweighted to the nominal truth distribution is shown. In the lower panel, the ratio of the unfolded distribution to its corresponding truth distribution is shown. The grey band shows the data's statistical uncertainty. The distributions are normalised to unit area.

7.5.3 Pull test

The pull test is an additional check; it does not only check the presence of a bias introduced by the unfolding method but also verifies the correct estimate of the statistical uncertainty. It is performed by smearing the corrected-level distribution according to the data statistical uncertainty in each bin. Each bin is smeared according to a Poisson distribution with a mean equal to the number of expected events in that bin to form a pseudo-experiment; 10000 pseudo experiments are generated in this way. Each replica j of the pseudo-experiments distribution is then unfolded, and the pulls are calculated with respect to the expected particle-level value for each bin i, defined as:

$$P_i^j = \frac{U_i^j - T_i}{\sigma_i} \tag{7.13}$$

where U_i^j is the unfolded value in bin i for pseudo-experiment j, T_i is the particle-level value and σ_i is the statistical uncertainty estimated in bin i. The σ_i is evaluated as the RMS of the unfolded pseudo-experiments distribution in bin i. The resulting distributions of pulls per bin are fitted to Gaussian functions. An exemplary pull distribution is shown in Fig. 7.9, for the first bin of n_{ch} observable.

The pull distribution should have a mean consistent with zero for an unbiased unfolding procedure and a width consistent with one for a correct assessment of the statistical uncertainties. Fig. 7.10 summarises the result of this test, and it shows the obtained pull mean and width in all bins of the three measured observables, which are consistent with the expected result. Therefore, the pull test is passed successfully.
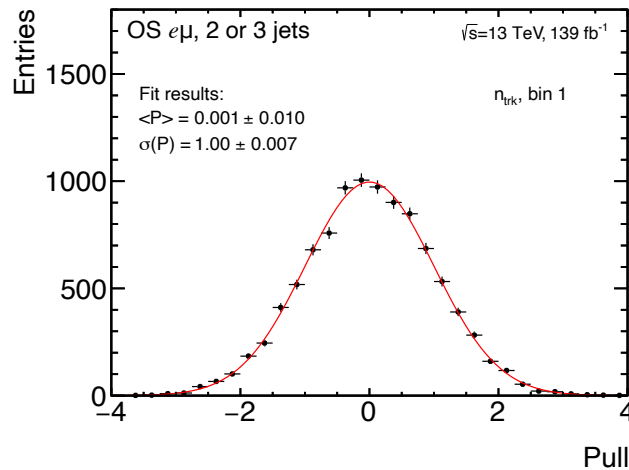
Figure 7.9: The pull distribution for the first bin of the n_{ch} observable. The solid red line corresponds to the fitted Gaussian function.

(a)

(b)

(c)

(d)

(e)

(f)
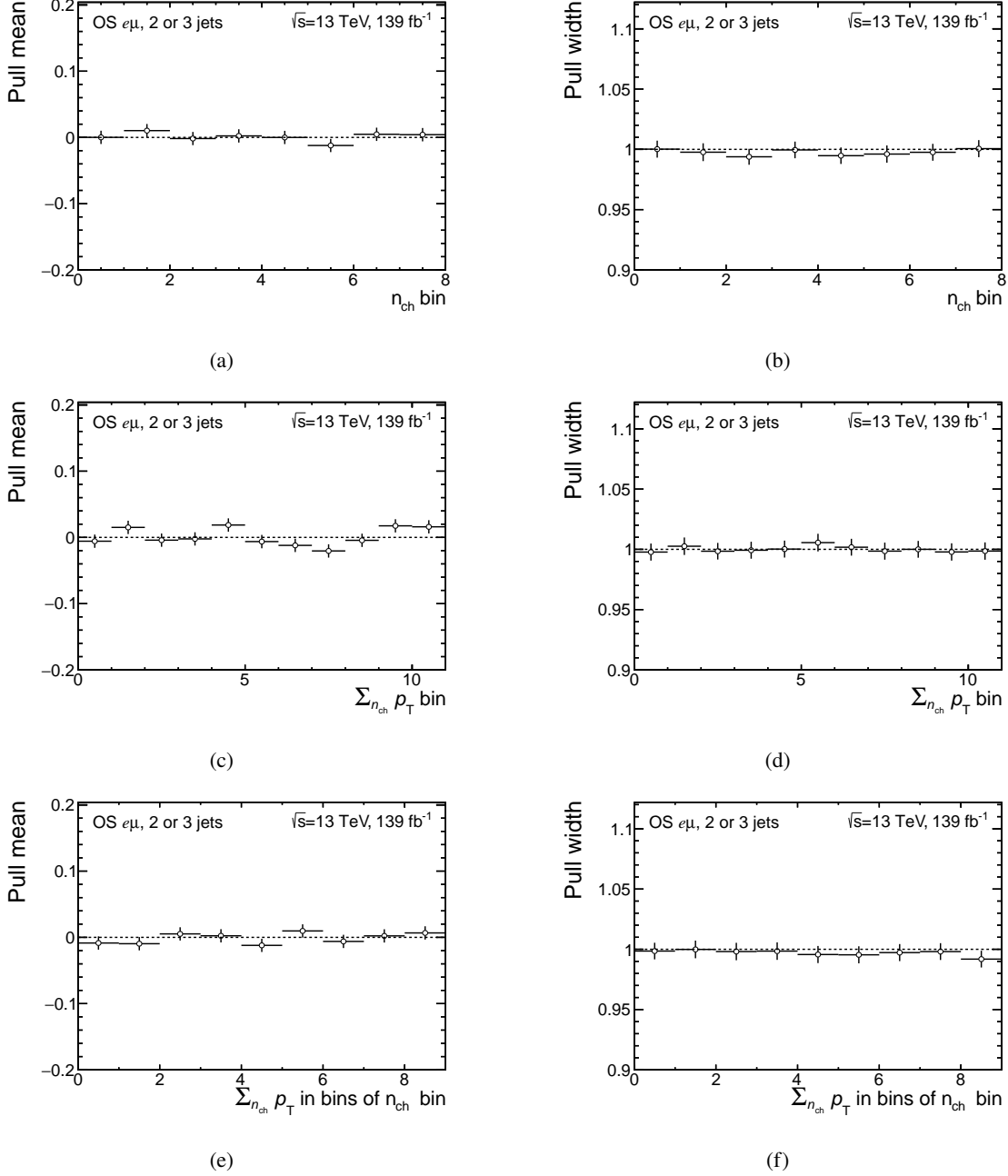
Figure 7.10: Pull test for the normalised (a) n_{ch}, (b) $\sum_{n_{ch}} p_T$, and (c) $\sum_{n_{ch}} p_T$ in bins of n_{ch} observables. The fitted pull width (left) and mean (right) in each bin of the shown observable.

Systematic uncertainties

The measured differential and total-fiducial cross-sections are affected by several sources of systematic uncertainties. The various sources can be grouped into four categories: experimental uncertainties, signal and background modelling uncertainties and uncertainty due to the unfolding procedure. In addition, the statistical uncertainty in the unfolded result is considered.

In the following, a brief description of the various sources of the systematic and statistical uncertainties is given, together with their propagation through the unfolding machinery and their impact. Each uncertainty is treated individually. Then, the total uncertainty is estimated by the quadratic sum of all uncertainties.

8.1 Experimental uncertainties

Experimental uncertainties are related to the reconstruction and calibration of the various physics objects: tracks, electrons, muons and jets, and the uncertainty in the luminosity determination.

The impact of these uncertainties is determined individually for each observable. The corrected-level distribution of the signal $t\bar{t}$ process and the tW background process is varied to account for the source of uncertainty. The varied total prediction, the sum of signal and all backgrounds, is then unfolded using Eq. (7.10), where the nominal background, migration matrix and unfolding corrections are used. Each unfolded distribution is compared with the nominal unfolded distribution, and the relative difference is assigned as an uncertainty associated with the differential cross-section measurement. Detailed lists of the contributions of different sources of systematic uncertainties in each bin of each distribution are given in Appendix B.

Tracks

Uncertainties are assigned to cover differences between simulation and observed data in the track-reconstruction efficiency, track fake-rate, track impact parameter (d_0, z_0) reconstruction and resolutions [105, 107]. A combination of simulated events and measured data were used from $Z \rightarrow \mu\mu$, dijet and minimum-bias events.

Two sources of uncertainty are considered for the track-reconstruction efficiency: the amount of material crossed by the track in the ID acceptance and the physics model used in the detector simulation. The effect of these uncertainties is assessed by comparing the efficiency in samples with

different configurations: i.e. the amount of material in the ID is scaled by a specific factor as described in Ref. [107], and the GEANT4 physics model is varied.

The estimation of the track fake-rate is based on observations of differences in the non-linear component of the evolution of track multiplicity as a function of $\langle \mu \rangle$ as described in Ref. [107] and the uncertainty is assumed to be 100 %.

Uncertainties associated with track impact parameter resolutions are applied to cover resolution differences between minimum-bias data and simulation. In addition, the impact parameter resolution is particularly sensitive to the accuracy of the simulation's modelling of the number of inactive modules in the pixel detector [107]. The uncertainty is estimated by randomly disabling 5 % of the pixel modules.

Finally, weak modes[1] in the ID detector alignment can lead to a bias in the impact parameter reconstructions, i.e. a rotation of the IBL. These are accounted for by applying bias corrections to tracks as a function of their angular position to simulate the impact of such modes. Variations biassing d_0 and z_0 are taken into account, as well as sagitta bias [149].

The combination of these uncertainties is labelled 'Track' in Fig. 8.1, with the main contribution coming from the uncertainty in the track reconstruction efficiency. The track-related uncertainties have a dominant impact among all experimental uncertainties for the n_{ch} and $\sum_{n_{\mathrm{ch}}} p_{\mathrm{T}}$ in bins of n_{ch} observables, while its impact is sub-dominant for the $\sum_{n_{\mathrm{ch}}} p_{\mathrm{T}}$ observable.

Jets

The jet energy scale uncertainty (JES) is derived using information from test-beam data, in-situ measurements and simulation [150]. It is decomposed into a set of 29 nuisance parameters (NPs) that depend on jet p_{T} and η. These NPs can be classified into several categories: 16 NPs arise from the in-situ calibrations, 4 NPs originate from the uncertainty on the pile-up corrections, 5 NPs comprise the uncertainty of the η-intercalibration[2], 2 NPs originate from the uncertainty on the jet flavour composition and response, 1 NPs originates from the uncertainty of the punch-through[3] modelling, and 1 NP describes the uncertainty in the modelling of high-p_{T} jets.

The jet energy resolution (JER) is measured separately for data and MC simulation using in-situ techniques in various jet p_{T} and η bins. Its uncertainty is represented by eight components accounting for jet-p_{T} and η-dependent differences between simulation and data [151].

Additionally, an uncertainty in the efficiency of the JVT requirement for pile-up jets suppression is considered. The scale factors derived to correct the JVT efficiency in simulation to match that in data are varied within their uncertainties [123].

The main contributions are from the jet-flavour response and the pile-up corrections, with an impact of up to 9 % in the tail of the $\sum_{n_{\mathrm{ch}}} p_{\mathrm{T}}$ observable. This category is combined with the flavour tagging uncertainties, explained below, and labelled as 'Jet' in Fig. 8.1.

Flavour tagging

As mentioned in Section 5.1, scale factors are applied to simulated events to correct for discrepancies

---

[1] Weak modes in the detector alignment are defined as detector deformations under which the χ^2 of the track fit remains invariant [107].

[2] η-intercalibration is a technique that uses well-measured jets in the central region ($|\eta| < 0.8$) to obtain calibrations for jets in the forward region ($0.8 < |\eta| < 4.5$) [150].

[3] Punch-though jets pass the calorimeter without depositing their entire energy.

of b-tagging efficiency between data and simulation. The uncertainties in these scale factors are estimated by varying the scale factors within their uncertainties. A total of 19 scale-factor variations are obtained, which accounts for uncertainties associated with the b-tagging, misidentification rate of c-jets and light-flavour jets.

Uncertainties in the b-tagging calibration have an average impact below 0.5 % on the normalised measured differential cross-sections (see Tables B.1 to B.3). The uncertainties in the misidentification rate of c-jets and light-flavour jets are found to be negligible.

The combination of the b-tagging-related uncertainties together with the previous category is labelled 'Jet' in Fig. 8.1. It can also be observed that the jet-related uncertainties have a sub-dominant impact among all experimental uncertainties for the n_{ch} and $\sum_{n_{ch}} p_T$ in bins of n_{ch} observables, while its impact is the one dominant for the $\sum_{n_{ch}} p_T$ observable.

Charged leptons: electrons and muons

The lepton trigger, reconstruction, identification and isolation efficiencies differ between observed data and simulated events. Scale factors are applied to simulated events to correct these differences, as explained briefly in Section 5.1. The uncertainties in the scale factors are derived using a tag-and-probe method applied to electrons and muons originating from Z bosons or J/ψ mesons [115, 152]. Similarly, corrections to the lepton momentum scale and resolution are derived using the aforementioned events to account for discrepancies between the observed data and the simulation. Uncertainties in both, the momentum scale and resolution, are considered.

The combination of these uncertainties is labelled 'Lepton' in Fig. 8.1. The uncertainties related to the lepton identification and isolation have a small impact on the measured observables, while other lepton-related uncertainties are found to be entirely negligible. These uncertainties have a very small impact, well below 0.1 % among all experimental uncertainties.

Pile-up reweighting

Scale factors are applied to reweight simulated events in order to obtain the distribution of the average number of additional pile-up events corresponding to the distribution obtained in data. An uncertainty in these reweighting scale factors is considered, based on the difference between the instantaneous luminosities in data and simulation, and is labelled as 'μ-reweight' in Fig. 8.1 and has an impact of a maximum of 1 % on the normalised measured-differential cross-sections.

Luminosity

The uncertainty in the combined 2015–2018 integrated luminosity is 1.7 % [97], obtained using the LUCID-2 detector [153] for the primary luminosity measurements. This uncertainty has no impact on the normalised-measured differential cross-sections, while its impact on the absolute-measured differential cross-sections and the total fiducial cross-section is considered.
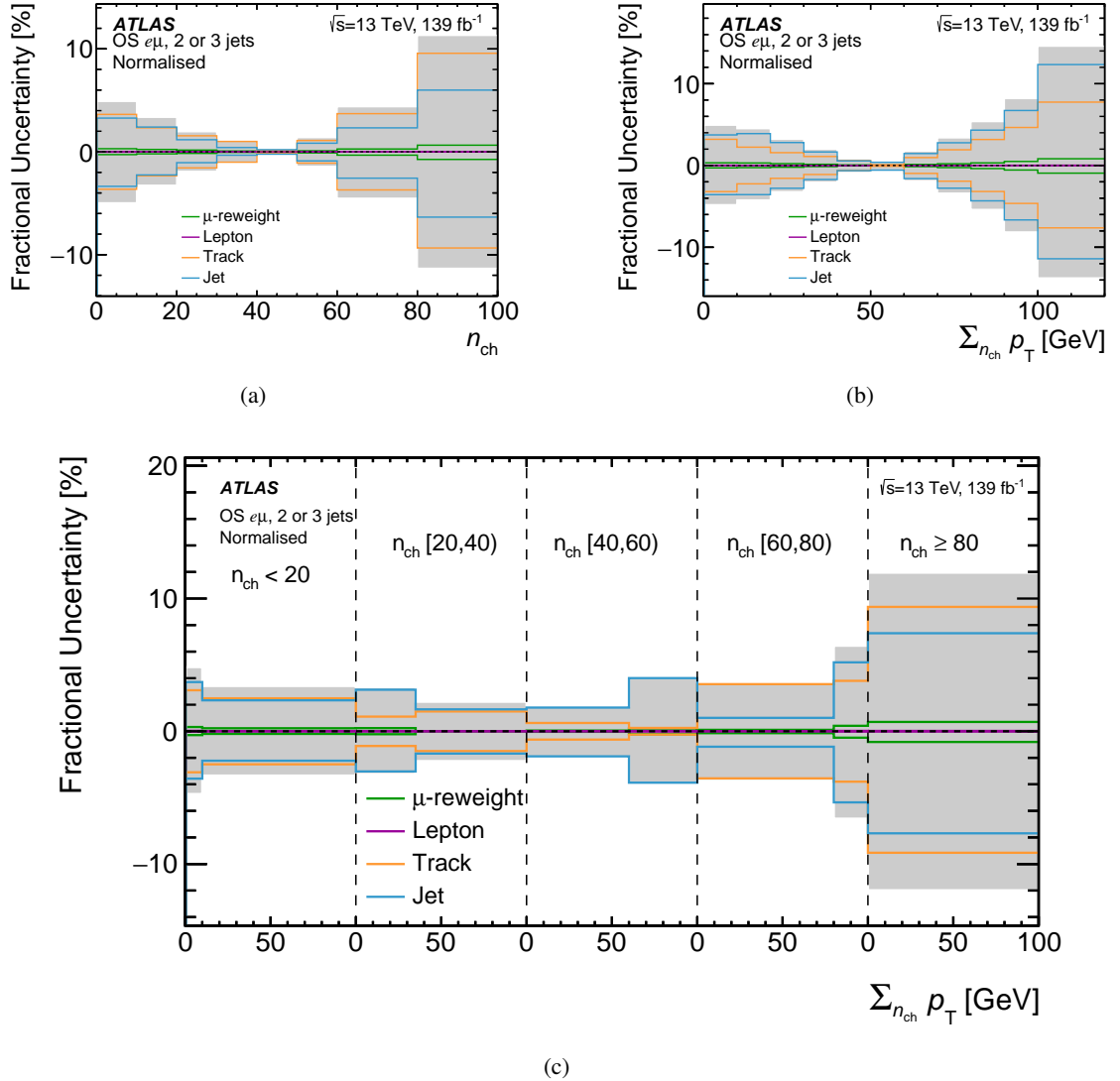
Figure 8.1: Fractional uncertainties in the measured normalised differential cross-section as a function of (a) n_{ch}, (b) $\sum_{n_{\text{ch}}} p_{\text{T}}$, and (c) $\sum_{n_{\text{ch}}} p_{\text{T}}$ in bins of n_{ch} for all experimental systematic uncertainties. The horizontal axis in (c) is split into five bins of n_{ch} by the dashed vertical lines and $\sum_{n_{\text{ch}}} p_{\text{T}}$ is presented in each bin. The grey bands represent the presented components added in quadrature. Events beyond the x-axis range are included in the last bin in (a) and (b), and in the corresponding last bin of each slice in (c).

8.2 Signal modelling uncertainties

Uncertainties in the modelling of the signal $t\bar{t}$ process affect the migration matrix and unfolding corrections. Several sources of uncertainties are considered: uncertainties in the parton-shower and colour-reconnection models, uncertainties in the parameter choice to model ISR and FSR, uncertainty in the choice of the ME-to-PS matching scale, uncertainties in the choice of the renormalisation and factorisation scales, and uncertainties related to the PDF set.

The method used to evaluate the signal modelling uncertainties differs from the one used to estimate the other sources of uncertainties. For each observable, the corrected-level distribution of the signal $t\bar{t}$ process is varied to account for the source of uncertainty. The varied total prediction, the sum of signal and all nominal backgrounds, is unfolded using Eq. (7.10), where the nominal background, migration matrix and unfolding corrections are used. In the next step, the unfolded distribution is compared with the particle-level distribution of the systematic variation, and the non-closure (deviation) is assigned as the uncertainty associated with the differential cross-section measurement. This procedure is applied to all following uncertainties if not stated otherwise. Detailed lists of the contributions of different sources of systematic uncertainties in each bin of each distribution are given in Appendix B.

Parton shower

Uncertainties in the modelling of parton showers, hadronisation, the underlying event, and colour reconnections are assigned by comparing the nominal sample to alternative samples for which POWHEG was interfaced to HERWIG 7.1 instead of PYTHIA 8.

This uncertainty is one-sided and therefore it is symmetrised and labelled as 'H7' in the following. Fig. 8.2 summarises the impact of this uncertainty in the three measured observables. It can be observed that the parton shower uncertainty has a significant impact among all modelling uncertainties, especially in the tails of the distributions. Its impact ranges between 0.18 % and 24 % on the normalised measured differential cross-sections.

Colour reconnection

Uncertainties in the modelling of CR effects are estimated using POWHEG interfaced with PYTHIA 8 samples with modified CR models, namely CR0, CR1 and CR2. A detailed description of these models is given in Section 3.2.1.

The final CR uncertainty is then given by the maximum and minimum envelope of the non-closure differences of CR0–CR2 comparisons and labelled as 'CR'. Fig. 8.2 summarises the impact of this uncertainty in the three measured observables. It can be observed that the CR uncertainty has a large impact compared to other modelling uncertainties, especially in the tails of the distributions. Its impact ranges between 0.9 % and 50 % on the normalised measured-differential cross-sections.

Matrix element to parton shower matching scale

The uncertainty due to the scale choice for matching the matrix-element calculation of the signal process to the parton shower is estimated using an additional $t\bar{t}$ sample produced with the h_{damp} parameter set to $3 \times m_{\mathrm{top}}$ instead of $1.5 \times m_{\mathrm{top}}$ while keeping all other generator settings the same as for the nominal sample of $t\bar{t}$ events.

This uncertainty is symmetrised and labelled as 'h_{damp}' in the following. Fig. 8.2 shows the impact of this uncertainty in the three measured observables. It can be observed that the h_{damp}

uncertainty has a small impact among all modelling uncertainties, which is below 1 % on the normalised measured-differential cross-sections.

Initial-state and final-state radiation

Uncertainties in the intensity of ISR, labelled as ISR α_s, are assessed by varying the parameter `Var3c` of the A14 parton-shower tune, which corresponds to a variation of the strong coupling constant α_s for ISR between 0.115 and 0.140 with respect to the nominal value of 0.121. The uncertainty in the FSR, labelled as FSR, is assessed by varying the renormalisation scale μ_r of FSR, at which the α_s is evaluated, by factors of 0.5 and 2.0.

Fig. 8.2 shows the impact of these uncertainties in the three measured observables. It can be observed that the ISR α_s uncertainty has an impact of up to 1 %, while the FSR uncertainty is larger, with an impact of up to 5 % on the normalised measured-differential cross-sections.

Renormalisation and factorisation scales

Uncertainties related to the choice of the renormalisation and factorisation scales in the matrix-element calculations, labelled as 'Scale μ_r' and 'Scale μ_f', are evaluated by varying the scales by factors of 2 and 0.5.

Fig. 8.2 shows the impact of these uncertainties in the three measured observables. It can be observed that both uncertainties have a small impact, which is below 0.2 % in all bins of the normalised measured-differential cross-sections.

Parton distribution functions

The uncertainty due to the choice of the PDF is evaluated following the PDF4LHC15 recommendations as described in Ref. [154]. The recommendations combine MMHT2014 [77], CT14 [155] and NNPDF3.0 [73] PDF sets with their uncertainties into a set of 30 one-sided variations, which are then symmetrised. In addition, the central value of the combined PDF set is evaluated.

The impact of this uncertainty is evaluated by comparing the unfolded systematic variation to the unfolded central variation, and the non-closure is assigned as an uncertainty associated with the differential cross-section measurement. The total uncertainty is represented by the quadratic sum of all variations and labelled as 'PDF4LHC' in the following.

Fig. 8.2 shows the impact of this uncertainty in the three measured observables. It can be observed that the total PDF4LHC uncertainty has an impact of up to 0.6 % on the normalised measured-differential cross-sections.
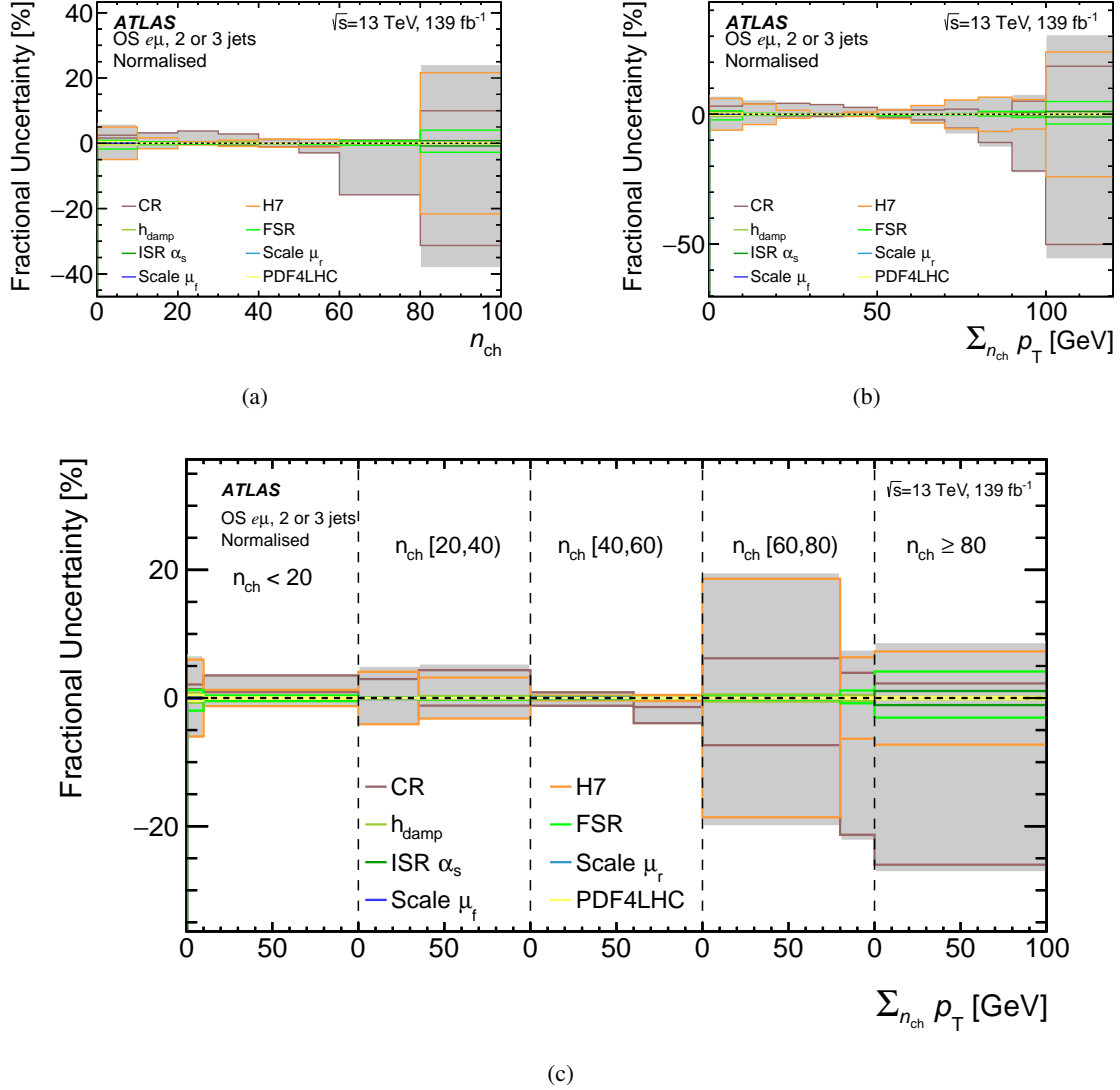
Figure 8.2: Fractional uncertainties in the measured normalised differential cross-section as a function of (a) n_{ch}, (b) $\sum_{n_{ch}} p_T$, and (c) $\sum_{n_{ch}} p_T$ in bins of n_{ch} for all signal modelling uncertainties. The horizontal axis in (c) is split into five bins of n_{ch} by the dashed vertical lines and $\sum_{n_{ch}} p_T$ is presented in each bin. The grey bands represent the presented components added in quadrature. Events beyond the x-axis range are included in the last bin in (a) and (b), and in the corresponding last bin of each slice in (c).

8.3 Background modelling uncertainties

In this section, systematic uncertainties in the estimation of the background rates are discussed, which include uncertainties in the event-based backgrounds, presented in Section 6.1, and the track-based backgrounds, presented in Section 6.2. Detailed lists of the contributions of different sources of systematic uncertainties in each bin of each distribution are given in Appendix B.

Event-based-background uncertainties

Uncertainties in this category include uncertainties in the background normalisation and the modelling of the tW background process. They are evaluated by building distributions, where the signal and the systematically varied background processes are added together. The resulting distribution is then unfolded using Eq. (7.10), where the nominal background, migration matrix and unfolding corrections are used. Similar to the experimental uncertainties, the unfolded distribution is compared with the nominal unfolded distribution and the relative difference is assigned as an uncertainty associated with the differential cross-section measurement.

Uncertainties in the normalisation of the background processes are assessed by varying the normalisation of a given background process according to the respective uncertainty. The following uncertainties, based on inclusive cross-section uncertainties, are considered: single top-quark and $t\bar{t}V$ processes 10 %, fake leptons 50 % [127], and other processes 20 %. The combination of these uncertainties is labelled 'Background rates'.

Uncertainties related to tW background modelling are assessed using samples where the renormalisation, labelled as 'tW Scale μ_r', the factorisation scales, labelled as 'tW Scale μ_f' of the matrix-element calculations, uncertainties in the intensity of ISR, labelled as 'tW ISR α_s', and FSR, labelled as 'tW FSR', are varied. The parameter variations in the generation of these samples are identical to the one used for the signal process, described in Section 8.2.

The uncertainty in the scheme for removing the overlap of the tW process with $t\bar{t}$ production is evaluated by comparing the nominal tW sample, using the diagram-removal scheme, to a sample produced with an alternative scheme (diagram subtraction) [81]. This uncertainty is symmetrised and labelled as 'tW DS vs. DR'.

Fig. 8.3 shows the fractional uncertainty from each of the above-mentioned categories for the three measured observables. It can be observed that the total event-based background uncertainty has an impact below 2 % in all bins of the normalised measured-differential cross-sections.

Track-based-background uncertainties

Two sources of uncertainties are included in this category. The uncertainty due to the non-closure of the track-background-subtraction method in simulation (shown in Figs. 6.7 and 6.17), and the uncertainty in the pile-up scale-factor estimation (see Section 6.2.3).

The uncertainty in the pile-up-tracks background-rate is evaluated by subtracting a systematically varied number of pile-up tracks from the reconstructed number of tracks in $t\bar{t}$ simulated events using Eqs. (6.2) and (6.3). The resulting distribution is then unfolded using the nominal migration matrix and unfolding corrections. The relative deviation from the nominal unfolded distribution is assigned as a systematic uncertainty.

The quadratic sum of both uncertainties is labelled as 'PU subtraction' in Fig. 8.4. It can be observed that this uncertainty is dominant in the first bin of the measured observables, mainly due to

the uncertainty in the pile-up scale factor originating from differences in the modelling of the UE between PYTHIA 8 and HERWIG 7.

(a)

(b)

(c)
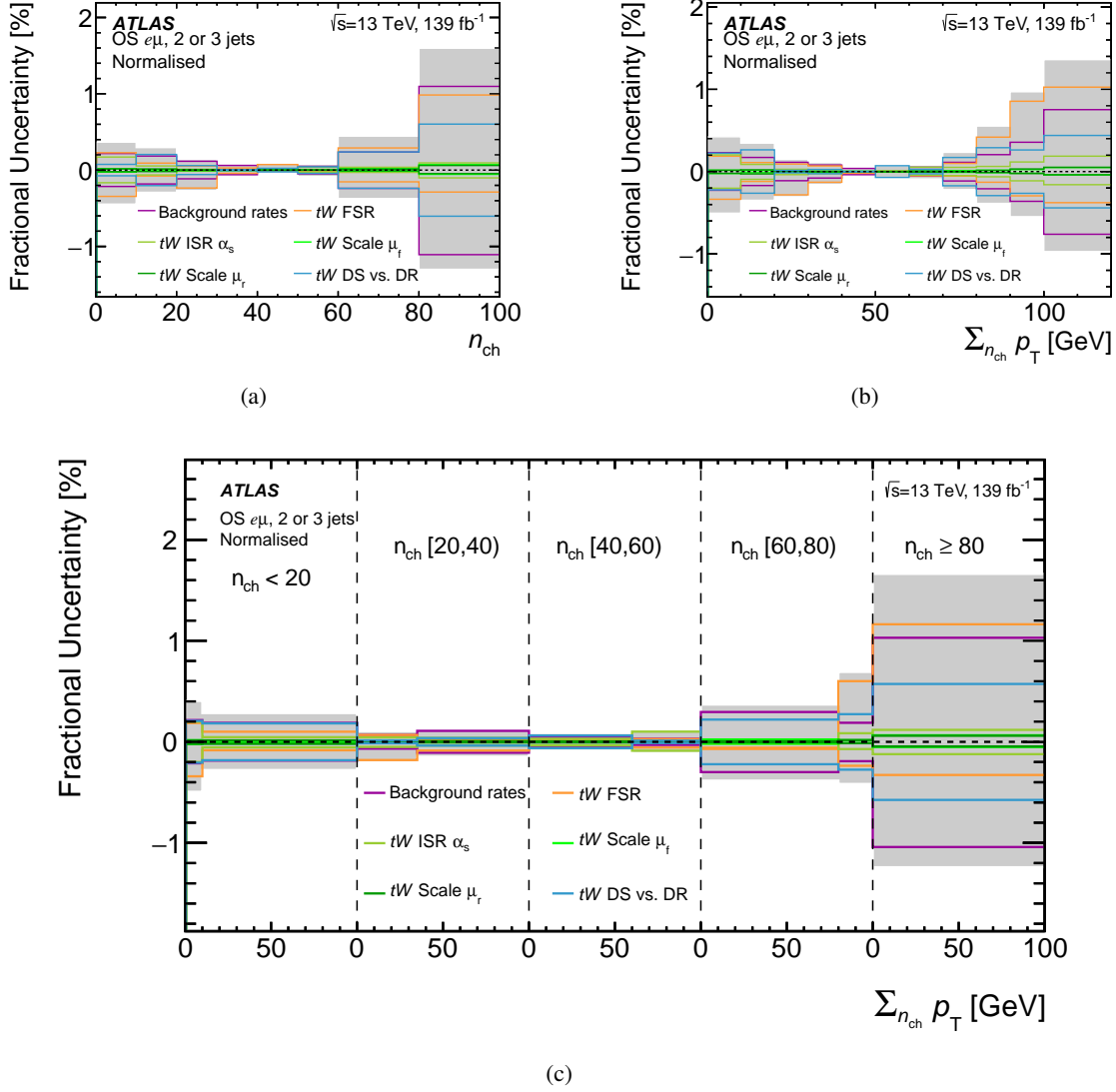
Figure 8.3: Fractional uncertainties in the measured normalised differential cross-section as a function of (a) n_{ch}, (b) $\sum_{n_{ch}} p_T$, and (c) $\sum_{n_{ch}} p_T$ in bins of n_{ch} for all event-based-background uncertainties. The horizontal axis in (c) is split into five bins of n_{ch} by the dashed vertical lines and $\sum_{n_{ch}} p_T$ is presented in each bin. The grey bands represent the presented components added in quadrature. Events beyond the x-axis range are included in the last bin in (a) and (b), and in the corresponding last bin of each slice in (c).

8.4 Unfolding-technique uncertainties

Based on the non-closure of the stress tests using the MC distribution reweighted to background-subtracted data and the cross-reweighting scenario, discussed in Section 7.5, an unfolding-technique

uncertainty is defined. This uncertainty, together with generator uncertainties, described in Section 8.2, cover potential differences in the responses of the measured observables due to track-p_{T} differences between simulation and data.

The envelope of non-closures of both tests given in Table 7.1, is assigned as a systematic uncertainty, referred to as 'Unfolding technique' in Fig. 8.4. For the distributions of n_{ch} and $\sum_{n_{\mathrm{ch}}} p_{\mathrm{T}}$, the unfolding-technique uncertainty ranges between 0.1% and 2.2%, and is less than the statistical uncertainty of the data in all bins except the first one in each of these distributions. In the two-dimensional measurement of $\sum_{n_{\mathrm{ch}}} p_{\mathrm{T}}$ in bins of n_{ch} the unfolding-technique uncertainty ranges between 0.3% and 3.6%, and exceeds the statistical uncertainty of the data in five of the nine bins.

8.5 Statistical uncertainty

The statistical uncertainty due to the limited number of simulated events is evaluated using pseudo-experiments. They are built starting from the total MC prediction, that is the sum of signal and all backgrounds. The content of each bin is fluctuated with a Gaussian distribution of a width corresponding to the bin error. Each pseudo-experiment is then unfolded with the nominal migration matrix and unfolding corrections, and the RMS of the resulting distribution for each bin is used as an estimator of the MC statistical uncertainty.

The statistical uncertainty of the data is also evaluated using pseudo-experiments. Here, the content of each bin is fluctuated with a Poisson distribution of the bin content in the pseudo-experiments. Similarly, the RMS of the spread of unfolded results in each bin is taken as the estimator of the uncertainty.

The combination of these uncertainties is labelled as 'Statistical' in Fig. 8.4. The statistical uncertainty of the data in the normalised spectra is about 1 %, peaking approximately at 2 % in the first and last bins of the three observables, while the MC statistical uncertainty reaches at most 0.8 %.

8.6 Total uncertainty

A summary of the fractional uncertainty from each of the previously mentioned categories is shown for the three normalised-differential cross-sections in Fig. 8.4. The pile-up tracks background and the modelling uncertainties generally have the largest impact on the measurement. The contribution of each category in each bin of the measured observables is shown in Tables 8.1 to 8.3.

(a)

(b)

(c)
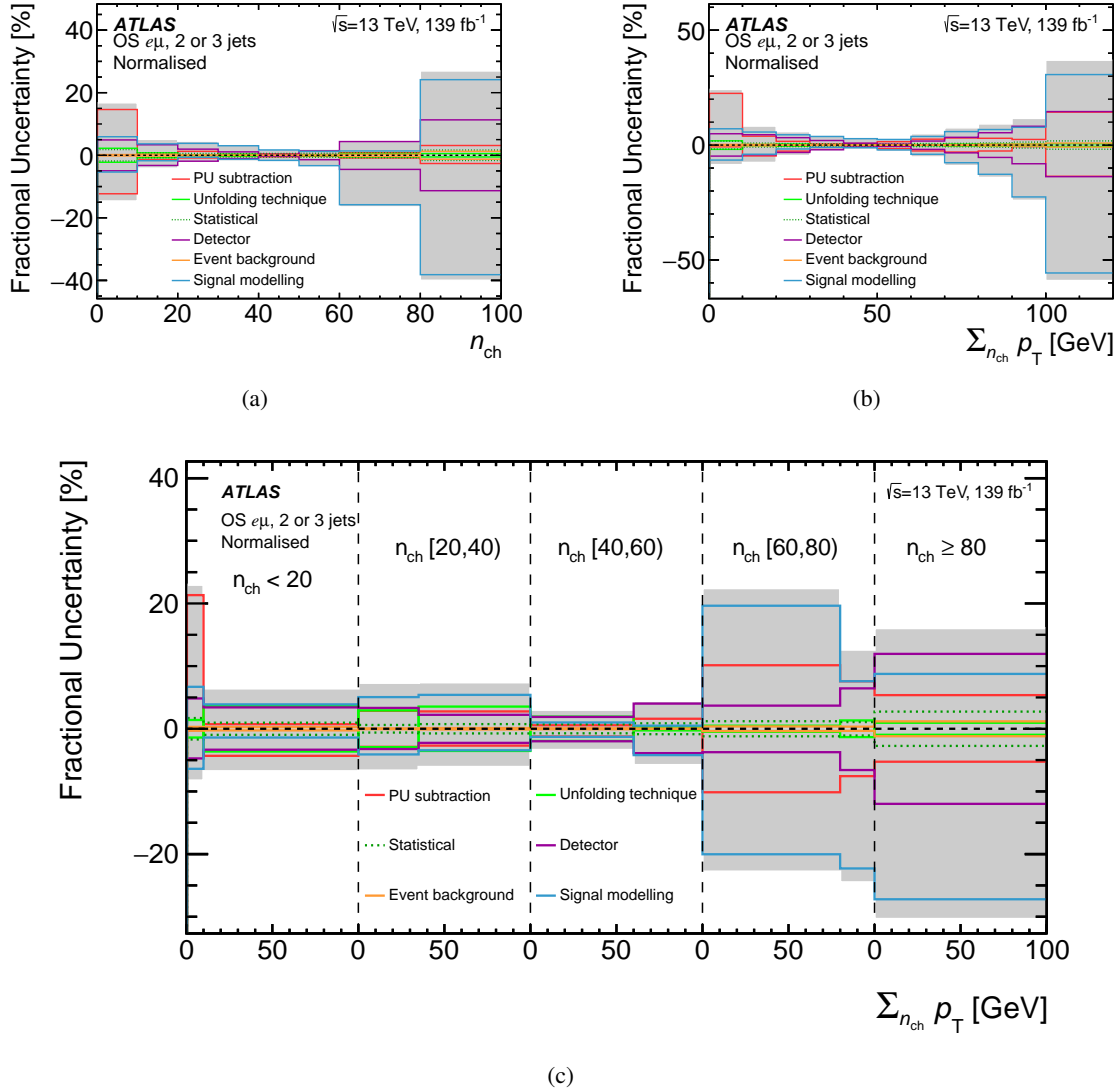
Figure 8.4: Fractional uncertainties in the measured normalised differential cross-section as a function of (a) n_{ch}, (b) $\sum_{n_{ch}} p_T$, and (c) $\sum_{n_{ch}} p_T$ in bins of n_{ch} for all systematic and statistical uncertainties. The horizontal axis in (c) is split into five bins of n_{ch} by the dashed vertical lines and $\sum_{n_{ch}} p_T$ is presented in each bin. The grey bands represent the presented components added in quadrature. Events beyond the x-axis range are included in the last bin in (a) and (b), and in the corresponding last bin of each slice in (c).

Table 8.1: Total uncertainties in the normalised measured n_{ch} distribution per bin in percentage. For each source of uncertainty, the up and down uncertainties are given.

Source	bin 1	bin 2	bin 3	bin 4	bin 5	bin 6	bin 7	bin 8
Experimental	4.9 −4.9	3.4 −3.3	1.9 −1.9	1.1 −1.1	0.25 −0.27	1.4 −1.4	4.4 −4.5	11 −11
Signal modelling	5.9 −5.4	3.7 −1.8	3.8 −0.64	3.1 −1.3	1.7 −1.6	1.2 −3.3	1.4 −16	24 −38
Event background	0.37 −0.45	0.30 −0.29	0.14 −0.27	0.07 0.07	0.08 0.03	0.07 0.09	0.45 −0.37	1.6 −1.3
PU subtraction	15 −12	0.32 −1.4	1.3 −0.86	0.26 −0.22	0.46 −0.51	0.26 −0.32	0.83 −0.87	3.1 −2.6
Unfolding technique	−2.2 2.2	−0.78 0.78	0.18 −0.18	0.35 −0.35	0.10 −0.10	−0.16 0.16	−0.54 0.54	−0.54 0.54
MC statistical	0.35 −0.35	0.16 −0.16	0.12 −0.12	0.11 −0.11	0.12 −0.12	0.14 −0.14	0.17 −0.17	0.36 −0.36
Data statistical	1.8 −1.8	0.74 −0.74	0.57 −0.57	0.55 −0.55	0.58 −0.58	0.64 −0.64	0.76 −0.76	1.6 −1.6
Total	17 −15	5.1 −4.1	4.5 −2.3	3.3 −1.8	1.9 −1.8	1.9 −3.7	4.8 −16	27 −40

Table 8.2: Total uncertainties in the normalised measured $\sum_{n_{\mathrm{ch}}} p_{\mathrm{T}}$ distribution per bin in percentage. For each source of uncertainty, the up and down uncertainties are given.

Source	bin 1	bin 2	bin 3	bin 4	bin 5	bin 6	bin 7	bin 8	bin 9	bin 10	bin 11
Experimental	4.9 −4.8	4.5 −4.2	3.2 −3.2	2.0 −2.1	0.82 −0.87	0.40 −0.58	1.7 −1.9	3.4 −3.4	5.4 −5.4	8.2 −8.1	15 −14
Signal modelling	7.1 −6.5	5.7 −3.9	4.5 −1.7	3.7 −0.98	2.8 −1.2	2.5 2.1	3.8 −4.0	5.9 −7.7	6.8 −13	7.7 −23	31 −56
Event background	0.42 −0.51	0.35 −0.35	0.15 −0.31	0.11 −0.16	0.04 −0.04	0.07 −0.07	0.08 −0.09	0.23 −0.22	0.55 −0.39	0.97 −0.55	1.4 −0.97
PU subtraction	23 −0.76	3.9 −4.7	1.6 −2.6	0.47 −1.04	0.69 −0.95	1.5 −1.5	2.6 −2.6	3.1 −3.0	3.0 −2.6	2.5 −0.68	14 −14
Unfolding technique	−1.9 1.9	0.28 −0.28	0.48 −0.48	0.14 −0.14	0.15 −0.15	0.19 −0.19	0.25 −0.25	0.44 −0.44	0.47 −0.47	0.48 −0.48	0.61 −0.61
MC statistical	0.34 −0.34	0.17 −0.17	0.13 −0.13	0.12 −0.12	0.11 −0.11	0.12 −0.12	0.13 −0.13	0.16 −0.16	0.19 −0.19	0.26 −0.26	0.38 −0.38
Data statistical	1.7 −1.7	0.84 −0.84	0.65 −0.65	0.55 −0.55	0.53 −0.53	0.57 −0.57	0.65 −0.65	0.72 −0.72	0.92 −0.92	1.3 −1.3	1.8 −1.8
Total	24 −8.5	8.3 −7.6	5.8 −4.6	4.3 −2.6	3.0 −1.8	2.9 −2.7	4.9 −5.2	7.5 −9.0	9.2 −14	12 −24	37 −59

Table 8.3: Total uncertainties in the normalised measured $\sum_{n_{ch}} p_T$ in bins of n_{ch} distribution per bin in percentage. For each source of uncertainty, the up and down uncertainties are given.

Source	bin 1	bin 2	bin 3	bin 4	bin 5	bin 6	bin 7	bin 8	bin 9
Experimental	4.8 −4.7	3.4 −3.3	3.3 −3.2	2.2 −2.3	1.9 −2.0	4.0 −3.9	3.7 −3.7	6.5 −6.6	12 −12
Signal modelling	6.7 −6.4	3.9 −1.4	5.1 −4.1	5.4 −3.4	1.0 −1.3	0.49 −4.2	20 −20	7.6 −22	8.8 −27
Event background	0.41 −0.49	0.29 −0.28	0.11 −0.20	0.12 −0.15	0.09 −0.09	0.11 −0.11	0.37 −0.38	0.69 −0.42	1.7 −1.2
PU subtraction	21 −0.25	0.73 −4.3	2.9 −2.9	2.8 −2.7	0.56 −1.2	1.6 −0.01	10 −10	7.6 −7.6	5.4 −5.3
Unfolding technique	−1.4 1.4	3.6 −3.6	−2.9 2.9	3.5 −3.5	−1.9 1.9	0.26 −0.26	−0.49 0.49	−1.3 1.3	0.96 −0.96
MC statistical	0.33 −0.33	0.19 −0.19	0.13 −0.13	0.15 −0.15	0.14 −0.14	0.18 −0.18	0.25 −0.25	0.23 −0.23	0.76 −0.76
Data statistical	1.7 −1.7	0.94 −0.94	0.59 −0.59	0.73 −0.73	0.71 −0.71	0.85 −0.85	1.2 −1.2	1.0 −1.0	2.6 −2.6
Total	23 −8.3	6.4 −6.8	7.3 −6.7	7.4 6.1	3.0 −3.4	4.4 5.8	22 −23	13 −25	16 −30

Results and interpretation

In this chapter, the differential cross-section results are presented as a function of the observables sensitive to colour reconnection effects, namely the charged-particle multiplicity, the scalar sum of the transverse momenta of the charged particles, and the same scalar sum in bins of charged-particle multiplicity. In Section 9.1, the measured normalised distributions are compared with a variety of predictions obtained from simulation. The comparisons are presented for the normalised differential cross-sections, while the absolute differential cross-sections are presented in Appendix C. The systematic and statistical uncertainties affecting the measured distributions are estimated as described in the previous chapter.

In order to quantify how well the measured differential cross-sections agree with the various model predictions, their respective χ^2 values are calculated as explained in Section 9.2. In addition, the total fiducial cross-section is measured as given in Section 9.3.

9.1 Particle-level normalised differential cross-section results

Fig. 9.1 shows the normalised differential cross-sections as a function of n_{ch}, $\sum_{n_{\mathrm{ch}}} p_{\mathrm{T}}$, and $\sum_{n_{\mathrm{ch}}} p_{\mathrm{T}}$ in bins of n_{ch}. They are compared with predictions obtained from Powheg+Pythia 8, Sherpa 2, and Powheg+Herwig 7 using three versions of Herwig 7, namely 7.0.4, 7.1.3, and 7.2.1 [11, 78, 156].

In the Pythia 8 event generator, the MPI-based CR model is used in combination with the A14 tune. In the three versions of Herwig 7, the plain CR model is used, but with a different tune for the CR and UE. For Herwig 7.0, the H7-UE-MMHT tune is used, while for Herwig 7.1 and Herwig 7.2 the default settings are used. In the latest version, the MPI model was improved [157]. The Sherpa 2 event generator has an MPI model based on the Pythia 8 one but without any CR. Therefore it gives an insight into how the distribution would change in the absence of CR.

The n_{ch} measured differential cross-section is approximately equally well described by Pythia 8 and Herwig 7, while the $\sum_{n_{\mathrm{ch}}} p_{\mathrm{T}}$ measured normalised cross-section has a better agreement for Herwig 7, especially in the lower part of the distribution. The $\sum_{n_{\mathrm{ch}}} p_{\mathrm{T}}$ in bins of n_{ch} distribution is best described by Herwig 7 compared with Pythia 8 and Sherpa 2. An overall small difference between the various Herwig 7 versions can be observed. The unfolded data disagree with the predictions from Sherpa 2 in the three observables, which do not include CR effects, thus illustrating their importance.
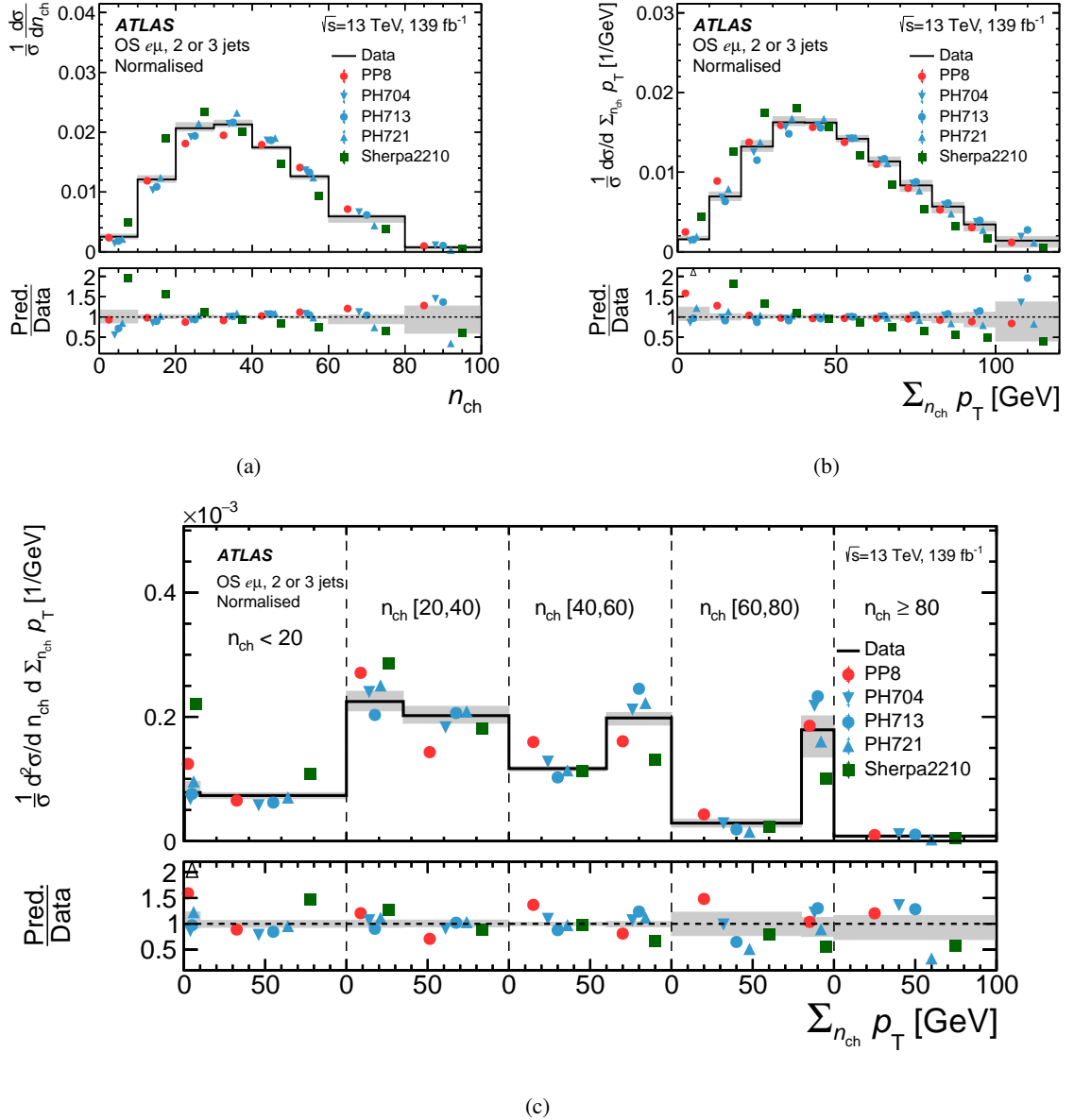
Figure 9.1: Normalised differential cross-section as a function of (a) n_{ch}, (b) $\sum_{n_{ch}} p_T$, and (c) $\sum_{n_{ch}} p_T$ in bins of n_{ch}. The x-axis in (c) is split into five bins of n_{ch} by the dashed vertical lines and $\sum_{n_{ch}} p_T$ is presented in each bin. Unfolded data are shown as the black line with the grey band corresponding to the total uncertainty in each bin. The results are compared with the predictions of different MC event generators. Events beyond the x-axis range are included in the last bin. The lower panels show the ratio of each prediction to data in each bin. The black triangular markers in the lower panels point to prediction-to-data ratio values which lie beyond the shown y-axis range.

Comparison with different CR models in PYTHIA 8

In Fig. 9.2, the normalised differential cross-sections are compared with predictions from the CR0, CR1, and CR2 models, which are introduced in Section 3.2.1. It can be observed that the n_{ch} and the $\sum_{n_{ch}} p_T$ in bins of n_{ch} observables are best described by the CR0 model. For the $\sum_{n_{ch}} p_T$ observable, it can be observed that none of the models can describe the lower part of the distribution well. The values of each CR model's tuned parameters are summarised in Table 9.1 and compared with their values from the nominal A14 tune.

Table 9.1: Definition, parameter range and tuned value for the A14, CR0, CR1, and CR2 models in PYTHIA 8 [79]. The parameters that are not defined for a particular model are left blank.

Parameter	description	A14 / Default (range)	CR0	CR1	CR2
MPI:pT0Ref	MPI p_T dampening	2.09 (0.5-10)	2.15	1.89	2.21
MPI:expPow	Exponent of matter overlap function	1.85 (0.4-10)	1.81	2.10	1.63
CR:range	CR strength	1.71 (1.0-10)	2.92	–	–
CR:m0	Mass parameter used in the λ measure	0.3 (0.1-5)	–	2.17	–
CR:junctionCorrection	Correction to m0 for junctions	1.2 (0.01-10)	–	9.33	–
CR:m2Lambda	m_λ^2 used in the λ measure	1.0 (0.25-16)	–	–	6.73
CR:fracGluon	Fraction of gluons that undergo a CR	1.0 (0-1)	–	–	0.93

Comparison with top-quark-specific CR models in PYTHIA 8

In Fig. 9.3, the normalised differential cross-sections are compared with the predictions obtained from different top-quark-specific CR models (TCR1-TCR5) implemented in PYTHIA 8, which are described in Section 3.2.1. For each model, the strength parameter s is varied down to 0.1 and up to its maximum value of 1.0. The spread between the distributions obtained with $s = 0.1$ and $s = 1.0$ is therefore a measure of the sensitivity of the observables to the corresponding model. It can be observed that only the TCR1 and TCR3 show sizable differences between the two settings out of the five TCR models, which is mainly seen in the $\sum_{n_{ch}} p_T$ in bins of n_{ch} observables. The differences between the $s = 0.1$ and $s = 1.0$ variations hint that a lower value of this parameter is preferred over a higher one.

(a)

(b)

(c)
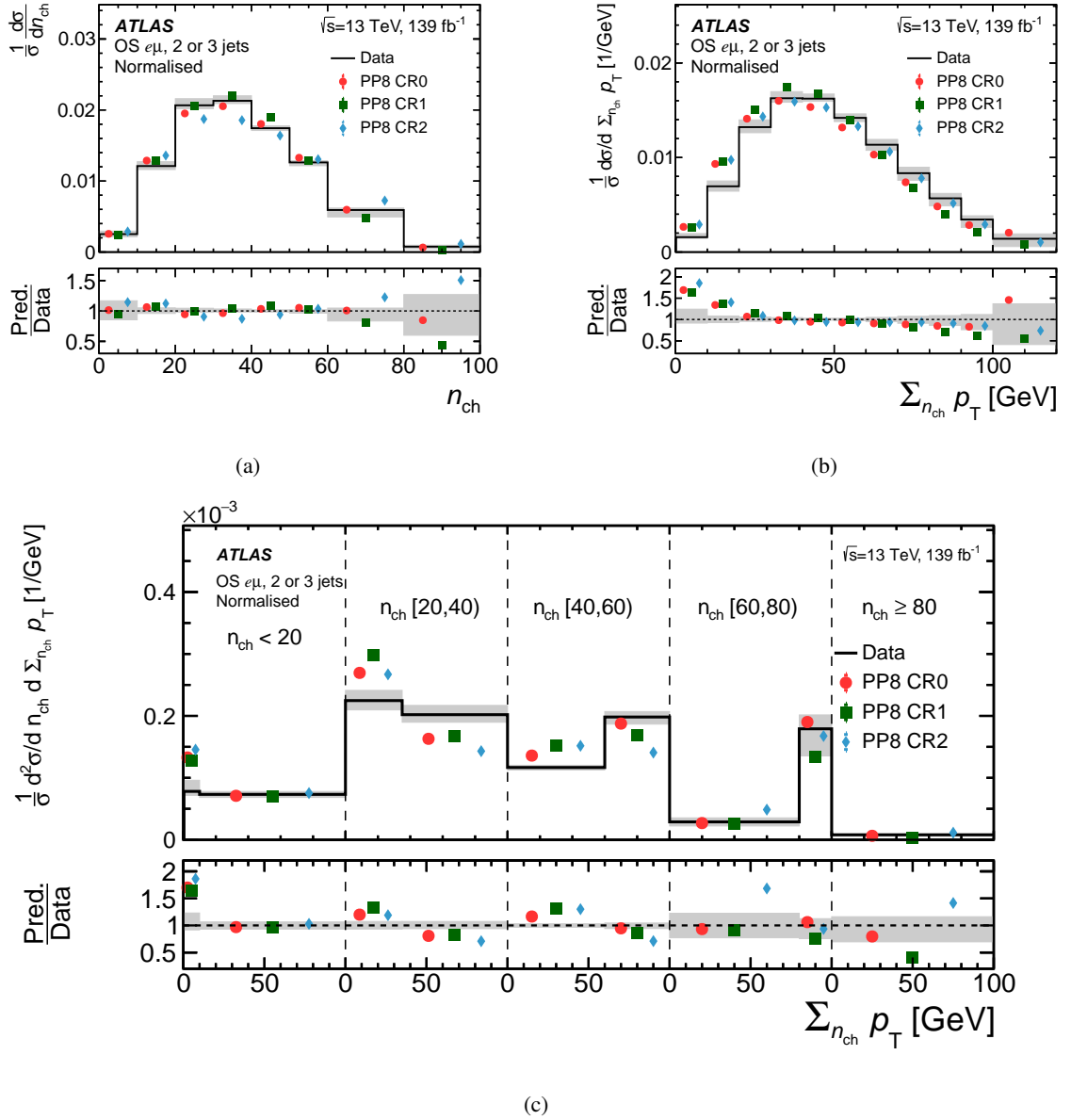
Figure 9.2: Normalised differential cross-section as a function of (a) n_{ch}, (b) $\sum_{n_{\text{ch}}} p_{\text{T}}$, and (c) $\sum_{n_{\text{ch}}} p_{\text{T}}$ in bins of n_{ch}. The x-axis in (c) is split into five bins of n_{ch} by the dashed vertical lines and $\sum_{n_{\text{ch}}} p_{\text{T}}$ is presented in each bin. Unfolded data are shown as the black line with the grey band corresponding to the total uncertainty in each bin. The results are compared with the predictions of different CR models in PYTHIA 8. Events beyond the x-axis range are included in the last bin. The lower panels show the ratio of each prediction to data in each bin.

(a)

(b)

(c)
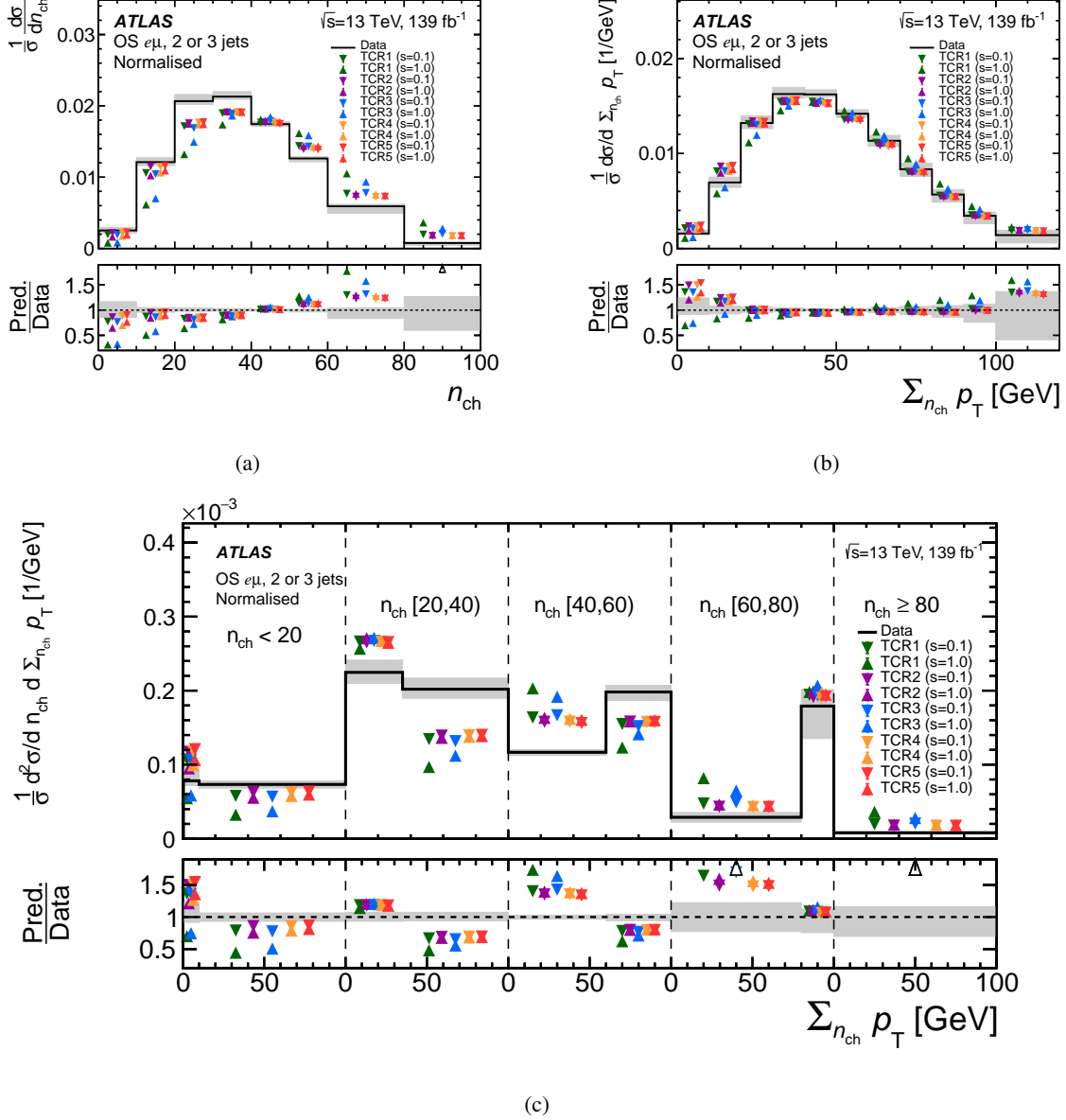
Figure 9.3: Normalised differential cross-section as a function of (a) n_{ch}, (b) $\sum_{n_{ch}} p_T$, and (c) $\sum_{n_{ch}} p_T$ in bins of n_{ch}. The x-axis in (c) is split into five bins of n_{ch} by the dashed vertical lines and $\sum_{n_{ch}} p_T$ is presented in each bin. Unfolded data are shown as the black line with the grey band corresponding to the total uncertainty in each bin. The results are compared with the predictions of different top-quark-specific CR models in PYTHIA 8. Events beyond the x-axis range are included in the last bin. The lower panels show the ratio of each prediction to data in each bin. The black triangular markers in the lower panels point to prediction-to-data ratio values which lie beyond the shown y-axis range.

Comparison with CR and UE parameters variation in Pythia 8

In Fig. 9.4, the normalised differential cross-sections are compared with the predictions obtained from Pythia 8 with variations of specific parameters connected with the CR and UE modelling. These variations are applied to the nominal Pythia 8 set-up using the A14 tune. The varied parameters are:

- The CR range R_{rec} parameter introduced in Eq. (3.3) is set to its maximal value of ten, such that the reconnection probability reaches saturation. The parameter value for the A14 tune is 1.71 [80]. This variation is labelled as 'maxCR' in the following.

- The CR is switched off by setting the CR range parameter to zero. This variation is labelled as 'noCR' in the following.

- The MPI parameter p_{T0}^{ref} introduced in Eq. (3.4) is varied down to 2.0 and up to 2.2. The parameter value for the A14 tune is 2.09 [80].

- The UE activity is varied by using the Var1 eigentune of the A14 tune [80]. This eigentune includes variations of the MPI α_s and variations of R_{rec}. For the down (up) variation, the MPI α_s is varied to 0.121 (0.131) and simultaneously the R_{rec} is varied to 1.69 (1.73). The MPI α_s value for the A14 tune is 0.126 [80].

In Fig. 9.4, it can be seen that the predictions without CR cannot describe the data while using a maximal probability for CR is still compatible with the measurement; 'maxCR' can describe the n_{ch} distribution very well, but not the $\sum_{n_{ch}} p_T$ distribution. Another observation is that the $\sum_{n_{ch}} p_T$ is not sensitive to the CR range, however the n_{ch} distribution is sensitive. Finally, a clear sensitivity to the p_{T0}^{ref} and Var1 variations is observed. The measurement of the n_{ch} observable suggests a higher value of p_{T0}^{ref} over a lower value. Thus, it can be concluded that for further tuning of CR models both parameters of the CR model itself and parameters of the UE should be included.

Comparison with CR models in Herwig 7

In Fig. 9.5, the normalised differential cross-sections are compared with the predictions obtained from the plain, the baryonic and the statistical CR models implemented in Herwig 7.2, which are introduced in Section 3.2.2. In addition, a prediction without any CR is shown. Similar to Pythia 8, predictions without CR do not describe data well, but in the case of Herwig 7.2 some deficits are compensated by the UE modelling. Among the various CR models in Herwig 7.2, the statistical CR model performs the best for the n_{ch} distribution mainly in the tail, while for $\sum_{n_{ch}} p_T$ and $\sum_{n_{ch}} p_T$ in bins of n_{ch} an overall low sensitivity can be observed. In general, the agreement of the predictions by Herwig for the $\sum_{n_{ch}} p_T$ distribution is better than for any other generator considered in this analysis.

In Fig. 9.6, the normalised differential cross section as a function of the n_{ch} observable is compared with predictions without CR, namely Sherpa 2 and the 'noCR' variations in Pythia 8 and Herwig 7. It is expected that these variations will predict higher particle multiplicity because of the lack of the suppression mechanism from CR. In the case of Pythia 8 and Herwig 7, this is true, while Sherpa 2 predicts too few particles.
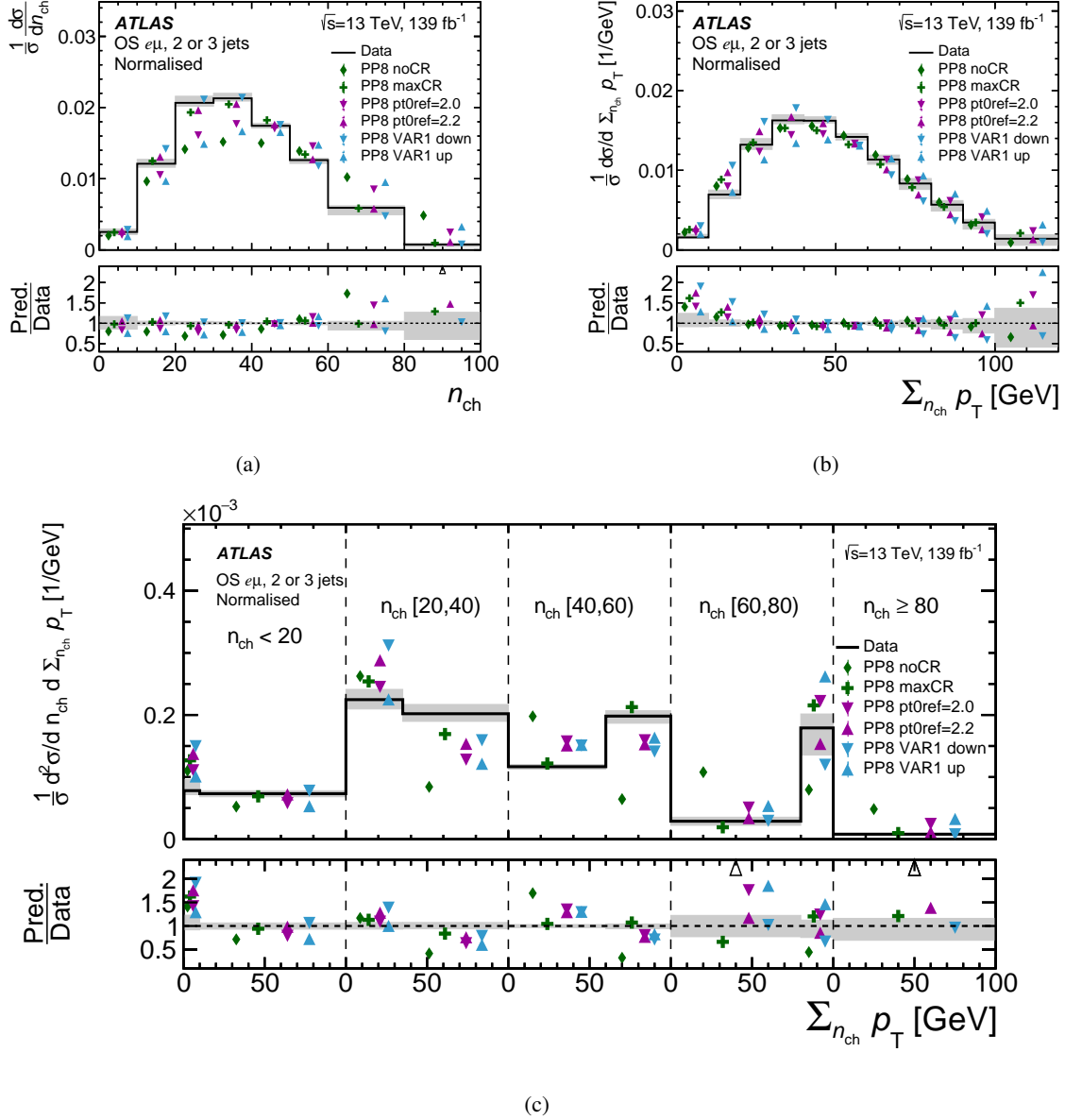
Figure 9.4: Normalised differential cross-section as a function of (a) n_{ch}, (b) $\sum_{n_{ch}} p_T$, and (c) $\sum_{n_{ch}} p_T$ in bins of n_{ch}. The x-axis in (c) is split into five bins of n_{ch} by the dashed vertical lines and $\sum_{n_{ch}} p_T$ is presented in each bin. Unfolded data are shown as the black line with the grey band corresponding to the total uncertainty in each bin. The results are compared with the predictions of different CR and UE parameter variations in PYTHIA 8. Events beyond the x-axis range are included in the last bin. The lower panels show the ratio of each prediction to data in each bin. The black triangular markers in the lower panels point to prediction-to-data ratio values which lie beyond the shown y-axis range.

(a)

(b)

(c)

Figure 9.5: Normalised differential cross-section as a function of (a) n_{ch}, (b) $\sum_{n_{\text{ch}}} p_{\text{T}}$, and (c) $\sum_{n_{\text{ch}}} p_{\text{T}}$ in bins of n_{ch}. The x-axis in (c) is split into five bins of n_{ch} by the dashed vertical lines and $\sum_{n_{\text{ch}}} p_{\text{T}}$ is presented in each bin. Unfolded data are shown as the black line with the grey band corresponding to the total uncertainty in each bin. The results are compared with the predictions of different CR models in HERWIG 7.2. Events beyond the x-axis range are included in the last bin. The lower panels show the ratio of each prediction to data in each bin.
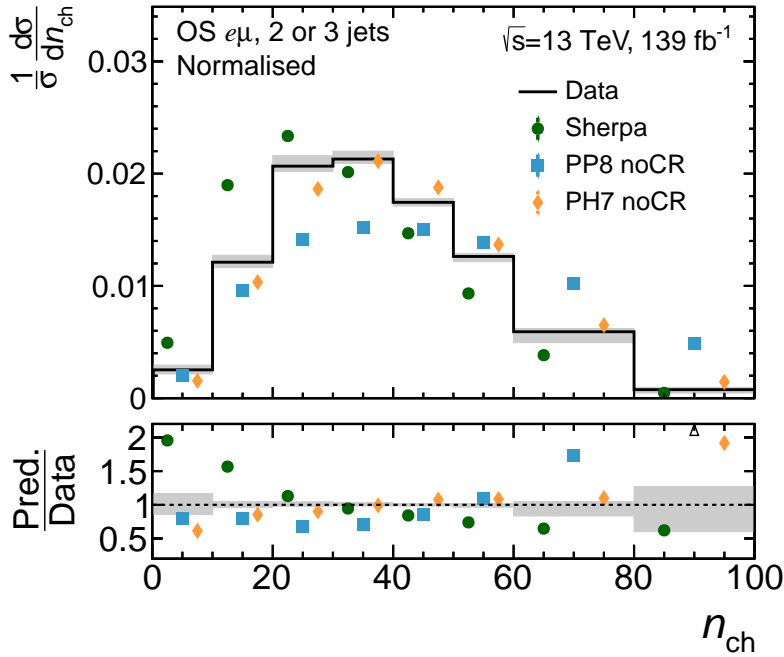
Figure 9.6: Normalised differential cross-section as a function of n_{ch} compared with the predictions of noCR models in different event generators.

9.2 Interpretation: χ^2 evaluation

In order to quantify how well the measured differential cross-sections agree with the various model predictions, their respective χ^2 values are calculated according to:

$$\chi^2 = V_{NDF}^{T} \cdot \mathrm{Cov}_{NDF}^{-1} \cdot V_{NDF}\,, \tag{9.1}$$

where NDF is the number of degrees of freedom, V_{NDF} is the vector of differences between the particle level measured cross-section and the prediction, and Cov_{NDF}^{-1} is the inverse of the covariance matrix. The NDF corresponds to the number of bins for the absolute distributions, while for the normalised distributions it is lowered by one unit; one bin is removed from the vector of differences. Consequently, one row and its corresponding column are removed from the covariance matrix. This is necessary to obtain an invertible covariance matrix. The resulting value for χ^2 does not depend on which bin is dropped.

In addition to the individual χ^2-values that are evaluated for each observable, a global χ^2 is evaluated for the n_{ch} and $\sum_{n_{ch}} p_T$ observables. The equation above is used, where the full vector of differences from both distributions is used and the global covariance matrix. The global covariance matrix is of a size of 19×19 for the absolute distributions, corresponding to the number of bins of both n_{ch} and $\sum_{n_{ch}} p_T$, while for the normalised distributions two rows and the corresponding columns are discarded.

Covariance matrix evaluation

The covariance matrix incorporates both the statistical and the systematic uncertainties. The systematic uncertainties include experimental uncertainties, signal modelling and background-related uncertainties described in the previous chapter. In addition, uncertainties in the theoretical predictions are considered, which are referred to as 'theory uncertainties'. These theory uncertainties include scale variations in the matrix element and parton shower, including μ_r, μ_f, ISR and FSR variations, as well as the variation of the matrix-element-to-parton-shower matching scale h_{damp}. These variations are independent of the CR modelling, and thus they are considered as theory uncertainties. The relative difference between the unfolded variation and the nominal unfolded distribution is taken as uncertainty.

The covariance matrix is obtained by performing pseudo-experiments. A set of 1000 pseudo-experiments is produced, where for each pseudo-experiment *toy*, the following procedure is followed:

1. Data statistical uncertainty: each bin j of the data distribution at the corrected level is fluctuated according to a Poisson distribution, $\mathcal{P}(N_j^{\mathrm{corr}})$.

2. MC statistical uncertainty: A Gaussian shift is added for each bin, where the bin error, $\Delta_{\mathrm{mcstat},j}$, is shifted according to a random number, λ_j^{toy}, drawn from a Gaussian distribution with a mean of zero and a width of one: $\lambda_j^{\mathrm{toy}} \cdot \Delta_{\mathrm{mcstat},j}$.

3. Experimental and background-rate uncertainties: for each experimental systematic uncertainty k, Gaussian-distributed shifts are added by scaling each Poisson-fluctuated bin with the variation from the associated systematic uncertainty, $\Delta_{k,j}$.

The number of events in bin j of a pseudo-experiment, incorporating the data and MC statistical uncertainties as well as the experimental systematic uncertainties, can be summarised as:

$$N_j^{\mathrm{toy}} = \mathcal{P}(N_i^{\mathrm{corr}}) \cdot \left(1 + \frac{\lambda_j^{\mathrm{toy}} \cdot \Delta_{\mathrm{mcstat},j} + \sum_{k=1}^{N_{\mathrm{sys}}} |\lambda_k^{\mathrm{toy}}| \cdot \Delta_{k,j}}{N_j^{\mathrm{sig,\ nominal}} + N_j^{\mathrm{bkg,\ nominal}}} \right), \qquad (9.2)$$

where the sum of $N_j^{\mathrm{sig,\ nominal}}$ and $N_j^{\mathrm{bkg,\ nominal}}$ represent the total nominal prediction, and λ_k^{toy} represents a random number drawn from a Gaussian distribution with a mean of zero and a width of one. It is worth noting that a different λ_k^{toy} is obtained for each systematic variation and applied to all bins; in this way, bin-by-bin correlations are fully taken into account. The sign of λ_k^{toy} determines if the upward or the downward variation of the uncertainty source is used to calculate $\Delta_{k,j}$.

4. Unfolding: Each of the varied pseudo-experiment distributions is then unfolded using the nominal migration matrix and unfolding corrections. The number of events in each bin of the unfolded distribution is referred to as $N_i^{\mathrm{toy,unf}}$.

5. Signal modelling and theory uncertainties: for each signal modelling and theory uncertainty, an additional Gaussian-distributed shift of the relative difference is added to give the final bin content of each pseudo-experiment:

The relative difference

$$N_i^{\text{toy,final}} = N_i^{\text{toy,unf}} \cdot \left(1 + \sum_{l=1}^{N_{\text{model.+theory}}} \Delta_{l,i}^{\text{toy}} \right) \quad (9.3)$$

The resulting differential cross-sections, obtained from each pseudo-experiment, are then used to calculate the covariance in each bin i, j according to:

$$\text{Cov}_{i,j} = \frac{1}{n} \cdot \sum_{\text{toy}=1}^{N_{\text{toys}}} (N_i^{\text{nominal, unf}} - N_i^{\text{toy,final}})(N_j^{\text{nominal, unf}} - N_j^{\text{toy,final}}) \quad (9.4)$$

where N_{toys} is the number of pseudo-experiments. Fig. 9.7 shows as an example the covariance matrices for the normalised cross-section as a function of n_{ch} and $\sum_{n_{\text{ch}}} p_{\text{T}}$ together with the global covariance matrix including both n_{ch} and $\sum_{n_{\text{ch}}} p_{\text{T}}$ distributions. All covariance matrices have large off-diagonal elements, mainly due to the modelling uncertainties.
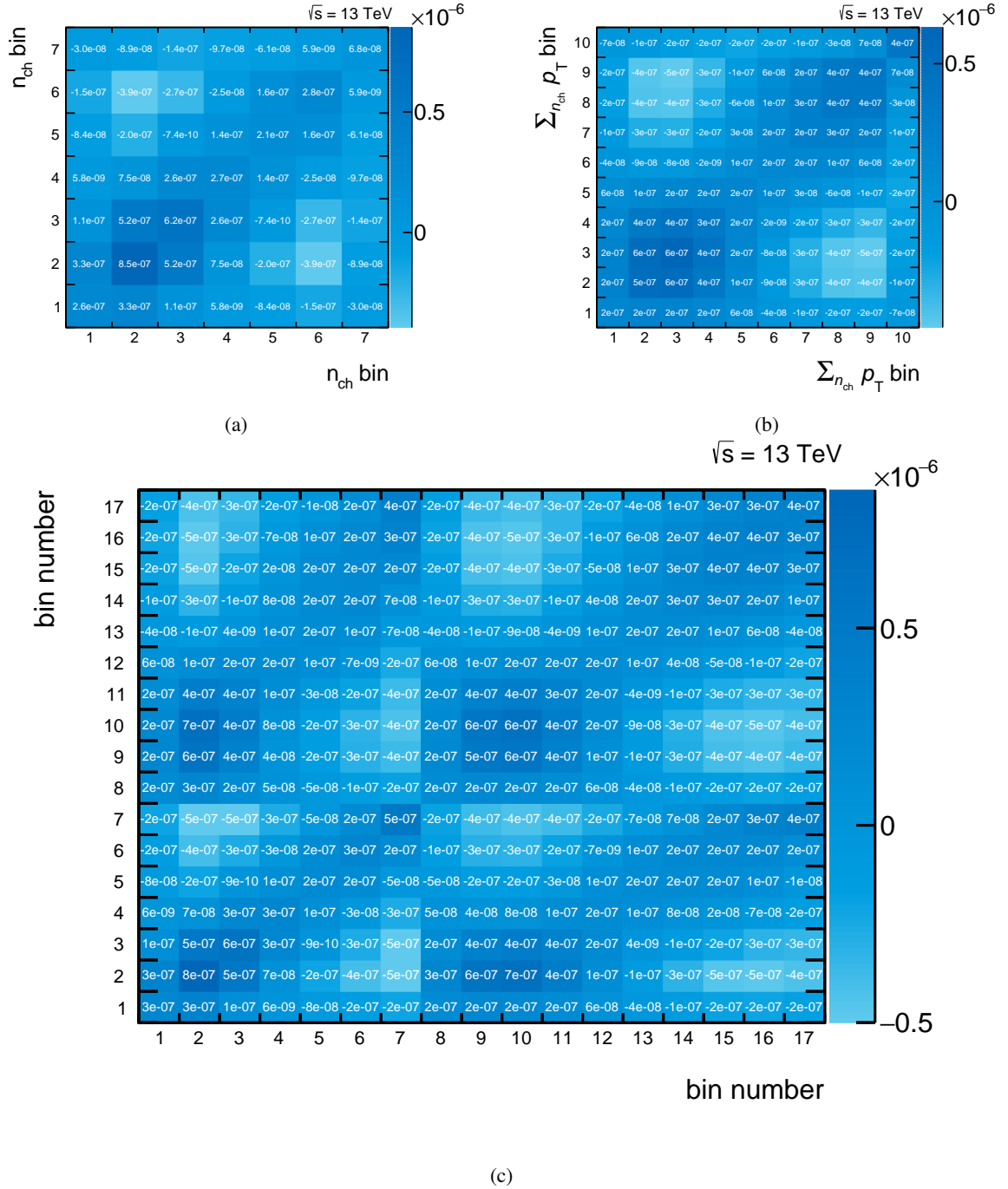
Figure 9.7: Covariance matrices of the normalised cross-section. For (a) n_{ch}, (b) $\sum_{n_{ch}} p_T$ observables, and (c) the global covariance matrix of both observables. The matrices account for the statistic and all systematic uncertainties presented in Chapter 8, as well as uncertainties in the theoretical prediction. In (c), the bin numbers from 1 to 7 correspond to the n_{ch} observable, while the bin numbers from 8 to 17 correspond to the $\sum_{n_{ch}} p_T$ observable.

χ^2/NDF results

Table 9.2 summarises the χ^2/NDF results for the normalised differential cross-sections. Most predictions do not describe the measured particle-level data well, with predictions obtained from POWHEG+HERWIG 7 being the best to describe the measured data. This is also seen in the figures presented earlier in this chapter. Among PYTHIA 8 models, CR0 describes the measured n_{ch} and the two-dimensional observables better. The CR0 model is based on the same MPI-based CR model as the nominal POWHEG+PYTHIA 8 sample. One can see that the measured data is in better agreement with the sample using the dedicated CR0 tune than with the nominal sample without a dedicated CR tune. The $\sum_{n_{ch}} p_T$ is best described by CR1. Among HERWIG 7.2 models, for the n_{ch} distribution, the newly introduced statistical CR model performs the best, while for $\sum_{n_{ch}} p_T$ the baryonic CR model agrees better with the observed distribution. Thus, even without dedicated retuning of the alternative CR models, they agree better with the measured data than the default plain CR model. In the $\sum_{n_{ch}} p_T$ in bins of n_{ch} observable, the lower χ^2/NDF value for SHERPA 2, relative to PYTHIA 8, is due to the inclusion of the theory uncertainties.

An alternative χ^2 scenario is considered to confirm the reason behind the large values. This scenario is referred to as *De-correlate modelling*, in which the contribution of the modelling and the theory uncertainties to off-diagonal elements of the covariance matrix is not taken into account. In other words, bin-to-bin correlations are not taken into account for these uncertainties. The result of this scenario is summarised in Table 9.3, which clearly explains, that the modelling uncertainties correlations between the bins are the reason for the large χ^2 values in the nominal scenario.

Table 9.2: The $\chi2$/NDF for the measured normalised differential cross-sections obtained by comparing the different predictions to the measured particle-level data. Global(n_{ch},$\sum_{n_{ch}} p_T$) denotes the scenario, in which the covariance matrix is built including correlations of systematic uncertainties between the two observables n_{ch} and $\sum_{n_{ch}} p_T$.

Generator set-up	n_{ch}	$\sum_{n_{ch}} p_T$	Global(n_{ch},$\sum_{n_{ch}} p_T$)	$\sum_{n_{ch}} p_T$ in bins of n_{ch}
PP8	9	11	26	28
PP8 CR0	8	11	37	16
PP8 CR1	14	6	34	20
PP8 CR2	8	20	24	30
PH7.0	6	2	9	4
PH7.1	8	4	11	5
PH7.2	11	3	18	11
PH7.2 Baryonic	11	2	14	4
PH7.2 Statistical	3	4	7	5
SHERPA 2	11	21	16	16

Table 9.3: The $\chi 2$/NDF associated with the 'De-correlate modelling' scenario for the measured normalised differential cross-sections obtained by comparing the different predictions to the measured particle-level data. Global($n_{ch}, \sum_{n_{ch}} p_T$) denotes the scenario, in which the covariance matrix is built including correlations of systematic uncertainties between the two observables n_{ch} and $\sum_{n_{ch}} p_T$.

Generator set-up	n_{ch}	$\sum_{n_{ch}} p_T$	Global($n_{ch}, \sum_{n_{ch}} p_T$)	$\sum_{n_{ch}} p_T$ in bins of n_{ch}
PP8	3.4	1.8	3.7	19
PP8 CR0	0.33	2.1	0.84	0.34
PP8 CR1	2.3	0.62	0.92	2.0
PP8 CR2	2.6	1.7	2.2	1.2
PH7.0	0.4	0.05	0.19	0.22
PH7.1	0.7	5.5	0.95	0.96
PH7.2	2.3	0.45	1.9	0.70
PH7.2 Baryonic	0.75	1.0	0.81	0.84
PH7.2 Statistical	0.29	2.6	0.6	0.63
SHERPA 2	21	12	14	13

9.3 Total fiducial cross-section

The total fiducial cross-section is obtained as described in Section 7.3, by integrating any of the absolute differential cross-sections over all bins. It is found to be:

$$\sigma_{t\bar{t}}^{\text{fid}} = 4.94^{+0.43}_{-0.41}(\text{syst}) \pm 0.03(\text{stat}) \pm 0.08(\text{lumi})\,\text{pb}. \tag{9.5}$$

The uncertainty in the measured cross-section is dominated by systematic uncertainties, with the main contribution coming from uncertainties in the signal modelling and the pile-up tracks background estimation.

Summary and conclusions

In this thesis, a measurement of three observables sensitive to colour reconnection effects in $t\bar{t}$ events is presented using a data sample of $139\,\mathrm{fb}^{-1}$ recorded by the ATLAS experiment at the LHC in proton–proton collisions at a centre-of-mass energy of $\sqrt{s} = 13\,\mathrm{TeV}$ from 2015 to 2018. The sensitive observables are the charged-particle multiplicity, the scalar sum of the charged-particles transverse momenta, and the scalar sum of the charged-particles transverse momenta in bins of charged particle-multiplicity.

The signature of dileptonic top-quark pair production in the $e\mu$ channel comprises one isolated electron and one isolated muon with opposite charge, and two or three jets, where exactly two jets are required to be b-tagged. This channel has a high signal purity. The total background contribution to the expected event yields is $4\,\%$, which is mainly from single-top-quark tW events.

The measured observables are constructed from primary hard-scatter tracks with $p_\mathrm{T} > 500\,\mathrm{MeV}$ and within $|\eta| < 2.5$. Furthermore, in order to best describe the colour reconnection effect, tracks associated with either a jet or a lepton from the top-quark decay are discarded. The contribution of background tracks, mainly from pile-up interactions, is estimated in a stochastic way based on a method using simulated event templates.

To remove detector effects, the background-subtracted observables are unfolded to stable-particle level, and the particle level normalised differential cross-sections are compared with several theoretical predictions obtained from simulation. None of the predictions is found to describe all measured observables adequately. Distributions of $\sum_{n_\mathrm{ch}} p_\mathrm{T}$ obtained from HERWIG 7.2 are able to describe data well, while predictions from PYTHIA 8 for n_ch are better than those for $\sum_{n_\mathrm{ch}} p_\mathrm{T}$. The event generator SHERPA 2 does not include a colour reconnection model, which should lead to a higher particle multiplicity because the suppression mechanism from CR is missing. Instead, it predicts too few particles, and also its $\sum_{n_\mathrm{ch}} p_\mathrm{T}$ distribution is softer than measured in data. Among the studied PYTHIA 8 colour reconnection models, the best agreement is achieved with the default MPI-based tune and the largest disagreement is found for the set of parameters based on the gluon-move model. In the case of the MPI-based model, variations of the colour-reconnection range parameter to its minimal and maximal values are investigated and, similarly to SHERPA 2, a model without colour reconnection is excluded, while a maximal strength is still compatible with the measurement. Finally, top-quark-specific colour reconnection models are compared with the measured distributions and sensitivity to the strength parameter variations is mainly seen in the distribution of $\sum_{n_\mathrm{ch}} p_\mathrm{T}$ in bins of n_ch for two of the five models. Variation of the PYTHIA 8 MPI model parameter $p_\mathrm{T0}^\mathrm{ref}$ showed that a

value higher than the one used in the A14 tune is suggested by the measurement. Additionally, a clear sensitivity is observed for the UE activity. In the case of HERWIG 7.2, the newly introduced statistical colour-reconnection model agrees best for the n_{ch} distribution, while for the $\sum_{n_{\text{ch}}} p_{\text{T}}$ distribution the baryonic CR model agrees best.

The measurement has a precision of 2 %–10 % in the central bins and up to 50 % in the outer bins. Therefore, providing a more precise measurement of n_{ch} and $\sum_{n_{\text{ch}}} p_{\text{T}}$ observables in the central bins compared to a previous measurement, which has a precision of about 20 %, performed using only the data collected in 2016 by the CMS experiment [24].

The measured observables provide stringent constraints on the colour reconnection models in mainstream Monte Carlo generators. They are not only sensitive to parameters related to colour reconnection models, but also the MPI and UE parameters. Thus, these results can be used as input to future tuning of Monte Carlo generators for colour reconnection, MPI and UE parameters, which should be handled simultaneously. In addition, they can be used to improve the estimate of systematic uncertainty in future top-quark mass analyses. In addition, this measurement could be repeated with a low pile-up dataset [158] to benefit from the small pile-up background contribution. Furthermore, the average transverse momenta of charged particles as a function of charged-particle multiplicity could (partially) provide further information about CR and UE.

APPENDIX **A**

Simulated samples

Lists of MC samples used in this analysis are given in Table A.1 for the top quark processes, in Tables A.2 to A.4 for the Z+jets process for different slices in $\max(H_T,\ p_T)$, where p_T is the transverse momentum of the Z boson and the H_T[1] of the event, and in Table A.5 for the diboson process.

---

[1] H_T is the scalar sum of the transverse momenta of all jets, leptons and the missing transverse momentum.

Table A.1: Top quark event MC samples used for this analysis. The cross-section column includes branching ratios. The quoted k-factor corrects for the absence of higher-order terms in the perturbative expansion of the cross-section calculation.

Process	σ [pb]	Generator	k-factor	Parameter / tune
$t\bar{t}$ dileptonic	76.95	Powheg+Pythia 8	1.14	
$t\bar{t}$ no fully hadronic	396.87	Powheg+Pythia 8	1.14	
$t\bar{t}$ dileptonic	76.94	Powheg+Pythia 8	1.14	$h_{\mathrm{damp}} = 3 \times m_t$
$t\bar{t}$ dileptonic	77.02	Powheg+Herwig 7.1	1.14	
$t\bar{t}$ dileptonic	76.98	Powheg+Pythia 8	1.14	CR0
$t\bar{t}$ dileptonic	77.01	Powheg+Pythia 8	1.14	CR1
$t\bar{t}$ dileptonic	76.97	Powheg+Pythia 8	1.14	CR2
$t\bar{t}$ dileptonic	76.93	Powheg+Pythia 8	1.14	$R_{\mathrm{rec}} = 10$
$t\bar{t}$ dileptonic	76.98	Powheg+Pythia 8	1.14	MPI $p_{\mathrm{T0}}^{\mathrm{ref}} = 2.2$
$t\bar{t}$ dileptonic	76.91	Powheg+Pythia 8	1.14	MPI $p_{\mathrm{T0}}^{\mathrm{ref}} = 2.0$
$t\bar{t}$ dileptonic	76.92	Powheg+Pythia 8	1.14	no CR
$t\bar{t}$ dileptonic	76.92	Powheg+Herwig 7.2	1.14	
$t\bar{t}$ dileptonic	76.89	Powheg+Herwig 7.2	1.14	SCR
$t\bar{t}$ dileptonic	76.89	Powheg+Herwig 7.2	1.14	BCR
$t\bar{t}$ dileptonic	76.93	Powheg+Herwig 7.2	1.14	no CR
tW or $\bar{t}W$ dileptonic	3.99	Powheg+Pythia 8	0.95	
tW inclusive	37.93	Powheg+Pythia 8	0.95	
$\bar{t}W$ inclusive	37.91	Powheg+Pythia 8	0.95	
tW dileptonic	3.89	Powheg+Pythia 8	0.97	DS scheme
$\bar{t}W$ dileptonic	3.97	Powheg+Pythia 8	0.95	DS scheme
ttW	0.55	Powheg+Pythia 8	1.10	
$ttZ(Z \to \ell\nu\bar{\ell}\nu)$	0.15	Powheg+Pythia 8	1.11	
$ttZ(Z \to q\bar{q})$	0.53	Powheg+Pythia 8	1.11	
$ttZ(Z \to e^+e^-)$	0.037	Powheg+Pythia 8	1.12	
$ttZ(Z \to \mu^+\mu^-)$	0.037	Powheg+Pythia 8	1.12	
$ttZ(Z \to \tau^+\tau^-)$	0.037	Powheg+Pythia 8	1.12	

Table A.2: $(Z \rightarrow \mu\mu)$+jets process MC samples used for this analysis, generated with the Sherpa event generator. The cross-section column includes branching ratios. The quoted k-factor corrects for the absence of higher-order terms in the perturbative expansion of the cross-section calculation.

Process	σ [pb]	k-factor	Slice
$(Z \rightarrow \mu\mu)$+light-jets	1 630.22	0.98	$0 < \max(H_{\mathrm{T}}, p_{\mathrm{T}}) < 70\,\mathrm{GeV}$
$(Z \rightarrow \mu\mu)$+c-jets	223.72	0.98	$0 < \max(H_{\mathrm{T}}, p_{\mathrm{T}}) < 70\,\mathrm{GeV}$
$(Z \rightarrow \mu\mu)$+b-jets	127.18	0.98	$0 < \max(H_{\mathrm{T}}, p_{\mathrm{T}}) < 70\,\mathrm{GeV}$
$(Z \rightarrow \mu\mu)$+light-jets	75.02	0.98	$70 < \max(H_{\mathrm{T}}, p_{\mathrm{T}}) < 140\,\mathrm{GeV}$
$(Z \rightarrow \mu\mu)$+c-jets	20.34	0.98	$70 < \max(H_{\mathrm{T}}, p_{\mathrm{T}}) < 140\,\mathrm{GeV}$
$(Z \rightarrow \mu\mu)$+b-jets	12.39	0.98	$70 < \max(H_{\mathrm{T}}, p_{\mathrm{T}}) < 140\,\mathrm{GeV}$
$(Z \rightarrow \mu\mu)$+light-jets	24.28	0.98	$140 < \max(H_{\mathrm{T}}, p_{\mathrm{T}}) < 280\,\mathrm{GeV}$
$(Z \rightarrow \mu\mu)$+c-jets	9.27	0.98	$140 < \max(H_{\mathrm{T}}, p_{\mathrm{T}}) < 280\,\mathrm{GeV}$
$(Z \rightarrow \mu\mu)$+b-jets	6.01	0.98	$140 < \max(H_{\mathrm{T}}, p_{\mathrm{T}}) < 280\,\mathrm{GeV}$
$(Z \rightarrow \mu\mu)$+light-jets	4.77	0.98	$280 < \max(H_{\mathrm{T}}, p_{\mathrm{T}}) < 500\,\mathrm{GeV}$
$(Z \rightarrow \mu\mu)$+c-jets	2.26	0.98	$280 < \max(H_{\mathrm{T}}, p_{\mathrm{T}}) < 500\,\mathrm{GeV}$
$(Z \rightarrow \mu\mu)$+b-jets	1.49	0.98	$280 < \max(H_{\mathrm{T}}, p_{\mathrm{T}}) < 500\,\mathrm{GeV}$
$(Z \rightarrow \mu\mu)$+jets	1.79	0.98	$500 < \max(H_{\mathrm{T}}, p_{\mathrm{T}}) < 1\,000\,\mathrm{GeV}$
$(Z \rightarrow \mu\mu)$+jets	0.15	0.98	$\max(H_{\mathrm{T}}, p_{\mathrm{T}}) > 1\,000\,\mathrm{GeV}$
$(Z \rightarrow \mu\mu)$+0 b-jets	2 330.19	0.98	$0 < \max(H_{\mathrm{T}}, p_{\mathrm{T}}) < 70\,\mathrm{GeV}, 10 < m(\ell\ell) < 40\,\mathrm{GeV}$
$(Z \rightarrow \mu\mu)$+b-jets	82.26	0.98	$0 < \max(H_{\mathrm{T}}, p_{\mathrm{T}}) < 70\,\mathrm{GeV}, 10 < m(\ell\ell) < 40\,\mathrm{GeV}$
$(Z \rightarrow \mu\mu)$+0 b-jets	44.88	0.98	$70 < \max(H_{\mathrm{T}}, p_{\mathrm{T}}) < 280\,\mathrm{GeV}, 10 < m(\ell\ell) < 40\,\mathrm{GeV}$
$(Z \rightarrow \mu\mu)$+b-jets	5.11	0.98	$70 < \max(H_{\mathrm{T}}, p_{\mathrm{T}}) < 280\,\mathrm{GeV}, 10 < m(\ell\ell) < 40\,\mathrm{GeV}$
$(Z \rightarrow \mu\mu)$+0 b-jets	2.76	0.98	$\max(H_{\mathrm{T}}, p_{\mathrm{T}}) > 280\,\mathrm{GeV}, 10 < m(\ell\ell) < 40\,\mathrm{GeV}$
$(Z \rightarrow \mu\mu)$+b-jets	0.47	0.98	$\max(H_{\mathrm{T}}, p_{\mathrm{T}}) > 280\,\mathrm{GeV}, 10 < m(\ell\ell) < 40\,\mathrm{GeV}$

Table A.3: $(Z \rightarrow ee)$+jets process MC samples used for this analysis, generated with the SHERPA event generator. The cross-section column includes branching ratios. The quoted k-factor corrects for the absence of higher-order terms in the perturbative expansion of the cross-section calculation.

Process	σ [pb]	k-factor	Slice
$(Z \rightarrow ee)$+light-jets	1 627.17	0.98	$0 < \max(H_T, p_T) < 70\,\text{GeV}$
$(Z \rightarrow ee)$+c-jets	223.73	0.98	$0 < \max(H_T, p_T) < 70\,\text{GeV}$
$(Z \rightarrow ee)$+b-jets	126.45	0.98	$0 < \max(H_T, p_T) < 70\,\text{GeV}$
$(Z \rightarrow ee)$+light-jets	76.29	0.98	$70 < \max(H_T, p_T) < 140\,\text{GeV}$
$(Z \rightarrow ee)$+c-jets	20.33	0.98	$70 < \max(H_T, p_T) < 140\,\text{GeV}$
$(Z \rightarrow ee)$+b-jets	12.62	0.98	$70 < \max(H_T, p_T) < 140\,\text{GeV}$
$(Z \rightarrow ee)$+light-jets	25.03	0.98	$140 < \max(H_T, p_T) < 280\,\text{GeV}$
$(Z \rightarrow ee)$+c-jets	9.37	0.98	$140 < \max(H_T, p_T) < 280\,\text{GeV}$
$(Z \rightarrow ee)$+b-jets	6.08	0.98	$140 < \max(H_T, p_T) < 280\,\text{GeV}$
$(Z \rightarrow ee)$+light-jets	4.87	0.98	$280 < \max(H_T, p_T) < 500\,\text{GeV}$
$(Z \rightarrow ee)$+c-jets	2.28	0.98	$280 < \max(H_T, p_T) < 500\,\text{GeV}$
$(Z \rightarrow ee)$+b-jets	1.49	0.98	$280 < \max(H_T, p_T) < 500\,\text{GeV}$
$(Z \rightarrow ee)$+jets	1.81	0.98	$500 < \max(H_T, p_T) < 1\,000\,\text{GeV}$
$(Z \rightarrow ee)$+jets	0.15	0.98	$1000 < \max(H_T, p_T) < 70\,\text{GeV}$
$(Z \rightarrow ee)$+0 b-jets	2 331.22	0.98	$0 < \max(H_T, p_T) < 70\,\text{GeV}, 10 < m(\ell\ell) < 40\,\text{GeV}$
$(Z \rightarrow ee)$+b-jets	81.36	0.98	$0 < \max(H_T, p_T) < 70\,\text{GeV}, 10 < m(\ell\ell) < 40\,\text{GeV}$
$(Z \rightarrow ee)$+0 b-jets	44.97	0.98	$70 < \max(H_T, p_T) < 280\,\text{GeV}, 10 < m(\ell\ell) < 40\,\text{GeV}$
$(Z \rightarrow ee)$+b-jets	5.48	0.98	$70 < \max(H_T, p_T) < 280\,\text{GeV}, 10 < m(\ell\ell) < 40\,\text{GeV}$
$(Z \rightarrow ee)$+0 b-jets	2.77	0.98	$280 < \max(H_T, p_T) < 70\,\text{GeV}, 10 < m(\ell\ell) < 40\,\text{GeV}$
$(Z \rightarrow ee)$+b-jets	0.47	0.98	$280 < \max(H_T, p_T) < 70\,\text{GeV}, 10 < m(\ell\ell) < 40\,\text{GeV}$

Table A.4: $(Z \rightarrow \tau\tau)$+ jets process MC samples used for this analysis, generated with the SHERPA event generator. The cross-section column includes branching ratios. The quoted k-factor corrects for the absence of higher-order terms in the perturbative expansion of the cross-section calculation.

Process	σ [pb]	k-factor	Slice
$(Z \rightarrow \tau\tau)$+light-jets	1 627.73	0.98	$0 < \max(H_{\mathrm{T}}, p_{\mathrm{T}}) < 70\,\mathrm{GeV}$
$(Z \rightarrow \tau\tau)$+c-jets	223.88	0.98	$0 < \max(H_{\mathrm{T}}, p_{\mathrm{T}}) < 70\,\mathrm{GeV}$
$(Z \rightarrow \tau\tau)$+b-jets	127.73	0.98	$0 < \max(H_{\mathrm{T}}, p_{\mathrm{T}}) < 70\,\mathrm{GeV}$
$(Z \rightarrow \tau\tau)$+light-jets	76.03	0.98	$70 < \max(H_{\mathrm{T}}, p_{\mathrm{T}}) < 140\,\mathrm{GeV}$
$(Z \rightarrow \tau\tau)$+c-jets	20.21	0.98	$70 < \max(H_{\mathrm{T}}, p_{\mathrm{T}}) < 140\,\mathrm{GeV}$
$(Z \rightarrow \tau\tau)$+b-jets	12.29	0.98	$70 < \max(H_{\mathrm{T}}, p_{\mathrm{T}}) < 140\,\mathrm{GeV}$
$(Z \rightarrow \tau\tau)$+light-jets	24.80	0.98	$140 < \max(H_{\mathrm{T}}, p_{\mathrm{T}}) < 280\,\mathrm{GeV}$
$(Z \rightarrow \tau\tau)$+c-jets	9.33	0.98	$140 < \max(H_{\mathrm{T}}, p_{\mathrm{T}}) < 280\,\mathrm{GeV}$
$(Z \rightarrow \tau\tau)$+b-jets	5.48	0.98	$140 < \max(H_{\mathrm{T}}, p_{\mathrm{T}}) < 280\,\mathrm{GeV}$
$(Z \rightarrow \tau\tau)$+light-jets	4.79	0.98	$280 < \max(H_{\mathrm{T}}, p_{\mathrm{T}}) < 500\,\mathrm{GeV}$
$(Z \rightarrow \tau\tau)$+c-jets	2.28	0.98	$280 < \max(H_{\mathrm{T}}, p_{\mathrm{T}}) < 500\,\mathrm{GeV}$
$(Z \rightarrow \tau\tau)$+b-jets	1.50	0.98	$280 < \max(H_{\mathrm{T}}, p_{\mathrm{T}}) < 500\,\mathrm{GeV}$
$(Z \rightarrow \tau\tau)$+jets	1.81	0.98	$500 < \max(H_{\mathrm{T}}, p_{\mathrm{T}}) < 1\,000\,\mathrm{GeV}$
$(Z \rightarrow \tau\tau)$+jets	0.15	0.98	$1000 < \max(H_{\mathrm{T}}, p_{\mathrm{T}}) < 70\,\mathrm{GeV}$
$(Z \rightarrow \tau\tau)$+0 b-jets	2 333.93	0.98	$0 < \max(H_{\mathrm{T}}, p_{\mathrm{T}}) < 70\,\mathrm{GeV}, 10 < m(\ell\ell) < 40\,\mathrm{GeV}$
$(Z \rightarrow \tau\tau)$+b-jets	81.10	0.98	$0 < \max(H_{\mathrm{T}}, p_{\mathrm{T}}) < 70\,\mathrm{GeV}, 10 < m(\ell\ell) < 40\,\mathrm{GeV}$
$(Z \rightarrow \tau\tau)$+0 b-jets	44.84	0.98	$70 < \max(H_{\mathrm{T}}, p_{\mathrm{T}}) < 280\,\mathrm{GeV}, 10 < m(\ell\ell) < 40\,\mathrm{GeV}$
$(Z \rightarrow \tau\tau)$+b-jets	5.54	0.98	$70 < \max(H_{\mathrm{T}}, p_{\mathrm{T}}) < 280\,\mathrm{GeV}, 10 < m(\ell\ell) < 40\,\mathrm{GeV}$
$(Z \rightarrow \tau\tau)$+0 b-jets	2.79	0.98	$280 < \max(H_{\mathrm{T}}, p_{\mathrm{T}}) < 70\,\mathrm{GeV}, 10 < m(\ell\ell) < 40\,\mathrm{GeV}$
$(Z \rightarrow \tau\tau)$+b-jets	0.47	0.98	$280 < \max(H_{\mathrm{T}}, p_{\mathrm{T}}) < 70\,\mathrm{GeV}, 10 < m(\ell\ell) < 40\,\mathrm{GeV}$

Table A.5: Diboson process MC samples used for this analysis, generated with the SHERPA event generator. V refers to the vector bosons, Z and W, while ℓ refers to the three lepton flavours, μ, e and τ. The cross-section column includes branching ratios. The quoted k-factor corrects for the absence of higher-order terms in the perturbative expansion of the cross-section calculation.

Process	σ [pb]	k-factor	comment
$VV \rightarrow \ell\ell\ell\ell$	1.25	1.0	
$VV \rightarrow \ell\ell\ell\nu$	4.58	1.0	
$VV \rightarrow \ell\ell\nu\nu$	12.50	1.0	
$VV \rightarrow \ell\nu\nu\nu$	3.23	1.0	
$VV \rightarrow \ell\ell\ell\ell$+2 jets	0.01	1.0	
$VV \rightarrow \ell\ell\ell\nu$+2 jets	0.046	1.0	
$VV \rightarrow \ell\ell\nu\nu$+2 jets	0.12	1.0	opposite-sign dilepton
$VV \rightarrow \ell\ell\nu\nu$+2 jets	0.04	1.0	same-sign dilepton
$VV \rightarrow \ell\ell\ell\ell$	1.43	1.0	low $m(\ell\ell)$ and p_{T}
$VV \rightarrow \ell\ell\ell\nu$	2.92	1.0	low $m(\ell\ell)$ and p_{T}
$VV \rightarrow \ell\ell\nu\nu$	0.17	1.0	low $m(\ell\ell)$ and p_{T}
$gg \rightarrow \ell\ell\ell\ell$	0.0099	1.0	$0 < m(\ell\ell\ell\ell) < 130$
$gg \rightarrow \ell\ell\ell\ell$	0.01	1.0	$m(\ell\ell\ell\ell) > 130$
$ZZ \rightarrow qq\nu\nu$	15.56	0.28	
$ZZ \rightarrow qq\ell\ell$	15.56	0.14	
$WZ \rightarrow qq\nu\nu$	6.79	1.0	
$WZ \rightarrow qq\ell\ell$	3.44	1.0	
$WW \rightarrow qq\ell\nu$	24.72	1.0	
$WW \rightarrow \ell\nu qq$	24.7	1.0	
$WZ \rightarrow \ell\nu qq$	11.41	1.0	

Systematic uncertainties

Lists of the contribution of each source of uncertainty to the total relative uncertainty on the three normalised-measured differential cross-sections is given in Tables B.1 to B.3 for the experimental uncertainties, and in Tables B.4 to B.6 for the signal and background modelling uncertainties.

Table B.1: Experimental uncertainties on the normalised measured n_{ch} distribution per bin in percentage. For each source of uncertainty, the up and down uncertainties are given.

Source	bin 1	bin 2	bin 3	bin 4	bin 5	bin 6	bin 7	bin 8
Track efficiency global	3.33 −3.34	2.12 −2.13	1.44 −1.45	0.93 −0.93	0.14 −0.14	−1.03 1.02	−3.41 3.41	−8.54 8.76
Track efficiency PP0	1.45 −1.45	0.96 −0.96	0.60 −0.60	0.38 −0.38	0.04 −0.05	−0.40 0.40	−1.45 1.45	−3.81 3.86
JES b-jes response	−0.12 0.03	−0.03 0.04	−0.02 −0.01	−0.02 0.01	0.01 0.00	0.04 −0.01	0.04 −0.02	0.05 −0.08
JES NP modelling 1	0.69 −0.81	0.55 −0.54	0.29 −0.28	0.07 −0.06	−0.06 0.03	−0.19 0.21	−0.57 0.58	−1.41 1.41
JES η-intercalibration	0.76 −0.84	0.53 −0.55	0.24 −0.24	0.07 −0.09	−0.06 0.03	−0.19 0.22	−0.53 0.57	−1.27 1.38
JES flavor response	−2.33 2.09	−1.58 1.46	−0.72 0.68	−0.23 0.21	0.14 −0.15	0.58 −0.54	1.62 −1.48	4.21 −3.66
JES pile-up offset N_{PV}	0.66 −0.80	0.52 −0.49	0.27 −0.25	0.06 −0.08	−0.07 0.07	−0.17 0.20	−0.52 0.51	−1.39 1.24
JES pile-up ρ topology	1.90 −1.95	1.39 −1.32	0.64 −0.63	0.19 −0.19	−0.13 0.12	−0.49 0.47	−1.41 1.37	−3.53 3.57
JER NP 1	0.20 0.20	0.18 0.18	0.14 0.14	0.08 0.08	−0.01 −0.01	−0.08 −0.08	−0.29 −0.29	−0.70 −0.70
JER NP 2	0.42 0.42	0.32 0.32	0.18 0.18	0.11 0.11	0.01 0.01	−0.15 −0.15	−0.44 −0.44	−1.06 −1.06
JER NP 3	0.32 0.32	0.26 0.26	0.17 0.17	0.07 0.07	−0.00 −0.00	−0.10 −0.10	−0.36 −0.36	−0.83 −0.83
JER NP 4	0.42 0.42	0.36 0.36	0.19 0.19	0.09 0.09	−0.02 −0.02	−0.15 −0.15	−0.42 −0.42	−1.08 −1.08
JER NP 5	0.18 0.18	0.17 0.17	0.09 0.09	0.05 0.05	0.00 0.00	−0.08 −0.08	−0.20 −0.20	−0.51 −0.51
JER NP 6	0.18 0.18	0.14 0.14	0.08 0.08	0.02 0.02	0.00 0.00	−0.04 −0.04	−0.19 −0.19	−0.45 −0.45
JER NP 7	0.24 0.24	0.22 0.22	0.14 0.14	0.06 0.06	−0.00 −0.00	−0.08 −0.08	−0.31 −0.31	−0.70 −0.70
JVT	0.07 −0.05	0.02 −0.02	−0.00 0.00	−0.01 0.01	−0.01 0.00	−0.01 0.01	−0.00 0.00	−0.01 0.00
b-tagging SF - NP 0	−0.12 0.13	−0.06 0.07	−0.03 0.03	−0.01 0.01	−0.00 0.00	0.02 −0.03	0.07 −0.08	0.25 −0.26
b-tagging SF - NP 1	0.03 −0.03	0.01 −0.01	0.00 −0.00	−0.00 0.00	−0.00 0.00	−0.01 0.01	−0.01 0.01	0.01 −0.01
b-tagging SF - NP 2	−0.02 0.02	−0.00 0.00	0.00 −0.00	0.00 −0.00	0.00 −0.00	0.00 −0.00	−0.00 0.00	−0.03 0.03
e SF ID	0.01 −0.01	0.00 −0.00	−0.00 0.00	0.00 −0.00	−0.00 0.00	−0.00 0.00	−0.00 0.00	0.01 −0.01
μ SF isol stat	−0.01 0.01	−0.01 0.01	−0.00 0.00	−0.00 0.00	0.00 −0.00	0.00 −0.00	0.01 −0.01	0.02 −0.02
μ SF isol syst	0.03 −0.03	0.01 −0.02	0.01 −0.01	0.00 −0.00	−0.00 0.00	−0.01 0.01	−0.01 0.01	−0.00 0.00
μ-reweight	0.30 −0.27	0.23 −0.20	0.17 −0.16	0.08 −0.06	−0.02 0.02	−0.11 0.10	−0.33 0.27	−0.74 0.64

Table B.2: Experimental uncertainties on the normalised measured $\sum_{n_{\mathrm{ch}}} p_{\mathrm{T}}$ distribution per bin in percentage. For each source of uncertainty, the up and down uncertainties are given.

Source	bin 1	bin 2	bin 3	bin 4	bin 5	bin 6	bin 7	bin 8	bin 9	bin 10	bin 11
Track efficiency global	2.91	2.05	1.43	1.01	0.55	−0.09	−0.88	−1.76	−2.92	−4.24	−6.97
	−2.91	−2.05	−1.43	−1.01	−0.56	0.08	0.88	1.76	2.92	4.25	7.09
Track efficiency PP0	1.32	0.91	0.65	0.43	0.22	−0.04	−0.40	−0.76	−1.25	−1.89	−3.09
	−1.32	−0.91	−0.65	−0.43	−0.22	0.04	0.40	0.76	1.25	1.89	3.11
JES b-jes response	−0.11	−0.00	−0.01	−0.01	−0.00	0.02	0.02	0.02	0.02	0.00	−0.04
	0.08	0.03	−0.01	−0.01	−0.02	−0.01	0.01	−0.01	0.00	0.00	0.06
JES NP modelling 1	0.79	0.90	0.70	0.40	0.15	−0.10	−0.36	−0.69	−1.09	−1.65	−2.87
	−0.82	−0.86	−0.69	−0.43	−0.16	0.10	0.36	0.70	1.04	1.61	2.98
JES η-intercalibration	0.83	0.89	0.66	0.36	0.13	−0.11	−0.38	−0.66	−1.01	−1.50	−2.60
	−0.86	−0.87	−0.67	−0.39	−0.14	0.09	0.35	0.68	1.02	1.56	2.87
JES flavor response	−2.50	−2.48	−1.91	−1.17	−0.42	0.26	1.00	1.90	2.97	4.65	8.52
	2.28	2.30	1.77	1.05	0.36	−0.34	−0.95	−1.69	−2.69	−4.16	−7.25
JER NP 7 (rest term)	0.37	0.36	0.15	0.11	0.02	−0.07	−0.15	−0.21	−0.28	−0.43	−0.49
	0.37	0.36	0.15	0.11	0.02	−0.07	−0.15	−0.21	−0.28	−0.43	−0.49
JES pile-up offset μ	0.34	0.41	0.27	0.14	0.05	−0.06	−0.12	−0.26	−0.44	−0.70	−1.09
	−0.36	−0.37	−0.27	−0.18	−0.06	0.06	0.17	0.30	0.41	0.64	1.07
JES pile-up offset N_{PV}	0.76	0.86	0.62	0.35	0.12	−0.14	−0.32	−0.60	−0.94	−1.45	−2.47
	−0.83	−0.79	−0.59	−0.37	−0.15	0.12	0.35	0.62	0.94	1.41	2.45
JES pile-up ρ topology	2.07	2.25	1.73	1.03	0.35	−0.30	−0.91	−1.67	−2.66	−4.09	−7.15
	−2.05	−2.08	−1.66	−1.03	−0.38	0.22	0.85	1.63	2.58	4.01	7.43
JER NP 1	0.32	0.31	0.11	0.08	0.03	−0.07	−0.16	−0.17	−0.19	−0.31	−0.29
	0.32	0.31	0.11	0.08	0.03	−0.07	−0.16	−0.17	−0.19	−0.31	−0.29
JER NP 2	0.58	0.55	0.16	0.10	0.02	−0.07	−0.21	−0.28	−0.37	−0.52	−0.54
	0.58	0.55	0.16	0.10	0.02	−0.07	−0.21	−0.28	−0.37	−0.52	−0.54
JER NP 3	0.44	0.44	0.18	0.10	0.03	−0.07	−0.20	−0.24	−0.31	−0.49	−0.56
	0.44	0.44	0.18	0.10	0.03	−0.07	−0.20	−0.24	−0.31	−0.49	−0.56
JER NP 4	0.58	0.57	0.26	0.16	0.04	−0.09	−0.26	−0.33	−0.41	−0.66	−0.94
	0.58	0.57	0.26	0.16	0.04	−0.09	−0.26	−0.33	−0.41	−0.66	−0.94
JER NP 5	0.25	0.29	0.09	0.06	0.01	−0.06	−0.13	−0.13	−0.15	−0.27	−0.36
	0.25	0.29	0.09	0.06	0.01	−0.06	−0.13	−0.13	−0.15	−0.27	−0.36
JER NP 6	0.25	0.25	0.08	0.04	−0.00	−0.05	−0.11	−0.11	−0.11	−0.18	−0.19
	0.25	0.25	0.08	0.04	−0.00	−0.05	−0.11	−0.11	−0.11	−0.18	−0.19
JER NP 7	0.37	0.36	0.15	0.11	0.02	−0.07	−0.15	−0.21	−0.28	−0.43	−0.49
	0.37	0.36	0.15	0.11	0.02	−0.07	−0.15	−0.21	−0.28	−0.43	−0.49
JVT	0.09	0.05	0.02	0.00	−0.01	−0.01	−0.02	−0.02	−0.02	−0.03	−0.04
	−0.06	−0.04	−0.01	−0.00	0.01	0.01	0.01	0.01	0.02	0.02	0.03
b-tagging SF - NP 0	−0.12	−0.06	−0.02	−0.02	−0.00	0.01	0.02	0.03	0.05	0.08	0.14
	0.13	0.06	0.03	0.02	0.01	−0.01	−0.02	−0.04	−0.06	−0.09	−0.15
b-tagging SF - NP 1	0.03	0.01	0.00	−0.00	−0.00	−0.00	−0.01	−0.01	−0.01	−0.00	0.01
	−0.03	−0.01	−0.00	0.00	0.00	0.00	0.01	0.01	0.01	0.00	−0.01
b-tagging SF - NP 2	−0.02	−0.01	−0.00	0.00	0.00	0.00	0.00	0.00	0.00	0.00	0.00
	0.02	0.01	0.00	−0.00	−0.00	−0.00	−0.00	−0.00	−0.00	−0.00	−0.00
e SF ID	0.01	0.00	0.00	0.00	−0.00	−0.00	−0.00	−0.00	−0.00	−0.00	0.01
	−0.01	−0.00	−0.00	−0.00	0.00	0.00	0.00	0.00	0.00	0.00	−0.01
μ SF isol syst	0.03	0.02	0.01	0.01	0.00	−0.00	−0.01	−0.02	−0.02	−0.02	−0.03
	−0.03	−0.02	−0.02	−0.01	−0.00	0.00	0.01	0.02	0.02	0.03	0.03
μ-reweight	0.33	0.31	0.23	0.15	0.07	−0.04	−0.14	−0.26	−0.38	−0.56	−0.94
	−0.29	−0.26	−0.22	−0.14	−0.03	0.04	0.13	0.21	0.32	0.49	0.82

Table B.3: Experimental uncertainties on the normalised measured $\sum_{n_{\mathrm{ch}}} p_{\mathrm{T}}$ in bins of n_{ch} distribution per bin in percentage. For each source of uncertainty, the up and down uncertainties are given.

Source	bin 1	bin 2	bin 3	bin 4	bin 5	bin 6	bin 7	bin 8	bin 9
Track efficiency global	2.81 −2.82	2.27 −2.28	1.00 −1.01	1.40 −1.40	−0.59 0.59	−0.21 0.21	−3.25 3.25	−3.51 3.50	−8.38 8.59
Track efficiency PP0	1.28 −1.28	1.01 −1.01	0.46 −0.46	0.52 −0.52	−0.21 0.21	−0.13 0.13	−1.43 1.43	−1.47 1.47	−3.70 3.74
JES b-jes response	−0.11 0.07	−0.03 0.03	0.00 −0.02	−0.04 0.02	0.05 −0.03	−0.01 0.04	0.05 −0.05	0.02 0.00	0.05 −0.06
JES NP modelling 1	0.79 −0.83	0.53 −0.53	0.77 −0.76	−0.42 0.42	0.48 −0.48	−1.00 0.98	0.25 −0.21	−1.28 1.26	−1.75 1.74
JES η-intercalibration	0.83 −0.86	0.52 −0.54	0.73 −0.71	−0.42 0.39	0.44 −0.45	−0.95 0.96	0.23 −0.19	−1.18 1.22	−1.58 1.70
JES flavor response	−2.50 2.28	−1.54 1.41	−2.08 1.93	1.14 −1.06	−1.29 1.11	2.75 −2.45	−0.64 0.63	3.58 −3.30	5.15 −4.56
JES pile-up offset μ	0.34 −0.35	0.23 −0.23	0.30 −0.30	−0.17 0.15	0.17 −0.17	−0.35 0.40	0.08 −0.03	−0.53 0.49	−0.72 0.64
JES pile-up offset N_{PV}	0.76 −0.83	0.50 −0.48	0.68 −0.65	−0.36 0.32	0.36 −0.37	−0.82 0.86	0.15 −0.16	−1.11 1.10	−1.67 1.52
JES pile-up ρ topology	2.07 −2.05	1.35 −1.29	1.90 −1.80	−1.08 0.99	1.16 −1.14	−2.44 2.39	0.69 −0.62	−3.23 3.10	−4.42 4.40
JER NP 1	0.30 0.30	0.16 0.16	0.18 0.18	0.05 0.05	−0.03 −0.03	−0.07 −0.07	−0.22 −0.22	−0.35 −0.35	−0.71 −0.71
JER NP 2	0.54 0.54	0.30 0.30	0.27 0.27	0.02 0.02	−0.01 −0.01	−0.15 −0.15	−0.27 −0.27	−0.56 −0.56	−1.12 −1.12
JER NP 3	0.42 0.42	0.24 0.24	0.26 0.26	−0.03 −0.03	0.04 0.04	−0.18 −0.18	−0.18 −0.18	−0.51 −0.51	−0.89 −0.89
JER NP 4	0.55 0.55	0.33 0.33	0.35 0.35	−0.07 −0.07	0.07 0.07	−0.31 −0.31	−0.16 −0.16	−0.63 −0.63	−1.17 −1.17
JER NP 5	0.24 0.24	0.16 0.16	0.14 0.14	−0.01 −0.01	0.01 0.01	−0.11 −0.11	−0.08 −0.08	−0.29 −0.29	−0.55 −0.55
JER NP 6	0.24 0.24	0.13 0.13	0.12 0.12	−0.02 −0.02	−0.01 −0.01	−0.04 −0.04	−0.14 −0.14	−0.23 −0.23	−0.46 −0.46
JER NP 7 (rest term)	0.35 0.35	0.20 0.20	0.22 0.22	−0.02 −0.02	0.03 0.03	−0.14 −0.14	−0.15 −0.15	−0.43 −0.43	−0.76 −0.76
b-tagging SF - NP 0	−0.12 0.13	−0.06 0.07	−0.01 0.01	−0.03 0.03	0.02 −0.03	−0.01 0.01	0.09 −0.09	0.06 −0.06	0.24 −0.25
b-tagging SF - NP 1	0.03 −0.03	0.01 −0.01	0.00 −0.00	−0.00 0.00	−0.00 0.00	−0.01 0.01	−0.00 0.00	−0.01 0.01	0.01 −0.01
b-tagging SF - NP 2	−0.02 0.02	−0.00 0.00	−0.01 0.01	0.01 −0.01	−0.01 0.00	0.01 −0.01	−0.01 0.01	0.00 −0.00	−0.02 0.02
JVT	0.09 −0.06	0.02 −0.01	0.03 −0.02	−0.04 0.03	0.01 −0.01	−0.03 0.02	0.01 −0.01	−0.02 0.01	−0.02 0.01
e SF ID	0.01 −0.01	0.00 −0.00	0.00 −0.00	−0.00 0.00	−0.00 0.00	−0.00 0.00	0.00 −0.00	−0.01 0.01	0.01 −0.01
μ SF isol stat	−0.01 0.01	−0.01 0.01	−0.00 0.00	0.00 −0.00	−0.00 0.00	0.00 −0.00	0.00 −0.00	0.01 −0.01	0.02 −0.02
μ SF isol syst	0.03 −0.03	0.01 −0.02	0.01 −0.02	−0.01 0.01	0.00 −0.00	−0.02 0.02	0.00 0.00	−0.03 0.03	−0.01 0.01
μ-reweight	0.32 −0.29	0.23 −0.20	0.24 −0.22	0.01 0.01	0.05 −0.04	−0.23 0.21	−0.14 0.11	−0.48 0.41	−0.81 0.70

Table B.4: Signal and background modelling uncertainties on the normalised measured n_{ch} distribution per bin in percentage. For each source of uncertainty, the up and down uncertainties are given.

Source	bin 1	bin 2	bin 3	bin 4	bin 5	bin 6	bin 7	bin 8
H7	−4.97	−1.65	0.52	0.95	1.21	1.22	0.18	−21.63
	4.97	1.65	−0.52	−0.95	−1.21	−1.22	−0.18	21.63
CR	2.48	3.18	3.76	2.86	1.18	−0.92	1.01	9.95
	1.62	0.34	−0.13	−0.76	−1.09	−2.92	−15.78	−31.30
h_{damp}	−0.60	−0.37	0.21	−0.45	0.16	0.02	0.50	0.20
	0.60	0.37	−0.21	0.45	−0.16	−0.02	−0.50	−0.20
ISR α_s	−0.58	−0.13	−0.08	−0.01	0.03	0.02	0.15	0.81
	0.46	0.13	0.08	−0.01	−0.02	0.01	−0.14	−0.83
FSR	0.89	0.41	0.17	0.06	0.03	0.05	−0.58	−2.76
	−1.77	−0.40	−0.27	−0.06	−0.06	−0.34	0.76	4.02
Scale μ_r	−0.03	0.02	−0.00	−0.01	−0.00	0.02	0.01	−0.11
	0.00	−0.02	0.01	−0.02	0.01	0.02	−0.01	0.10
Scale μ_f	−0.06	0.03	0.01	−0.01	−0.00	0.03	−0.01	−0.10
	0.04	−0.02	−0.01	−0.01	0.01	0.01	0.01	0.04
PDF4LHC	0.53	0.13	0.03	0.03	0.03	0.05	0.10	0.19
	−0.53	−0.13	−0.03	−0.03	−0.03	−0.05	−0.10	−0.19
Background rates	0.22	0.18	0.12	0.06	0.02	−0.05	−0.24	−1.11
	−0.21	−0.18	−0.11	−0.06	−0.02	0.05	0.24	1.10
tW FSR	0.23	0.09	0.05	0.03	−0.00	−0.02	−0.15	−0.29
	−0.34	−0.08	−0.24	−0.04	0.07	−0.04	0.29	0.98
tW ISR α_s	−0.17	−0.06	−0.01	0.00	0.01	0.04	0.04	0.09
	0.17	0.05	0.01	−0.00	−0.01	−0.03	−0.03	−0.10
tW Scale μ_f	0.02	0.01	0.00	0.00	0.00	−0.00	−0.01	−0.06
	−0.03	−0.01	−0.01	−0.01	−0.00	0.00	0.02	0.07
tW Scale μ_r	0.02	0.01	0.00	−0.00	0.00	0.00	−0.01	−0.05
	−0.02	−0.02	−0.00	0.01	−0.00	−0.00	0.01	0.06
tW DS vs. DR	0.08	0.20	0.06	−0.01	0.02	0.04	−0.24	−0.60
	−0.07	−0.20	−0.06	0.01	−0.02	−0.04	0.24	0.60
PU non-closure	1.86	0.14	−0.55	0.17	−0.46	0.22	0.24	1.10
	−1.86	−0.14	0.55	−0.17	0.46	−0.22	−0.24	−1.10
PU scale factor	14.48	−1.36	−0.75	0.22	0.31	0.18	−0.87	−2.29
	−12.14	0.32	1.18	−0.17	−0.38	−0.27	0.82	2.83

Table B.5: Signal and background modelling uncertainties on the normalised measured $\sum_{n_{ch}} p_T$ distribution per bin in percentage. For each source of uncertainty, the up and down uncertainties are given.

Source	bin 1	bin 2	bin 3	bin 4	bin 5	bin 6	bin 7	bin 8	bin 9	bin 10	bin 11
H7	−6.07 6.07	−3.94 3.94	−1.52 1.52	−0.31 0.31	0.85 −0.85	1.70 −1.70	3.36 −3.36	5.52 −5.52	6.59 −6.59	5.70 −5.70	−23.99 23.99
CR	3.13 0.95	4.04 0.17	4.22 −0.66	3.72 −0.89	2.66 −0.77	1.76 −1.10	1.67 −2.16	1.96 −5.32	0.95 −10.85	5.07 −21.80	18.48 −50.10
h_{damp}	−0.76 0.76	−0.14 0.14	−0.11 0.11	−0.27 0.27	0.06 −0.06	0.04 −0.04	0.05 −0.05	0.18 −0.18	0.53 −0.53	0.58 −0.58	0.34 −0.34
ISR α_s	−0.57 0.46	−0.22 0.20	−0.05 0.04	−0.04 0.03	−0.02 0.04	−0.04 0.05	0.02 −0.02	0.09 −0.10	0.13 −0.12	0.42 −0.41	1.09 −1.05
FSR	1.35 −2.15	0.39 −0.43	0.25 −0.30	0.18 0.03	0.13 −0.15	0.07 −0.58	−0.02 −0.23	−0.16 0.30	−0.65 1.10	−1.21 1.12	−3.75 4.93
Scale μ_r	0.00 −0.05	0.01 0.00	−0.01 0.01	0.00 −0.02	−0.01 0.03	0.01 −0.02	0.03 −0.03	0.02 −0.03	−0.03 0.03	−0.02 0.01	−0.12 0.19
Scale μ_f	−0.05 0.01	0.05 −0.04	−0.02 0.01	0.00 −0.02	0.00 0.01	0.02 −0.02	−0.02 0.05	0.01 −0.01	−0.00 −0.01	−0.04 0.01	−0.04 0.04
PDF4LHC	0.50 −0.50	0.17 −0.17	0.06 −0.06	0.02 −0.02	0.02 −0.02	0.04 −0.04	0.06 −0.06	0.09 −0.09	0.11 −0.11	0.13 −0.13	0.19 −0.19
Background rates	0.23 −0.23	0.17 −0.17	0.11 −0.11	0.08 −0.08	0.04 −0.04	−0.00 0.00	−0.05 0.05	−0.11 0.11	−0.21 0.21	−0.36 0.36	−0.76 0.75
tW FSR	0.19 −0.34	0.11 −0.12	0.09 −0.28	0.07 −0.13	−0.02 −0.00	−0.00 −0.01	−0.05 −0.00	−0.06 0.10	−0.13 0.42	−0.29 0.85	−0.38 1.03
tW ISR α_s	−0.20 0.20	−0.09 0.09	−0.04 0.03	−0.03 0.02	−0.00 0.00	0.01 −0.01	0.05 −0.04	0.05 −0.05	0.06 −0.06	0.12 −0.11	0.19 −0.16
tW Scale μ_f	0.02 −0.02	0.01 −0.01	0.01 −0.01	0.00 −0.01	0.00 −0.00	−0.00 0.00	−0.01 0.01	−0.01 0.01	−0.01 0.02	−0.02 0.02	−0.04 0.05
tW Scale μ_r	0.02 −0.02	0.02 −0.03	0.00 −0.00	−0.00 0.00	0.00 −0.00	0.00 −0.00	−0.01 0.01	−0.00 0.00	−0.01 0.01	−0.02 0.03	−0.04 0.05
tW DS vs. DR	0.22 −0.22	0.26 −0.26	0.02 −0.02	0.03 −0.03	−0.00 0.00	0.07 −0.07	0.03 −0.03	−0.17 0.17	−0.29 0.29	−0.26 0.26	−0.44 0.44
PU non-closure	0.52 −0.52	−3.68 3.68	−1.54 1.54	−0.67 0.67	0.54 −0.54	1.52 −1.52	2.68 −2.68	3.12 −3.12	2.52 −2.52	−0.68 0.68	−13.44 13.44
PU scale factor	22.73 2.99	−2.77 −0.94	−1.98 −0.25	−0.66 −0.61	−0.16 −0.64	0.08 −0.46	0.29 −0.01	0.36 0.65	0.18 1.43	−0.01 2.35	0.16 4.50

Table B.6: Signal and background modelling uncertainties on the normalised measured $\sum_{n_{ch}} p_T$ in bins of n_{ch} distribution per bin in percentage. For each source of uncertainty, the up and down uncertainties are given.

Source	bin 1	bin 2	bin 3	bin 4	bin 5	bin 6	bin 7	bin 8	bin 9
H7	−5.99 5.99	−1.26 1.26	−4.09 4.09	3.20 −3.20	0.37 −0.37	0.48 −0.48	18.62 −18.62	−6.35 6.35	−7.28 7.28
CR	2.11 1.39	3.52 0.92	2.96 −0.15	4.35 −1.19	0.90 −1.20	−1.41 −3.93	6.21 −7.36	3.94 −21.35	2.28 −26.02
h_{damp}	−0.76 0.76	−0.32 0.32	−0.01 0.01	−0.31 0.31	0.24 −0.24	−0.06 0.06	0.56 −0.56	0.48 −0.48	0.20 −0.20
ISR α_s	−0.52 0.41	−0.15 0.14	−0.10 0.08	0.00 −0.01	0.04 −0.01	0.00 −0.01	0.13 −0.14	0.13 −0.11	1.10 −1.10
FSR	1.24 −1.97	0.39 −0.48	0.12 −0.15	0.13 −0.21	0.05 −0.12	−0.09 −0.10	−0.22 0.23	−0.82 1.18	−3.06 4.14
Scale μ_r	0.00 −0.04	0.01 −0.01	−0.02 0.02	0.01 −0.03	−0.01 0.03	0.03 −0.01	0.00 −0.01	0.02 −0.02	−0.12 0.12
Scale μ_f	−0.05 0.02	0.02 −0.01	0.01 −0.02	−0.02 0.00	0.01 0.00	0.01 0.01	−0.02 0.03	−0.01 0.01	−0.10 0.04
PDF4LHC	0.50 −0.50	0.13 −0.13	0.05 −0.05	0.07 −0.07	0.02 −0.02	0.09 −0.09	0.09 −0.09	0.12 −0.12	0.19 −0.19
Background rates	0.22 −0.21	0.19 −0.19	0.07 −0.07	0.11 −0.11	−0.05 0.05	0.03 −0.03	−0.30 0.30	−0.19 0.19	−1.04 1.03
tW FSR	0.19 −0.34	0.10 −0.08	0.07 −0.18	0.01 −0.09	0.02 0.01	−0.06 0.03	−0.06 −0.07	−0.24 0.60	−0.33 1.16
tW ISR α_s	−0.20 0.20	−0.06 0.05	−0.05 0.04	0.04 −0.04	−0.03 0.03	0.10 −0.09	−0.02 0.02	0.09 −0.07	0.12 −0.12
tW Scale μ_f	0.02 −0.02	0.01 −0.01	0.01 −0.01	0.00 −0.00	0.00 −0.00	−0.00 0.00	−0.02 0.02	−0.01 0.02	−0.05 0.07
tW Scale μ_r	0.01 −0.02	0.01 −0.02	0.00 −0.01	−0.01 0.01	0.00 −0.01	−0.00 0.01	−0.00 0.01	−0.01 0.02	−0.05 0.06
PU non-closure	−0.55 0.55	0.89 −0.89	−2.78 2.78	2.66 −2.66	−0.61 0.61	−0.04 0.04	10.23 −10.23	−7.33 7.33	−4.84 4.84
PU scale factor	21.64 2.03	−3.35 −2.76	−0.99 0.93	0.70 0.08	−0.61 −0.90	1.51 0.58	−0.67 0.85	−0.97 0.95	−2.46 2.60

Particle-level absolute differential cross-section results

The absolute measured differential cross-section results are presented as a function of the observables sensitive to colour reconnection effects, defined earlier in Section 5.4. The measured distributions are compared to a variety of predictions obtained from simulation and shown in Figs. C.1 to C.5.
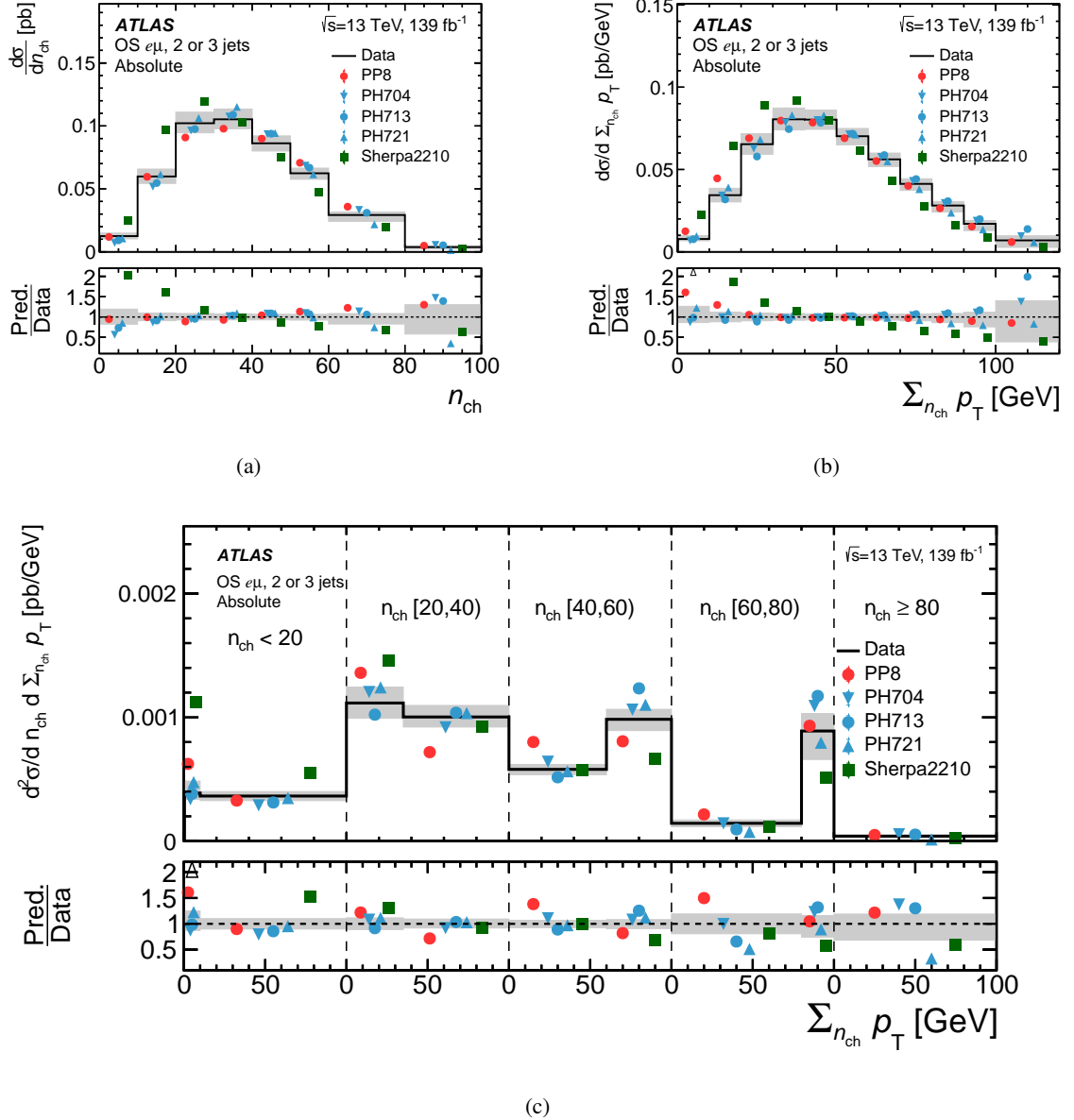
Figure C.1: Absolute differential cross-section as a function of (a) n_{ch}, (b) $\sum_{n_{ch}} p_T$, and (c) $\sum_{n_{ch}} p_T$ in bins of n_{ch}. The x-axis in (c) is split into five bins of n_{ch} by the dashed vertical lines and $\sum_{n_{ch}} p_T$ is presented in each bin. Unfolded data are shown as the black line with the grey band corresponding to the total uncertainty in each bin. The results are compared with the predictions of different MC event generators. Events beyond the x-axis range are included in the last bin. The lower panels show the ratio of each prediction to data in each bin. The black triangular markers in the lower panels point to prediction-to-data ratio values which lie beyond the shown y-axis range.

(a)

(b)

(c)

Figure C.2: Absolute differential cross-section as a function of (a) n_{ch}, (b) $\sum_{n_{ch}} p_T$, and (c) $\sum_{n_{ch}} p_T$ in bins of n_{ch}. The x-axis in (c) is split into five bins of n_{ch} by the dashed vertical lines and $\sum_{n_{ch}} p_T$ is presented in each bin. Unfolded data are shown as the black line with the grey band corresponding to the total uncertainty in each bin. The results are compared with the predictions of different CR models in PYTHIA 8. Events beyond the x-axis range are included in the last bin. The lower panels show the ratio of each prediction to data in each bin.

(a)

(b)

(c)
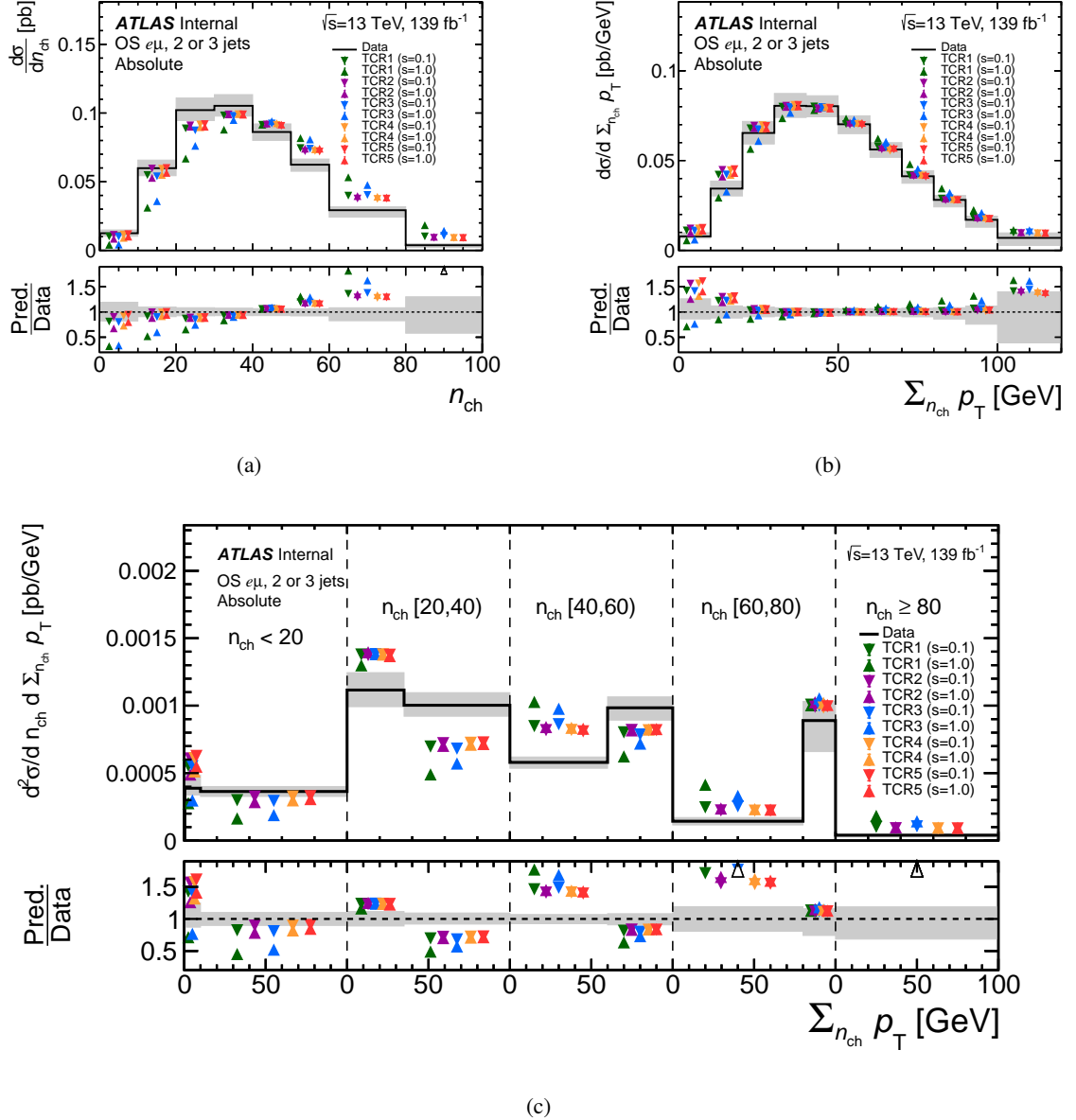
Figure C.3: Absolute differential cross-section as a function of (a) n_{ch}, (b) $\sum_{n_{ch}} p_T$, and (c) $\sum_{n_{ch}} p_T$ in bins of n_{ch}. The x-axis in (c) is split into five bins of n_{ch} by the dashed vertical lines and $\sum_{n_{ch}} p_T$ is presented in each bin. Unfolded data are shown as the black line with the grey band corresponding to the total uncertainty in each bin. The results are compared with the predictions of different top-quark-specific CR models in PYTHIA 8. Events beyond the x-axis range are included in the last bin. The lower panels show the ratio of each prediction to data in each bin. The black triangular markers in the lower panels point to prediction-to-data ratio values which lie beyond the shown y-axis range.

Figure C.4: Absolute differential cross-section as a function of (a) n_{ch}, (b) $\sum_{n_{\text{ch}}} p_{\text{T}}$, and (c) $\sum_{n_{\text{ch}}} p_{\text{T}}$ in bins of n_{ch}. The x-axis in (c) is split into five bins of n_{ch} by the dashed vertical lines and within each bin the is presented. Unfolded data is shown as the black line with the grey band corresponding to the total uncertainty in each bin. The results are compared to the predictions of different CR and UE parameter variations in PYTHIA 8. Events beyond the x-axis range are included in the last bin. In the lower panel, the ratio between data and the corresponding prediction in each bin is shown. The black triangular markers in the lower panels point to prediction-to-data ratio values which lie beyond the shown y-axis range.

(a)

(b)

(c)
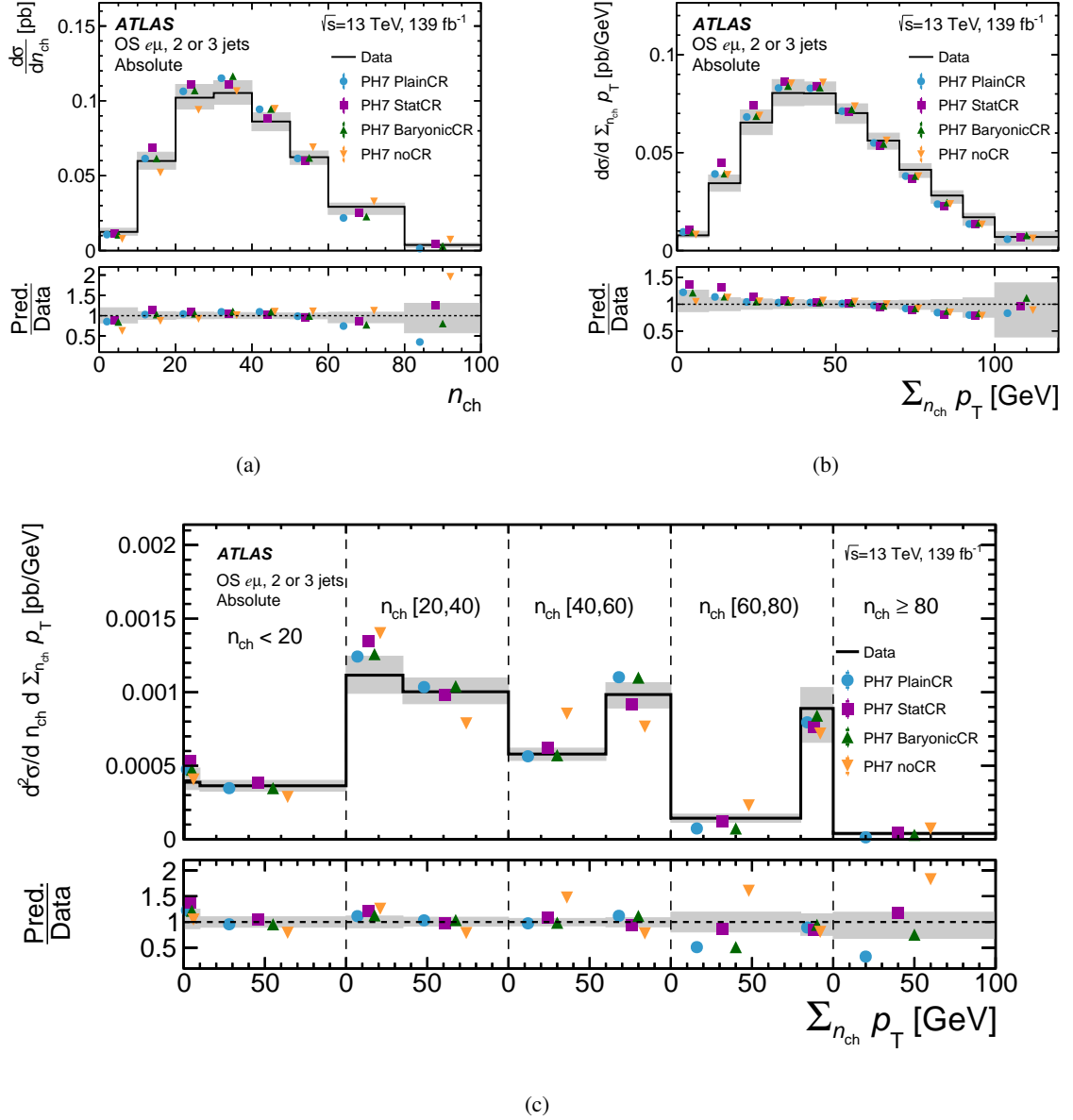
Figure C.5: Absolute differential cross-section as a function of (a) n_{ch}, (b) $\sum_{n_{\mathrm{ch}}} p_{\mathrm{T}}$, and (c) $\sum_{n_{\mathrm{ch}}} p_{\mathrm{T}}$ in bins of n_{ch}. The x-axis in (c) is split into five bins of n_{ch} by the dashed vertical lines and $\sum_{n_{\mathrm{ch}}} p_{\mathrm{T}}$ is presented in each bin. Unfolded data are shown as the black line with the grey band corresponding to the total uncertainty in each bin. The results are compared with the predictions of different CR models in HERWIG 7.2. Events beyond the x-axis range are included in the last bin. The lower panels show the ratio of each prediction to data in each bin.

Bibliography

[1] S. L. Glashow, *Partial Symmetries of Weak Interactions*, Nucl. Phys. **22** (1961) 579 (cit. on pp. 1, 6).

[2] S. Weinberg, *A Model of Leptons*, Phys. Rev. Lett. **19** (1967) 1264 (cit. on pp. 1, 6).

[3] A. Salam, *Weak and Electromagnetic Interactions*, Conf. Proc. C **680519** (1968) 367 (cit. on pp. 1, 6).

[4] M. Gell-Mann, *The Eightfold Way: A Theory of strong interaction symmetry*, (1961) (cit. on p. 1).

[5] D. J. Gross and F. Wilczek, *Ultraviolet Behavior of Nonabelian Gauge Theories*, Phys. Rev. Lett. **30** (1973) 1343, ed. by J. C. Taylor (cit. on pp. 1, 7).

[6] H. D. Politzer, *Reliable Perturbative Results for Strong Interactions?*, Phys. Rev. Lett. **30** (1973) 1346, ed. by J. C. Taylor (cit. on p. 1).

[7] F. Wilczek, *Quantum Chromodynamics (QCD): The Modern Theory of the Strong Interaction*, Ann. Rev. Nucl. Part. Sci. **32** (1982) 177 (cit. on p. 1).

[8] L. Evans and P. Bryant, *LHC Machine*, JINST **3** (2008) S08001 (cit. on pp. 1, 30).

[9] ATLAS Collaboration, *The ATLAS Experiment at the CERN Large Hadron Collider*, JINST **3** (2008) S08003 (cit. on pp. 1, 31–33, 35, 36).

[10] T. Sjöstrand et al., *An introduction to PYTHIA 8.2*, Comput. Phys. Commun. **191** (2015) 159, arXiv: `1410.3012` `[hep-ph]` (cit. on p. 2).

[11] J. Bellm et al., *Herwig 7.0/Herwig++ 3.0 release note*, Eur. Phys. J. C **76** (2016) 196, arXiv: `1512.01178` `[hep-ph]` (cit. on pp. 2, 26, 107).

[12] E. Bothmann et al., *Event generation with Sherpa 2.2*, SciPost Phys. **7** (2019) 034, arXiv: `1905.09127` `[hep-ph]` (cit. on pp. 2, 20).

[13] CMS Collaboration, *CMS PYTHIA 8 colour reconnection tunes based on underlying-event data*, (2022), arXiv: `2205.02905` `[hep-ex]` (cit. on p. 2).

[14] T. Sjostrand and M. van Zijl, *A Multiple Interaction Model for the Event Structure in Hadron Collisions*, Phys. Rev. D **36** (1987) 2019 (cit. on p. 2).

[15] T. Sjöstrand, "Colour reconnection and its effects on precise measurements at the LHC", 2013, arXiv: `1310.8073` `[hep-ph]` (cit. on p. 2).

[16] Particle Data Group, P. Zyla et al., *Review of Particle Physics*, PTEP **2020** (2020) 083C01 (cit. on pp. 2, 11).

[17]   Argyropoulos, Spyros and Sjöstrand, Torbjorn,
         Effects of color reconnection on tt̄ final states at the LHC, JHEP **11** (2014) 043,
         arXiv: `1407.6653` [`hep-ph`] (cit. on pp. 2, 21, 22, 24).

[18]   CMS Collaboration, *Measurement of the top quark mass in the all-jets final state at*
         $\sqrt{s} = 13$ *TeV and combination with the lepton+jets channel*, Eur. Phys. J. C **79** (2019) 313,
         arXiv: `1812.10534` [`hep-ex`] (cit. on p. 2).

[19]   ATLAS Collaboration, *Measurement of the top quark mass in the tt̄ → lepton+jets channel*
         from $\sqrt{s} = 8$ *TeV ATLAS data and combination with previous results*,
         Eur. Phys. J. C **79** (2019) 290, arXiv: `1810.01772` [`hep-ex`] (cit. on p. 2).

[20]   ATLAS Collaboration,
         Measurement of charged-particle distributions sensitive to the underlying event in
         $\sqrt{s} = 13$ *TeV proton–proton collisions with the ATLAS detector at the LHC*,
         JHEP **03** (2017) 157, arXiv: `1701.05390` [`hep-ex`] (cit. on p. 2).

[21]   CMS Collaboration, *Measurement of the underlying event activity in inclusive Z boson*
         production in proton–proton collisions at $\sqrt{s} = 13$ *TeV*, JHEP **07** (2018) 032,
         arXiv: `1711.04299` [`hep-ex`] (cit. on p. 2).

[22]   ATLAS Collaboration, *Measurement of distributions sensitive to the underlying event in*
         inclusive Z-boson production in pp collisions at $\sqrt{s} = 7$ *TeV with the ATLAS detector*,
         Eur. Phys. J. C **74** (2014) 3195, arXiv: `1409.3433` [`hep-ex`] (cit. on p. 2).

[23]   ATLAS Collaboration, *Measurement of distributions sensitive to the underlying event in*
         inclusive Z boson production in pp collisions at $\sqrt{s} = 13$ *TeV with the ATLAS detector*,
         Eur. Phys. J. C **79** (2019) 666, arXiv: `1905.09752` [`hep-ex`] (cit. on p. 2).

[24]   CMS Collaboration,
         Study of the underlying event in top quark pair production in pp collisions at 13 *TeV*,
         Eur. Phys. J. C **79** (2019) 123, arXiv: `1807.02810` [`hep-ex`] (cit. on pp. 2, 48, 122).

[25]   ATLAS Collaboration, *Measurements of observables sensitive to colour reconnection in tt̄*
         events with the ATLAS detector at $\sqrt{s} = 13$ *TeV*, (2022), arXiv: `2209.07874` [`hep-ex`]
         (cit. on p. 2).

[26]   E. Fermi, *On the Quantization of the Monoatomic Ideal Gas*, (1999),
         arXiv: `cond-mat/9912229` (cit. on p. 5).

[27]   P. A. M. Dirac, *On the Theory of quantum mechanics*,
         Proc. Roy. Soc. Lond. A **112** (1926) 661 (cit. on p. 5).

[28]   S. N. Bose, *Planck's law and light quantum hypothesis*, Z. Phys. **26** (1924) 178 (cit. on p. 5).

[29]   Y. Fukuda et al., *Evidence for oscillation of atmospheric neutrinos*,
         Phys. Rev. Lett. **81** (1998) 1562, arXiv: `hep-ex/9807003` (cit. on p. 6).

[30]   Q. R. Ahmad et al., *Direct evidence for neutrino flavor transformation from neutral current*
         interactions in the Sudbury Neutrino Observatory, Phys. Rev. Lett. **89** (2002) 011301,
         arXiv: `nucl-ex/0204008` (cit. on p. 6).

[31]   G. Galati, *Final results of the OPERA experiment on* ν_τ *appearance in the CNGS beam*,
         J. Phys. Conf. Ser. **1226** (2019) 012022 (cit. on p. 6).

[32] Particle Data Group, R. L. Workman et al., *Review of Particle Physics*,
PTEP **2022** (2022) 083C01 (cit. on pp. 6–10, 15).

[33] F. Halzen and A. D. Martin,
Quarks and Leptons: An Introductory Course in Modern Particle Physics, Wiley, 1984,
ISBN: 9780471887416 (cit. on p. 7).

[34] M. Kobayashi and T. Maskawa,
CP Violation in the Renormalizable Theory of Weak Interaction,
Prog. Theor. Phys. **49** (1973) 652 (cit. on p. 9).

[35] N. Cabibbo, *Unitary Symmetry and Leptonic Decays*, Phys. Rev. Lett. **10** (1963) 531
(cit. on p. 9).

[36] F. Englert and R. Brout, *Broken Symmetry and the Mass of Gauge Vector Mesons*,
Phys. Rev. Lett. **13** (1964) 321, ed. by J. C. Taylor (cit. on p. 10).

[37] P. W. Higgs, *Broken symmetries, massless particles and gauge fields*,
Phys. Lett. **12** (1964) 132 (cit. on p. 10).

[38] P. W. Higgs, *Broken Symmetries and the Masses of Gauge Bosons*,
Phys. Rev. Lett. **13** (1964) 508, ed. by J. C. Taylor (cit. on p. 10).

[39] G. S. Guralnik, C. R. Hagen and T. W. B. Kibble,
Global Conservation Laws and Massless Particles,
Phys. Rev. Lett. **13** (1964) 585, ed. by J. C. Taylor (cit. on p. 10).

[40] CMS Collaboration,
Observation of a new boson at a mass of 125 GeV with the CMS experiment at the LHC,
Phys. Lett. B **716** (2012) 30, arXiv: `1207.7235` [`hep-ex`] (cit. on p. 11).

[41] ATLAS Collaboration, *Observation of a new particle in the search for the Standard Model
Higgs boson with the ATLAS detector at the LHC*, Phys. Lett. B **716** (2012) 1,
arXiv: `1207.7214` [`hep-ex`] (cit. on p. 11).

[42] S. W. Herb et al.,
Observation of a Dimuon Resonance at 9.5-GeV in 400-GeV Proton-Nucleus Collisions,
Phys. Rev. Lett. **39** (1977) 252 (cit. on p. 11).

[43] C. Campagnari and M. Franklin, *The Discovery of the top quark*,
Rev. Mod. Phys. **69** (1997) 137, arXiv: `hep-ex/9608003` (cit. on p. 11).

[44] CDF Collaboration, *Observation of top quark production in $\bar{p}p$ collisions*,
Phys. Rev. Lett. **74** (1995) 2626, arXiv: `hep-ex/9503002` [`hep-ex`] (cit. on p. 11).

[45] D0 Collaboration, *Observation of the top quark*, Phys. Rev. Lett. **74** (1995) 2632,
arXiv: `hep-ex/9503003` (cit. on p. 11).

[46] ATLAS Collaboration, *Measurement of the top quark mass in the $t\bar{t} \rightarrow$ lepton+jets channel
from $\sqrt{s} = 8$ TeV ATLAS data and combination with previous results*,
Eur. Phys. J. C **79** (2019) 290, arXiv: `1810.01772` [`hep-ex`] (cit. on p. 11).

[47] I. I. Y. Bigi, Y. L. Dokshitzer, V. A. Khoze, J. H. Kuhn and P. M. Zerwas,
Production and Decay Properties of Ultraheavy Quarks, Phys. Lett. B **181** (1986) 157
(cit. on p. 11).

[48] J. C. Collins, D. E. Soper and G. Sterman, *Factorization of Hard Processes in QCD*, (2004),
arXiv: `hep-ph/0409313` `[hep-ph]` (cit. on p. 12).

[49] H.-L. Lai et al., *New parton distributions for collider physics*, Phys. Rev. D **82** (2010) 074024,
arXiv: `1007.2241` `[hep-ph]` (cit. on p. 12).

[50] R. D. Ball et al., *Parton distributions from high-precision collider data*,
The European Physical Journal C **77** (2017), arXiv: `706.00428` `[hep-ph]`
(cit. on pp. 12, 13).

[51] Y. L. Dokshitzer, *Calculation of the Structure Functions for Deep Inelastic Scattering and e+
e- Annihilation by Perturbation Theory in Quantum Chromodynamics.*,
Sov. Phys. JETP **46** (1977) 641 (cit. on p. 12).

[52] V. Gribov and L. Lipatov, *Deep inelastic electron scattering in perturbation theory*,
Physics Letters B **37** (1971) 78 (cit. on p. 12).

[53] G. Altarelli and G. Parisi, *Asymptotic freedom in parton language*,
Nuclear Physics B **126** (1977) 298 (cit. on p. 12).

[54] M. Czakon and A. Mitov,
Top++: A program for the calculation of the top-pair cross-section at hadron colliders,
Comput. Phys. Commun. **185** (2014) 2930, arXiv: `1112.5675` `[hep-ph]` (cit. on p. 13).

[55] ATLAS Collaboration, *Top working group cross-section summary plots June 2022*, 2022,
URL: `https://cds.cern.ch/record/2812502` (cit. on p. 14).

[56] C. Monini, *Single-top s channel cross-section measurement with the ATLAS detector*,
PhD Thesis: Grenoble Alpes University, 2014,
URL: `https://cds.cern.ch/record/1973623` (cit. on p. 15).

[57] C. Bierlich et al., *A comprehensive guide to the physics and usage of PYTHIA 8.3*, (2022),
arXiv: `2203.11601` `[hep-ph]` (cit. on pp. 18, 21).

[58] B. Andersson, G. Gustafson, G. Ingelman and T. Sjöstrand,
Parton fragmentation and string dynamics, Phys. Rept. **97** (1983) 31 (cit. on p. 19).

[59] B. Webber, *A QCD model for jet fragmentation including soft gluon interference*,
Nuclear Physics B **238** (1984) 492, ISSN: 0550-3213 (cit. on p. 19).

[60] D. Amati and G. Veneziano, *Preconfinement as a property of perturbative QCD*,
Phys. Lett. B **83** (1979) 87 (cit. on p. 19).

[61] T. Sjöstrand, L. Lönnblad and S. Mrenna, *PYTHIA 6.2 physics and manual*, (2001),
arXiv: `hep-ph/0108264` (cit. on p. 19).

[62] P. Nason, *A new method for combining NLO QCD with shower Monte Carlo algorithms*,
JHEP **11** (2004) 040, arXiv: `hep-ph/0409146` (cit. on p. 20).

[63] S. Frixione, P. Nason and C. Oleari,
Matching NLO QCD computations with parton shower simulations: the POWHEG method,
JHEP **11** (2007) 070, arXiv: `0709.2092` `[hep-ph]` (cit. on p. 20).

[64] J. Alwall et al., *The automated computation of tree-level and next-to-leading order differential
cross sections, and their matching to parton shower simulations*, JHEP **07** (2014) 079,
arXiv: `1405.0301` `[hep-ph]` (cit. on p. 20).

[65] M. Bähr et al., *Herwig++ physics and manual*, Eur. Phys. J. C **58** (2008) 639,
arXiv: `0803.0883` `[hep-ph]` (cit. on p. 20).

[66] D. J. Lange, *The EvtGen particle decay simulation package*,
Nucl. Instrum. Meth. A **462** (2001) 152 (cit. on p. 20).

[67] A. Buckley et al., *General-purpose event generators for LHC physics*,
Phys. Rept. **504** (2011) 145, arXiv: `1101.2599` `[hep-ph]` (cit. on p. 21).

[68] Christiansen, Jesper R. and Sjöstrand, Torbjörn, *Color reconnection at future $e^+ e^-$ colliders*,
Eur. Phys. J. C **75** (2015) 441, arXiv: `1506.09085` (cit. on pp. 21, 23).

[69] Jesper R. Christiansen and Peter Z. Skands, *String formation beyond leading colour*,
J. Phys. Conf. Ser. **8** (2015) 032014, arXiv: `1505.01681` `[hep-ph]` (cit. on pp. 22, 23).

[70] Gieseke, Stefan and Röhr, Christian and Siódmok, Andrzej,
Colour reconnections in Herwig++, Eur. Phys. J. C **72** (2012) 2225,
arXiv: `1206.0041` `[hep-ph]` (cit. on pp. 24–26).

[71] S. Gieseke, P. Kirchgaesser and S. Plätzer, *Baryon production from cluster hadronisation*,
Eur. Phys. J. C **78** (2018) 99, arXiv: `1710.10906` `[hep-ph]` (cit. on p. 25).

[72] J. Bellm, C. B. Duncan, S. Gieseke, M. Myska and A. Siódmok,
Spacetime colour reconnection in Herwig 7, Eur. Phys. J. C **79** (2019) (cit. on p. 25).

[73] R. D. Ball et al., *Parton distributions for the LHC run II*, JHEP **04** (2015) 040,
arXiv: `1410.8849` `[hep-ph]` (cit. on pp. 26, 98).

[74] ATLAS Collaboration, *Studies on top-quark Monte Carlo modelling for Top2016*,
ATL-PHYS-PUB-2016-020, 2016, URL: `https://cds.cern.ch/record/2216168`
(cit. on p. 26).

[75] ATLAS Collaboration, *New ATLAS event generator tunes to 2010 data*,
ATL-PHYS-PUB-2011-008, 2011, URL: `https://cds.cern.ch/record/1345343`
(cit. on p. 26).

[76] R. D. Ball et al., *Parton distributions with LHC data*, Nucl. Phys. B **867** (2013) 244,
arXiv: `1207.1303` `[hep-ph]` (cit. on p. 26).

[77] L. Harland-Lang, A. Martin, P. Motylinski and R. Thorne,
Parton distributions in the LHC era: MMHT 2014 PDFs, Eur. Phys. J. C **75** (2015) 204,
arXiv: `1412.3989` `[hep-ph]` (cit. on pp. 26, 98).

[78] J. Bellm et al., *Herwig 7.1 Release Note*, (2017), arXiv: `1705.06919` `[hep-ph]`
(cit. on pp. 26, 107).

[79] ATLAS Collaboration, *A study of different colour reconnection settings for Pythia8 generator
using underlying event observables*, ATL-PHYS-PUB-2017-008, 2017,
URL: `https://cds.cern.ch/record/2262253` (cit. on pp. 26, 109).

[80] ATLAS Collaboration, *ATLAS Pythia 8 tunes to 7 TeV data*, ATL-PHYS-PUB-2014-021,
2014, URL: `https://cds.cern.ch/record/1966419` (cit. on pp. 26, 112).

[81] S. Frixione, E. Laenen, P. Motylinski, C. White and B. R. Webber,
Single-top hadroproduction in association with a W boson, JHEP **07** (2008) 029,
arXiv: `0805.3067` `[hep-ph]` (cit. on pp. 27, 100).

[82] N. Kidonakis and N. Yamanaka,
      Higher-order corrections for tW production at high-energy hadron colliders,
      JHEP **05** (2021) 278, arXiv: `2102.11300` [`hep-ph`] (cit. on p. 27).

[83] D. de Florian et al.,
      Handbook of LHC Higgs Cross Sections: 4. Deciphering the Nature of the Higgs Sector,
      (2016), arXiv: `1610.07922` [`hep-ph`] (cit. on p. 27).

[84] S. Myers, *The LEP Collider, from design to approval and commissioning*, CERN, 1991,
      URL: `https://cds.cern.ch/record/226776` (cit. on p. 29).

[85] CMS Collaboration,
      The CMS experiment at the CERN LHC. The Compact Muon Solenoid experiment,
      JINST **3** (2008) S08004. 361 p (cit. on p. 29).

[86] LHCb Collaboration, *The LHCb Detector at the LHC*, JINST **3** (2008) S08005 (cit. on p. 29).

[87] ALICE Collaboration,
      The ALICE experiment at the CERN LHC. A Large Ion Collider Experiment,
      JINST **3** (2008) S08002. 259 p (cit. on p. 29).

[88] E. A. Mobs, *The CERN accelerator complex. Complexe des accélérateurs du CERN*, (2016),
      URL: `https://cds.cern.ch/record/2225847` (cit. on p. 30).

[89] R. Bruce et al., "LHC Run 2: Results and challenges", *57th ICFA Advanced Beam Dynamics
      Workshop on High-Intensity and High-Brightness Hadron Beams*, 2016 MOAM5P50
      (cit. on p. 31).

[90] *ATLAS Luminosity Public Results*, URL: `https://twiki.cern.ch/twiki/bin/view/AtlasPublic/LuminosityPublicResultsRun2`
      (cit. on pp. 31, 38, 41).

[91] ATLAS Collaboration, *ATLAS Inner Detector: Technical Design Report, Volume 1*,
      ATLAS-TDR-4; CERN-LHCC-97-016, 1997,
      URL: `https://cds.cern.ch/record/331063` (cit. on p. 33).

[92] B. Abbott et al., *Production and integration of the ATLAS Insertable B-Layer*,
      JINST **13** (2018) T05008, arXiv: `1803.00844` [`physics.ins-det`] (cit. on p. 34).

[93] ATLAS Collaboration, *ATLAS Liquid Argon Calorimeter: Technical Design Report*,
      ATLAS-TDR-2; CERN-LHCC-96-041, 1996,
      URL: `https://cds.cern.ch/record/331061` (cit. on p. 35).

[94] ATLAS Collaboration, *ATLAS Muon Spectrometer: Technical Design Report*,
      ATLAS-TDR-10; CERN-LHCC-97-022, CERN, 1997,
      URL: `https://cds.cern.ch/record/331068` (cit. on p. 36).

[95] ATLAS Collaboration, *ATLAS Level-1 Trigger: Technical Design Report*,
      ATLAS-TDR-12; CERN-LHCC-98-014, 1998,
      URL: `https://cds.cern.ch/record/381429` (cit. on p. 37).

[96] ATLAS Collaboration,
      ATLAS High-Level Trigger, Data Acquisition and Controls: Technical Design Report,
      ATLAS-TDR-16; CERN-LHCC-2003-022, 2003,
      URL: `https://cds.cern.ch/record/616089` (cit. on p. 37).

[97] ATLAS Collaboration, *Luminosity determination in pp collisions at $\sqrt{s} = 13\,TeV$ using the ATLAS detector at the LHC*, ATLAS-CONF-2019-021, 2019, URL: https://cds.cern.ch/record/2677054 (cit. on pp. 37, 95).

[98] ATLAS Collaboration, *Performance of the ATLAS muon triggers in Run 2*, JINST **15** (2020) P09015, arXiv: 2004.13447 [hep-ex] (cit. on p. 37).

[99] ATLAS Collaboration, *Performance of electron and photon triggers in ATLAS during LHC Run 2*, Eur. Phys. J. C **80** (2020) 47, arXiv: 1909.00761 [hep-ex] (cit. on p. 37).

[100] GEANT4 Collaboration, S. Agostinelli et al., *GEANT4 – a simulation toolkit*, Nucl. Instrum. Meth. A **506** (2003) 250 (cit. on p. 37).

[101] ATLAS Collaboration, *The simulation principle and performance of the ATLAS fast calorimeter simulation FastCaloSim*, ATL-PHYS-PUB-2010-013, 2010, URL: https://cds.cern.ch/record/1300517 (cit. on p. 38).

[102] ATLAS Collaboration, *The Pythia 8 A3 tune description of ATLAS minimum bias and inelastic measurements incorporating the Donnachie–Landshoff diffractive model*, ATL-PHYS-PUB-2016-017, 2016, URL: https://cds.cern.ch/record/2206965 (cit. on p. 38).

[103] J. Pequenao and P. Schaffner, "How ATLAS detects particles: diagram of particle paths in the detector", 2013, URL: https://cds.cern.ch/record/1505342 (cit. on p. 40).

[104] R. Frühwirth, *Application of Kalman filtering to track and vertex fitting*, Nucl. Instrum. Meth. A **262** (1987) 444 (cit. on pp. 39, 45).

[105] ATLAS Collaboration, *Performance of the ATLAS track reconstruction algorithms in dense environments in LHC Run 2*, Eur. Phys. J. C **77** (2017) 673, arXiv: 1704.07983 [hep-ex] (cit. on pp. 40, 93).

[106] T. Cornelissen et al., *The new ATLAS track reconstruction (NEWT)*, J. Phys. Conf. Ser. **119** (2008) 032014, ed. by R. Sobie, R. Tafirout and J. Thomson (cit. on p. 40).

[107] ATLAS Collaboration, *Early Inner Detector Tracking Performance in the 2015 Data at $\sqrt{s} = 13\,TeV$*, ATL-PHYS-PUB-2015-051, 2015, URL: https://cds.cern.ch/record/2110140 (cit. on pp. 41, 59, 93, 94).

[108] L. de Nooij, *The $\Phi(1020)$-meson production cross section measured with the ATLAS detector at $\sqrt{S} = 7\,TeV$*, PhD Thesis: University of Amsterdam, 2014, URL: https://cds.cern.ch/record/1701359 (cit. on p. 41).

[109] S. Boutle et al., *Primary vertex reconstruction at the ATLAS experiment*, J. Phys. Conf. Ser. **898** (2017) 042056, ed. by R. Mount and C. Tull (cit. on p. 41).

[110] R. Fruhwirth, W. Waltenberger and P. Vanlaer, *Adaptive vertex fitting*, J. Phys. G **34** (2007) N343 (cit. on p. 41).

[111] ATLAS Collaboration,
       Vertex Reconstruction Performance of the ATLAS Detector at $\sqrt{s}$ = 13 TeV,
       ATL-PHYS-PUB-2015-026, 2015, URL: https://cds.cern.ch/record/2037717
       (cit. on p. 42).

[112] ATLAS Collaboration, *Electron and photon performance measurements with the ATLAS
       detector using the 2015–2017 LHC proton–proton collision data*, JINST **14** (2019) P12006,
       arXiv: 1908.00005 [hep-ex] (cit. on p. 42).

[113] ATLAS Collaboration, *Electron and photon energy calibration with the ATLAS detector using
       2015-2016 LHC proton-proton collision data*, JINST **14** (2018) P03017. 61 p,
       arXiv: 1812.03848 [hep-ex] (cit. on p. 42).

[114] ATLAS Collaboration, *Electron and photon reconstruction and performance in ATLAS using
       a dynamical, topological cell clustering-based approach*, ATL-PHYS-PUB-2017-022, 2017,
       URL: https://cds.cern.ch/record/2298955 (cit. on p. 43).

[115] ATLAS Collaboration, *Muon reconstruction performance of the ATLAS detector in
       proton–proton collision data at $\sqrt{s}$ = 13 TeV*, Eur. Phys. J. C **76** (2016) 292,
       arXiv: 1603.05598 [hep-ex] (cit. on pp. 43, 44, 95).

[116] ATLAS Collaboration, *Muon reconstruction and identification efficiency in ATLAS using the
       full Run 2 pp collision data set at $\sqrt{s}$ = 13 TeV*, Eur. Phys. J. C **81** (2021) 578,
       arXiv: 2012.00578 [hep-ex] (cit. on pp. 43, 44).

[117] ATLAS Collaboration,
       Jet reconstruction and performance using particle flow with the ATLAS Detector,
       Eur. Phys. J. C **77** (2017) 466, arXiv: 1703.10485 [hep-ex] (cit. on p. 44).

[118] M. Cacciari, G. P. Salam and G. Soyez, *The anti-k_t jet clustering algorithm*,
       JHEP **04** (2008) 063, arXiv: 0802.1189 [hep-ph] (cit. on pp. 44, 47).

[119] M. Cacciari, G. P. Salam and G. Soyez, *FastJet user manual*, Eur. Phys. J. C **72** (2012) 1896,
       arXiv: 1111.6097 [hep-ph] (cit. on p. 44).

[120] G. P. Salam, *Towards Jetography*, Eur. Phys. J. C **67** (2010) 637,
       arXiv: 0906.1833 [hep-ph] (cit. on p. 44).

[121] F. Nechansky, *Search for the production of a Higgs boson decaying into a pair of bottom
       quarks in association with a pair of top quarks at 13 TeV with the ATLAS detector*,
       Presented 07 Apr 2021, PhD Thesis: Humboldt-Universität zu Berlin, 2021,
       URL: https://cds.cern.ch/record/2783832 (cit. on pp. 45, 46).

[122] ATLAS Collaboration, *Jet energy scale and resolution measured in proton–proton collisions
       at $\sqrt{s}$ = 13 TeV with the ATLAS detector*, (2020), arXiv: 2007.02645 [hep-ex]
       (cit. on p. 45).

[123] ATLAS Collaboration, *Performance of pile-up mitigation techniques for jets in pp collisions
       at $\sqrt{s}$ = 8 TeV using the ATLAS detector*, Eur. Phys. J. C **76** (2016) 581,
       arXiv: 1510.03823 [hep-ex] (cit. on pp. 45, 94).

[124] ATLAS Collaboration, *ATLAS b-jet identification performance and efficiency measurement
       with t$\bar{t}$ events in pp collisions at $\sqrt{s}$ = 13 TeV*, Eur. Phys. J. C **79** (2019) 970,
       arXiv: 1907.05120 [hep-ex] (cit. on pp. 45, 46).

[125] ATLAS Collaboration, *Topological b-hadron decay reconstruction and identification of b-jets with the JetFitter package in the ATLAS experiment at the LHC*, ATL-PHYS-PUB-2018-025, 2018, URL: `https://cds.cern.ch/record/2645405` (cit. on p. 45).

[126] ATLAS Collaboration, *Monte Carlo to Monte Carlo scale factors for flavour tagging efficiency calibration*, ATL-PHYS-PUB-2020-009, 2020, URL: `https://cds.cern.ch/record/2718610` (cit. on p. 46).

[127] ATLAS Collaboration, *Measurement of the $t\bar{t}$ production cross-section and lepton differential distributions in $e\mu$ dilepton events from pp collisions at $\sqrt{s} = 13\,TeV$ with the ATLAS detector*, Eur. Phys. J. C **80** (2020) 528, arXiv: `1910.08819` [`hep-ex`] (cit. on pp. 47, 54, 56, 100).

[128] C. Bierlich et al., *Robust Independent Validation of Experiment and Theory: Rivet version 3*, SciPost Phys. **8** (2020) 026, arXiv: `1912.05451` [`hep-ph`] (cit. on p. 48).

[129] ATLAS Collaboration, *Measurements of top-quark pair differential and double-differential cross-sections in the ℓ+jets channel with pp collisions at $\sqrt{s} = 13\,TeV$ using the ATLAS detector*, Eur. Phys. J. C **79** (2019) 1028, arXiv: `1908.07305` [`hep-ex`] (cit. on p. 56).

[130] ATLAS Collaboration, *Differential $t\bar{t}$ cross-section measurements using boosted top quarks in the all-hadronic final state with $139\,fb^{-1}$ of ATLAS data*, (2022), arXiv: `2205.02817` [`hep-ex`] (cit. on p. 56).

[131] ATLAS Collaboration, *Measurements of top-quark pair differential cross-sections in the lepton+jets channel in pp collisions at $\sqrt{s} = 8\,TeV$ using the ATLAS detector*, Eur. Phys. J. C **76** (2016) 538, arXiv: `1511.04716` [`hep-ex`] (cit. on p. 56).

[132] CMS Collaboration, *Inclusive and differential cross section measurements of single top quark production in association with a Z boson in proton–proton collisions at $\sqrt{s} = 13\,TeV$*, JHEP **02** (2021) 107, arXiv: `2111.02860` [`hep-ex`] (cit. on p. 56).

[133] CMS Collaboration, *Measurement of differential $t\bar{t}$ production cross sections using top quarks at large transverse momenta in pp collisions at $\sqrt{s} = 13\,TeV$*, Phys. Rev. D **103** (2021) 052008, arXiv: `2008.07860` [`hep-ex`] (cit. on p. 56).

[134] CMS Collaboration, *Measurements of $t\bar{t}$ differential cross sections in proton–proton collisions at $\sqrt{s} = 13\,TeV$ using events containing two leptons*, JHEP **02** (2019) 149, arXiv: `1811.06625` [`hep-ex`] (cit. on p. 56).

[135] CMS Collaboration, *Measurement of the differential cross section for top quark pair production in pp collisions at $\sqrt{s} = 8\,TeV$*, Eur. Phys. J. C **75** (2015) 542, arXiv: `1505.04480` [`hep-ex`] (cit. on p. 56).

[136] S. Catani, S. Devoto, M. Grazzini, S. Kallweit and J. Mazzitelli, *Top-quark pair production at the LHC: Fully differential QCD predictions at NNLO*, JHEP **07** (2019) 100, arXiv: `1906.06535` [`hep-ph`] (cit. on p. 56).

[137] M. Czakon et al., *Top-pair production at the LHC through NNLO QCD and NLO EW*, JHEP **10** (2017) 186, arXiv: `1705.04105` [`hep-ph`] (cit. on p. 56).

[138] M. Czakon, D. Heymes and A. Mitov,
Dynamical scales for multi-TeV top-pair production at the LHC, JHEP **04** (2017) 071,
arXiv: `1606.03350` `[hep-ph]` (cit. on p. 56).

[139] M. Czakon, D. Heymes and A. Mitov,
High-precision Differential Predictions for Top-Quark Pairs at the LHC,
Phys. Rev. Lett. **116** (2016) 082003, arXiv: `1511.00549` `[hep-ph]` (cit. on p. 56).

[140] M. Czakon, P. Fiedler and A. Mitov,
Total Top-Quark Pair-Production Cross Section at Hadron Colliders Through $O(\alpha_S^4)$,
Phys. Rev. Lett. **110** (2013) 252004, arXiv: `1303.6254` `[hep-ph]` (cit. on p. 56).

[141] ATLAS Collaboration, *Characterization of Interaction-Point Beam Parameters Using the pp
Event-Vertex Distribution Reconstructed in the ATLAS Detector at the LHC*,
ATLAS-CONF-2010-027, 2010, URL: `https://cds.cern.ch/record/1277659`
(cit. on pp. 62, 67).

[142] *ATLAS Beam Spot Public Results*, URL:
`https://twiki.cern.ch/twiki/bin/view/AtlasPublic/BeamSpotPublicResults`
(cit. on p. 63).

[143] G. Cowan, *Statistical data analysis*, 1998, ISBN: 978-0-19-850156-5 (cit. on pp. 77, 78).

[144] G. D'Agostini, *A multidimensional unfolding method based on Bayes' theorem*,
Nucl. Instrum. Meth. A **362** (1995) 487, ISSN: 0168-9002 (cit. on pp. 77, 79).

[145] A. Tarek, *Measurement of Higgs boson production cross sections in the diphoton channel
with the full ATLAS Run-2 data and constraints on anomalous Higgs boson interactions*,
PhD Thesis: Paris City University, 2019, URL: `https://cds.cern.ch/record/2696211`
(cit. on p. 77).

[146] G. D'Agostini, "Improved iterative Bayesian unfolding",
Alliance Workshop on Unfolding and Data Correction, 2010,
arXiv: `1010.0632` `[physics.data-an]` (cit. on p. 79).

[147] S. Schmitt, *Data Unfolding Methods in High Energy Physics*,
EPJ Web Conf. **137** (2017) 11008, ed. by Y. Foka, N. Brambilla and V. Kovalenko,
arXiv: `1611.01927` `[physics.data-an]` (cit. on p. 79).

[148] T. Adye, "Unfolding algorithms and tests using RooUnfold",
*Proceedings, 2011 Workshop on Statistical Issues Related to Discovery Claims in Search
Experiments and Unfolding (PHYSTAT 2011)*
(CERN, Geneva, Switzerland, 17th–20th Jan. 2011) 313,
arXiv: `1105.1160` `[physics.data-an]` (cit. on p. 82).

[149] ATLAS Collaboration, *Alignment of the ATLAS Inner Detector in Run-2*,
Eur. Phys. J. C **80** (2020) 1194, arXiv: `2007.07624` `[hep-ex]` (cit. on p. 94).

[150] ATLAS Collaboration, *Jet energy scale measurements and their systematic uncertainties in
proton–proton collisions at $\sqrt{s} = 13$ TeV with the ATLAS detector*,
Phys. Rev. D **96** (2017) 072002, arXiv: `1703.09665` `[hep-ex]` (cit. on p. 94).

[151] ATLAS Collaboration,
Jet energy measurement with the ATLAS detector in proton–proton collisions at $\sqrt{s}$ = 7 TeV,
Eur. Phys. J. C **73** (2013) 2304, arXiv: `1112.6426` `[hep-ex]` (cit. on p. 94).

[152] ATLAS Collaboration, *Electron efficiency measurements with the ATLAS detector using the 2015 LHC proton–proton collision data*, ATLAS-CONF-2016-024, 2016,
URL: `https://cds.cern.ch/record/2157687` (cit. on p. 95).

[153] G. Avoni et al.,
The new LUCID-2 detector for luminosity measurement and monitoring in ATLAS,
JINST **13** (2018) P07017 (cit. on p. 95).

[154] J. Butterworth et al., *PDF4LHC recommendations for LHC Run II*,
J. Phys. G **43** (2016) 023001, arXiv: `1510.03865` `[hep-ph]` (cit. on p. 98).

[155] S. Dulat et al.,
New parton distribution functions from a global analysis of quantum chromodynamics,
Phys. Rev. D **93** (2016) 033006, arXiv: `1506.07443` `[hep-ph]` (cit. on p. 98).

[156] J. Bellm et al., *Herwig 7.2 release note*, Eur. Phys. J. C **80** (2020) 452,
arXiv: `1912.06509` `[hep-ph]` (cit. on p. 107).

[157] J. Bellm, S. Gieseke and P. Kirchgaesser,
Improving the description of multiple interactions in Herwig, Eur. Phys. J. C **80** (2020) 469,
arXiv: `1911.13149` `[hep-ph]` (cit. on p. 107).

[158] ATLAS Collaboration, *Luminosity determination for low-pileup datasets at $\sqrt{s}$ = 5 and 13 TeV using the ATLAS detector at the LHC*, ATLAS-CONF-2020-023, 2020,
URL: `https://cds.cern.ch/record/2725195` (cit. on p. 122).

List of Figures

List of Tables

Acknowledgements